(2)

The Institution of Engineers, Australia

DSTO AUSTRALIA

CSIRO

WORKSHOP ON LASER DIAGNOSTICS IN FLUID MECHANICS AND COMBUSTION

PROCEEDINGS

DSTO Aeronautical Research Laboratory
Fishermens Bend, Victoria

30 September - 1 October 1993

AR-008-393

Errata

p5. First line of §2.3 | χ_{CARS} |^2 should read:
In order to be able to apply eqn(19)....

p6. Eqn (23) should read:

$$\chi_j^{(R)} = \mathcal{A}_j \left[\frac{1}{2\Delta\omega_j - i\Gamma_j} \right]$$

p9. The 6th line of the second paragraph in §3 should read:
The dye spectrum is centred at the desired Stokes wavelength.....

p14. 6th line down below the figure 9 should read:
...simultaneously. One of the.....

AR-008-393

PROCEEDINGS OF WORKSHOP ON LASER DIAGNOSTICS IN FLUID MECHANICS AND COMBUSTION

Held at

DSTO Aeronautical Research Laboratory
Fishermens Bend, Victoria

30 September - 1 October 1993

FOREWORD

The development of laser-based methods for observation and measurement of fluid dynamic phenomena has provided new dimensions to experimental research into both reacting and non-reacting flows. The timeliness of this meeting, and the opportunity it provides for exchange between present and aspiring practitioners in the field, has been amply demonstrated by its popularity. Perhaps this will prove to be the first in a series of Australian conferences on this important and growing topic.

ORGANISING COMMITTEE

Mr Sam Fisher	DSTO Aeronautical Research Laboratory
Dr Simon Henbest	DSTO Aeronautical Research Laboratory
Dr Damon Honnery	Monash University
Dr Yoss Morsi	Swinburne University of Technology
Dr David Thompson	DSTO Aeronautical Research Laboratory
Mr Laurie Welch	CSIRO Division of Building, Construction & Engineering

SPONSORS

IEAust National Committee on Applied Thermodynamics & Fluid Mechanics
DSTO Aeronautical Research Laboratory
CSIRO Division of Building, Construction & Engineering

The support of the following organisations is acknowledged:

Coherent Scientific Pty Ltd
Kenelec Pty Ltd
Lastek Pty Ltd
Spectra Physics Pty Ltd

TABLE OF CONTENTS

Paper No

INVITED LECTURES

SESSION PAPERS

* Paper not available at time of printing.

Accuracy of Laser Doppler Anemometry

Professor Klaus Bremhorst

Department of Mechanical Engineering
The University of Queensland
Brisbane Queensland 4072

ABSTRACT

A number of sources of errors encountered with laser Doppler anemometry (LDA) are examined but it is assumed that an optimised optical and electronic burst processing system is used. Of the errors controllable by the user, the most important is velocity bias. Assessment of this requires an estimate of the relevant integral scale to be available as well as the particle data rate for sample and hold processors. For controlled processors the signal sampling rate must also be known but it should be noted that bias due to this processor cannot be less than that for a sample and hold one. The need for adequate information is established so that users of data can make an independent assessment of the quality of data presented. In the case of multichannel measurements, it is necessary to present all velocity data able to be measured simultaneously for proper assessment of accuracy. This includes all mean velocities and Reynolds stresses as some errors such as clock bias may otherwise go undetected. A clear case exists for innovative and exacting hardware and software tests for regular checking of system performance.

INTRODUCTION

Laser Doppler anemometry is a well established tool for flow measurement. Although the method has been researched and discussed thoroughly, it continues to disappoint that few authors reporting measurements attend to the most basic requirement of modern experimental work, namely, an analysis or statement of errors. Consequently, most reported results should be treated with caution, especially, if used as benchmark data for comparison with mathematically derived flow variables from the Navier-Stokes equations.

The day is fast approaching when numerical solutions of the time dependant flow equations will be available for even the most complex of turbulent flows, at least, in the subsonic range. Experimentalists are already faced with the challenge (or humiliation) of trying to measure some computed variables for which no suitable measurement technique exists so far. Present indications are that this situation will get worse unless some major breakthroughs occur in the measurement of variables such as point pressure and dissipation rates of turbulent kinetic energy.

Although many variants of optical arrangements have been reported for LDA, the most commonly used one, and the one to be addressed here, is that based on the fringe mode. For multichannel measurements, optics can be based on colour separation of signals or on optical polarisation. The latter is less popular but is cheaper and gives excellent results for situations where beam repolarisation by the working fluid is not likely and the signal-to-noise ratio is high enough to give good data rate with no cross-talk. Matters addressed in

this paper apply equally well to both methods of signal separation. Results to be discussed apply to counter as well as Fourier transform based processors.

As a starting point it will be assumed that commercially available equipment is used which has optimised optics generally as described in the comprehensive text by Durst, Melling and Whitelaw(1981). This "eliminates" a large source of possible errors. Those remaining are, however, still formidable and include velocity bias, fringe bias, clock errors and hardware and software errors or malfunctions.

BASIC THEORY

The fringe or dual scatter system, heterodynes scattered light from particles passing through interference fringes generated by the intersection of two or more suitably conditioned laser beams originating from a single source. The process is expressed by Eq.(1) where f_D is the "Doppler" frequency, n, the refractive index of the medium, λ, the wavelength of light, V, the particle velocity vector, and n_{SC1} and n_{SC2} are the unit vectors in the directions of the beams.

$$f_D = \frac{nV}{\lambda} \cdot (n_{SC1} - n_{SC2}) \tag{1}$$

For a dual-beam setup with half angle $\phi/2$ between the beams and $n=1$, this reduces to Eq.(2) where U is the velocity component perpendicular to the fringes formed.

$$f_D = \frac{2}{\lambda} U \sin\frac{\phi}{2} \tag{2}$$

In the case of more than two beams, a correction is made to this formula but is not elaborated on here. Since wavelength and beam angles are available to a very high accuracy, the final measurement accuracy should depend only on the accuracy to which the refractive index of the medium is known.

VELOCITY MEASURED

One of the most important sources of errors with LDA is that the velocity of seed particles in the flow is measured and not the fluid velocity itself. Consequently, all results represent particle statistics. It then becomes of paramount importance to know the relation between particle and fluid velocities. The analysis by Hjelmfelt and Mockros (1966) forms a valuable guide. For water particles in air, it is found that the amplitude ratio of particle and fluid velocity fluctuations approaches unity below 812 Hz for a 7 μm diameter water particle. Since frequency and the square of particle diameter are inversely related, it may be assumed that a 2 μm water particle, as is sometimes used, will follow fluctuations up to 10 kHz. Phase lag is still significant at these frequencies with a value of 27°.

Many authors assume on the basis of more indirect evidence that particles used for a particular application will lead to negligible errors due to this effect. No systematic and definitive studies appear to be available as a universal guide. As the above predictions are a strong function of particle density relative to fluid density, results for water and air will not apply to tungsten, silicone carbide or titanium oxide seed particles in air but can be expected to be less favourable as the cut-off frequency is inversely related to the particle-to-fluid density ratio.

Measurements of turbulent kinetic energy are unlikely to be affected when using micrometer sized seed particles as the bulk of turbulent energy occurs at relatively low frequencies even in laboratory flows. Spectral measurements for assessment of turbulent dissipation are, however, very susceptible to this source of error as the dissipation spectrum has the bulk of its contribution at the higher frequency end of the spectrum, typically, in the kHz range.

STATISTICAL CONSIDERATIONS

Unlike hot-wire anemometer signals which are a continuous function of time or are available in sampled form usually with a fixed time interval between samples, LDA data are available only in discretized form. Each sample represents the velocity of a particle which has passed through the measuring volume and has satisfied certain quality criteria. Furthermore, the time interval between samples is not constant but is determined by the time between particles passing through the measuring volume and whether or not the quality criteria have been met. Consequently, the normal sampling theorems such as the Nyquist criterion, do not apply.

Application of time series analysis has been discussed in detail by George *et al* (1978) for statistically stationary flows to which the ergodic hypothesis applies. Their analysis is for a random time series for which random variables become uncorrelated at large time delays and the memory of the process can be quantified by means of an integral scale. If $R_u(\tau)$ denotes the autocorrelation coefficient of the random variable u, then the integral time scale, T_u is given by

$$T_u = \int_0^\infty R_u(\tau) d\tau \tag{3}$$

where τ is the time delay. For randomly sampled data with an average sample rate of ν, George *et al* (1978) showed that the relative error, ϵ, of a measured variable such as u is given by

$$\epsilon^2 = \frac{2T_u}{T}\left[1 + \frac{1}{2\nu T_u}\right]\left[\frac{\sigma_u}{\bar{u}}\right]^2 \tag{4}$$

where the relative error is the ratio of the standard deviation of the variable's mean obtained from a given number of samples of length T, to its true mean value and σ_u is the

standard deviation of the variable u. An interesting observation made by George *et al* (1978) is that statistically speaking, there are $T/(2T_u)$ independent samples in an average formed over time T.

Eq.(4) applies to computation of mean velocity as well as mean square values such as the mean square of a fluctuating component of velocity or the turbulent kinetic energy. Clearly, for mean and r.m.s. estimates, as $T \rightarrow \infty$, the exact value is approached. The same does not, however, apply for $\nu \rightarrow \infty$.

It is relatively straightforward then to obtain an estimate of the statistical error associated with each measurement which is based on a limited number of samples. Unless this error is quoted in data presented, a reader must have the relevant variables in Eq.(4) to be able to estimate these errors. It seems reasonable, therefore, to expect reports of LDA data to include such error estimates.

VELOCITY BIAS

McLaughlin and Tiederman (1973) first recognised this common source of error. It arises from the fact that LDA measures particle statistics rather than flow velocity directly. When the velocity fluctuates, the fluid volume flow rate through the measuring volume of an LDA also fluctuates. Consequently, the particle rate, and hence the number of particles registered by the measurement system, associated with a particular level of velocity, will depend on the velocity level. That is, a correlation exists between the number of particles or velocity samples detected for a given velocity level and the velocity level itself. Higher velocities lead to more data samples than low velocities. In a turbulent flow, this leads to bias towards the higher velocities resulting in overestimates of velocities

Several methods of dealing with the problem have been proposed. One such method uses inverse velocity weighting of individual velocity realisations, McLachlan and Tiederman (1973). Another uses residence weighting applied to individual realisations, George (1975) and Hoesel and Rodi (1977). A third is the sample and hold weighting method which weights each realisation with the time to the next realisation while the arrival time weighting method uses the time from the last to the present realisation.

The sample and hold processor has been analysed in detail by Edwards and Jensen (1983) and more recently by Winter *et al* (1991a). The latter also produced measurements in a jet to verify the model. A reliable criterion for bias free results for mean and r.m.s. measurements using the sample and hold processor method is that

$$\nu T_u > 5 \qquad (5)$$

where ν is the data rate as used in Eq.(4) and corresponds to the validation rate of a processor with no dead time, that is, it processes all valid Doppler bursts. An inherent and as yet unquantified assumption is made with respect to this result, namely, that particle rate and data rate can be used interchangeably. No investigation of this assumption appears to have been undertaken so far. The importance of the integral time

scale of the variable, u, is again witnessed. This criterion is insensitive to the variable's probability density distribution as well as shape of the measuring volume.

Often it may not be possible to process all valid data due to speed limitations of the processor. This leads to the controlled processor which, by use of a slower and periodic sampling rate than the average valid data rate, is designed to eliminate velocity bias, Stevenson *et al* (1982), Erdmann and Tropea (1981, 1984) and Edwards (1981, 1987). Winter *et al* (1991b) also analysed this technique and tested it experimentally in a jet flow. The latter work shows that for the controlled processor to produce bias free results, the following two criteria must be met,

$$\nu T_u > 5 \qquad \nu T_s > 5 \tag{6}$$

where T_s is the periodic sampling period, the magnitude of which exceeds $(\nu)^{-1}$ so that some of the validated data are rejected. Furthermore, it is assumed that only the first data realisation to arrive in a sampling interval will be used, the others being rejected. The first of these criteria is the same as for the sample and hold processor as expressed by Eq.(5). Consequently, it was concluded by Winter *et al* that the controlled processor will not produce any less bias than a sample and hold one ($\nu T_s > 5$) and no more than the unweighted (free-running) processor. Its advantage is that slow data processing equipment can be used with simplified interfacing as timing information is no longer required for weighting purposes.

FRINGE BIAS

A common test of Doppler burst quality is that a preset minimum number of fringes must be present in the burst with a signal level above some arbitrary signal threshold. In flows with large changes in the direction of the velocity vector, occurrences approaching a direction parallel to the fringes, will lead to insufficient fringes being present in the burst. These occurrences will be rejected by the validation circuit. This is a well known phenomenon, the reduction of its effect being achieved by frequency shifting. Perhaps it should be noted that for simultaneous measurement of two and three component velocities, optimal frequency shifting is most important when a dominant mean velocity component exists. This is frequently the case in boundary layer and jet flow measurements.

Complete elimination of fringe bias is not possible due to the ellipsoidal shape of the measuring volume. Particles contributing to a measurement pass through all sections of the measuring volume so that some degree of fringe bias will always be present. The extent of this does not appear to have been defined or tested. A formal expression of the problem for a velocity component u which is normal to the fringes, is given by Eq.(7). A coordinate system is assumed to be located at the centre of the ellipsoid, the effective measurement volume is denoted by MV, the location of any point in the measurement volume is denoted by the vector r and dv denotes an elemental volume for the integration.

Most reported measurements relate to $u(r=0)$ with no allowance for variations of u throughout MV either due to fringe effects or due to spatial variations of u Kreid (1974)

$$\bar{u}_{MV}(r) = \frac{1}{MV}\int_{MV} \bar{u}(r)\,dv \qquad (7)$$

predicted errors due to gradients in the measuring volume and verified these by means of measurements in laminar pipe flow. Another example of the importance due to spatial variation is given in Durst *et al* (1993) for near wall measurements with a high velocity gradient.

CLOCK ERRORS

Two sources of errors can occur, one is due to limited clock resolution and the other is due to clock induced bias. The latter has been detailed by Graham *et al* (1989) for counter type processors. It becomes noticeable when high shift frequencies must be used for low velocity components such as in pulsed jets or where a large mean velocity exists in another direction which reduces the residence time of a particle in the measuring volume. Graham *et al* (1989) found this error to lead to an apparent shift from symmetry of the radial component of velocity in a free jet. It is due to a small error in the clock pulse which can be adjusted out or determined as a calibration constant to be applied to each velocity realisation. When clock bias exists, the range of shift frequencies suitable for accurate velocity measurements is small or non-existent as small shift frequencies, which reduce the significance of clock resolution and bias errors, border on the region giving fringe bias, Graham *et al* (1989).

Since this source of error is most probable in multichannel measurements, it is most important to record and report all velocity components in order to allow users of such data to assess the quality of measurements. Regrettably, the literature abounds with LDA data for which no such checks are possible. Even for jet and boundary layer measurements, few authors report mean velocity measurements in the two directions normal to each other.

HARDWARE AND SOFTWARE ERRORS

The error just discussed is typical of a hardware error. Countless others can be identified in systems of the complexity of laser Doppler anemometers. Few are ever reported and very little effort is generally put into their identification by practitioners. No standardised performance tests are available against which individual users can test their apparatus on a regular basis. Similar comments apply to the extensive software used for interfacing to computers and for data reduction. The task is very much one left to each user to devise as seen fit. Few authors ever report test procedures or whether these have in fact been implemented.

CLOSING COMMENTS

A number of sources of errors encountered with LDA measurements have been discussed. Some are very much in the domain of the user while others are a function of the equipment design and can rarely be adjusted by the user. The latter must, therefore, be prepared to devise novel and exacting test methods to lend credibility to results obtained.

As seen from the dates of references used, many of the sources of errors have been known for many years. Their application, however, seems to be lagging considerably.

On the fluid mechanics side, any multichannel results reported without all velocity components capable of simultaneous measurement, should be treated with the utmost caution. In the case of clock errors discussed above, the error involved shows very clearly in the lower velocity direction, for example, the radial velocity in a free jet. A study of how this would affect other measured components such as turbulence components or Reynolds stresses, does not appear to exist but another essential yet simple check on such data is available at points of zero shear stress. If full data reporting is followed, users of the data can form their own opinions regarding quality. Perhaps it is fair to claim that experimentalists are on notice from CFD that accuracy is becoming a significant issue if the whole art of measurement is not to become an anachronism.

ACKNOWLEDGMENTS

The work was made possible through Australian Research Council funding of a laser Doppler anemometer when the technology was still in its infancy.

BIBLIOGRAPHY

Buchhave, P. and George, W.K., Jr. (1979) "The measurement of turbulence with the laser-Doppler anemometer", *Ann. Rev. Fluid Mech.*, **11**, 443-503.

Durst, F., Jovanovic, J. and Sender, J. (1993) "Detailed measurements of the near wall region of turbulent pipe flow", FED-Vol. 146, *Data for validation of CFD Codes*, ASME, 79-87.

Durst, F., Melling, A. and Whitelaw, J.H. (1981) *Principles and Practice of Laser-Doppler Anemometry*, Academic Press, London.

Edwards, R.V. (1981) "A new look at particle statistics in laser-anemometry measurements", *J. Fluid Mech.*, **105**, 317-325.

Edwards, R.V. (1987) "Report of the Special Panel on Statistical Particle Bias Problems in Laser Anemometry", *J. Fluids Eng., Trans. ASME*, **109**, 89-93.

Edwards, R.V. and Jensen, A.S. (1983) "Particle-sampling statistics in laser anemometers: Sample-and-hold and saturable systems", *J. Fluid Mech.*, **133**, 397-411.

Erdmann, J.C. and Tropea, C. (1981) "Statistical bias in laser anemometry", SFB 80/ET/198, August, Sonderforschungsbereich 80, Universität Karlsruhe, Germany.

Erdmann, J.C. and Tropea, C. (1984) "Statistical bias of the velocity distribution function in laser anemometry", in: *Laser anemometry in fluid mechanics*, 393-403, Lisbon, Ladoan.

George, W.K., Jr. (1975) "Limitations to measuring accuracy inherent in the laser Doppler signal", in *1976: Appl. of non-intrusive instrumentation in flow research*, AGARD CP-193, 20-63.

George, W.K., Jr., Beuther, P.D. and Lumley, J.L. (1978) "Processing of random signals", *Proceedings of the Dynamic Flow Conference*, Skovlunde, Denmark, 757-800.

Graham, L.J.W., Winter, A.R., Bremhorst, K. and Daniel, B.C. (1989) "Clock-induced bias errors in laser Doppler counter processors", *J. Phys. E: Sci. Instrum*, **22**, 394-397.

Hjelmfelt, A.T., Jr. and Mockros, L.F. (1966) "Motion of discrete particles in a turbulent fluid", *Appl. Sci. Res.*, **16**, 149-161.

Hoesel,W. and Rodi, W. (1977) "New biasing elimination method for laser-Doppler velocimeter counter processing", *Rev. Sci. Instrum.*, **48**, 910-919.

Kreid, D.K. (1974) "Laser-Doppler velocimeter measurements in non-uniform flow: error estimates", *Appl. Optics*, **8**, 1872-1881.

McLaughlin, D.K. and Tiederman, W.G., Jr. (1973) "Biasing corrections for individual realisations of laser anemometer measurement in turbulent flow", *Phys. Fluids*, **16**, 2082-2088.

Stevenson, W.H., Thompson, H.D. and Roesler, T.C. (1982) "Direct measurement of laser velocimeter bias errors in a turbulent flow", *AIAA J.*, **20**, 1720-1723.

Winter, A.R., Graham, L.J.W. and Bremhorst, K. (1991a) "Effects of time scales on velocity bias in LDA measurements using sample and hold processing", *Experiments in Fluids*, **11**, 147-152.

Winter, A.R., Graham, L.J.W. and Bremhorst, K. (1991b) "Velocity bias associated with laser Doppler anemometer controlled processors", *J. Fluids Eng., Trans, ASME*, **113**, June, 250-255.

APPLICATIONS OF RAMAN-RAYLEIGH-LIF DIAGNOSTICS IN COMBUSTION RESEARCH

A.R. Masri
Department of Mechanical and Mechatronic Engineering
The University of Sydney
NSW, 2006

Abstract

This paper describes various applications of the Raman-Rayleigh-LIF diagnostic techniques to measure temperature and species concentrations in flames. Joint, as well as independent applications of these techniques to perform single-point measurements are discussed. The calibration and data processing procedures required to quantify the measurements are also detailed. Sample data are presented and comments are made regarding future applications of these techniques.

Introduction

The usefulness of a combustion diagnostic technique is gauged by a number of factors which include its range and ease of applicability; accuracy and usefulness of the data it provides; and resolution of the measurements in both time and space. Judging by these criteria, the spontaneous Raman scattering technique stands out as one of the best currently available. It is linear, relatively simple to apply and accurate. The nonresonant nature of the excitation allows many species to be detected simultaneously at high temporal and spatial resolution. The major drawback however, is the weak Raman signals which limit the range of application to flame regions which are free from soot. Also, the measurements are limited to the concentration of major species with mole fractions higher than about 0.1% (Lapp and Penny 1974, Lederman 1977).

Laser Induced Fluorescence (LIF) yields signals which are orders of magnitude higher than the Raman ones due to the resonant excitation process. The technique has recently become a standard combustion diagnostic tool and the measurements are becoming quantitative for a larger number of species. The LIF process involves absorption of laser light at a specific wavelength followed by a delay period and then spontaneous emission. The emission spectrum of the species to be detected must therefore be known. A unique advantage for the LIF technique is that the detection limit of species concentrations is in the ppm range. Crosley (1992) gives an extensive list of species which are detectable with LIF. The criterion is that the absorption wavelength must be in a region accessible by lasers which cover the range $\sim$ 200nm to 1500nm. Multi-photon excitation techniques are also possible for the detection of species with absorption bands below 200nm. The species are not limited to minor intermediates and flame radicals. Some stable species like O_2 and CO are also amenable to LIF (Lee *et*

al. 1986, Haumann *et al.* 1986). This is extremely useful since CO is a major pollutant and it cannot be measured at low concentrations with the Raman technique.

Rayleigh scattering (from gaseous molecules) is elastic and has signals which are orders of magnitude stronger than Raman signals. However, it can only yield limited information on mixing in nonreacting flows. In reacting flows, it provides a measure of temperature assuming that the Rayleigh cross section in the mixture remains constant. This may be achieved by a judicious choice of the fuel mixture. The Rayleigh signal is also strongly affected by Mie scattering (from particles) which has a cross section many orders of magnitude higher than Rayleigh. The technique is therefore only applicable to clean flows where particles are absent (Eckbreth 1988).

These techniques may be complementary in the information they provide. The joint application of Raman-Rayleigh-LIF techniques to reacting flows has the potential to map the compositional structure of the flame including temperature and the concentration of major species as well as selected flame radicals. Although the optical set-up can become extremely complex, more than one radical species can be excited by LIF and monitored simultaneously. In this paper, the joint or separate application of the Raman-Rayleigh-LIF techniques to reacting flows will be discussed. The calibration process which is essential for obtaining quantitative information is also described. The discussion will be restricted to single-point measurements only. Planar measurements have also been made using these techniques but these are not mentioned here. Future applications and extensions to these techniques for single-point measurements are also discussed.

The Raman Technique

There has been numerous studies of the Raman technique and its applications which have mainly been restricted to measurements in simple flames of non-hydrocarbon fuels (Lapp and Penny 1974, Lederman 1977, Drake *et al.* 1984, Magre and Dibble 1987). In the past ten years, the range of applicability of the Raman technique has been extended to flames of hydrocarbon fuels with more complex flow geometries (Dibble *et al.* 1987, Masri *et al.* 1992a, Stårner *et al.* 1991). This is a major step forward considering that it allowed not only the study of fuels of practical interest but also opened the door for investigating turbulence-chemistry interaction in reacting flows. A subject at the forefront of combustion research. A further extension to the application of the Raman technique has been made recently with measurements performed in turbulent flames inhibited with CF_3Br. Species like CF_3Br, HBr and HF have been monitored as well.

Figure 1 shows the variation of the Raman wavelength of many species of interest with laser excitation wavelength. The visible and UV ranges are covered in Figs. 1a and 1b respectively. The vertical lines shown in Figs. 1a and 1b are absorption bands for diatomic carbon C_2, and the CH radical respectively. Both C_2 and CH, as well as other molecules, are responsible for the fluorescence interference on the Raman signals. The $C-H$ stretch bands cover hydrocarbon fuels like CH_4, C_3H_8, CH_3OH and C_2H_5OH. The $C-F$ band covers CF_3Br and CF_3H. The same species are shown in Figs. 1a and 1b. The separation between the Raman lines of various species becomes smaller in the UV excitation region hence requiring smaller detection probes.

The vibrational Raman frequency and scattering cross section of many species are shown in Table 1 (Schrötter and Klöckner 1979). The Raman cross section of species

i, $d\sigma/d\Omega$ in cm^2/sr is given by:

$$\frac{d\sigma}{d\Omega} = (\nu_0 - \nu_i)^4 \times 10^{-48} \times K_i \tag{1}$$

where ν_0 is the laser source frequency in wavenumbers, ν_i is the Raman frequency shift of species i in wavenumbers and K_i is a factor for species i. Values of K_i as well as the Raman cross section, $d\sigma/d\Omega$ at various wavelength are listed in Table 1. Although the inverse fourth power dependence of $d\sigma/d\Omega$ favours shorter laser wavelength, the laser energy available in the UV ranges is far lower than that available in the visible and the overall Raman signal strength is roughly similar. Cheng *et al.* (1992) have performed Raman measurements in various turbulent flames of hydrogen fuels using UV laser sources. Broadening of the Raman spectrum at high temperature, or the existence of other Raman lines for a molecule due to rotational shifts, may cause interferences on other species. Methane, for example, always interferes with O_2 and CO_2 while N_2 interferes with CO at high temperature only. Species affected by Raman interferences are listed Table 1. Also shown in Table 1 are the Rayleigh scattering cross sections, γ_i.

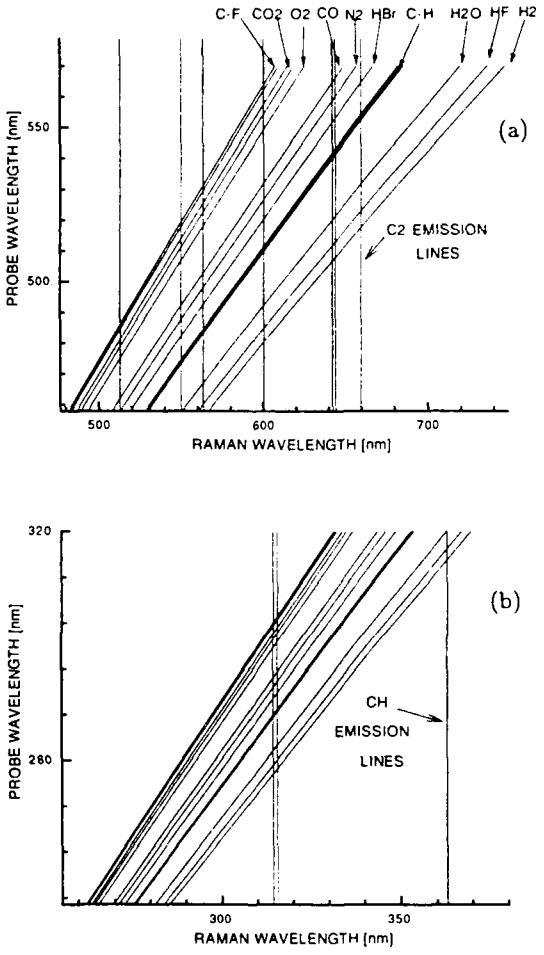

Figure 1: Variation of the vibrational Raman wavelength of selected molecules with laser wavelength. The visible and UV excitation ranges are shown in Figs. 1a and 1b respectively. Vertical lines in Fig. 1a are absorption lines of C_2 while those in Fig. 1b are absorption lines of CH.

Table 1: Vibrational Raman frequency shifts of selected species along with K_i and the Raman cross sections, $d\sigma/d\Omega$ at various laser wavelengths. Rayleigh scattering cross sections, γ_i at 532nm and the species affected by Raman interferences are also tabulated (superscript * indicates high temperature interference only).

Species	Raman Shift (cm^{-1})	K_i	$d\sigma/d\Omega$ ($cm^2/sr \times 10^{-30}$) 248nm	488nm	532nm	Raman Interference on	$\gamma_i \times 10^{-28}$ cm^2/sr (532nm)
H_2	4156	24	41.1	1.71	1.10	CO_2, O_2	1.32
HF	3962	9.6	16.8	0.72	0.46	-	6.3
H_2O	3652	18.6	33.6	1.50	0.98	-	4.4
CH_3OH	2955	43.7	85.2	4.13	2.75	O_2, H_2O	20.3
C_2H_5OH	2943	90	176	8.53	5.68	O_2, H_2O	51.0
CH_4	2917	41.6	81.4	3.97	2.65	O_2, CO_2	13.4
C_3H_8	2890	28.1	55.2	2.70	1.80	O_2, CO_2	79.0
HBr	2558	23.4	47.6	2.42	1.63	-	24.9
N_2	2331	5.05	10.5	0.55	0.37	CO^*	6.1
CO	2143	4.42	9.4	0.51	0.34	-	7.8
O_2	1555	4.81	10.9	0.62	0.42	CO_2^*	5.0
CO_2	1388	4.96	11.4	0.66	0.46	O_2^*	14.0
	1286	3.16	7.3	0.43	0.30	-	
CF_3Br	1207	3.6	8.4	0.50	0.34	CO_2	52.0
	1108	4.2	9.9	0.59	0.41	-	

Raman Measurements

The experiments described here have been performed at the Combustion Research Facility, Sandia National Laboratories, Livermore, CA. The facility laser, DIANA have been used at 532nm supplying one Joule of laser energy in a 2 μs pulse width. The measurement volume is a cylinder 1mm long and 0.5 mm in diameter. The monitored species are the hydrocarbon fuel, CO_2, O_2, CO, N_2, H_2O, H_2, HF, HBr, and CF_3Br are collected by photomultiplier (PM) tubes placed at the exit plane of the polychromator. A range of fuels have been investigated in two main flame geometries: a piloted flame configuration and a bluff-body recirculating flame configuration. The flames investigated range from ones with low mixing rates that are far from extinction to flames very close to blowoff. Further Details of the experimental set-up can be found in Masri *et al.* (1992b).

The simultaneous measurements of all stable species allows the determination of the mixture fraction, ξ which is a measure of how much mixing has occurred between the fuel and air stream. Mixture fraction is one in the fuel exit stream and zero in the air stream and it is calculated for each data point as follows:

$$\xi = \frac{\frac{2(Z_C - Z_{C,O})}{W_C} + \frac{(Z_H - Z_{H,O})}{2W_H} - \frac{(Z_O - Z_{O,O})}{W_O}}{\frac{2(Z_{C,F} - Z_{C,O})}{W_C} + \frac{(Z_{H,F} - Z_{H,O})}{2W_H} - \frac{(Z_{O,F} - Z_{O,O})}{W_O}} \quad (2)$$

where Z_i is a conserved scalar given by the total mass fraction of element i, and W_i is the molecular weight of element i. Subscripts F and O refer to the fuel and air streams,

respectively. This formulation preserves the stoichiometric value of the mixture fraction regardless of differential diffusion effects.

The Raman signals are affected by laser induced interference which may be due to flame chemiluminescence, nonresonant fluorescence and/or soot incandescence in flames of hydrocarbon fuels Masri *et al.* (1987). In order to correct for this interference, extra photomultiplier tubes are stationed around the Raman species to monitor the interference signals at 556nm, 583nm, 615nm and 672nm. These are referred to as F556, F583, F615 and F672, respectively. Figure 2a shows a scatter plot of F556 versus F583 obtained in a turbulent methane flame. The excellent correlation between the fluorescence interference monitors implies that only one monitor can be used to correct for all the Raman signals. Figures 2b, 2c and 2d show scatter plots for the raw Raman signals of CH_4, H_2O and O_2 plotted versus F583 for the same flame. A linear correlation exists between these Raman signals and the interference signals. This is also true for the remaining Raman lines not shown here. The solid lines shown on plots 2b, 2c and 2d represent the correction factors which will be used in data processing to remove the fluorescence on each of the Raman lines. This procedure is outlined in more detail in Dibble *et al.* (1990).

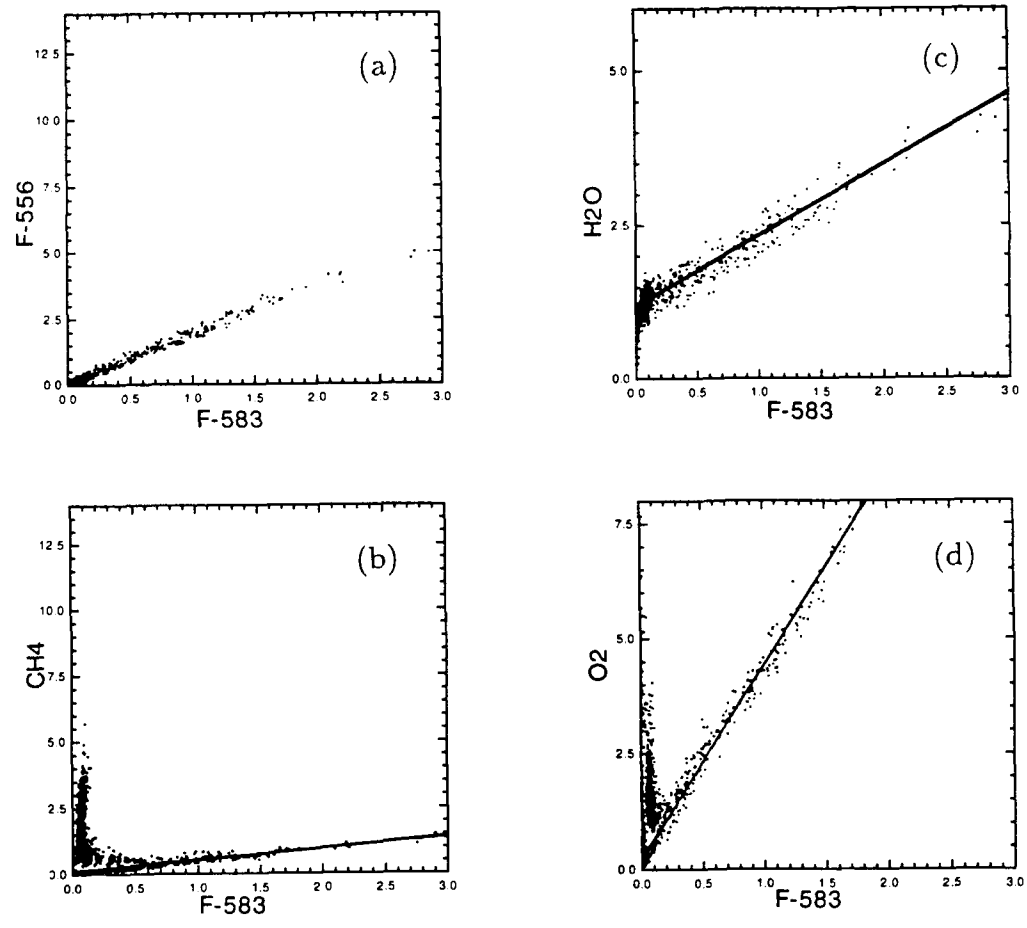

Figure 2: Scatter plots of the raw Raman signals from CH_4, H_2O and O_2 measured in a turbulent flame of CH_4 and plotted versus F-583 which monitors the fluorescence signal at 583nm. Also shown is the correlation between F-583 and F-556 which monitors the fluorescence signal at 556nm.

Calibration factors at a range of temperatures are generated for all the species except the hydrocarbon fuel. The procedure is described in detail in Dibble *et al.* (1990). A calibration factor for hydrocarbons can only be generated at a the fuel jet exit temperature since the hydrocarbon concentration is zero in the high temperature zone of premixed laminar flames used for calibration. The Raman interferences on other species are also corrected for on each data point. The species affected by Raman interferences are listed in Table 1. For each selected axial location in the flames, a few thousand data points are collected at one or more radial locations. Temperature is obtained from the Rayleigh signal as well as from the sum of the species number density.

The Raman/Rayleigh/LIF Technique

The main difficulty with quantifying the LIF measurements is in correcting for the collisional quenching of the species of interest. The fluorescence yield is reduced when the excited atom or molecule (which has a certain lifetime in its excited state) is quenched due to collisions with other species. The quenching rate depends on the temperature and the concentration of species in the measurement volume. The quenching cross section of various colliders are now well characterised for many species of interest like OH, CH, NO *etc* (Garland and Crosley 1986). If temperature and the concentration of the colliders is known then the quencing factor can be calculated. The number density of the species monitored by LIF, [i] is given by Barlow *at al.* (1990),

$$[i] = C_{ref} C_Q C_f \left(\frac{fluorescence\ signal}{laser\ energy}\right). \tag{3}$$

Here C_{ref} is a calibration constant obtained for species, i in a flame of known composition, C_Q is the quenching factor ratio: $C_Q = Q/\ Q_{ref}$ where

$$Q.Q_{ref} = C\Sigma X_i (TW_i)^{0.5} \delta_i(T). \tag{4}$$

Here C is a constant, X_i is the mole fraction of species i, $\delta_i(T)$ is quenching cross section of species i at temperature T and W_i its molecular weight. The ratio of the ground state population at the reference temperature as compared to the local temperature in the measurement volume, C_f is calculated using Boltzmann statistics. Since the mole fractions of the major species is also measured, the Rayleigh scattering cross section, $\gamma = \Sigma X_i \gamma_i$ can be calculated and the temperature can then be obtained from: $T = \gamma K_R / R$. Here K_R is a constant obtained from calibration and R is the measured Rayleigh signal. The Rayleigh cross section of selected species is also shown in Table 1.

Raman/Rayleigh/LIF Measurements

The joint Raman-Rayleigh-LIF single-point measurements described here have also been performed at Sandia's Combustion Research Facility. The Raman setup is as described earlier. The Rayleigh signal is measured separately and is prevented from entering the Raman spectrometer using a holographic filter. A beam from a Nd:YAG-pumped, frequency doubled dye laser is tuned to 283.63nm to excite one of the transitions of the hydroxyl radical, OH. The UV beam is collinear with the Raman beam, and

fluorescence from OH is collected on a photomultiplier tube at 317.0nm. The Q-switch from the Nd:YAG laser synchronises both the LIF-dye-laser and DIANA with a delay of $1\mu s$.

Measurements have been made in many flames with a range of fuel mixtures covering H_2, CO, CH_4, C_3H_8, CH_3OH and C_2H_5OH. Also, more recently flames of $CH_4 - CF_3Br$ have been investigated and a sample result is presented here for such flames. Figure 3 shows scatter plots for temperature and the mass fractions of H_2O, H_2, OH, CO, CO_2, HF and CF_3Br plotted versus mixture fraction, ξ. The laminar flamelet calculations for a simple flame of similar fuel mixture with low strain rate are shown

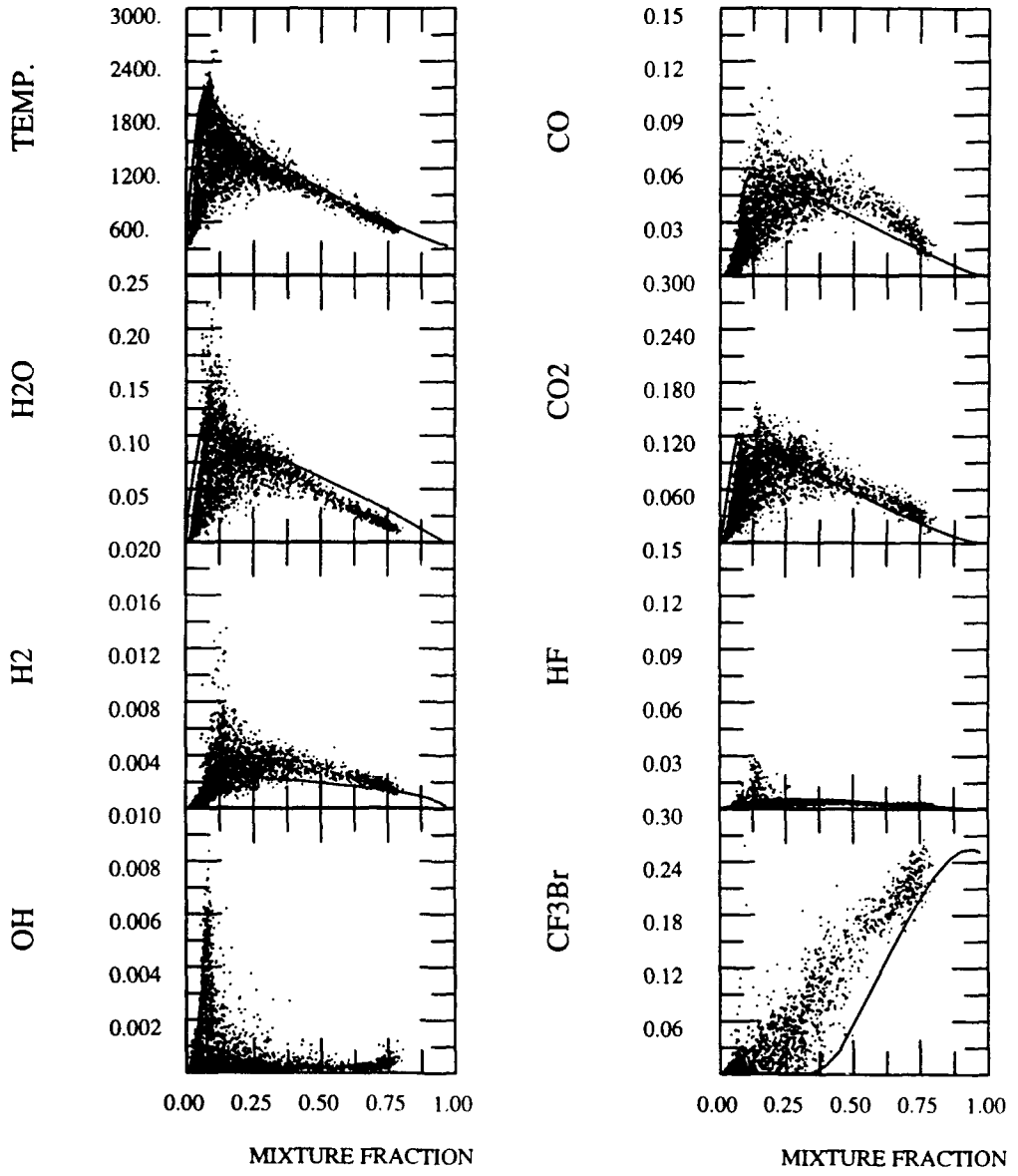

Figure 3: Scatter plots for temperature, and mass fractions of H_2O, H_2, OH, CO, CO_2, HF and CF_3Br versus mixture fraction measured at x/D=16 in a turbulent piloted flame of CH_4 mixed with 20% CF_3Br (by mass). The jet velocity is 62m/s. The solid lines represent calculation from a 'fully burnt' laminar flamelet with the same fuel mixture.

on each plot. The laminar flamelet profiles are shown only as guides and do not from theoretical limits on the data. The mixture fraction for the data as well as the laminar flamelets is calculated using Eq. 2. The data presented on each plot are collected at x/D=16 in a piloted flame of CH_4 mixed with 20% CF_3Br (by mass). The flame has a jet velocity of 62.0 m/s and this is 75% of the blowoff velocity. A large number of the measured fluid samples have temperature and species mass fractions below the flamelet values indicating that these fluid samples are either partially burnt or partially premixed or locally extinguished. The peak mass fractions of H_2 and OH are much higher than those calculated for the laminar flame. The results are very useful in revealing not only the compositional structure of these flames at various turbulent mixing levels but also the phenomena of flame extinction and reignition.

Other Raman Experiments

An alternative approach to monitoring each Raman line separately using PM tubes is to monitor the whole Raman spectrum covering all the species of interest. Using the same optical set described earlier for the Raman measurements, an intensified linear diode array with 1024 lines is positioned at the exit plane of a 1/4 spectrograph. The spectral dispersion is such that 35nm of the spectrum cover the full array and a full scan from 535nm to 685nm has to be made in five stages (allowing for some overlap). Figure 4 shows a full spectrum obtained in a laminar counterflow diffusion flame with a fuel mixture of $15\%H_2 - 45\%CO - 40\%N_2$ (by volume). The measurement is made on the fuel rich side and H_2, CO and N_2 are clearly detected. Combustion products like H_2O and CO_2 are also observed. The spectrum observed from 545 to 565nm is mainly due to nonresonant fluorescence from other species although some spikes are due to the rotational lines of H_2.

Another extremely useful application of the Raman technique is measurements of species concentration in dilute two-phase flows (Masri *et al.* 1993). The same Raman set-up is used to monitor temperature and the species concentration in dilute two-phase jet flow of methanol. With these experiments, temperature is obtained from the sum of the species number density as the Rayleigh signal cannot be used due to Mie scattering interference. The Raman signal from the fuel's liquid-gas mixture is enhanced slightly by the existence of droplets due to the higher number density of fuel molecules and the local field effect. The Raman signals from other reactants and combustion product species are not affected by the existence of droplets.

Other LIF Experiments

The quenching correction factors are becoming available for more species and quantitative LIF measurements are becoming more common. The simultaneous LIF measurement of more than one species has already been applied in conjunction with Raman-Rayleigh measurements. Carter and Barlow (1993) have measured NO and OH simultaneously with temperature and stable species concentrations. Other species, of significant importance in the combustion chemistry and/or in pollutants formation can also be measured. The most promising are OH, NO, CH, CO and H. Future application of the joint Raman-Rayleigh-LIF technique will see more species monitored jointly by

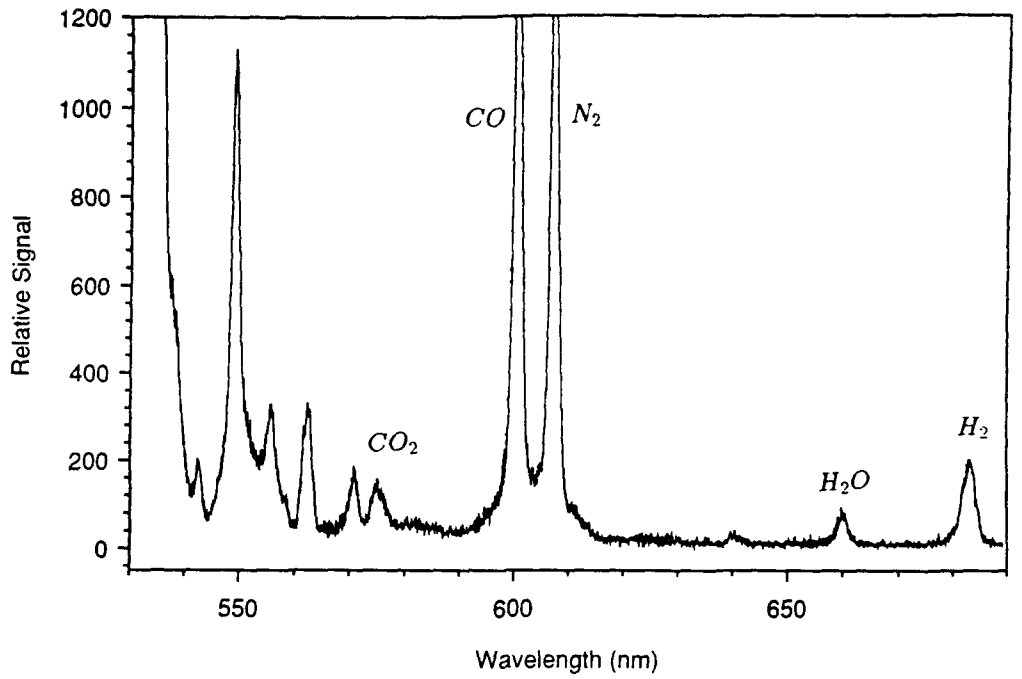

Figure 4: Raman spectrum measured on the fuel rich side of a laminar counterflow diffusion flame with $15\%H_2 - 45\%CO - 40\%N_2$ (by volume). The laser excitation wavelength is 532nm.

LIF. Combination of (OH, NO, CO) or (OH, CH, CO) or (OH, H, NO) are feasible. Further extensions to monitoring four species by LIF simultanously are much more difficult but not impossible.

For planar imaging, the quantitative measurement of species by LIF is more difficult since all major species cannot be measured and hence the quenching correction cannot be directly applied. The alternative is to use the existing knowledge of the laminar flame structure with detailed chemistry and generate correlations between the quenching corrections and temperature. This procedure has been tested for a range of fuels and proves successful (Kelman and Masri 1993). It requires measuring temperature and preferably mixture fraction since the quenching correction deviates slightly between lean and rich mixtures.

Acknowledgments

This work has been supported by the the Australian Research Council and the U.S. Department of Energy, Office of Basic Energy Sciences, Division of Chemical Sciences. The Author is grateful to Sandia National Laboratories for their continuing support. Thanks to Mr Bassam Dally for his assistance in preparing the figures.

References

1. Barlow, R.S., Dibble, R.W., Stårner, S.H. and Bilger, R.W. (1990). *Twenty-third Symposium (International) on Combustion*, The Combustion Institute, Pittsburgh, pp.583-589.

2. Carter, C.D. and Barlow, R.S. (1993). Simultaneous Measurements of NO, OH and the Major Species in a Nonpremxied Turbulent H_2 Jet Flame, *Eastern and Central States Sections of the Combustion Institute.*

3. Cheng, T.S., Wehrmeyer, J.A., and Pitz, R.W. (1992). *Combust. Flame* 91:323-343.

4. Crosley, D.R. (1992). Laser Measurement of Chemically Reactive Intermediates in Combustion, *Sixth Toyota Conference*, Nagoya, Japan. pp. 15-1 to 15-13.

5. Dibble, R.W., Masri, A.R. and Bilger, R.W. (1987). *Combust. Flame* 67:189-206.

6. Dibble, R.W., Stårner S.H., Masri, A.R. and Barlow, R.S. (1990). *Appl. Phys. B Special Issue on Combustion Diagnostics*, pp. 1727-1731.

7. Drake, M.C., Pitz, R.W. and Lapp, M. (1984). *AIAA 22th Aerospace Sciences Meeting*, Paper AIAA-84-0544, Reno, Nevada.

8. Eckbreth, A.C. (1988). Laser Diagnostics for Combustion Temperature and Species. Abacus Press, UK.

9. Garland, N.L., and Crosley, D.R. (1986). *Twenty-first Symposium (International) on Combustion*, The Combustion Institute, Pittsburgh, pp.1693-1702.

10. Haumann, J. , Seitzmann, J.M., and Hanson, R.K. (1986). *Optics Letters* 11(12):776-778.

11. Kelman, J.B. and Masri, A.R. (1993). *Applied Optics* (to appear).

12. Lapp, M. and Penny, C.M., Eds. (1974). Laser Raman Gas Diagnostics. Plenum Press, New York, NY.

13. Lederman, S. (1997). The Use of laser Raman Diagnostics in Flow Fields and Combustion', *Prog. Energy Combust. Sci.* 3:1-34.

14. Lee, M.P., Paul, P.H. and Hanson, R.K. (1986). *Optics Letters* 11(1):7-9.

15. Magre, P. and Dibble, R.W. (1987). *AIAA 25th Aerospace Sciences Meeting.* Paper AIAA 87-0378, Reno, Nevada.

16. Masri, A.R., Bilger, R.W. and Dibble, R.W. (1987). *Combust. Flame* 68:109-119.

17. Masri, A.R., Dibble, R.W. and Barlow, R.S. (1992). *Twenty-fourth Symposium (International) on Combustion*, The Combustion Institute, Pittsburgh, pp.317-324.

18. Masri, A.R., Dibble, R.W. and Barlow, R.S. (1992). *Combust. Flame* 89:167-185.

19. Masri, A.R., Dibble, R.W. and Barlow, R.S. (1993). *J. Raman Spec.* 24:83-89.

20. Schrötter, H.W. and Klöckner, H.W. (1979). In *Raman Spectroscopy of Gases and Liquids*, ed. by A. Weber, p. 123, Springer Verlag, New York.

21. Stårner, S.H., Bilger, R.W., Dibble, R.W. and Barlow, R.S. (1991). *Combust. Flame* 83:63-74.

PHASE DOPPLER ANEMOMETER TECHNIQUE CONCEPTS AND APPLICATIONS

Presented by Assoc. Prof. Yos S. Morsi
Modelling and Diagnostics Group
Energy Systems Engineering Centre
Swinburne University of Technology
John Street, Hawthorn, Victoria

Presented at the Workshop on Laser Diagnostics in Fluid Mechanics and Combustion
30 Sept. - 1 Oct. 1993

Members of the Group:
A/Prof. Yos S. Morsi
Dr. Dudley Atapattu
Mr. Ihab Elkatatny
Ms. Christine Larson
Mr. Xiao Yang Wan
Mr. Wei Yang

SUMMARY

Size measurement in Phase Doppler Anemometry (PDA) technique is based on the spatial phase shift of the Doppler signals obtained from multiple detectors located at different scattering angles. The difference in phase of the signals is linearly proportional to the spherical particle diameter. This technique is capable of measuring single particle events at a point in the flow. Simultaneous measurements can be made for the size, velocity and concentration of spherical particles in liquid and gaseous flow. This lecture covers the basic concept of PDA and gives some practical examples.

INTRODUCTION

For the last ten years or so, there has been a significant progress in the development of optical diagnostic for detailed two phase flow characterisation. The commercial instruments have now evolved to a stage where they can perform reliable measurements of the flow fields and sizing of solid particles/bubbles in many practical situations.

Although there are a number of methods that can be used for particle size measurement in this lecture we will only focus on the Phase Doppler technique which is based on light scattering interferometry. Such a technique takes advantage of the fact that there is a phase shift in the Doppler signal as a function of viewing angle, see Figure 1. This relative phase shift has an almost linear relationship with particle size. The processor measures bursts from individual particles, as shown in Figure 2, viewed from at least two different angles. The phase is computed along with the burst frequency and the phase difference between the signals is then measured and subsequently the particle size determined. In addition to a histogram of particle sizes, these processors can also provide information on velocity as well as concentration of particles.

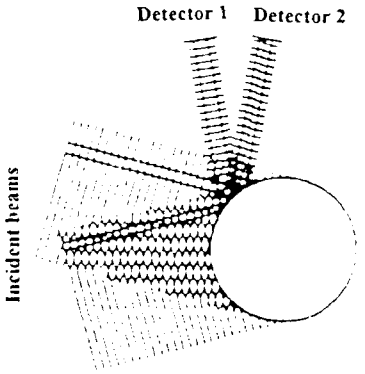

Figure 1 The interference patterns differ at the two photo detector surfaces

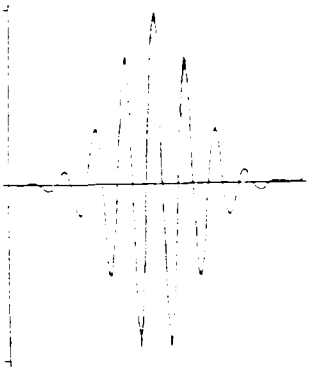

Figure 2 Doppler Burst

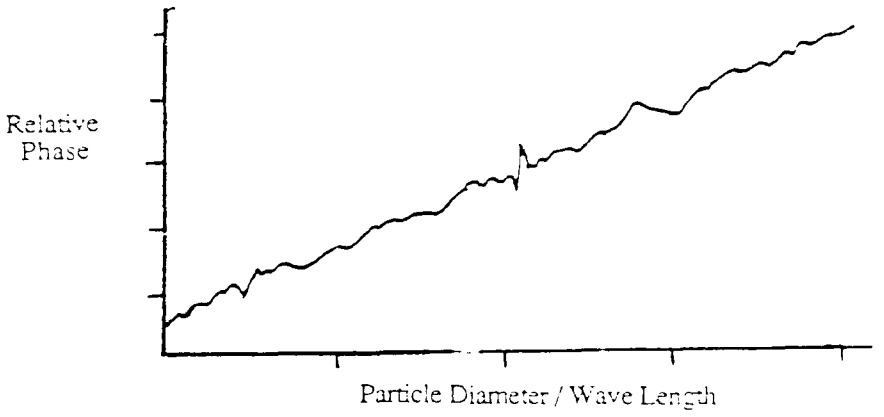

Figure 3 Phase shift as a function of particle size

Based on this concept there are not two commercially available Phase Doppler Anemometry (PDA) systems namely Dantec and Aerometrics. These systems are capable of measuring simultaneously the particle size and velocity magnitude, number density and volume flux. For the last ten years or so, these instruments have been extensively evaluated by different independent research establishments and it is now recognised as an important diagnostic tool for the two phase flow measurements.

BASIC CONCEPT

As mentioned earlier, this method is based on light scattering and incorporates an optical system similar to that of Laser Doppler Anemometry (LDA). To aid our explanation of this concept the fringe model of LDA is described and then extended to explain the concept of PDA.

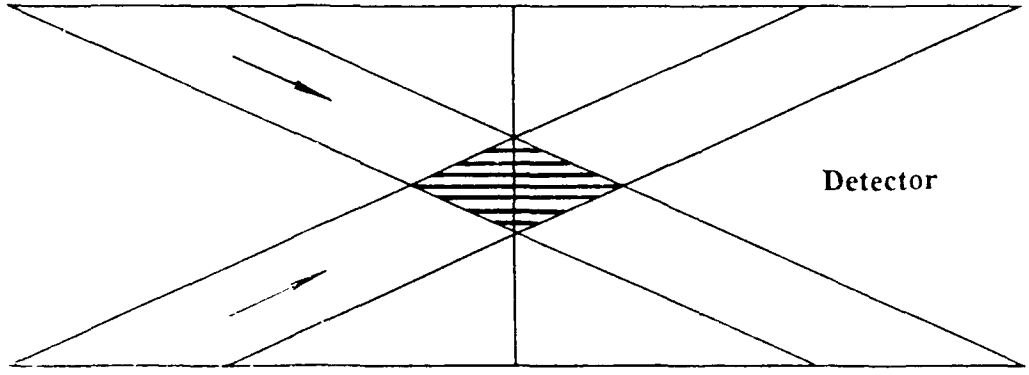

Figure 4 Beam Crossing - Intensity Distribution

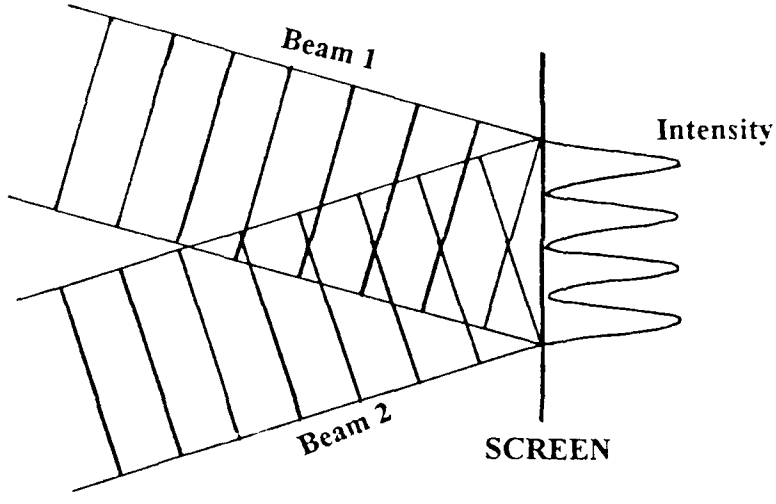

Figure 5 Fringe Formation

In this fringe model the laser beam is split into two parallel beams of equal intensity that pass through a lens and intersect at the focal point of the lens, see Figure 4. A set of parallel fringes are formed in the measuring volume. When a particle passes through this measuring region it scatters light, which is intensity modulated (see Figure 5) and is collected by a

receiving lens and then converted into an electrical signal by a high speed photo detector. This will be detected as a Doppler burst.

To describe phase shift and its relation to particle size the concept of PDA is explained as follows; as the particle moves through the measurement volume the projected fringes are swept through space. A stationary photo detector will see alternatively light and dark fringes moving by at the Doppler frequency. The difference in optical path length for the reflection from the incident beams changes with position of the photo detector. Therefore two detectors at separate locations record the same Doppler frequency but with a relative phase shift proportional to the angular position of the detectors.

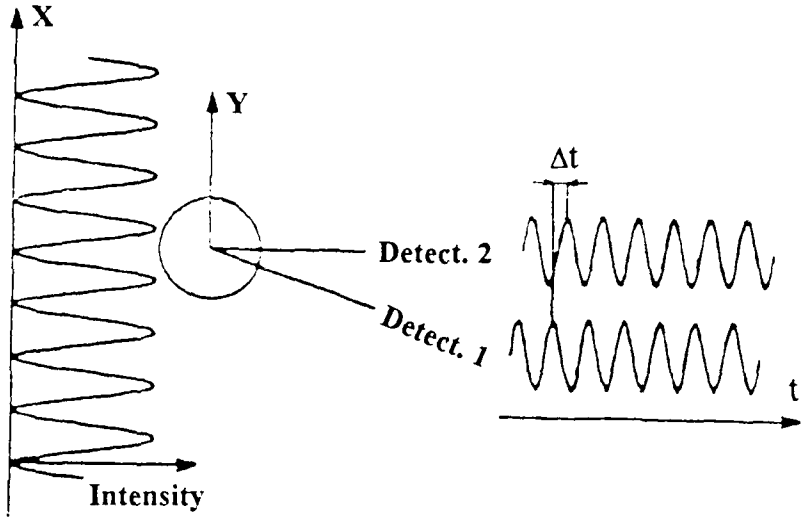

Figure 6 The phase difference between two detectors at two different angles

SIGNAL PROCESSING

As indicated earlier PDA uses the information on scattered signal gathered from multiple photo detectors to determine the relative phase difference which is nearly proportional to the size of the particle. By recording the frequency of the Doppler burst the velocity of the particle is also determined. The signal processing technique described here is based on the correlation technique used by Dantec 58N10 PDA Signal Processor.

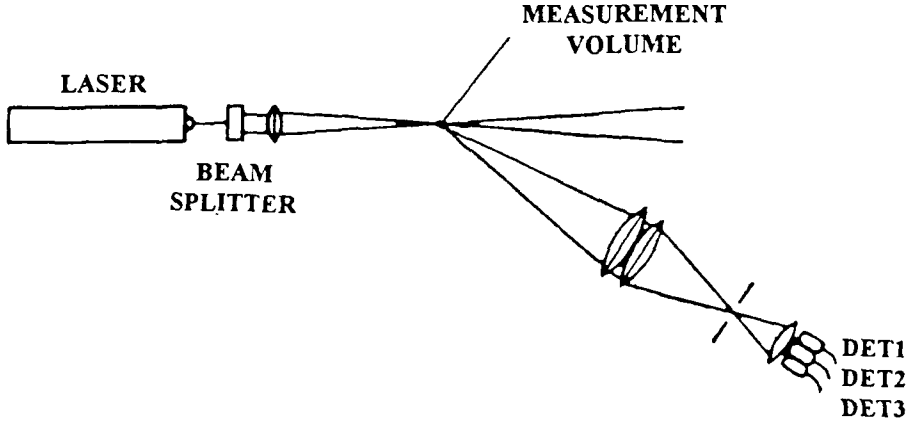

Figure 7 Schematic of optical system for PDA

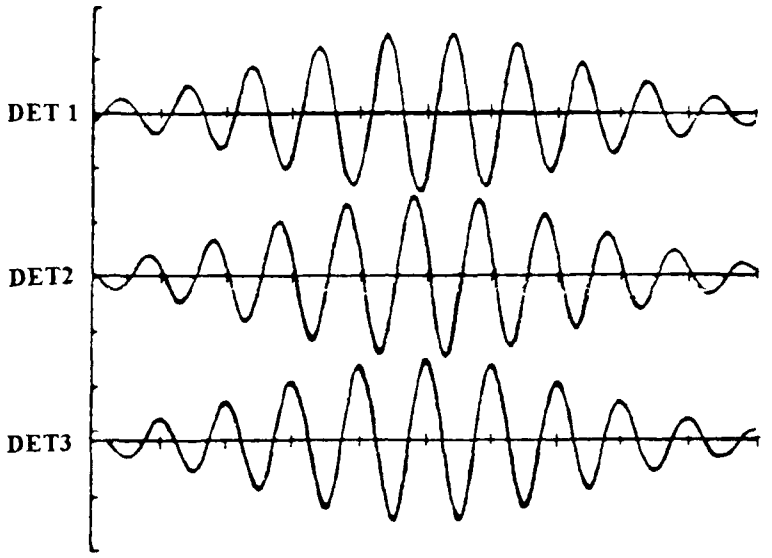

Figure 8 Doppler signal illustrating the phase shift

In the Dantec PDA Signal Processor the relative phase and frequency estimations are based on covariance processing technique. The relative phase is measured by two cross correlators. The first one performs a cross correlation on the output from two different photo detector signals with identical frequency but different phase. The second cross correlator performs a cross correlation by comparing the same two signals with one of the signals 90 degrees out of phase. The two cross correlator outputs are proportional to the sine and cosine of the original phase difference and by taking $\tan^{-1}$ of the ratio yields the relative phase difference, hence particle size can be found.

To determine the frequency for velocity measurement, the signal from one photo detector is split into two identical signals with a delay time added to one of the signals. By performing a auto correlation on these two signals their relative phase is determined. This measured relative phase is divided by the delay time to yield the signal frequency. This frequency multiplied by the fringe spacing determines the instantaneous velocity component. For more details see Dantec PDA User's Manual, 1992 and other cited references.

OPTICS AND INSTRUMENTATION

An Ar-ion laser was used in our PDA system. The beam is collimated and colour separated into the 488.0 nm (blue) and 514.5 nm (green) wavelength lines. Polarisation of the blue beam is rotated 90^0 from that of the green beam. Each beam is split into two equal intensity beams forming a cross pattern and focused to a point forming two overlapping orthogonal ellipsoid shaped measurement volumes. The dimension of the measurement volume is a function of lens focal length, beam separation and beam diameter. The range of velocity and size that can be measured depends on the optical arrangement used. A fourth detector is necessary to obtain two velocity components and particle size simultaneously. For two or three dimensional flow measurements additional frequency measuring channels are also required.

GENERAL APPLICATIONS OF PDA

As indicated by the manufactures, Dantec and Aerometrics, the main applications of PDA are in multi-phase systems. Some of these application are in:

- dispersion and mixing
- powder metallurgy
- combustion
- cavitation

Below is a summary of our experience using the Dantec PDA system:

- *Gas injection into liquid baths*

  Velocities of fluid and bubbles as well as size of bubbles were measured in a top gas injection system where the gas was injected into a water bath through the annulus of a lance. The annulus was fitted with helical vane swillers which imparts swirling motion to the gas going into the water which contained in a cylindrical perspex container of 230 mm diameter. The cylinder was immersed in a rectangular glass tank filled with water in order to minimise optical distortions (for more details see Atapattu et al, 1992). Given in Figure 9 is a schematic of the experimental facility used by our group for PDA measurements.

- *Flow within a tube bank*

  Air and particle velocities were measured upstream and within a tube bank which is normally used in coal fired furnaces. Velocity and concentration of particles will help in better understanding of the erosion and heat transfer processes taking place. The results of this work is given in the next paper.

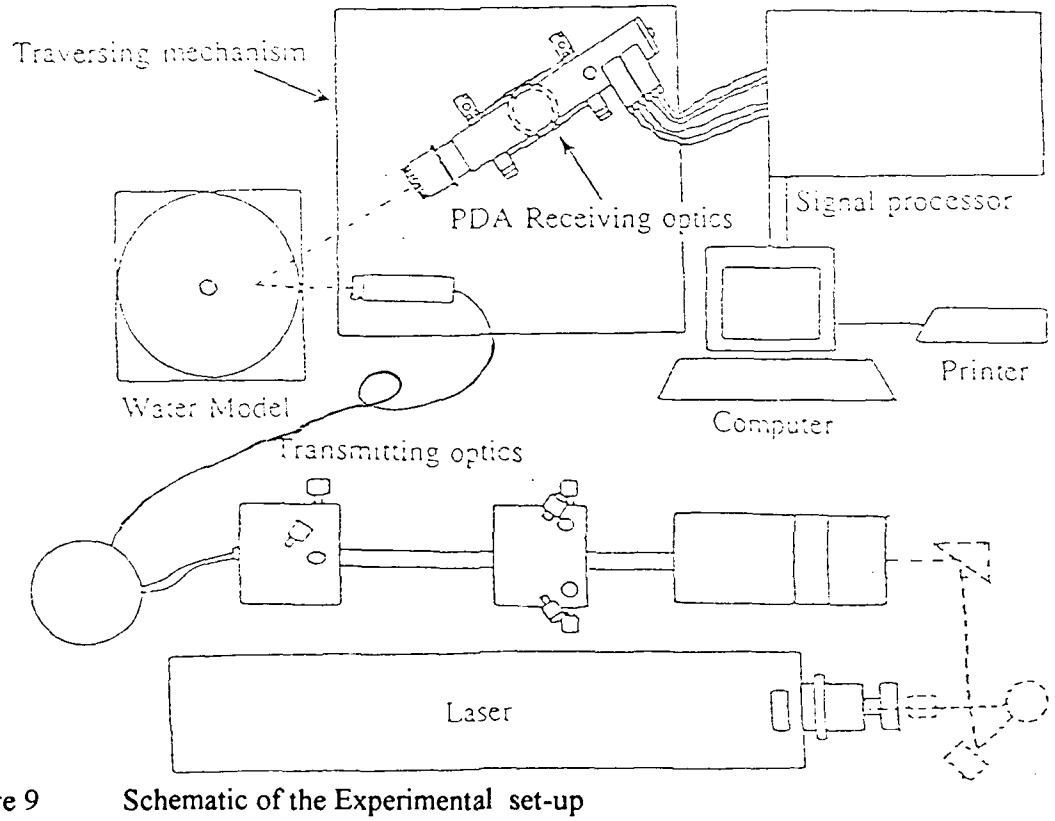

Figure 9 Schematic of the Experimental set-up

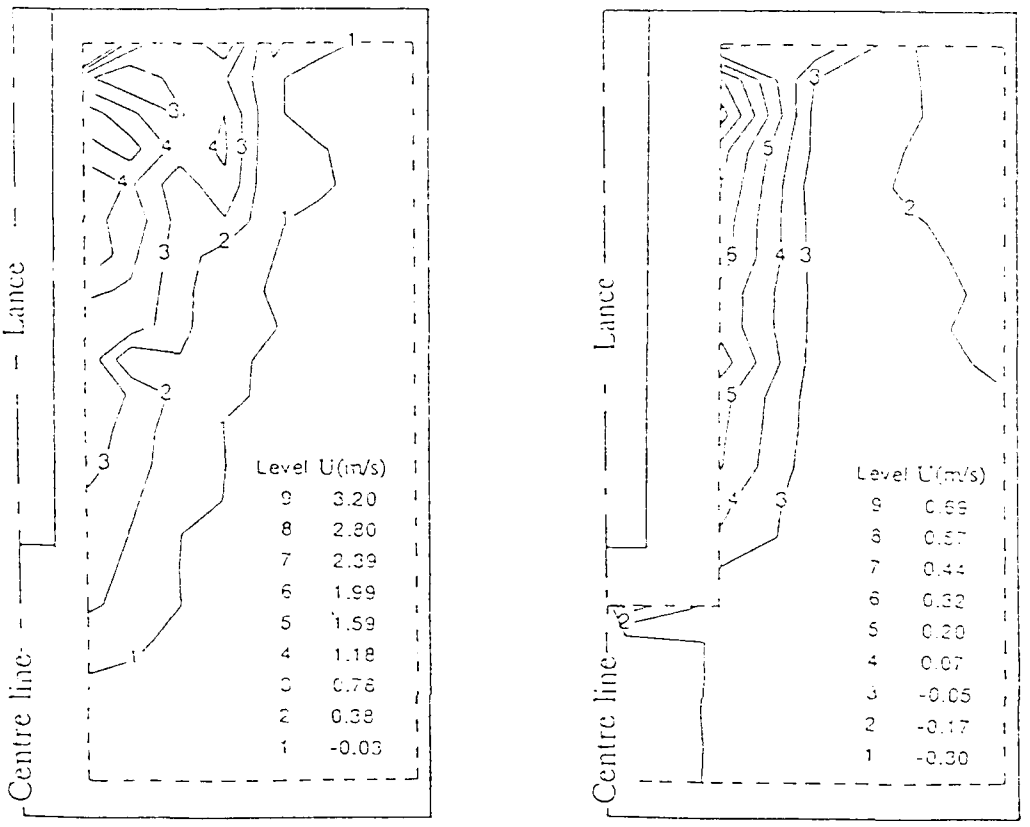

(a) Without swirl (ψ = 0°) (b) With swirl (ψ = 57.5°)

Figure 10 Liquid phase velocity distribution

CONCLUSIONS

PDA is capable of providing a significant amount of information on the behaviour of flows involving particles, bubbles or droplets, which will be useful in developing and validating numerical models. It is the opinion of the speaker that more experience is needed for gas-particle flow using different sizes of particles and air velocities. Also, the system is yet to be tried out by our group for other multi-phase flow applications such as combustion and cavitation.

REFERENCES

Atapattu, D. D., Morsi, Y. S. and Gray, N. B "Two component velocity measurements in top-submerged gas injection systems", *Proc. 13th Symp. on Turbulence*, University of Missouri-Rolla, USA, B13.1 - B13.14, 1992.

Buchalo, W. D. and Houser, M. J. "Phase Doppler Spray Analyser for simultaneous measurements of drop size and velocity distributions", *Optical Engineering*, **23**, 15, 183, 1984.

Durst, F. and Zare', M. "Laser-Doppler measurements in two-phase flows", *LDA-Symposium*, University of Denmark, 1975.

PDA User's Manual, Dantec measurement technology, Denmark, 1992.

Saffman, M., Bucchave, P. and Tanger, H. "Simultaneous measurement of size concentration, and velocity of spherical particles by a laser Doppler method", *Second Int. Symp. on Application of Laser Anemometry to Fluid Mechanics*, Lisbon, July 1984.

CARS

D. Proctor

CSIRO Division of Building, Construction & Engineering
PO Box 56 Highett, VIC 3190
Internet David.Proctor@dbce.csiro.au

1. INTRODUCTION

What is CARS? First of all what does it stand for? CARS is Coherent Anti-Stokes Raman Spectroscopy. Secondly, CARS belongs to the set of nonlinear Raman processes, such as simulated Raman gain/loss spectroscopy (SRGS), Raman induced Kerr effect spectroscopy (RIKES), photo acoustic Raman spectroscopy (PARS) and higher order Raman spectral excitation spectroscopy (HORSES). These process involve two different rotational–vibrational molecular energy states separated by a Raman transition.

All optical phenomena are governed by Maxwell's equations[35] , which can be manipulated to give the wave equation:

$$\left[\nabla \times (\nabla \times) + \frac{1}{c^2}\frac{\partial^2}{\partial t^2}\right] \vec{E}(\vec{r},t) = \mu_0 \frac{\partial^2 \vec{P}(\vec{r},t)}{\partial t^2} \tag{1}$$

In the above nonlinear Raman processes more than one monochromatic or partially monochromatic electric fields are involved and we can expand E and P into their Fourier components. Consequently, the induced polarisation can be written as function of $E(\omega_i)$, viz.,

$$\begin{aligned} P_i(\pm\omega_i) = {} & \epsilon_0 \chi^{(1)}(\pm\omega_i) E(\pm\omega_i) + \Sigma_{j,k} \epsilon_0 \chi^{(2)}(\pm\omega_i, \pm\omega_j, \pm\omega_k) E(\pm\omega_j) E(\pm\omega_k) \\ & + \Sigma_{j,k,l} \epsilon_0 \chi^{(3)}(\pm\omega_i, \pm\omega_j, \pm\omega_k, \pm\omega_l) E(\pm\omega_j) E(\pm\omega_k) E(\pm\omega_l) + etc.... \end{aligned} \tag{2}$$

It can be seen from the above equation that the $\pm\omega$ terms can give rise to a large number of frequency mixing by addition and/or subtraction under the right conditions. This, in part, expains why CARS is possible and will be expanded upon later below.

The susceptibilities, $\chi^{(\ )}$, are an indication of how susceptible the medium is to being polarised. The linear susceptibility, $\chi^{(1)}$, is responsible for Raman and Rayleigh scattering. Bloembergen[6] has shown that the higher order polarisations can be expressed by the following approximation:

$$\frac{P^{(n+1)}}{P^{(n)}} = \frac{E}{E_{at}}. \tag{3}$$

Typically E_{at} is of the order 30GV/m, and hence very high electric fields are required to produce the higher order polarisations. It was not until the advent of Q-switched lasers that the higher order polarisations could be generated. At high laser intensities the nonlinear processes are quite strong as a result of resonance domination in the nonlinear susceptibilities. Even order polarisations do not occur in isotropic media, such as gases, due to inversion symmetry. Thus in combustion systems, the primary nonlinear process of interest is the 3rd order one. The 2nd order nonlinear polarisations are important in frequency doubling and parametric addition processes in crystals to produce

wavelengths not obtainable directly from lasers, (see Yariv[72] for a complete description on these processes).

In stimulated Raman scattering using intense laser radiation, a process is set in train where by the spontaneously generated Stokes photons experience exponential growth in the direction of the incident laser propagation. The net effect is that the Stokes photons emerge as a coherent beam. CARS spectroscopic modelling is much more complex than spontaneous Raman scattering. This is due to the fact that CARS spectra contain both constructive and destructive interference effects and are also sensitive to the Raman linewidths and the exact position of the transitions. As a consequence computationally intensive numerical programs are required to calculate the spectra for comparison with measured spectra. CARS does offer other advantages over spontaneous Raman. In non–sooting and particle free combustion environments, single pulse thermometry can be performed with a CARS set–up using laser intensities an order of magnitude less than that required for spontaneous Raman scattering. Furthermore, because of CARS coherent nature it needs much smaller optical access ports than other incoherent techniques such as spontaneous Raman, Rayleigh and laser induced fluorescence spectroscopy (LIFS).

CARS was first demonstrated in liquids by Terhune[47,70] and co–workers thirty years ago in 1963. It was another 10 years before the CARS process was demonstrated in gases by the group at ONERA lead by Taran[60] .

2. SOME OF THE UNDERLYING THEORY

Only a brief outline of how and why a CARS signal is generated and what is the resultant signal strength will be given here. A much fuller picture may be had from the following sources – Eckbreth[13] , Eesley[18] , Greenhalgh *et al.*[25,26] , Harvey[31] , Kataoka *et al.*[37] , Moosmüller and She[48] , Tolles *et al.*[71] and Yuratich[73,74] .

The various nonlinear optical processes are also distinguished by the number of discrete frequencies involved, including the signal[31] . In the above mentioned nonlinear Raman processes all except the CARS process are two–colour techniques. CARS, on the other hand, is a three or four colour process. Due to the coherent nature of the wave mixing process, a phase matching condition must be satisfied for efficient signal generation as follows:

$$\vec{k}_i = \pm\vec{k}_j \pm \vec{k}_k \pm \vec{k}_l, \tag{4}$$

where $\vec{k}_m$ is the wave vector at frequency ω_m with magnitude $|k_m| = n_m\omega_m/c$. Phase matching therefore dictates that there is precise angular orientation of the input wave mixing beams, especially in dispersive media. In many cases the phase matching is easily satisfied. Fortunately, for combustion gases applications, gases are virtually dispersionless and a collinear alignment of the input fields satisfies eqn(4) above for phase matching.

Typically CARS is performed as a three colour process since, as will be seen later, it is an easier experiment to set up and control. CARS is therefore a more difficult diagnostic technique to implement than the other nonlinear Raman processes, which in turn are more difficult than spontaneous Raman and Rayleigh scattering. So why do it?

In many combustion processes there are highly luminous, particle (soot or fuel) laden flames, which cannot be probed by spontaneous Raman[11,12] . Thus the development of the nonlinear techniques. The group at ONERA in France lead by Taran provided the

basis[60-62,49,50] for subsequent CARS investigations. For certain spectroscopic applications, CARS may not be the preferred approach for optimum signal to noise. However, for combustion probing, it is probably the best technique to get quantitative information about main species, at a point, in the combusting media. The reason for this is that CARS is a signal generation process. The other nonlinear approaches encode the signal via beam modulation. Consequently these other approaches are also subject to error caused by attenuation from soot and fuel particles, varying refactive effects and optical access window fouling. Having said all that, SRGS underpins the CARS work since it provides the fundamental spectroscopic input required for CARS spectral synthesis.

2.1 NONLINEAR SUSCEPTIBILITY

In the introduction section the concept of the nonlinear susceptibility was introduced and is responsible for producing the conditions necessary to obtain, among others, a CARS signal from the third order nonlinear susceptibility, $\chi^{(3)}$. $\chi^{(3)}$ is a fourth rank tensor with 81 components. In isotropic media there are only four non-vanishing tensor components, of which only three are independant. The susceptibility is expressed as follows:

$$\chi^{(3)}_{ijkl}(\pm\omega_i \pm \omega_j \pm \omega_k \pm \omega_l), \tag{5}$$

where $ijkl$ refer to the polarisation of the fields participating in the wave mixing process. ω_i is the signal frequency and occurs as a result of one of the linear combinations of the input frequencies, i.e.:

$$\omega_i = \pm\omega_j \pm \omega_k \pm \omega_l. \tag{6}$$

The susceptibility comprises of two parts, the resonant part which is complex and a nonresonant part, $\chi^{(NR)}$, and may be express as follows:

$$\chi^{(3)} = \Sigma_j \left(\chi'_j + i\chi''_j\right) + \chi^{(NR)}. \tag{7}$$

The resonant part of the susceptibility provides the information about the medium of interest, be it concentration or temperature. The real part, χ'_j, displays the dispersive behavior around the centre of a Raman resonance. It leads to wave speed changes with frequency. The imaginary part, χ''_j, exhibits a lineshape profile, and leads to gain or loss of amplitude. The nonresonant part, $\chi^{(NR)}$, derives from the molecular cloud distortions and remote Raman resonances. It is essentially flat far from resonance and is basically an unwanted "background" signal which can limit detection sensitivity of the desired resonant part. Although the nonresonant susceptibility is undesirable, it can be exploited to provide internal referencing in combustion diagnostics.
The CARS process is governed by a functional dependence on $\chi^{(3)}$, namely $\mid \chi_{CARS} \mid^2$. This in turn leads to complicated lineshapes. The CARS mixing occurs through $\chi^{(3)}_{ijkl}(-\omega_3, +\omega_0, +\omega_1, -\omega_2)$. The various wave-mixing combinations contributing to the CARS susceptibility are shown in Figure 1. The solid lines represent the real vibrational/rotational states and the dashed lines the virtual states in the molecule being probed.

2.2 THE CARS SIGNAL

If the electric field is assumed to be of the form $\exp(-i\omega_m t)$ and a travelling wave, i.e.

$$\vec{E}(\omega_m, \vec{r}) = \vec{E}(\omega_m) \exp\left(i\vec{k}\cdot\vec{r}\right), \tag{8}$$

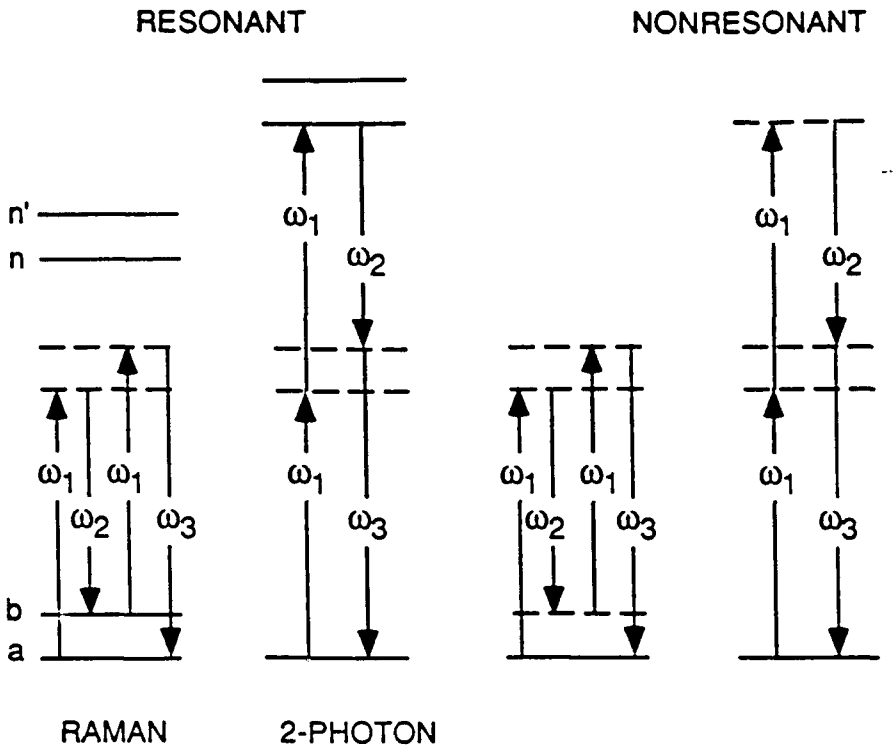

Figure 1: CARS resonant and nonresonant signal generation.

where ω_m is any of the frequencies mentioned in the paragraph above, then we may write eqn(1) for each frequency as:

$$\nabla^2 \vec{E}(\omega_m, \vec{r}) + \frac{\omega_m^2}{c^2} \vec{E}(\omega_m, \vec{r}) = -\mu_0 \omega_m^2 \vec{P}(\omega_m, \vec{r}). \tag{9}$$

If the CARS signal frequency at ω_3 is now investigated for gaseous media, recalling eqn(2) and the fact that there will be no even order susceptibilities, the polarisability in eqn(9) can be written as:

$$\vec{P}(\omega_3, \vec{r}) = \epsilon_0 \chi^{(1)} \vec{E}(\omega_3, \vec{r}) + \vec{P}^{(3)}(\omega_3, \vec{r}), \tag{10}$$

also, from eqn(2) $P^{(3)}$ can be written as:

$$P_i^{(3)}(\omega_3, \vec{r}) = \Sigma_{jkl} \epsilon_0 \chi_{ijkl}^{(3)}(\omega_3, \omega_0, \omega_1, \omega_2) \vec{E}_j(\omega_0, \vec{r}) \vec{E}_k(\omega_1, \vec{r}) \vec{E}_l(\omega_2, \vec{r}). \tag{11}$$

There will be 27 components for each term of$P_i^{(3)}(\omega_3, \vec{r})$. Because of symmetry, the situation can be greatly simplified. Firstly $\chi^{(3)}$ is invariant to the 6 permutations of the pairs (ω_0, j),(ω_1, k) and (ω_l, l), and there are 6 equivalent terms for any sequence of the fields. If any of the m frequencies are the same, then the six equivalent terms are reduced by $m'!$, where m' is the number of frequencies that are the same. In addition $\chi^{(3)}$ must transform in accord with the medium's macroscopic symmetry properties. There are 21 non-zero elements in an isotropic medium of which only 3 are independent.

Consider first the situation where all the wave mixing lasers' polarisations are parallel, i.e. $i = j = k = l = x$ and $m'! = 1$, eqn(11) becomes:

$$P^{(3)}(\omega_3, \vec{r}) = 6\epsilon_0 \chi_{xxxx}(-\omega_3, \omega_0, \omega_1, -\omega_2) \vec{E}_x(\omega_0, \vec{r}) \vec{E}_x(\omega_1, \vec{r}) \vec{E}_x(\omega_2, \vec{r}), \tag{12}$$

or

$$P^{(3)}(\omega_3, \vec{r}) = \epsilon_0 \chi_{CARS} \vec{E}_x(\omega_0, \vec{r})\, \vec{E}_x(\omega_1, \vec{r})\, \vec{E}_x(\omega_2, \vec{r}). \tag{13}$$

If $\vec{E}_x(\omega_0, \vec{r}) = \vec{E}_x(\omega_1, \vec{r})$, i.e. the same laser is used (degenerate wave mixing) to provide ω_0 and ω_1, $m'!$ now has a value of 2 and χ_{CARS} is half that shown in eqn(13) above.

The wave equation, eqn(5), can be rearranged by substituting eqn(10) in eqn(9) for $\vec{P}(\omega_3, \vec{r})$, and eqn(13) for $\vec{P}^{(3)}(\omega_3, \vec{r})$ and eqn(8) for $\vec{E}(\omega_m, \vec{r})$ in eqn(10), with the following additional expressions substituted:

$$\frac{\epsilon}{\epsilon_0} = 1 + \chi^{(1)} \tag{14}$$

and

$$c^2 = \frac{1}{\mu_0 \epsilon_0} \tag{15}$$

to give, with $\vec{E}_x(\omega_0, \vec{r}) = \vec{E}_x(\omega_1, \vec{r})$,

$$\nabla^2 \vec{E}(\omega_3, \vec{r}) + \frac{\omega_3^2}{c^2}\frac{\epsilon}{\epsilon_0}\vec{E}(\omega_3, \vec{r}) = -\frac{\omega_3^2}{c^2}\chi_{CARS} E^2(\omega_1)\, E^*(\omega_2) \exp\left(i\left(2\vec{k}_1 - \vec{k}_2\right)\cdot\vec{r}\right). \tag{16}$$

The exponential term determines which way the CARS field, $E(\omega_3)$, will develop, i.e. along the direction in which

$$\left(2\vec{k}_1 - \vec{k}_2\right)\cdot\vec{r} = 0. \tag{17}$$

This term also indicates how the phase matching requirement of eqn(4) arises. It can be shown that eqn(16) can be integrated along the direction from 0 to ℓ, over which the intersecting lasers are phase matched to give the following expression for the CARS electric field:

$$E(\omega_3, \ell) = \frac{\omega_3}{2 n_3 c}\chi_{CARS} E^2(\omega_1)\, E^*(\omega_2)\, \frac{\exp(i\Delta k \ell) - 1}{\Delta k}, \tag{18}$$

where $E^*(\omega_2)$ is a complex conjugate, and from which the time averaged CARS signal intensity can be derived and is as follows:

$$I_3 = \frac{\omega_3^2}{n_1^2 n_2 n_3 c^4 \epsilon_0^2} I_1^2 I_2 |\chi_{CARS}|^2 \ell^2 \left(\frac{\sin\frac{\Delta k \ell}{2}}{\frac{\Delta k \ell}{2}}\right)^2, \tag{19}$$

based on the fact that the intensity of an electric field is given by:

$$I_m = \frac{n_m c \epsilon_0}{2} |E_m|^2. \tag{20}$$

A note of caution, care should be used in the source used to calculate χ_{CARS} since difference arise depending on the convention used, see Orr & Ward[51] and Bogaard & Orr[7] for more details.

2.3 χ_{CARS}

In order to be able to apply eqn(20) the value of χ_{CARS} needs to be known. Expressions for the resonant part of χ_{CARS} may be derived from either classical or quantum mechanical stand point. Taking χ_{CARS} as:

$$\chi_{CARS} = \chi^{(R)} + \chi^{(NR)} \tag{21}$$

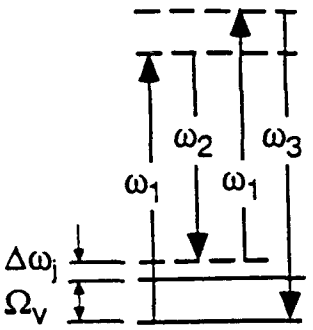

Figure 2: Off-resonance definition

The resonant part of the CARS third order susceptibility can be shown to be as follows[32,44,10] :

$$\chi^{(R)} = \frac{8\pi 2 n_1 \epsilon_0 \mathcal{N} c^4}{n_2 \hbar \omega_2^4} \left(\frac{d\sigma}{d\Omega}\right)_j \frac{\Omega_v \Delta_j}{\Omega_v^2 - (\omega_1 - \omega_2)^2 - i\Gamma_j (\omega_1 - \omega_2)}, \tag{22}$$

where $\mathcal{N}\Delta_j$ is the difference in populations between the lower and upper states for a particular transition j, and accounts for the statistical distribution[49,44] , i.e. $\Delta_j = 1$ for low temperature and $\Delta_j = 0$ for infinite temperature. The factor Δ_j is a direct consequence of the quantum mechanical approach by density matrix methods[10] . $d\sigma/d\Omega$ is the differential scattering cross-section of the molecule exposed to electromagnetic radiation.

If $\Delta\omega$ is defined as $\Omega_v - (\omega_1 - \omega_2)$, as shown in Figure 2, and make the assumption that $\Delta\omega_j/\Omega_v \ll 1$, which is usually a very valid approximation in the vicinity of each Raman resonance, j, then eqn(22) can be simplified to:

$$\chi_j^{(R)} = \mathcal{A}_j \left[\frac{1}{2\omega_j - i\Gamma_j}\right], \tag{23}$$

where

$$\mathcal{A}_j = \frac{(4\pi)^2 n_1 \epsilon_0 \mathcal{N} \Delta_j c^4}{n_2 \hbar \omega_2^4} \left(\frac{d\sigma}{d\Omega}\right)_j. \tag{24}$$

Thus the total CARS susceptibility signal, summed over the entire CARS band is:

$$\chi_{CARS} = \Sigma_j \frac{\mathcal{A}_j}{2\Delta\omega_j - i\Gamma_j} + \chi^{(NR)} \tag{25}$$

At resonance $\Delta\omega_j = 0$ and $\mid \chi^{(R)} \mid = \mathcal{A}_j$. It is clear that there are resonant denominators which show that $\chi^{(3)}$ is resonantly enhanced as the anti-Stokes signal or the laser frequency spectrally approaches an electronic resonance. Such an effect is analogous to resonance Raman effect in conventional Raman spectroscopy. From the work of De Witt *et al.*[10] , it is clear that resonance enhancement is very complex and may not be a benefit in every case, such as at saturation laser intensities, which can lead to anomalous results and "hole burning" in the spectra[42] .

Recalling eqn(7), from eqn(25) the real and imaginary parts of χ_{CARS} are given by the following two equations respectively:

$$\chi'_j = \mathcal{A}_j \frac{2\omega_j}{4\omega_j^2 + \Gamma_j^2} \tag{26}$$

and

$$\chi''_j = \mathcal{A}_j \frac{\Gamma_j}{4\omega_j^2 + \Gamma_j^2}. \tag{27}$$

2.4 OBSERVATIONS FROM THE ABOVE EQUATIONS

Firstly, χ_{CARS}, as mentioned on page 3, the χ' term exhibits dispersive behaviour, while the χ'' displays lineshape behaviour. Since CARS spectra depend on $\mid \chi_{CARS} \mid^2$ which includes the nonresonant background component, the CARS spectra are much more complicated due to the effects of both destructive and constructive interference. If the $\mid \chi_{CARS} \mid^2$ is examined by squaring eqn(7) and expanding, i.e.,

$$\mid \chi_{CARS} \mid^2 = \mid \Sigma_j (\chi' + i\chi'')_j + \chi^{(NR)} \mid^2 \tag{28}$$

$$= \left(\Sigma_j \chi'_j\right)^2 + \left(\Sigma_j \chi''_j\right)^2 + 2\chi^{(NR)} \Sigma_j \chi'_j + \left(\chi^{(NR)}\right)^2. \tag{29}$$

When the species concentration is high, ie large $\mathcal{A}_j$, χ' and χ''_j are very much greater than $\chi^{(NR)}$ and the last two terms in eqn(29) can be neglected in some circumstances, since they can still cause subtle spectral effects. At very low concentrations the nonresonant term dominates and eqn(29) becomes:

$$\mid \chi_{CARS} \mid^2 = \left(\chi^{(NR)}\right)^2 + 2\chi^{(NR)} \Sigma_j \chi'_j \tag{30}$$

These two extremes of the CARS spectral signal are illustrated in Figure 3. Clearly there

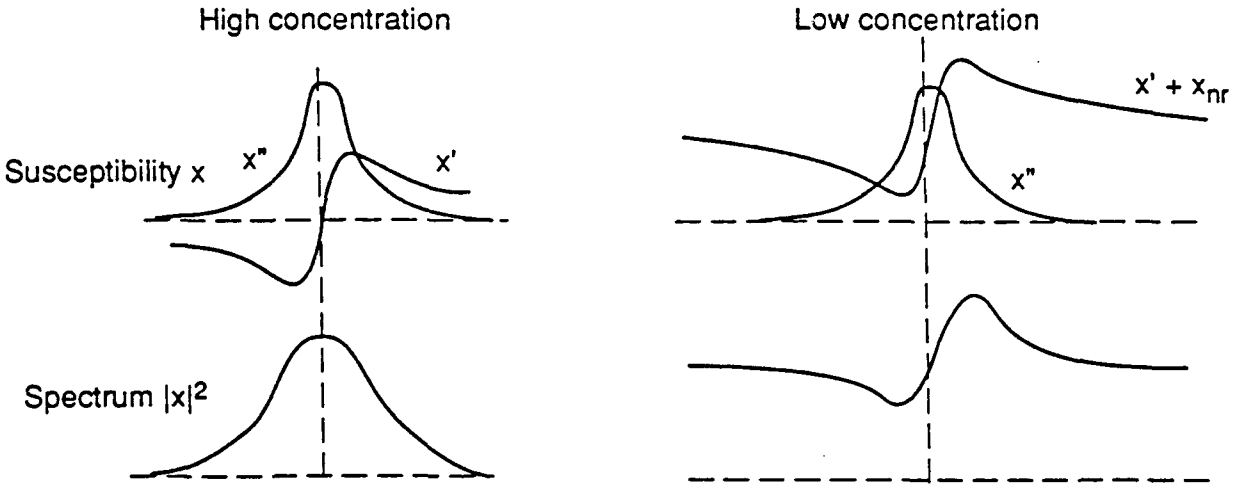

Figure 3: The effect of concentration on $\mid \chi_{CARS} \mid^2$.

are many resultant lineshapes for the $\mid \chi_{CARS} \mid_j^2$ depending on the concentration. The

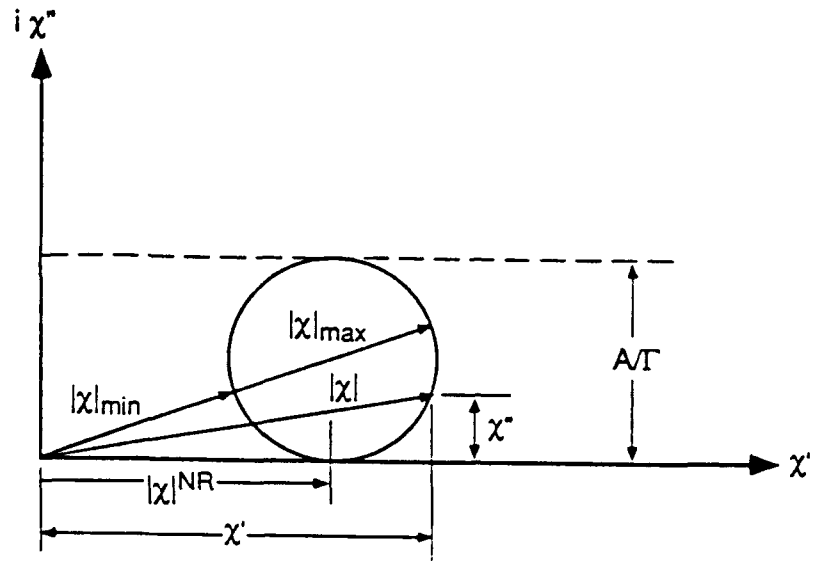

Figure 4: Pictorial representation of the CARS susceptibility components.

general picture can be sumarised in Figure 4. There are further complications if there are two or more closely spaced Raman transitions. Interferences can occur among neighbouring resonances which add a frequency dependent background to the susceptibility. This mixing allows better resolution of the peaks. The reason for this is not hard to see, as the negative part of one resonance containing $\chi^{(NR)}$, cancels or partly cancels the positive part of the other, creating less overlap between the peaks. The $\mid \chi_{CARS} \mid^2$ in this case for two closely spaced peaks at Ω_j and Ω_k can be shown to be given by:

$$\mid \chi_{CARS} \mid^2 = \left(\chi'^2_j + \chi''^2_j\right) + \left(\chi'^2_k + \chi''^2_k\right) + 2\left(\chi'_j\chi'_k + \chi''_j\chi''_k\right). \tag{31}$$

The first two terms in brackets on the right-hand side above, contribute to the two peaks, but the third term accounts for the constructive interference between the two Raman transitions, the strength of the interference depending on the separation between the transitions and the magnitude of the Raman transition linewidths. In combustion systems, O_2, N_2, CO and H_2O have many overlapping and closely spaced transitions, which therefore require a very detailed synthesis via computers.

The second observation concerns the CARS signal intensity. From eqn(19) it can be seen that signal intensity depends on the square of the pump laser power times the probe laser power. There is no lower limit or threshold power required to generate the CARS signal. CARS signal can in fact be generated with CW lasers as demonstrated by Barrett[3] and Begley *et al.*[4] , Henesian *et al.*[33] and Henesian & Byer[34] . For non-overlapped Doppler broadened transitions, the CARS signal intensity varies as the square of the density through the $\mathcal{A}_j$ term which contains the population $\mathcal{N}$. In this case the Raman linewidths depend only on temperature and there is no constructive/destructive interference effects. However, for pressure-broadened isolated transitions it can be shown that the intensity of I_3 is approximately proportional to $\mathcal{N}$:

$$\int_{-\infty}^{\infty} \mid \chi_{CARS} \mid^2 d(\Delta\omega_j) = \frac{\pi\mathcal{A}^2}{2\Gamma} \tag{32}$$

and $\Gamma \sim \mathcal{N}$. Thus the RHS approximates to $\mathcal{N}$. Roh and Schreiber[63,64] have shown that depending on the molecules present, the amount of overlapping and pressure broadening, the CARS signal is proportional to $\mathcal{N}^x$, where x can take values between 1.3 and 1.96, the latter figure as a result of constructive interference from overlapping close transitions. This point is often overlooked in the correlation between I_3 and concentration.

3. EXPERIMENTAL REQUIREMENTS

From the previous section, the main requirement in the three colour laser CARS system is for two lasers, one, the pump laser, at ω_1, and the other, the probe, at ω_2. There are two ways of generating the CARS signal. The first is to use a tunable laser for the probe and to scan across the CARS band of the species of interest. This requires steady state conditions during the period of the probe laser scan. Thus it is not of much use for measurements in combustion situations.

The second approach, which was first demonstrated by Roh *et al.*[64] , circumvents this problem of scanning for combustion or any other time varying process. In this case the narrow line tunable dye laser is replaced by a broad-band pulsed dye laser. This enables the total CARS spectra to be obtained during a single laser pulse. This has enabled temperature and species measurement during the period, typically 9ns, of the three simultaneous laser pulses. The dye spectrum is centred at the desired CARS wavelength either through the appropriate selection of the dye or dyes and/or via solvent tuning. A mixture of two dyes gives a better conversion efficiency. The spectral response of a single dye pulse laser, centered at 16470 cm^{-1} (607.16nm) with a bandwidth of 143cm^{-1}, is shown in Figure 5. The shape of this dye spectral response is required for the deconvolution of the CARS signal, see eqn(19) due to the I_2 term.

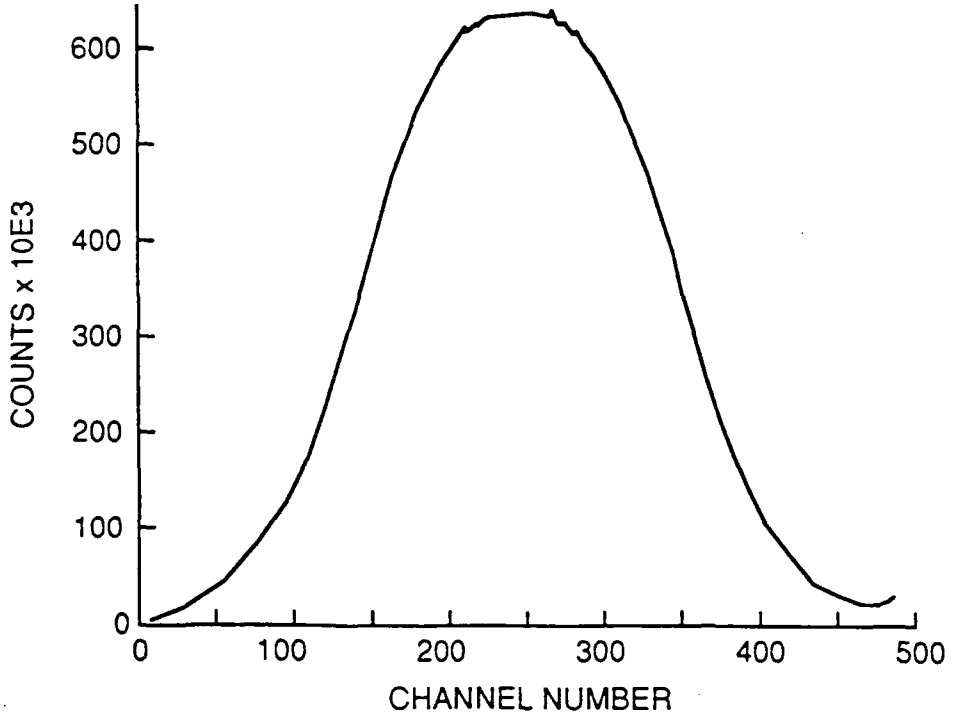

Figure 5: Intensity/spectral response of the probe laser.

The usual laser employed as the pump in most CARS work has been the Quanta-Ray DCR-1 Nd^{3+}:YAG, frequency doubled to produce ω_1 at 532nm. It is not necessary to have a single mode laser. In fact Snelling *et al.*[66] and Kröll *et al.*[38] have both shown independently that in some instances a multi-mode pump laser gives less noise in the CARS signal. Most dye lasers used to produce the probe wavelength at ω_2, will be multi-mode. Teets[69] has shown that higher order modes produce weaker signals than for TEM_{00} beams. However, the beam areas and energies can be larger than for the TEM_{00} mode beams. This latter fact has advantages when making measurements near optical access windows, as the higher order modes disperse much more rapidly. Instead of using a TEM_{00} mode Nd^{3+}:YAG, there are a number of advantages to use a TEM^*_{00} mode Nd^{3+}:YAG as will be seen below in the discussion of the phase matching geometries.

On page 3, it was stated that the nonresonant background signal could be either a hindrance or a help, depending on what was being measured. There are a number of ways in which $\chi^{(NR)}$ can be suppressed. The most effective of these involves the appropriate polarisation orientation of the input wave mixing and CARS detection fields. Recalling Figure 1, there are 2-photon processes involving virtual states. The net result of this is that the $\chi^{(NR)}$ term shows symmetry properties different to $\chi^{(R)}$ term. Consequently it responds differently to the polarisation of the laser fields. Bunkin *et al.*[8] were the first to demonstrate that it is possible to suppress $\chi^{(NR)}$ with proper orientation of the laser field and CARS polarisations. Under these circumstances, from Figure 3, the right hand set of figures can be transformed into the left hand set of figures, and hence measurement of much lower concentration levels are possible. This is despite a considerably lower signal in some situations.

Other workers to demonstrate the usefulness of the polarisation technique in a BOXCARS configuration are Akhmanov *et al.*[1] , Attal *et al.*[2] , Eckbreth and Hall[17] , Farrow *et al.*[19] , Oudar *et al.*[52] and Rahn *et al.*[58] . An example of what can be achieved by polarisation $\chi^{(NR)}$ suppression is shown in Figure 6. The labelled peaks in the upper figure are the O-branch lines of ground state N_2 and further details may be found in Rahn *et al.*[58] .

The other methods of nonresonant background suppression are double-resonance CARS[43] , and a time delay technique developed by Kamga and Sceats[36] . Both of these are harder to implement than the polarisation technique described above. Of the three techniques, polarisation is also the most effective and the best approach for combustion diagnostics.

The next point that has to be addressed is the phase matching of the three laser beams. From eqns(4) and (17), the following requirement of the wave vectors must be met:

$$\vec{k}_3 = \vec{k}_0 + \vec{k}_1 - \vec{k}_2, \tag{33}$$

or in the more usual case when $\omega_0 \equiv \omega_1$,

$$\vec{k}_3 = 2\vec{k}_1 - \vec{k}_2. \tag{34}$$

These conditions can be met with a number of geometries. The first is the general planar system, the second is collinear and only applies to gaseous systems since the variation of refractive index with wavelength is almost invariant. This therefore means that $\omega_3 = 2\omega_1 - \omega_2$. The last is the BOXCARS geometry, in which the three laser beams are phase matched at different angles. Each of the above geometries is illustrated in Figure 7.

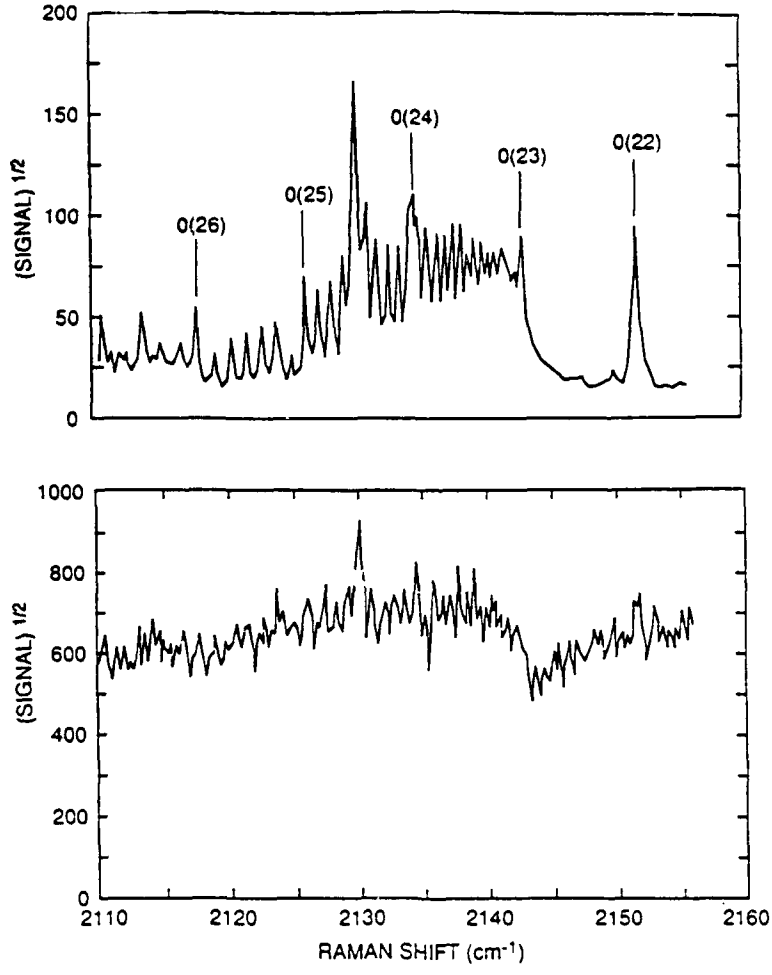

Figure 6: Square–root of the CARS signal from a rich, methane–air flame in the region of the CO Q–branch, (upper) background–free spectrum with $\Theta = 60°$and $\Phi = 57°$;(lower) conventional CARS spectrum with all polarisations parallel, i.e. $\Theta = \Phi = 0$. Both vertical axis scaled in the same arbitrary units.

There are two derivatives of the BOXCARS approach, the first being that the probe and the CARS signal beams lie in a different plane to the pump beam. The advantages of this approach are that:

(a) It removes the need for a dichroic mirror to bring in the other half of the pump beam with the probe beam.

(b) It provides spatial separation of the CARS signal from the input laser beams, and hence requires no filters or dispersing prism.

(c) In high spatial resolution requirements planar BOXCARS confounds the issue due to the production of a CARS signal along the laser beams coming from the dichroic mirror. This other CARS signal must be blocked to give good spatial resolution from the main CARS signal generated from the intersection of the three laser beams.

This geometry is termed Folded–BOXCARS and is a three–dimensional system, as shown in Figure 8. The second derivative of the BOXCARS approach could be considered an

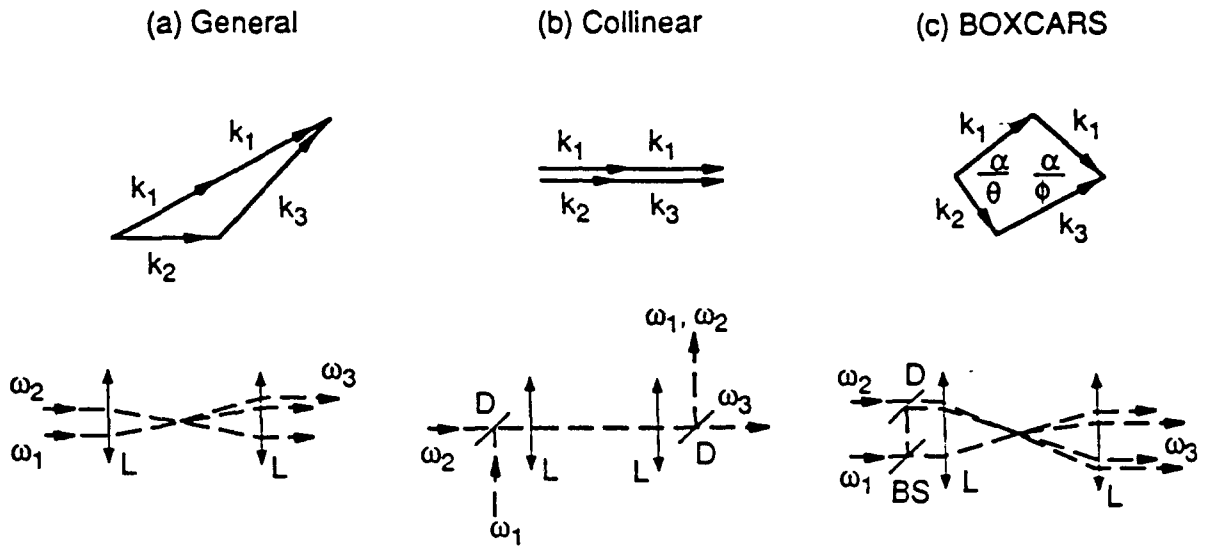

Figure 7: Phase–matching geometries for CARS signal generation.

amalgamation of the collinear and the folded–BOXCARS geometries. It relies on an unstable resonator in the Quanta–Ray DCR–3 Nd^{3+}:YAG, which produces the TEM^{*}_{00} mode mentioned in passing above. The TEM^{*}_{00} mode laser beam is "doughnut" shaped. This enables one to pass the probe laser at ω_2, down the centre of the pump laser beam. Thus the beam steering problems of manipulating the "three" laser beams to the experiment are greatly simplified and the resultant collinear beams need only be considered as a single beam. This geometry is called USED–CARS, the USED part standing for Unstable–resonator Spatially Enhanced Detection, and is the system in use at CSIRO Division of Building, Construction & Engineering. There is also an off–axis variant of USED–CARS in which two CARS signal beams are generated – one through BOXCARS geometry and the other via collinear geometry. The USED–CARS beam positions are illustrated in Figure 9.

The next point that has to be considered if the nonresonant susceptibility, $\chi^{(NR)}$, is not being suppressed or if normalisation of the CARS signal is being carried out, is how and where are the measurements made in the experiment. In all experiments where more than a single laser shot is involved, one has to have a means of being able to normalise the CARS spectrum to account for the shot to shot variability of the lasers. There will always be some jitter in the pump laser intensity. This then feeds onto the dye laser if the same pump laser is used to pump the dye cells. Also, the dye laser power will vary with time as the dye molecules get slowly destroyed by the continued pumping with the focused laser. Reference cells are used for scanned CARS generated signals, either in parallel with the CARS experiment or in series with it, as shown in Figure 10. In the series case, the reference cell should be before the CARS experiment. This is particularly so in combustion diagnostics, since the combustion process can cause the pump and the probe laser

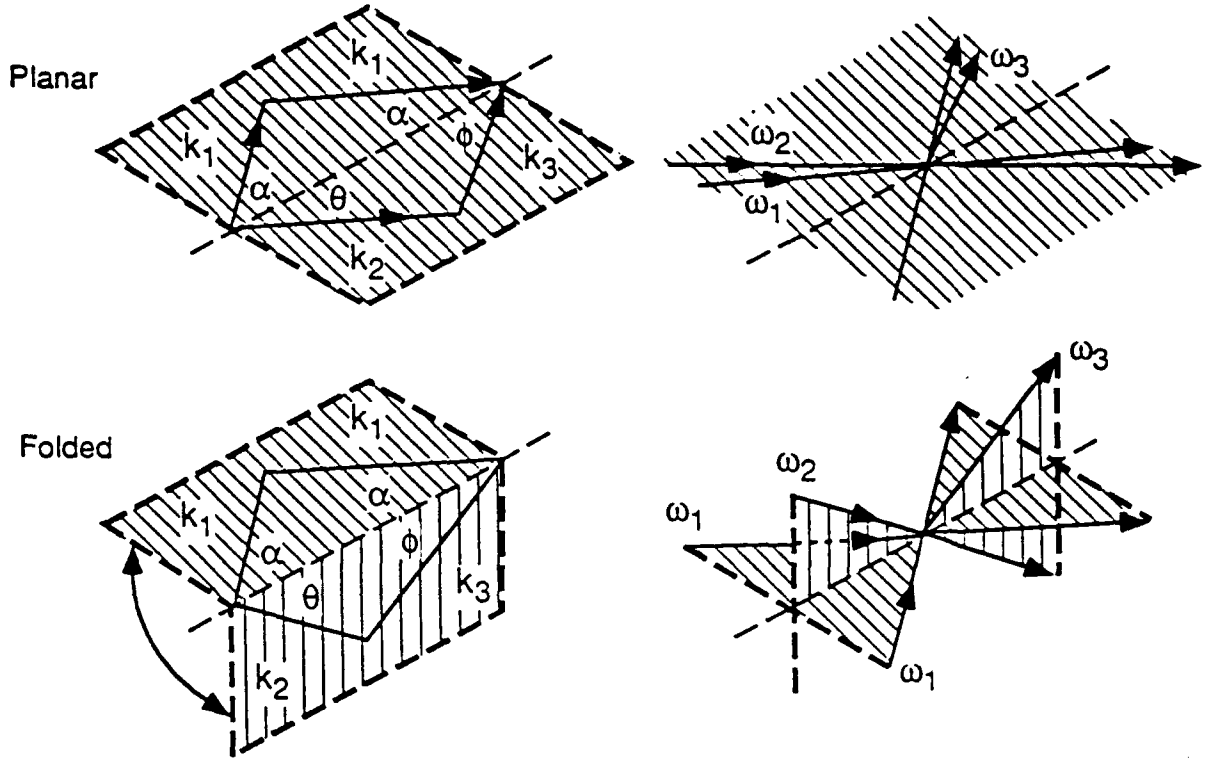

Figure 8: BOXCARS phase–matching variants.

beams to be distorted and hence very difficult, if not impossible, to phase match into the reference cell. For absolute signal intensity measurements, as in the case of concentration determination, a reference cell is necessary if internal referencing is not used. Reference cells although eliminating some problems introduce others such as the inability to maintain the same longitudinal phasing between the pump and the probe laser beams in the reference cell and the CARS experiment. Temporal mode beating can also arise causing large fluctuations in the CARS signal of the order of $\pm 25\%$[68,23] . Attempts have been made to get round these problems by developing *in–situ* referencing techniques. This referencing technique relies on the nonresonant background susceptibility being used as the *in–situ* calibrating standard. The technique stems from the method of polarisation background suppression and has been demonstrated by Oudar & Shen[53] and Farrow *et al.*[19,20] .

The approach is to insert a beam splitter in the CARS signal beam after the probe and pump beams have been removed, via spatial or optical filters, but before a Glan Thomson polariser in the signal beam. The beam splitter only splits off a small amount of the CARS signal beam and is then passed through another Glan Thomson polariser, but this time the polariser is set normal to the CARS signal beam, such that only the nonresonant part can be viewed. The $\chi^{(NR)}$ intensity is proportional to the gas density, in gaseous systems, and therefore serves as the reference to the CARS signal, which is viewed through through the first mentioned Glan Thomson polariser, which is this time set at right angles to the nonresonant beam polarisation. The only possible drawback with this technique is that the if there are any compositional changes in the media, the value of $\chi^{(NR)}$ will change

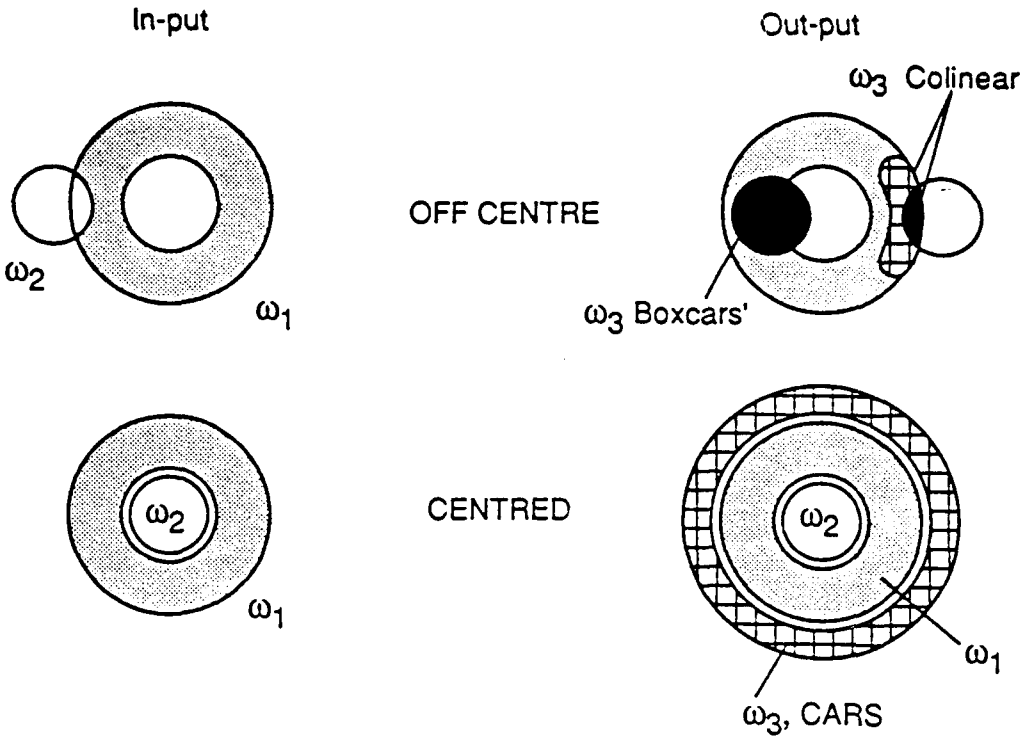

Figure 9: USED-CARS geometries.

in an unpredictable manner. In some situations it may be possible to tailor the mixture so that a single species dominates the $\chi^{(NR)}$ signal, see Table 1 for relativities between combustion species.

A totally different approach is based again on polarisation suppression of the background, but relies on the use of either two different pump laser lines or broad-band dye lasers, whose spectral properties have been chosen such that several species can be recorded by the detection system simultaneously. On of the species must be at a known high concentration in the CARS generation area during all of the measurements. This species serves as the reference. This approach is based on true four colour CARS and will be discussed in more detail in the next section.

The last part of the CARS system is the capture of the CARS signal. This involves two parts - a monochrometer, usually a 1m double monochrometer, such as a Spex 1704, and a detector system to capture and store the dispersed CARS signal at the exit to the monochrometer. The detector systems normally employed in CARS work are optical multichannel analysers (OMA) based on either intensified self-scanned diode arrays or intensified silicon intensified target (ISIT). Details of these devices can be found in Chang and Long[9] . The main problem with ISIT based systems is the cross-talk between the pixel elements, i.e. a single spectral line, which would normally fall on a single column of pixels, bleeds out to cover about 5 pixels. As well as cross-talk, ISIT devices also suffer from read-out delays, which then controls the laser repetition rate. This latter disadvantage of ISITs can be, to some extent, circumvented by controlling where on a typical 500×512 pixel array of the detector, that the signal is recorded from, such as in

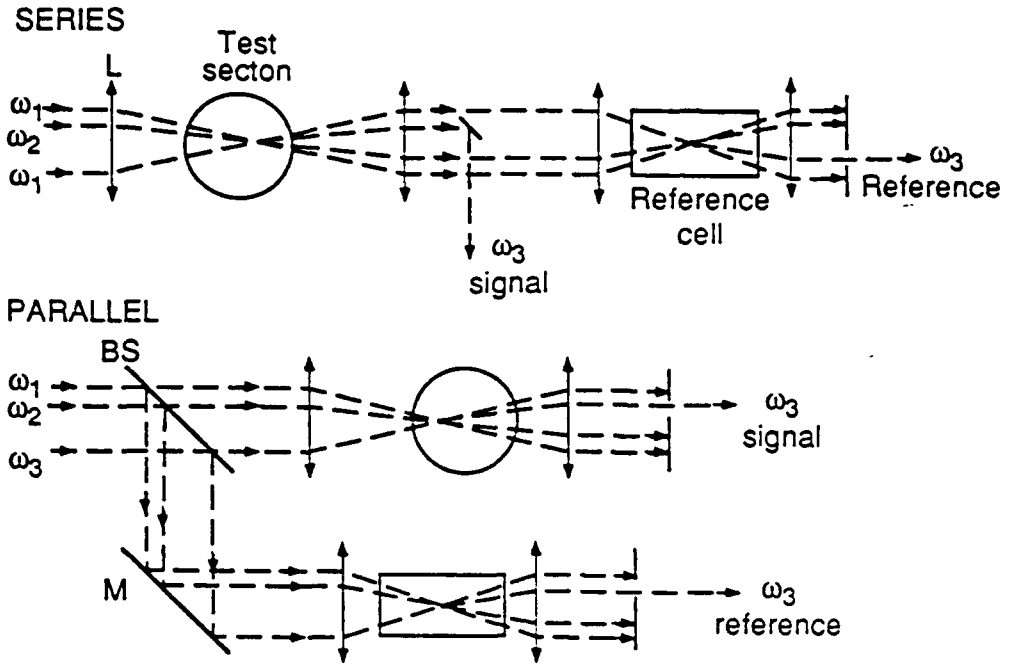

Figure 10: Arrangements for reference cells.

the Princetom Applied Research OMA III/ 1245E ISIT software/hardware system.

The complete CARS system, including the resultant signal processing, is shown schematically in Figure 11. The controlling factors on the resultant resolution of the CARS spectra will be:

(a) the laser linewidths, which can range from 0.05 to 1.0cm^{-1} depending on whether an intercavity etalon is used,

(b) the monochrometer resolving power, for the Spex 1704 it is about 0.8cm^{-1}, and

(c) the diode array or ISIT resolving power, which will depend on the number of elements in the array and where they are situated in relation to the exit plane of the monochrometer, e.g. for the PAR 1245E ISIT it is $\sim$1cm^{-1}.

For broad-band CARS, only the last two items control the CARS spectral resolution. Typically one can produce CARS spectra with resolutions between 0.5 and 1.0cm^{-1}, which is more than adequate for combustion diagnostics.

4. MEASUREMENTS

There are two quantities that one can measure with a CARS system:

- temperature, and
- species concentrations.

Both these measurements are "point" measurements, and therefore require many measurements to build up a picture of what conditions exist. If the conditions within the measurement envelop are continually changing, the measurement problem becomes even more complex, especially if the variations in the time domain are random. In some cases

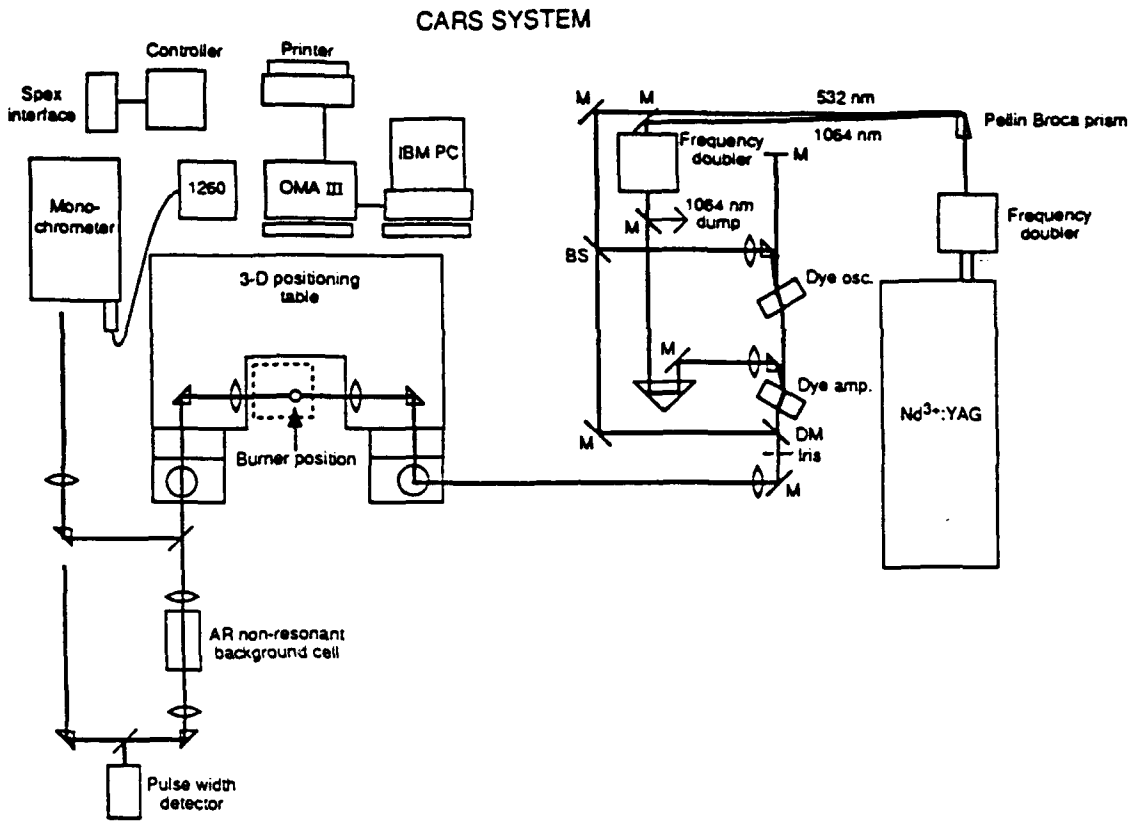

Figure 11: A complete possible arrangement for a CARS signal generation and collection.

it may be possible to drive the processes being studied by some external means, such as acoustic forcing to some resonant frequency of the apparatus. This then locks the process into a repetitive mode, enabling the process to be studied over a longer period of time[55, 54] . Kurtz[39] has developed a technique to speed-up the CARS signal generation process and data acquisition, which enables multiple CARS signals to be obtained in a single step using a pair of dichroic mirrors and lenses. The spatial resolution is determined by the angle between the two dichroic mirrors. The lens diameters and the OMA resolving power controls the maximum number of linear points where the CARS measurements are made.

Before going into the temperature and species concentration measurements in more detail, there are some points which first of must be addressed. Firstly there is a limit to the laser intensities that can be used. High power pump lasers can lead to growth of the Stokes field at ω_2 and this can interfere with the probe laser amplitude profile leading to distorted CARS spectra. Fortunately this is only a problem at high pressures around 3MPa and above. Secondly, the high power lasers can inadvertently alter the population states involved in the CARS process[62] , i.e. Δ_j is not what it ought to be, leading to the wrong value for $\mathcal{A}$. To avoid this, the characteristic time for population pumping, τ_Δ, has to obey the following relationship with relation to the laser pulse width τ_ℓ:

$$\tau_\Delta \equiv \left[2 \left(\frac{4\pi c}{\hbar \omega_2^2} \right)^2 \left(\frac{\partial \sigma}{\partial \Omega} \right)_j \frac{I_1 I_2}{\Gamma_j} \right]^{-1} \gg \tau_\ell. \tag{35}$$

Hence the upper limit for the product $I_1 I_2$ for most CARS work is in the vicinity of

Combustion species	Normalised $\chi^{(NR)13}$	Normalised $\chi^{(NR)57}$
Ar	1.249	1.148
CO	1.477	1.333
CO_2	1.457	1.481
CH_4	3.147	2.185
C_2H_6	5.042	4.593
H_2	0.761	NA
H_2O	1.844	NA
NO	3.046	3.111
N_2	1.000	1.000
O_2	1.343	0.963

Table 1: Normalised nonresonant susceptibilities for some combustion species with respect to nitrogen.

$1000EW^2\ m^{-4}$. Lastly, one should be aware of the contributions of each species participating in the $\chi^{(NR)}$ term. This is especially so in combustion situations when fuel rich conditions exist, since, as can be seen from Table 1, the hydrocarbons have a much higher $\chi^{(NR)}$ value than the major species N_2. Argon nonresonant value is given in Table 1 since it is usually used as reference gas when reference cells are employed. Note, the values in Table 1 are for atmospheric pressure only.

4.1 TEMPERATURE MEASUREMENT

The main use for CARS has been for temperature measurement in hostile combustion environments and shock tube work. In most cases the approach has been to make CARS measurements of the N_2 Q-branch transition. In air/fuel combustion it is not hard to see why the nitrogen molecule is used. It constitutes around 70% of the gas composition and is usually present in high concentrations throughout the mixture, except in diffusion flames. Therefore care has to be taken in using CARS in these flames.

There are two CARS temperature measurement techniques with N_2. The main one is vibrational CARS and the other is rotational CARS. The former is based on the various N_2 Q-branch transitions. Until the temperature of the N_2 reaches 1000K, only the $v = 0 \rightarrow v = 1$ Q-branch transition is observed, which remains as an unresolved broadening band as the temperature increases. At about 1000K, the $v = 1 \rightarrow v = 2$ Q-branch starts to become apparent and is quite pronounced by the time the temperature reaches 2000K. This is the first "hot" band of N_2. A second "hot" band starts to appear above 2000K, not shown in Figure 12, and is due to $v = 2 \rightarrow v = 3$ Q-branch transition. The ripples on the higher temperature spectra in Figure 12 correspond to the even J Q-branch transitions. The odd J Q-branch transitions are about a quarter that of the even ones, (see upper Figure 13), and hence do not stand out due to the OMA/spectrometer resolving power. The two peaks in the first "hot" band at 21085 and $21100cm^{-1}$ are due to close coincidences of the J levels in the $v = 0 \rightarrow v = 1$ state and those in the $v = 1 \rightarrow v = 2$ state. This point was discussed as one method of removing the background nonresonant susceptibility in the previous section.

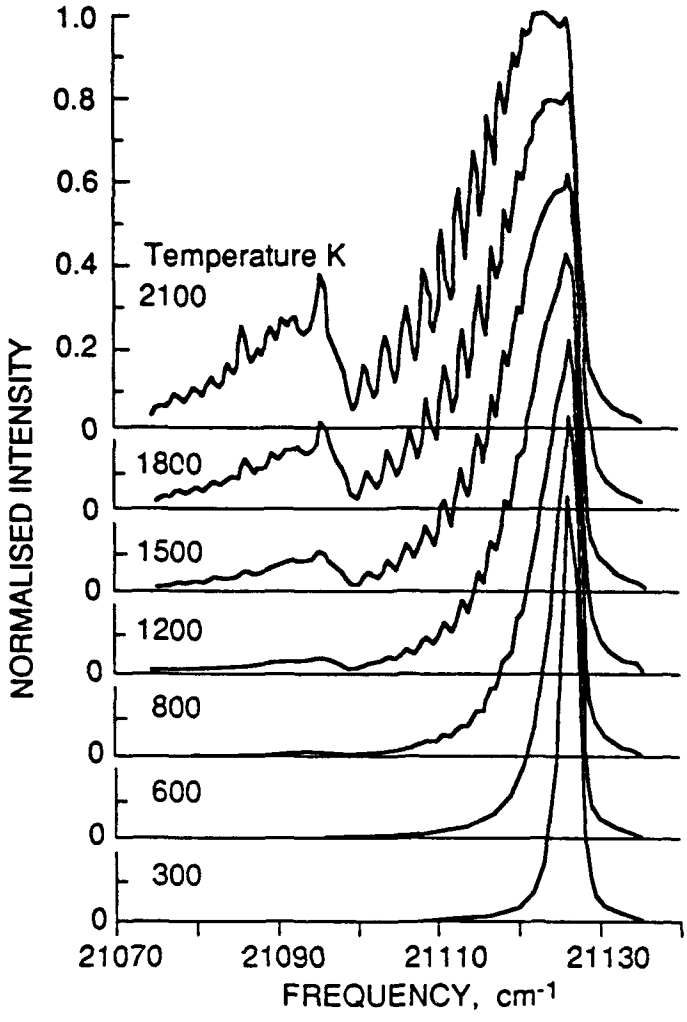

Figure 12: N_2 vibrational CARS spectra as a function of temperature.

Figure 13 shows the idealised CARS N_2 spectrum at 1700K in the upper figure. The lower figure is the upper figure convolved over the pump Gaussian linewidth of $0.4cm^{-1}$ HWHM and a $4.0cm^{-1}$ HWHM Gaussian slit function. The spectral constant of Hall[28] , nonresonant susceptibilities from Eckbreth & Hall[17] and the Raman linewidth variation with temperature and J level from Hall[29] were used in the convolution calculation. The lower figure is indicative of what might be seen with reasonable, but not good, instrumental resolving power. Even so, this spectrum is adequate to make temperature measurements from. Lõfström *et al.*[40] have demonstated a technique for vibrational CARS temperature measurement which uses 3 narrow linewidth lasers, one at 532 and the others to produce ω_{3_1} at $J = 6$ and ω_{3_2} at $J = 22$ both in the N_2 Q–branch fundamental band or again at $J = 6$ and this time ω_{3_2} in the first hot band at $J = 42$. This technique can be considered as a variant of scanned CARS, except that the two CARS lines are genarated within a single pulse width. At this stage of development the technique shows some promise over the broadband approach, but it is not without its attendant difficulties.

Changes in the pressure of the environment also affect the shape of the CARS spectra through pressure broadening of the linewidths and collisional narrowing. Figure 14 illus-

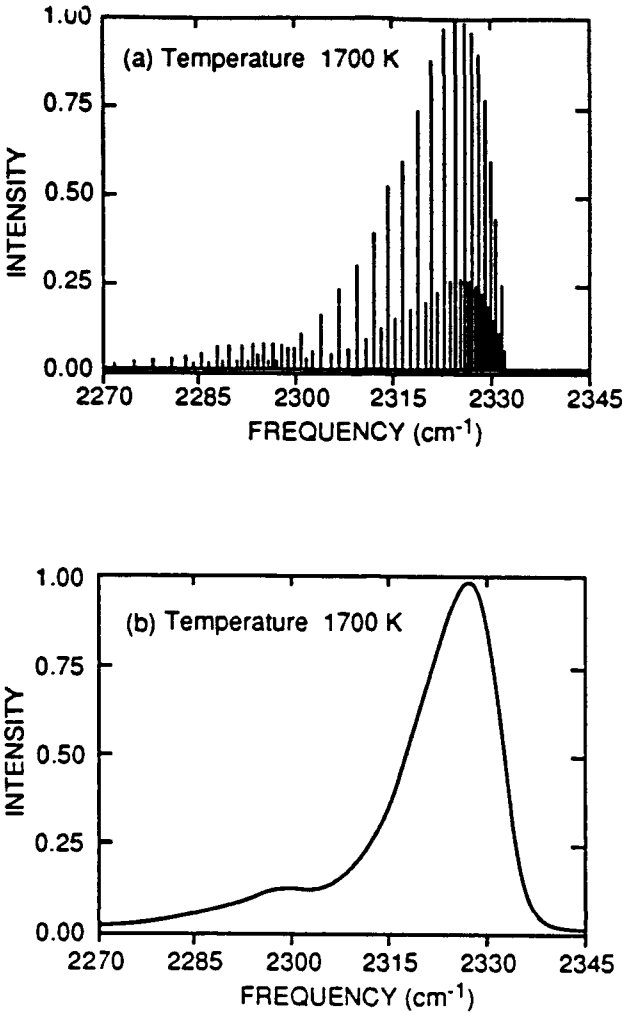

Figure 13: Comparison between idealised N_2 vibrational CARS spectra and measured spectra at 1700K.

trates this for room temperature N_2. The left hand spectrum is a highly resolved view of the same spectra shown in Figure 12. At the high pressure (10MPa), the even J in the $Q_{v=0 \rightarrow v=1}$ branch have disappeared. This occurs once the pressure reaches 1MPa. At temperatures where the "hot" band exists, the $Q_{v=1 \rightarrow v=2}$ band is still resolvable from the $Q_{v=0 \rightarrow v=1}$ band.

It will be noticed from Figure 12, that below about 1000K it is much more difficult to determine the temperature accurate unless one has both very high resolution spectra and a low pressure system. The solution is to use rotational CARS in which $\Delta v = 0$, $\Delta J = \pm 2$, for which the rotational Raman cross sections are about an order of magnitude larger than the vibrational Raman cross section. Also, the rotational transitions are widely spaced simplifying the computation and delaying the onset of collisional narrowing due to pressure increases, as in the case of vibrational spectra. Rotational CARS begins to fail at the higher temperatures when species such as CO_2 and H_2O are present due to smearing of the N_2 spectra, as the higher J number lines of each species begin to overlap one another, and the major species present dominates the spectra. The advantage of the large Raman

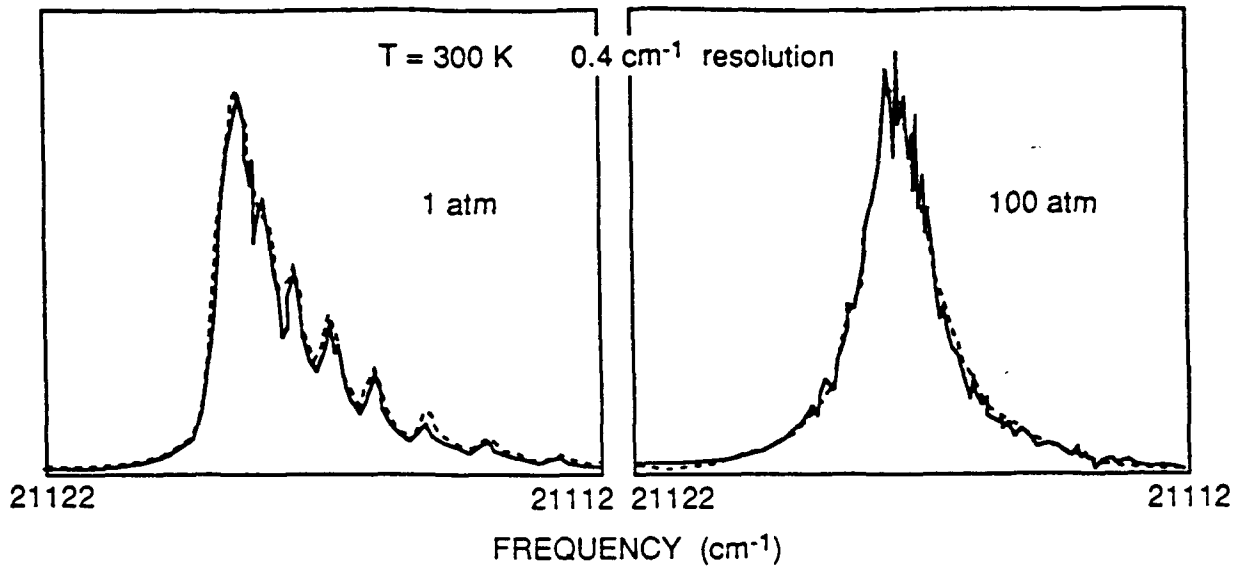

Figure 14: Effects of pressure on CARS N_2 spectrum.

cross sections is counter balanced by the smaller populations in the rotational states. The net effect is that the signal strengths are about the same as those from vibrational CARS[30] .

Since one is dealing with rotational states within a particular vibrational state ($\Delta v = 0$), the separation between ω_1 and ω_2 is very small and the pump laser at ω_1 can't be used to generate the probe at ω_2. Either one has to generate a third harmonic from the Nd^{3+}:YAG at 355nm by wave mixing the residual 1064nm with some of the 2^{nd} harmonic 532nm, and using the 355nm Nd^{3+}:YAG to pump the dye laser to generate the probe laser over the range 532nm to 540nm. Or a separate laser, such as an excimer, can be used to produce the appropriate probe dye laser, which introduces a timing problem[54] in that two different nanosecond events have to be timed to coincide at the focus of the experiment. Theoretically one should be able to generate rotational CARS signals from any arbitrary chosen broadband dye laser, since the spectral range is more than sufficient and all the necessary wavelengths are present. Eckbreth and Anderson[15] have shown how this can be achieved.

The accuracy of CARS thermometry at low pressures (i.e. less than 1MPa), is at its worst ± 25 K for vibrational CARS above 1000K. With narrow linewidths and good resolving power in the detection equipment, the standard deviation on the measured value can be ± 9 K. Generally, with vibrational CARS the higher the temperature the smaller the absolute error in the measurement. With rotational CARS the reverse is true. At room temperature the standard deviation is $\sim \pm 4$ K and remains at this level until about 1000K, whereupon the error starts to increase rapidly.

In order to derive the temperature from CARS spectra, one needs some code to perform the comparison of theoretically derived spectra with the maesured CARS spectra for the experimental constants. These CARS codes can be had from SANDIA Labs[22] and Marcus

Aldén's group at Lund Unversity, Sweden. The latter group have developed two separate CARS codes, one for vibrational CARS temperature measurement[5] and the other for rotational CARS temperature measurement[46] , both of which have been derived from the SANDIA code and updated..

4.2 SPECIES CONCENTRATION MEASUREMENT

There are two requirements necessary for CARS species concentrations to be effected. These are that the species possess

(a) a Raman transition, and

(b) concentration is high enough to enable the nonresonant background to be overcome either naturally or through polarisation suppression or electronic enhancement.

In combustion systems it is unfortunate that many of the species present do not meet the second criterion. Fortunately, there are techniques such as DFWM[45] , that will detect the low concentrations of species. Thus, in combustion systems CARS species measurement is restricted to the major species - CO, CO_2, CH_4, C_2, H_2O, N_2, NO, NO_2, OH and O_2.

Concentration measurements are calculated either from the intensity of the CARS spectrum or from the shape of the spectrum. The first approach requires background free or suppressed nonresonant signals, and because it relies on signal strength it has to be referenced appropriately. Referencing techniques have been dealt with in the section on *Experimental Requirements*. The intensity approach is ideally suited to moderate to high concentrations.

The line shape approach come about from the underlying principle behind Figure 3. From Figure 3 it is obvious that there are a whole family of lineshape between the two extremes of high and low concentration. Figure 15 illustrates the calculated lineshapes for CO in a 1800K flame. It can be seen from Figure 15 that one is able to resolve concentrations of CO quite readily between 0.5% and 20%. Above 20%, the shape of the spectral curve does not change much and hence it is difficult to resolve concentrations between 20% and 100% with any degree of confidence. Below 0.5%, the spectral profile disappears into the nonresonant background. The curved shape of the spectral profile at low concentration is due to the dye laser profile, see middle third of Figure 5 which spans the range of Figure 15.

Clearly one could speed up information gathering on a chemically reacting system, such as a combustion process, if one could measure several species concentrations simultaneously, preferably along with temperature. This can be done for some sets of molecules. It is based on the "true" four colour CARS briefly mentioned in the *Experimental Requirements* section. There are two approaches to carrying out the four colour CARS.

The first involves two single line pump lasers and a broadband dye probe laser. The system can then be considered as two 'three colour CARS' system, in which either the two single line pump laser are closely spaced, about 15 to 20nm separation, with a 10nm bandwidth broadband dye laser; or the single laser line spacing can be relaxed if a dye such as DCM or a tailored mixture of dyes is used. The second method involves the use of one single line pump laser and two broadband dye probe lasers. These techniques have been demonstrated by Switzer *et al.*[67] , Eckbreth & Anderson[14,16] , Lucht[41] and Grisch *et al.*[27] Table 2 gives the CARS wavelengths for a range of gases and vapours relative to

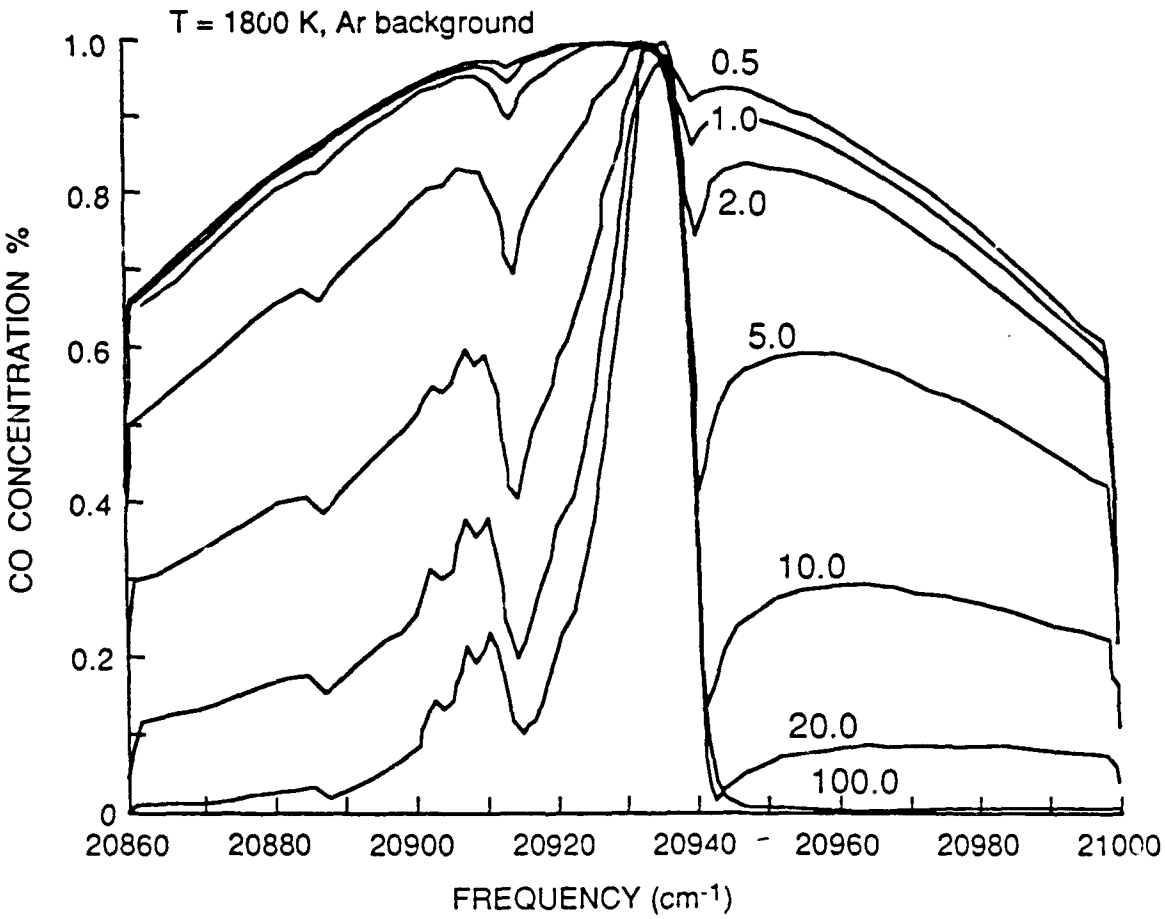

Figure 15: CO vibrational CARS spectra as a function of concentration.

species	Ω_v (cm^{-1})	Resultant CARS λ nm	laser dye required	probe λ nm
SO_2	519	517.7	Fluorescein 548	547.1
C_2H_6	992	505.3	Fluorescein 548, Rhodamine 590	561.6
C_6H_6	992	505.3	Fluorescein 548, Rhodamine 590	561.6
O_3	1103	502.5	Fluorescein 548, Rhodamine 590	565.2
SO_2	1151	501.3	Fuorescein 548, Rhodamine 590	566.7
CO_2	1286	497.9	Rhodamine 590	571.1
N_2O	1287	497.9	Rhodamine 590	571.1
CO_2	1388	495.4	Rhodamine 590	574.4
CH_4	1533	491.9	Rhodamine 610 & 590, Kiton Red 620	579.2
O_2	1556	491.3	Rhodamine 610, Kiton Red 620	580.0
NO	1877	483.7	Rhodamine 610, Kiton Red 620	591.0
CO	2143	477.6	Rhodamine 640, Kiton Red 620	600.5
N_2O	2223	475.7	Sulforhodamine 640, Rhodamine 640	603.4
N_2	2330	473.3	DCM, Sulforhodamine 640, Rhodamine 640	607.3
H_2S	2611	467.1	DCM, Sulforhodamine 640, Rhodamine 640	617.8
CH_4	2914	460.6	DCM, Sulforhodamine 640	629.6
CH_4	3020	458.4	DCM	633.8
C_6H_6	3062	457.5	DCM	635.5
NH_3	3334	451.9	DCM	646.7
H_2O	3654	445.4	DCM	660.4
H_2	4160	435.6	DCM	683.2

Table 2: CARS wavelengths for various gases and vapours relative to 532nm pump laser and dye laser required.

532nm radiation along with the probe laser wavelength required and the corresponding dyes. Table 2 can be repeated for other pump wavelengths. If one now considers the case of pump lasers at 18797cm^{-1} (532nm) and 19436cm^{-1} (514.5nm) in conjunction with a rhodamine 610 dye laser, there are four basic cases to consider:

1. there is the CARS signal generated solely due to the interaction between the 514.5nm pump and the dye laser probe to produce N_2, N_2O and CO CARS signals between 459nm and 463nm.

2. there is the CARS signal generated solely due to the following sequence of interactions. First of all up-shifting by the 19436cm^{-1} pump, then down-shifting with the dye laser probe, then the second up-shifting with the 18797cm^{-1} pump laser to produce the same set of CARS signals as before, i.e. N_2, N_2O and CO, but this time between 473nm and 478nm.

3. there is the CARS signal generated solely due to the following sequence of interactions. First of all up-shifting by the 18797cm^{-1} pump, then down-shifting with the dye laser probe, then the second up-shifting with the 19436cm^{-1} pump laser to produce a different set of CARS signals for O_2 and CH_4, at around 476–477nm.

4. there is the CARS signal generated solely due to the interaction between the 532nm pump and the dye laser probe to produce O_2 and CH_4 CARS signals between 491nm and 492nm.

It can be seen from the second and third items, that there exists the possibility of measuring the concentrations of four species along with temperature. For natural gas combustion it should also be possible to measure fuel/air ratios, providing the conditions for generating CARS signals are met.

5. PROBLEM AREAS

Like most other laser diagnostic techniques, CARS is not without its drawbacks. Some of these problems have counterparts in other laser diagnostic techniques.

The first problem is window fluorescence. With the high radiation fluxes normally used in combustion CARS measurements, fluorescence from impurities in the two optical access windows will occur. Fortunately it will be at the same wavelengths as the pump and probe lasers or longer and is easily separated from the shorter wavelength CARS signal. Secondly, particles in the combusting material, such as soot and fuel particles or drops, i.e. carbon particles in the main; can absorb substantial amounts of the incident radiation to cause local heating, except in the case of lasers with pulse widths less than 10ns. In some cases the carbon particles can ignite due to the absorbed radiation and lead to very high temperatures at the point of measurement, leading to an anomalously high temperature measurement from CARS nitrogen spectrum. Besides absorbing the laser radiation, the particles can also cause defocusing or beam steering. This causes undue problems with the reference cell technique. Under these conditions the only solution is to use *in-situ* referencing. The carbon particles combustion also leads to a third problem. The combusting carbon will be emitting strongly at the C_2-Swan bands, one of which unfortunately resides at 473.7nm degraded to the UV, which overlaps the N_2 vibrational CARS signal produced via a 532nm pump laser. The only solution to this problem is to chose another pump source so that N_2 vibrational CARS signal is away from any of the C_2-Swan bands.

The fourth problem is optical breakdown of the medium being probed. This occurs when very high laser fluxes are focused in a medium and result in ionisation of that medium. It is easily encountered at room temperature, but not normally in combustion, where the temperatures are much higher. Fifth problem only concerns those interested in carrying out high-resolution CARS spectroscopy, and it is optical Stark effects of broadening and splitting[59,21] . Stark splitting only occurs in transitions where there is a change in rotational quantum number and is laser power density dependant at about $0.1 cm^{-1}$ per $10PW\ m^{-2}$. The splitting sets in at about power densities of $0.1PW\ m^{-2}$.

The last problem is probably the most serious as far as temperature measurements are concerned. In some combustion systems there can be very large temperature gradients over a short distance. Under these conditions the CARS probe volume can straddle a large temperature gradient[56,65,75] . A typical probe volume is an oblate spheroid 0.7mm long in the direction of the CARS signal propagation and 0.3mm in diameter. When this straddling occurs, the CARS temperature signal is strongly biased towards the colder temperature. Unless one has some knowledge of how the temperature gradient varies with distance, one can end up with considerable errors in temperatures measured via CARS. Zhu and Dunn-Rankine[75] show how one can go about minimising these errors.

6. CONCLUSIONS

Although the CARS signal generation, collection and interpretation appears straight forward, it is not a technique which lends itself to routine diagnostic procedures. Where its advantage lies is that it can provide quantitative bench-marks for qualitative techniques such as LIF, which are much more readily carried out and provide the sought after information much quicker. It is also an expensive technique to implement.

NOMENCLATURE

$\mathcal{A}$	constant.
c	speed of light in vacuum.
E	the electric field of the incident electromagnetic light wave.
E_{at}	the intra-atomic electric field.
$\hbar$	Planck's constant $\div 2\pi$
k	wave vector.
ℓ	length over which the CARS signal is generated.
$\mathcal{N}$	total population in the lower and upper state.
n	refractive index.
P	the generalised electric polarisation induced in the medium.
r	the radial coordinate.
t	time.
Γ	linewidth.
Δk	detuned wave vector or phase mismatch.
$\Delta\omega$	off resonance frequency mismatch.
Δ_j	fraction of the population residing in the lower state.
ϵ	permittivity
ϵ_0	permittivity of free space
Θ	angle between polarisations of ω_1 and ω_2.
μ_0	the permittivity of free space.
σ	Raman cross-section.
τ_ℓ	laser pulse width.
τ_Δ	time to pump population between states.
Φ	angle between polarisation of ω_3 and the direction of the analyser.
$\chi^{(1)}$	the linear susceptibility of the medium.
$\chi^{(n)}$	the n^{th} order nonlinear susceptibility of the medium ($n \neq 1$).
ω	the circular or radian frequency.
ω_m	frequency of laser m radiation.
Ω_v	vibrational Raman frequency.

REFERENCES

[1] Akhmanov, S.A.; Bunkin, A.F.; Ivanov, S.G. & Koroteev, N.I. Polarisation active Raman spectroscopy and coherent Raman ellipsometry. *Sov. Phys. JETP* **47** 667–678 (1978).

[2] Attal, B.; Pealat, M. & Taran, J.P.E., CARS diagnostics of combustion. *J. Energy* 4135–141(1980).

[3] Barrett, J.J & Begley, R.F., Low-power CW generation of coherent anti-Stokes Raman radiation in CH_4 gas. *Appl. Phys. Lett.* **27** 129–131 (1975).

[4] Begley, R.F.; Harvey, A.B.; Byer, R.L. & Hudson, B.S., A new spectroscopic tool – coherent anti-Stokes Raman spectroscopy. *American Laboratory* Nov., 1974.

[5] Bengtsson, P.-E., Department of Combustion Physics, LTH, Box 118, S-22100 Lund, Sweden, *personal communication* (1993).

[6] Bloembergen, N. *Nonlinear Optics.* Benjamin, New York, 1965.
[7] Bogaard, M.P. & Orr, B.J., *International Review of Science.* Physical Chemistry, Series 2, Vol. 2, A.D. Buckingham (ed), Butterworths, UK.
[8] Bunkin, A.F.; Ivanov, S.G. & Korotev, N.I. Gas analysis by coherent active Raman spectroscopy with polarization discrimination. *Sov. Tech. Phys. Letts.* **3** 182–184 (1977).
[9] Chang, R.K. & Long, M.B. Optical multichannel detection. pp179–205, in M. Cardona and G. Guntherodt, (Eds.) *Topics in Applied Physics. Vol 50, Light Scattering in Solids II.* Springer–Verlag, Berlin, FRG, (1982).
[10] De Witt, R.W., Harvey, A.B. & Tolles, W.M, *Theoretical development of third order susceptibility as related to coherent anti–Stokes Raman spectroscopy.* NRL Memorandum Report, N^{O}. 3260 (April 1976).
[11] Eckbreth, A.C., Effects of laser–modulated particle incandescence on Raman scattering diagnostics. *J. Appl. Physics* 48 4473–4479 (1977).
[12] Eckbreth, A.C., CARS investigations in sooting and turbulent flames. Project SQUID Technical Report UTRC–5–PU, 1979.
[13] Eckbreth, A.C., *Laser Diagnostics for Combustion Temperature and Species*, Energy & Engineering Science Series, Eds A.K. Gupta and D.G. Lilley, Abacus Press, Kent, UK, 1988.
[14] Eckbreth, A.C. & Anderson, T.J., Dual broadband CARS for simultaneous, multiple species measurements. *Appl. Optics* 24 2731–2736 (1985).
[15] Eckbreth, A.C. & Anderson, T.J., Simulaneous, pure rotational CARS/CSRS with a spectrally–arbitrary Stokes source. *Opt. Lett.* 11 496–498 (1986).
[16] Eckbreth, A.C. & Anderson, T.J., Dual broadband USED CARS. *Appl. Optics* 25 1534–1536 (1986).
[17] Eckbreth, A.C. & Hall, R.J., CARS concentration sensitivity with and without nonresonant background suppression. *Combust. Science & Tech.* 25 175–192 (1981).
[18] Eesley, G.L., *Coherent Raman Spectroscopy.* Pergamon, Oxford, UK, 1981.
[19] Farrow, R.L.; Mattern, P.L. & Rahn, L.A., Crossed–beam background–free CARS measurements in a methane diffusion flame. *AIAA* Paper 81–0182, (1981).
[20] Farrow, R.L.; Mattern, P.L. & Rahn, L.A., Coparison between CARS and corrected thermocouple temperature measurements in a diffusion flame. *Appl. Optics* 21 3119–3125 (1982).
[21] Farrow, R.L. & Rahn, L.A., Optical Stark splitting of rotational Raman transitions. *Phys. Rev. Let.* 48 395–398 (1982).
[22] Farrow, R.L. & Palmer, R.E., Sandia CARS code.
[23] Goss, L.P.; Switzer, G.L. & Schreiber, P.W., Flame studies with coherent anti–Stokes Raman spectroscopy technique. *AIAA* Paper 80–1543 (1980).
[24] Goss, L.P.; Trump, D.D. M^{ac}Donald, B.G. & Switzer, G.L., 10-Hz coherent anti–Stokes Raman spectroscopy apparatus for turbulent combustion studies. *Rev. Sci. Instrum.* 54 563–571 (1983).
[25] Greenhalgh, D.A. & Hall, R.J., A closed solution for the CARS intensity convolution. *Opt. Comm.* 57125–128(1986).
[26] Greenhalgh, D.A.; Porter, F.M. & Barton, S.A., A polynomial energy gap model for molecular linewidths. AERA – R 11260 , Harwell, UK, Jun 1984.
[27] Grisch, F.; Bouchardy, P.; Pélat, M.; Chanetz, B.; Pot, T. & Coët, M.C. Rotational temperature and density measurements in a hypersonic flow by dual–line CARS. *Appl. Phys.* B Photo–physics and Laser Chemistry B56 14–20 (1993).
[28] Hall, R.J., CARS spectra of combustion gases. *Combust. & Flame* 35 47–60 (1979).
[29] Hall, R.J., Pressure broadened linewidths for N_2 coherent anti–Stokes Raman spectroscopy thermometry. *Appl. Spectroscopy.* 34 700–702 (1980).
[30] Hall, R.J. & Eckbreth, A.C., Coherent anti–Stokes Raman spectroscopy (CARS): Application to combustion diagnostics. pp213–309, in J.F. Ready & R.K. Erf (Eds.) *Laser Applications, Vol 5* Academic Press, Orlando, Fl, (1984).

[31] Harvey, A.B., *Chemical Applications of Nonlinear Raman Spectroscopy.* Academic Press, New York, 1981.
[32] Hauchecorne, G; Kerherve, F. & Mayer, G., *J. Phys.* 3247(1971).
[33] Henesian, M.A.; Kulevskii, L.; Byer, R.L. & Herbst, R.L., CW high-resolution CAR spectroscopy of H_2, D_2, and CH_4. *Opt. Comm.* 18225(1976).
[34] Henesian, M.A. & Byer, R.L., High resolution CARS lineshape function. *J. Opt. Soc. Am.* 68 648 (1978).
[35] Jackson, J.D. *Classical Electrodynamics* John Wiley, New York 1963.
[36] Kamga, F.M. & Sceats, M.G., Pulse-sequenced coherent anti-Stokes Raman scattering spectroscopy: A method for supression of nonresonant background. *Opt. Lett.* 52 126-128 (1980).
[37] Kataoka, H.; Maeda, S. & Hirose, C., Effects of laser linewidth on coherent anti-Stokes Raman spectroscopy spectral profile. *Appl. Spectroscopy.* 36 565-569 (1982).
[38] Kröll, S.; Aldén, M.; Berglind, T. & Hall, R.J., Noise characteristics of single shot broadband Raman-resonant CARS with single- and multimode lasers. *Appl. Optics* 26 1068-1073 (1987).
[39] Kurtz, A. Multipoint CARS. *Appl. Optics* 28 5206-5208 (1989).
[40] Löfström, C.; Kröll, S. & Aldén, M. *Investigation of the precision and accuracy of 2-λ CARS and its application in temperature measurements in turbulent flames.* 24th Symp on Combustion, The Combustion Institute, pp1637-1644, Sydney, July (1992).
[41] Lucht, R.P. Three-laser coherent anti-Stokes Raman scattering measurements of two species. *Opt. Lett.* 12 78-80 (1987).
[42] Lucht, R.P. & Farrow, R.L., Calculation of saturation line shapes and intensitites in coherent anti-Stokes Raman scattering spectra of nitogen. *J. Opt. Soc. Am.* B 5 1243-1252 (1988).
[43] Lynch, R.T.; Kramer, S.D.; Lotem, H. & Bloembergen, N., Double resonance interference in third-order light mixing. *Opt. Comm.* 16373-375(1976).
[44] Maier, M.; Kaiser, W. & Giordmaine, J.A., *Phys. Rev.* 177580(1969).
[45] Mann, B.A. & White, R.F., Detection of nitrogen dioxide using LIF and DFWM : Effect of buffer gas. DSTO Workshop on Laser Diagnostics in Fluid Mechanics and Combustion, DSTO-ARL, Melbourne, 30th Sep.-1st Oct. 1993.
[46] Martinso, L., Department of Combustior Physics, LTH, Box 118, S-22100 Lund, Sweden, *personal communication* (1993).
[47] Minck, R.W.; Terhune, R.W. & Rado, W.G., *Appl. Phys. Lett.* 3 181 (1963).
[48] Moosmüller, H. & She, C.Y., Simultaneous four-wave mixing and stimulated Ramman spectroscopy: effects of Doppler broadening and neighboring lines. *J. Opt. Soc. Am.* B 4 1977-1983 (1987).
[49] Moya, F.S.; Druet, S.A.J. & Taran, J.P.E., Gas spectroscopy and temperature measurement by coherent anti-Stokes scattering. *Opt. Comm.* 13169-174(1975).
[50] Moya, F.S.; Druet, S.A.J. & Taran, J.P.E., Flame Investigation by Coherent Anti-Stokes Scattering. in Zinn, B.T. ed *Experimental Diagnostics in Gas Phase Combustion Systems.* Progress in Astronautics & Aeronautics 53, AIAA, New York, 1977.
[51] Orr, B.J. & Ward, J.F., *Mol. Phys.* 20513(1971).
[52] Oudar, J.-L.; Smith, R.W & Shen, Y.R., Polarization-sensitive coherent anti-Stokes Raman spectroscopy. *Appl. Phys. Lett.* 34 758-760 (1979).
[53] Oudar, J.-L. & Shen, Y.R., Nonlinear spectroscopy by multiresonant four-wave mixing.. *Phys. Rev.* A221141-1158(1980).
[54] Pearson, I.G. *Timing problems in laser based combustion diagnostics.* DSTO Workshop on Laser Diagnostics in Fluid Mechanics and Combustion, DSTO-ARL, 30th Sep - 1st Oct (1993).
[55] Proctor, D.; Pearson, I.G. & M^{c}Leod *Co-visualisation of flame structures and species.* 1st Int. Conf. on Combustion Technologies for a Clean Environment, Vol I paper 20.1 pp1-8, Vilamoura, Portugal, 3-6 Sep (1991).

[56] Proctor, D.; Nathan, G.J.; Luxton, R.E.; Pearson, I.G.; Brumale, S.A.; Mann, B.A.; Schnieder, G.M. & Newbold, G.J.R., *Efficient low NO_X burning of gas for large scale ndustrial applications.* 2nd Int. Conf. on Combustion Technologies for a Clean Environment, Vol II, paper 26.1 pp1-8 , Lisbon, Portugal, 19th -22nd Sep. (1993)..
[57] Rado, W.G., *Appl. Phys. Lett.* 11 123 (1967).
[58] Rahn, L.A.; Zych, L.J. & Mattern, P.L., Background-free CARS studies of carbon monoxide in a flame. *Opt. Comm.* 30249-252(1979).
[59] Rahn, L.A.; Farrow, R.L.; Koszykowski, M.L. & Mattern, P.L., Observation of an optical Stark effect on vibrational rotational transitions. *Phys. Rev. Let.* 45 620-623 (1980).
[60] Regnier, P.R. & Taran, J.P.E., On the possibility of measuring gas concentrations by stimulated Anti-Stokes Scattering *Appl. Phys. Lett.* 23 240-242 (1973).
[61] Regnier, P.R. & Taran, J.P.E., Gas concentration measurement by Coherent Raman Anti-Stokes Scattering *AIAA* paper 73-702, 1973.
[62] Regnier, P.R.; Moya, F. & Taran, J.P.E., Gas concentration by Coherent Raman Anti-Stokes Scattering *AIAA J.* 12 826-831 (1974).
[63] Roh, W.B. & Schreiber, P.W., Pressure dependence of integrated CARS power. *Appl. Optics* 17 1418-1424 (1978).
[64] Roh, W.B.; Schreiber, P.W. & Taran, J.P.E., Single pulse coherent anti-Stokes Raman scattering. *Appl. Phys. Lett.* 29 174-176 (1976).
[65] Shepherd, I.G.; Porter, F.M. & Greenhalgh, D.A., Spatial resolution effects of CARS in turbulent premixed combustion thermometry. *Combust. & Flame* 82 106-109 (1990).
[66] Snelling, D.R.; Smallwood, G.J.; Sawchuk, R.A. & Parameswaran, T., Precision of multiplex CARS temperatures using both single-mode and multimode pump lasers. *Appl. Optics* 26 99-109 (1987).
[67] Switzer,G.L.; Trump, D.D.; Goss, L.P.; Roquemore, W.M.; Bradley, R.P.; Stutrud, J.S. & Reeves, C.M., Simultaneous CARS and luminosity measurements in a bluff-body combustor. *AIAA* Paper 83-1481, (1983).
[68] Taran, J.P.E., Coherent anti-Stokes Raman spectroscopy. pp595-606, in *Proceedings 5th Int. Conf. on Raman Spectroscopy*, Schulz, Freiburg, FRG, (1976).
[69] Teets, R.E., CARSsignals: phase matching, transverse modes, and optical damage effects. *Appl. Optics* 25 855-862 (1986).
[70] Terhune, R.W., *Bull. Am. Phys. Soc.* 8 359 (1963).
[71] Tolles, W.M.; Nibler, J.W.; McDonald, J.R & Harvey, A.B., A review of the theory and application of coherent anti-Stokes Raman spectroscopy (CARS). *Appl. Spectroscopy.* 31 252-271 (1977).
[72] Yariv, A., *Quantum Electronics.* 3rd Ed John Wiley & Sons, New York, 1989.
[73] Yuratich, M.A. & Hanna, D.C. Coherent anti-Stokes Raman spectroscopy (CARS) selection rules, depolarization ratios and rotational structure. *Mol. Phys.* 33671-682(1977).
[74] Yuratich, M.A., Effects of laser linewidth on coherent anti-Stokes Raman scattering. *Mol. Phys.* 38625-655(1979).
[75] Zhu, J.Y. & Dunn-Rankin, D., CARS thermometry in high temperature gradients. *Appl. Phys.* B Photo-physics and Laser Chemistry B56 47-55 (1993).

PARTICLE IMAGE VELOCIMETRY

J. SORIA

Department of Mechanical Engineering, Monash University, Clayton, VIC 3168, Australia

INTRODUCTION

Particle image velocimetry (PIV), sometimes referred to particle image displacement velocimetry (PIDV), and laser speckle velocimetry (LSV) can be used to measure instantaneous in-plane velocity fields by recording the location of the images of the markers at multiple times. These technique are different from the conventional particle tracking methods which suffer from the complication of identifying and following individual particles in the flow field. PIV and LSV do not require the tracking of individual particles as the in-plane velocity components in the flow are determined using a finite interrogation region or analysis window in an image of multi-exposed tracer particles. Good and current reviews on this subject are given by Lauterborn & Vogel (1984), Adrian (1986), Hesselink (1988), Dudderar *et al* (1988) and Adrian (1991).

As with most optical field and point velocity measurement techniques PIV and LSV use as their cornerstone the fundamental definition of velocity to arrive at an estimate of the local velocity **u**, i.e.

$$\mathbf{u}(\mathbf{x},t) = \lim_{\Delta t \to 0} \frac{\Delta \mathbf{x}(\mathbf{x},t)}{\Delta t} \tag{1}$$

where $\Delta \mathbf{x}$ is the displacement of the marker particles, located at $\mathbf{x}$ at time t, over a short time period Δt. The principle behind the implementation of *equation (1) in PIV* is simple: the flow is seeded with small tracer particles which *faithfully* follow the flow; the flow is illuminated by a powerful light source in the form of a thin light sheet; the particle positions are recorded by imaging the scattered light from the tracer particles in the light sheet onto a recording medium (i.e. photographic film or an electronic photo-array detector). The in-plane displacement and hence the in-plane velocity is then estimated from sequential images of particle positions. The most significant attraction in the use of PIV for fluid velocity measurements is the ability to simultaneously measure the in-plane velocity of a relatively large region of the flow.

Historically laser speckle velocimetry proceeded PIV in its application to fluid flow measurements. LSV has its foundations in solid mechanics, where coherent light scattered from solid surfaces forms an interference pattern known as a specklegram. A manual analysis of a double-exposed speckle patterns to determine displacement is not possible because the human brain cannot untangle the superimposed random-looking speckle fields. Analysis of such superimposed fields became possible with the development of a fast and efficient statistical analysis method known as Young's fringe method of interrogation by Burch & Tokarski (1968). In the Young's fringe method an interrogation spot on a double-exposed specklegram is illuminated by coherent light such as from a laser

beam. The speckle field from each exposure diffracts the light wave from the coherent interrogation beam, which interfere to form a Young's fringe pattern (see Figure 1 (b)). The orientation of the fringes is perpendicular to the direction of the displacement and the spacing is inversely proportional to the magnitude of the displacement.

Barker & Fourney (1977) applied this technique in low Reynolds number Poiseuille flow, while Simpkins & Dudderar (1978) use LSV to study transient Benard convection. Meynart (1983) applied LSV to velocity measurements in axisymmetric vortex roll-up and pairing events of an air jet. Laser speckle velocimetry (LSV) requires a very high seeding density in order to form speckle patterns. However in most practical cases low flow tracer seeding is the prevailing situation. The result of low seeding density is that individual particles are imaged rather than the interference pattern generated by neighbouring particle images. This fact was first pointed out by Adrian (1984). Therefore, most of the fluid experiment measurements conducted using multi-exposed images are PIV measurements rather than LSV measurements. Kompenhans & Reithmuth (1987) and Lourenco & Krothapalli (1987) looked at turbulent wake flows from circular cylinder using PIV measurements. Vogel & Lauterborn (1988) studied the flow around cavitation bubbles by measuring the flow field using PIV. Adrian (1986) showed how PIV flow field measurements could be used to study the flow field of water jets, while Shepherd *et al* (1991)) showed how PIV can be used to measure the in-plane velocity field of a laminar circular cylinder wake flow without and with transverse forced oscillations. Velocity field data obtained using PIV was used by Wu *et al* (1991) to study the feedback effect of sound and velocity perturbations on the flow around two airfoils in tandem. Liu *et al* (1991) have investigated the spatial turbulent structure in a channel flow at $Re = 2872$ by using autocorrelation PIV analysis yielding more than 10,000 velocity points per image. PIV was used by Grant *et al* (1992) to measure the mean flow and turbulence characteristics in the separated flow behind a rearward facing step. Arroyo & Saviron (1992) have studied the spatial features of Rayleigh-Benard convection in a small box using spatial velocity PIV measurements.

PIV has also been recently applied to studies of flows of a more applied nature where great care has been exercised in the application of PIV methodology to arrive at accurate velocity field measurements. For example Shih *et al* (1992) used PIV velocity field measurements to study the unsteady flow past an airfoil which is pitching at a constant rate. Shekarriz *et al* (1992) studied the development of the junction and tip vortex behind a sail attached to an axisymmetric underwater body by using PIV measurements to map the instantaneous velocity field around this geometry. Dong *et al* (1992[a], 1992[b]) implemented quantitative flow visualisations within the volute of a centrifugal pump by using PIV measurements. Shekarriz *et al* (1993) investigated the near-field behaviour of a tip vortex trailing behind a low aspect ratio wing attached to an axisymmetric body.

PIV measurements and its variations can be divided into two separate stages - (i) a recording stage and (ii) an analysis stage. Each stage can be implemented separately, for example the recording of multi-exposed images can be performed using photographic film or using an electronic photosensitive array; the analysis can take the form of analog optical processing or digital optical processing. Various combinations of these two stages are possible. Each stage can be optimised separately, although, it must be noted that there is an interrelationship between both stages which will be pointed out in subsequent

sections where appropriate.

IMAGING OF PARTICLES - PARTICLE RECORDING AND DYNAMICS

PARTICLE IMAGING

Consider an ideal aberration-free lens of focal length f, the distance from this lens to the object is d_0, while the distance from the lens to the image is d_i. Denoting the object plane normal to the lens axis by coordinates x_j and the image plane normal to the lens axis by y_j such that the coordinates are centred on the lens axis, then a small particle at $\mathbf{x}$ maps onto the image plane at the point $-\mathbf{y}$ assuming the paraxial approximation by (see Young (1986))

$$y_j = \frac{d_i}{d_o - x_3} x_j \, , j = 1, 2. \tag{2}$$

The value of x_3 denotes the distance of the particle from the object plane. The magnification depends upon this value and can be expressed as

$$M(x_3) = \frac{d_i}{d_o - x_3}. \tag{3}$$

It can be easily shown from equations (2) and (3) that a small displacement of a particle in the object plane results in an image displacement given by

$$\Delta y_j = M(0)\Delta x_j + M(0)\frac{x_j}{d_0}\Delta x_3 \, , j = 1, 2 \tag{4}$$

The diameter of the particle image is a function of the particle diameter d_p, the magnification and the *point-spread function* or the *impulse response* of the lens. For diffraction limited lenses, the impulse response is an Airy function of diameter

$$d_l = 2.44(1 + M)f^{\#}\lambda, \tag{5}$$

$d_l/2$ corresponds to the radius of the first zero of the Airy pattern (see Goodman (1988) or Young (1986)), $f^{\#}$ is the f-number of the lens and λ is the wavelength of the light. Fourier optics (Goodman (1988)) can be used tc show that the image of a finite-diameter object (particle) is the convolution of the impulse response of the imaging system (Airy function for a diffraction limited lens) with the geometric image of the object (particle). Adrian & Yao (1985) approximated both functions by Gaussians and their analysis resulted in the following approximation for the image diameter

$$d_e = (M^2 d_p^2 + d_l^2)^{1/2}. \tag{6}$$

To illustrate the implications of these two equations consider a case with the following typical parameters: $M = 1$, $f^{\#} = 8$ and $\lambda = 514.5nm$. For these parameters the value of $d_l = 20\mu m$, hence for particles of diameter $d_p = 5\mu m$ the image diameter $d_e = 20.6\mu m$, while for $d_p = 50\mu m$ $d_e = 53.9\mu m$. Therefore, the image diameter is approximately independent of particle diameter for d_p less than $5\mu m$ and approaches to a diameter equal to the diameter of the impulse response of the diffraction limited lens, while for particle diameters greater than $50\mu m$ the image diameter is effectively Md_p.

Equations (5) and (6) apply to particles within the depth of field of a lens (see Young (1986) and Adrian (1991)) given by

$$\delta x_3 = 4(1 + M^{-1})^2 f^{\#^2} \lambda. \tag{7}$$

Outside this range the image is blurred by an amount exceeding 20%. For the parameters given above, the depth of field is found to be only $0.5mm$. If small particles are to be imaged with high spatial resolution the depth of field will be very small. To image over a larger depth of field a larger $f^{\#}$ is necessary which increases the point-spread function of the lens which in turn results in larger images of the particles and a loss of spatial resolution.

The amount of information contained in a multi-exposed image depends on the number of particles per unit volume C. The concentration of particles should be high enough to resolve the smallest scales of interest (e.g. thin shear layers, viscous boundary layer, etc.). Adrian (1986[b]) defines a dimensionless *data density*

$$N_\lambda = C\lambda^3 \tag{8}$$

where λ is a characteristic length, e.g. in a turbulent flow λ can be taken as the Taylor microscale. When N_λ is large many particles provide velocity information of the small scales in the flow and the motion is well resolved. When N_λ is small only the large scale motions are resolved.

It is possible to define an interrogation cell as the intersection of the illumination sheet and the interrogation spot on the recording medium. Adrian & Yao (1984) defined the diameter of this interrogation spot d_I when projected back onto the fluid as d_I/M. Assuming an illumination sheet of thickness Δz, they defined an image density parameter

$$N_I = C\Delta z \pi d_I^2/4M^2. \tag{9}$$

For $N_I << 1$, the probability of finding more than one particle in the interrogation cell is small, corresponding to the low image density limit, while for $N_I >> 1$, each interrogation cell contains many particle images, with each particle image pair capable of providing velocity information. Good measurements are only possible if the spatial resolution defined by the interrogation cell parameters is small compared to the smallest significant fluid length scale λ. If this condition is satisfied then $N_\lambda >> N_I$, and increasing the concentration of particle tracers to achieve $N_I \sim 1$ guarantees high velocity data density and the flow field is well resolved. This argument implicitly states the necessity for small particle tracers in order to be able to increase the information density on the recorded image. If tracer particles are too large, it may not be possible to achieve high image density, and hence high velocity data density. Thus, high image density maximises the spatial resolution of PIV.

An important operational aspect of the recording stage is the light scattering properties of the seed (tracer) particles. Adrian & Yao (1985) applied Mie's scattering theory to calculate the scattering power of different seeding particles. They found that the scattered light energy oscillates about a generally increasing mean value as a function of particle diameter. The average energy increases as $(d_p/\lambda)^4$ in the Rayleigh scattering range when

$d_p << \lambda$, whereas for $d_p >> \lambda$ the energy scattering is geometric and increases on the average as $(d_p/\lambda)^2$.

The light scattered by a particle depends strongly on the refractive index between the particle and the fluid. The same particle will scatter light energy ten times more effectively in air than in water. Therefore, investigations carried out using water or other liquids require larger particles to scatter more energy or require higher illumination levels (i.e. very powerful lasers). Adrian & Yao (1985) provide results to estimate the imaging capabilities of various particle sizes, $f^{\#}$, illumination geometries and energy levels and film or detector sensitivities. For example for Kodak Technical Pan film, their calculations indicate that particles as small as $1 - 2\mu m$ can be imaged in air using a $2.5J$ pulse ruby laser, whereas using the same illumination, the particles must be larger than $10\mu m$ to be imaged in water.

The mean exposure of a particle image in the Rayleigh scattering range is proportional to d_p^3 and inversely proportional to λ^3. This means that since many films are more sensitive to shorter wavelength light, the use of short wavelength illumination (i.e. green light) is more effective that long wavelength light (i.e. red light). The cubic dependence on particle diameter implies that image recording will be biased towards larger particles which may not *faithfully* follow the flow. Hence, it is desirable to use uniform sized particles as tracers. In the geometric energy scattering regime the mean exposure of a particle image becomes independent of particle diameter. Thus, little is gained in using bigger particles beyond $d_p \sim 100\mu m$.

PARTICLE DYNAMICS

All image-based velocity measurement methods inherently measure the material (Lagrangian) velocity of the particles. It is from this material velocity that the position (Eulerian) velocity is inferred. The immediate question which comes to mind is how accurately do the particles follow the fluid motion. The particle response is often described in terms of the flow velocity and a frequency of oscillation, i.e. how fast can the flow change before the particles fail to follow the fluid motion without significant slip. Ideally the particles should be neutrally buoyant and as small as possible, preferably smaller than the Kolmogorov scale. However, as pointed out earlier, smaller particles (less than $10\mu m$) are harder to image and more difficult to detect. The question of slip velocity of particles has been addressed by Agui & Jimenez (1987) who provide the following estimate for the slip velocity Δu

$$(\frac{\Delta u}{u})^2 = (\frac{\Delta \rho}{\rho})^2 \frac{d_p^2 f}{10\nu}, \tag{10}$$

where $\Delta\rho$ is the density difference, d_p is the particle diameter, ν is the kinematic viscosity and f is a typical eddy frequency. For a $10\mu m$ diameter particle with a density difference of 5% following an oscillatory air flow with a frequency of $100Hz$, the velocity difference will be less than 0.04%. In water for slip velocities of less than 0.5% the tracer particles should be kept to diameters smaller than $30\mu m$ and their density should not differ by more than 5% from that of the water.

AUTOCORRELATION ANALYSIS OF MULTI-EXPOSED PARTICLE IMAGES

In the traditional PIV analysis stage the multi-exposed photographically recorded image of particle tracers is interrogated using a finite analysis window. This results in the measurement of the mean instantaneous in-plane velocity components within this window. The analysis consists of obtaining the optical two-dimensional Fourier transform of the image portion within the analysis window. This is achieved by illuminating the analysis window with a coherent laser beam and passing the diffracted laser beam through a converging lens. If the window region contains multi-exposed particle images or speckles, a Young's fringe pattern results in the back focal plane of the lens. Burch & Tokarski (1968) showed that the spacing and angle of these fringes correspond directly to the displacement of the particle images or the speckle patterns. Figure 1 (a) and (b) show a typical image-Young's fringe pattern pair.

Figure 1. Computer generated typical double-exposed PIV (a) image, (b) autospectrum and (c) autocorrelation.

The analog two-dimensional Fourier transform is extremely fast since it is performed optically and hence at the speed of light. However, the setting up of the distances between the transparency (film) containing the image, the processing lens and the back focal plane of the lens, as well as, the acquisition of the Fourier transform from the back focal plane of the lens require great accuracy. Using readily available image acquisition and using digital computer processing it is possible to acquire digital frames from the film or transparency containing the multi-exposed image and to perform the same operation as the lens but digitally on the computer. Although, the digital processing is somewhat slower than the analog processing, current computer workstations with increasing processing power makes this a viable proposition.

Given that the Young's fringe pattern has been evaluated, which corresponds to the evaluation of the two-dimensional autospectrum function, it is still necessary to establish the distance between the fringes and the angle of the fringes. Since digital Fourier processing can be efficiently performed using the Fast Fourier Transform (FFT) in $NlogN$ operations rather than N^2 operations (see Bracewell (1986)), performing an inverse Fourier

transform of the Young's fringe pattern which results in the two-dimensional autocorrelation function is a relatively inexpensive operation. The reason for doing this additional FFT step rather than establishing the distance and orientation of the particle image displacement directly from the autospectrum function can be seen from the typical autospectrum-autocorrelation pair of Figure 1 (b) and (c). The Young's fringes in the autospectrum plane transform to peaks in the autocorrelation plane and it is easier to find the distance between peaks corresponding to maxima in a autocorrelation plane than the distance between the ridges or fringes in the autospectrum plane. Figure 1 shows the relationships between the original image, its Fourier transform in the form of the autospectrum and the autocorrelation function of the image. The mean displacement of the particles in the multi-exposed image is given in the autocorrelation plane by the distance from the off-centred peaks to the center peak and the orientation of the line between the off-centred maxima and the central maximum peak. The central peak corresponds to the correlation of each particle image with itself and hence to zero displacement, i.e. the origin. As can be shown easily (Bracewell (1986)) and as illustrated in Figure 1 (b) and (c), both the autospectrum and autocorrelation functions are symmetric and hence, only the orientation of the displacement can be determined from multi-exposed single images. This is intuitively correct since once the multi-exposed picture of particle images is recorded only intensity is recorded and all phase information as to which particle images were recorded first is lost. There are methods by which this directional ambiguity in multi-exposed single images can be overcome such as image shifting, which introduces a known displacement bias during recording (Adrian (1986^b)).

The *autocorrelation* analysis (interrogation) method of multi-exposed single images can be performed on any digital image representation irrespective of its origin (i.e. photographic film, CCD camera, etc.). However, since high quality scientific work requires high quality data which can only be achieved using high spatial resolution images, this type of work should still be undertaken by using photographic film as the original recording medium rather than a CCD array. The highest resolution CCD arrays presently available, with 2048×2048 pixels, are only now starting to reach the spatial resolution of the lowest resolution photographic film (i.e. $60 lines/mm$ $35mm$ film). Compared to high spatial resolution film (holographic film) with $2000 lines/mm$ available in film sizes of $50mm \times 50mm$ (containing 10^{10} pixels of information), CCD arrays still have a long way to go. Nevertheless, CCD video cameras are useful for the efficient set-up of the experiments, since immediate feedback can be obtained for factors such as particle concentration, illumination, etc. Also, in order to use digital processing of the multi-exposed single images it is necessary to digitise the photographic film, and this can be achieved with a standard CCD array which typically has 512×512 pixels. However, the film has to be digitised in sub-frames to maintain the high spatial resolution of the original recording film.

The digital autocorrelation method consists of dividing an image into a large number of sub-images or interrogation windows. The multi-exposed single image can be considered a function of two spatial variables, i.e. the image is described by the recorded intensity $I \quad I(x, y)$ of the light scattered by tracer particles in the flow. The image when digitised with a CCD array (video camera) is discrete and the discrete *grey level* pixel intensity distribution is given by

$$I \quad I(i, j), 1 \quad i \quad N, 1 \quad j \quad M, \tag{11}$$

where N and M is the pixel array size of the digital camera. Typically the image is digitised using an 8 bit dynamic resolution such that the values of $I(x, y)$ range from 0 (black) to 255 (white).

The displacements of particles (flow tracers) from this type of image is determined by considering sub-images (or interrogation windows) of $I(i, j)$. Consider such a sub-image of $I(i, j)$ centred at (i_o, j_o) of size $n \times m$ given by

$$I_s = I_s(i, j)\,, i_o - n/2 < i \leq i_o + n/2, j_o - m/2 < j \leq j_o + m/2. \tag{12}$$

The size of the interrogation window depends on the particular experiment and the desired measurement accuracy. The two-dimensional autocorrelation of I_s can be expressed as

$$R(\xi, \psi) = \sum_{i=0}^{n-1} \sum_{j=0}^{m-1} I_s(i, j) I_s(i - \xi, j - \psi), \tag{13}$$

where $0 \leq \xi \leq n - 1$ and $0 \leq \psi \leq m - 1$.

The autocorrelation function (13) contains information on all the permutations of the displacements between all particle images in the sub-image. If all the particles within this sub-image undertake a uniform displacement between exposures, then in the permutations of displacements between particles this information adds constructively, while the remaining displacement permutations are *random* and behave like noise. Hence, the off-centred maximum peaks of the function $R(\xi, \psi)$ are at $\xi = \pm\Delta x$, $\psi = \pm\Delta y$. Note that there are two off-centred maxima due to the symmetry of the autocorrelation function. The values Δx and Δy correspond to the mean displacement in the x and y directions respectively of the imaged tracer particles in sub-image I_s.

The direct computation of the autocorrelation function (13) is a computationally intensive task. It is preferable to use the Wiener-Khinchin Theorem which relates the autocorrelation to the autospectrum by the two-dimensional Fourier transform. Noting that (13) is a convolution in two-dimensional physical space, and hence the corresponding operation in spectral space is a multiplication, the following operations are necessary to calculate (13) using the Fourier transform.

If $\mathcal{I}_s(k_i, k_j) = \mathcal{F}[I_s(i, j)]$ is the discrete Fourier transform (DFT) of I_s, then the autospectrum of the sub-image I_s is given by

$$\mathcal{G}_{II}(k_i, k_j) = \mathcal{I}_s^*(k_i, k_j)\mathcal{I}_s(k_i, k_j) \tag{14}$$

where * denotes the complex conjugate of the function. Taking the discrete inverse Fourier transform of (14) yields the autocorrelation by the Wiener-Khinchin Theorem (see Bracewell (1986)), i.e.

$$R(\xi, \psi) = \mathcal{F}^{-1}[\mathcal{G}_{II}(k_i, k_j)]. \tag{15}$$

This indirect procedure of calculating the two-dimensional autocorrelation function of a digitised image is computationally more efficient because the FFT can be used to calculate the DFT of I_s and the inverse DFT of $\mathcal{G}_{II}$.

Once the auto-correlation function for a sub-image is calculated, it remains to determine the location of the largest off-centred peaks of this two-dimensional function. Due to the symmetry of (13) only half the space has to be searched for one peak. Recalling that the image is in digital (i.e. discrete) pixel format, the resolution of the peak location can only be within ± 1 pixel in each direction. However, by using the information of the autocorrelation function around this maximum it is possible to calculate the location of the off-centred autocorrelation maximum to *sub-pixel* resolution.

It is obvious that to ensure that the velocity and hence, the displacement is uniform within the sub-image, the sub-image (or interrogation window) must be as small as possible. Yet, it must be large enough to contain enough multi-exposed images of particles to produce visible peaks in the autocorrelation function (13). From the analysis point of view the criteria for optimum PIV measurements using a multi-pulsed system can be developed based on computer simulation. Keane & Adrian (1990) used a Monte Carlo simulation of the autocorrelation method to reveal the following broad criteria for optimum double-exposure PIV using autocorrelation analysis:

1. $N_I > 10 - 20$,
2. $\sqrt{u^2 + v^2}\Delta t M/d_I < 0.25$,
3. $w\Delta t/\Delta z < 0.25$,
4. $|\Delta \mathbf{u}|/|\mathbf{u}| < 0.2$,

where u, v are the in-plane velocity components, w is the out-of-plane velocity component, d_I is the effective radius or size of the interrogation window (sub-image) and $|\Delta \mathbf{u}|$ is the velocity variation across the interrogation volume due to local velocity gradients. By satisfying these criteria the success rate of valid measurements is over $90 - 95\%$ of the interrogation windows with small bias error.

Figures 2 to 7 illustrates the relationship of double-exposed single particle images with their respective autospectra and autocorrelations as a function of particle size and particle displacement by using computer generated images. The interrogation window is kept constant at 128^2 pixels for all these cases, and it must be kept in mind that the following discussion regarding the detection of the autocorrelation off-centred maxima and the autospectrum fringe visibility is relative to this interrogation window size. The particles are represented in the images by Gaussian intensity distributions with standard deviations of d_p, which is similar to the intensity distribution of scattered light from spherical particles of diameter d_p. Figures 2 to 4 are for particles with a $d_p = 2$ pixels and for particle displacements of $\Delta x/d_p = 2, 10$ and 20 respectively, while Figures 5 to 7 are for particles with a $d_p = 20$ pixels and particle displacements of $\Delta x/d_p = 1, 1.5$ and 2 respectively.

These examples illustrate clearly the advantage of small particles. Firstly, it is obvious that $N_I > 1$ is going to be very difficult to achieve with particles which produce such large images as shown in Figures 5 to 7. Secondly, the determination of the autocorrelation peaks is overwhelmed by the maximum at zero displacement and the Young's fringes have very poor visibility and hence, are difficult to detect. Particle displacements must be such that $\Delta x \geq 2d_p$ for displacements to be detectable and considering condition (2) above results in a very small dynamic measurement range. On the other hand small particles

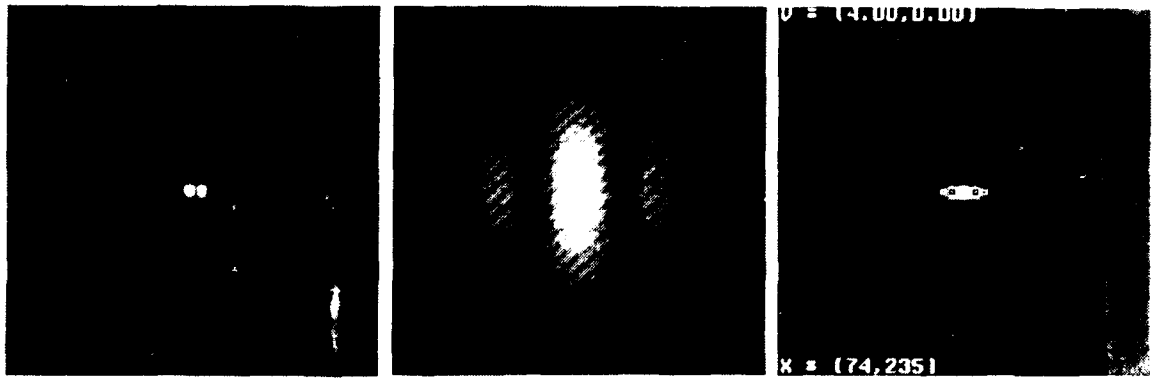

Figure 2. Computer generated single particle double-exposed PIV image with an interrogation window size of 128^2 pixels, particle diameter d_p 2 pixels and a displacement of $\Delta x/d_p$ 2, (a) image, (b) autospectrum and (c) autocorrelation.

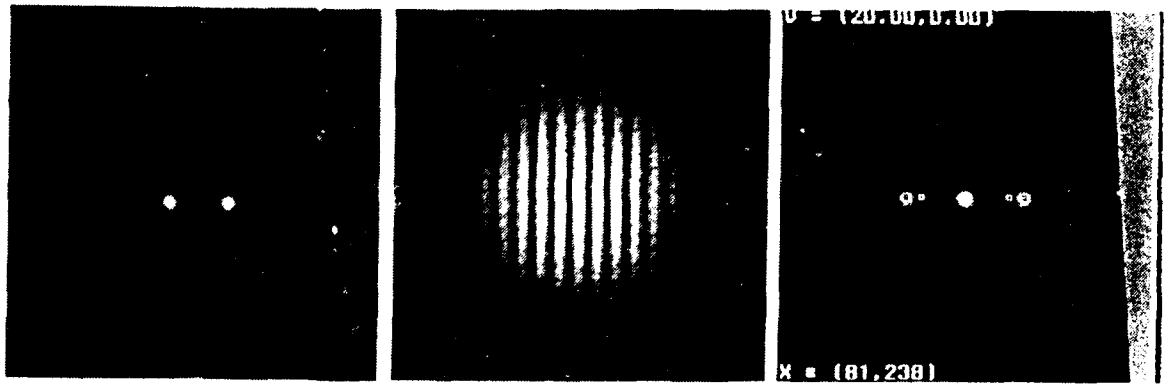

Figure 3. Computer generated single particle double-exposed PIV image with an interrogation window size of 128^2 pixels, particle diameter d_p 2 pixels and a displacement of $\Delta x/d_p$ 10, (a) image, (b) autospectrum and (c) autocorrelation.

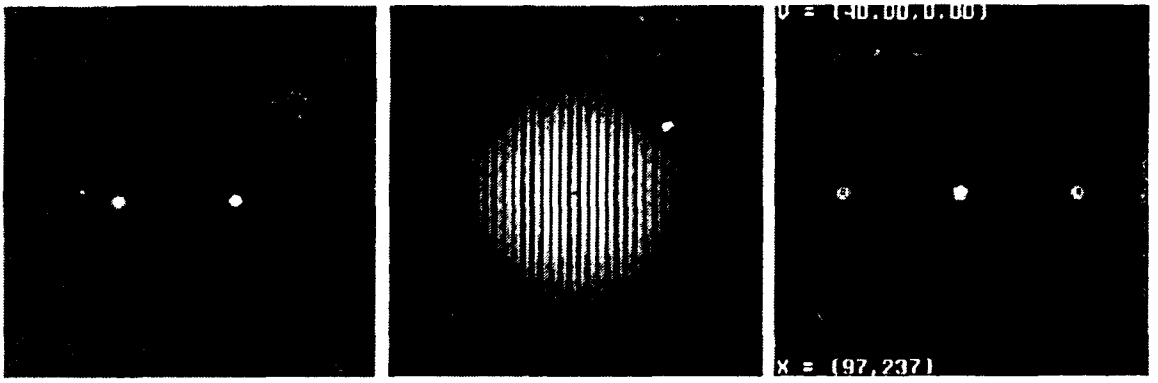

Figure 4. Computer generated single particle double-exposed PIV image with an interrogation window size of 128^2 pixels, particle diameter $d_p = 2$ pixels and a displacement of $\Delta x/d_p = 20$, (a) image, (b) autospectrum and (c) autocorrelation.

Figure 5. Computer generated single particle double-exposed PIV image with an interrogation window size of 128^2 pixels, particle diameter $d_p = 20$ pixels and a displacement of $\Delta x/d_p = 1$, (a) image, (b) autospectrum and (c) autocorrelation.

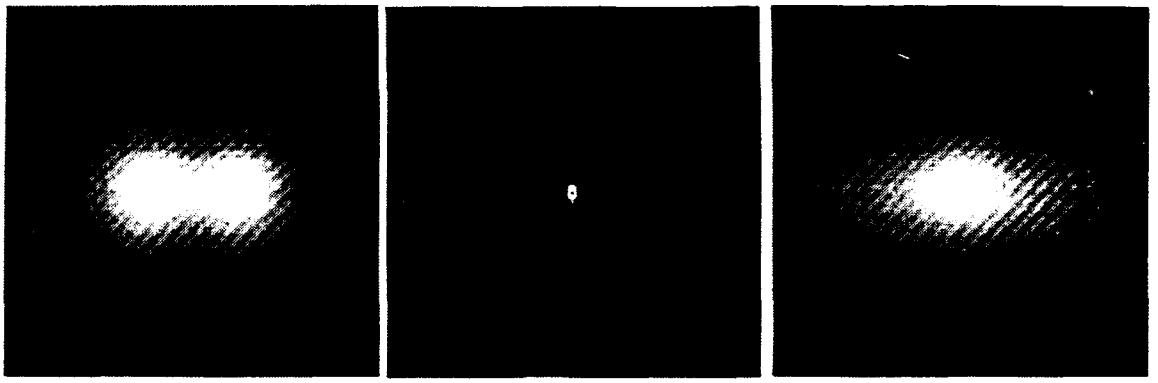

Figure 6. Computer generated single particle double-exposed PIV image with an interrogation window size of 128^2 pixels, particle diameter $d_p = 20$ pixels and a displacement of $\Delta x/d_p = 1.5$, (a) image, (b) autospectrum and (c) autocorrelation.

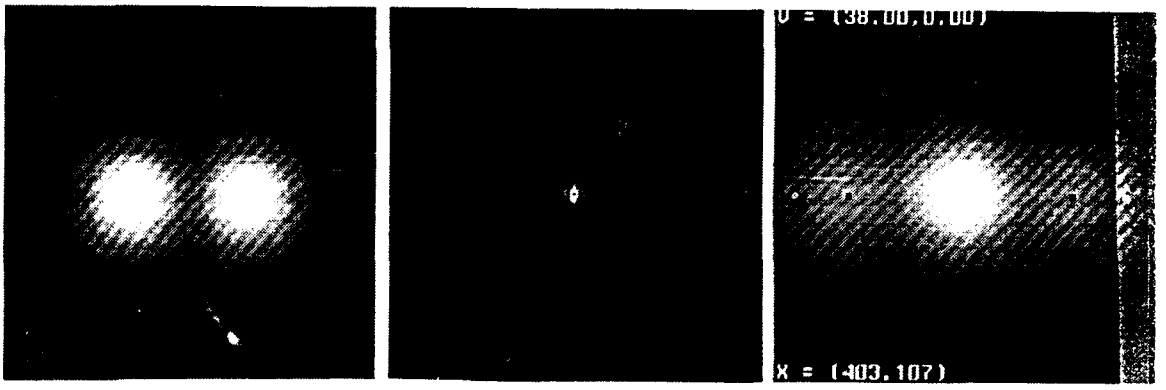

Figure 7. Computer generated single particle double-exposed PIV image with an interrogation window size of 128^2 pixels, particle diameter $d_p = 20$ pixels and a displacement of $\Delta x/d_p = 2$, (a) image, (b) autospectrum and (c) autocorrelation.

(relative to the interrogation window size) will satisfy condition (1) above. Also. it is observed that the central peak in the autocorrelation function for these cases is small ($\sim d_p$) and hence, does not contaminate the off-centred maxima in the autocorrelation, even for small displacements (see Figure 2). The fringe visibility in the autospectrum is considerably better for these smaller particles than for the larger ones.

AN APPLICATION OF AUTOCORRELATION PIV

The autocorrelation PIV methodology is illustrated by applying it to a *known* two-dimensional velocity field for flow around a circular cylinder computed by Thompson (1993) using a time-accurate spectral element method for $Re = 200$. The domain of the computation ranges from -7 to 24 in the streamwise direction and from -7 to 7 in the cross-stream direction. The cylinder is located at $(0, 0)$ and has a diameter of 2. A velocity field at a given phase in the shedding cycle was used to generate a double-exposed image. The computer generated double-exposed image has a spatial resolution of 300 pixel/(non dimensional length), a typical resolution of a standard $35mm$ frame of Kodak Technical Pan film.

The domain of interest was reduced to $(-2, 6)$ in the streamwise direction and $(-2, 2)$ in the cross-stream direction. This resulted in an image of size 2400×1200 pixels. Note that this area represents only 3.8% of a $35mm$ frame, i.e. a $35mm$ frame contains approximately 4×6 of these images. The particles where chosen to have a $\overline{d_p} = 7.5\mu$ ($\overline{d_p} = 2.25$ pixels) with a standard deviation around this mean of 0.8μ (0.24 pixels). The intensity distribution of individual particles in the image was represented by a Gaussian function with a standard deviation equal to d_p. The interrogation window was chosen a priori to be 64^2, with an average of 10 particles/(interrogation window). This resulted in 7032 particles being randomly positioned on the image using the computer's random number generator.

An image shift of 8 pixels was applied to the second exposure to give all displacements a positive bias, this allows the correct velocity measurement even in regions of flow reversal. Figure 8 (a) is the double exposed image without image shift and Figure 8 (b) is the image with the displacement bias which was used for the autocorrelation PIV analysis. The images where generated on an Silicon Graphics workstation and all the autocorrelation PIV analysis and post-processing was performed with menu-driven software on the Silicon Graphics workstation.

The interrogation window was shifted 32 pixels in each direction which resulted in 74×36 possible velocity vector measurements. Out of the possible 2664 vectors the autocorrelation PIV analysis produced 2645 vectors, of which 2618 vectors were deemed *good* after going through some discrimination criteria and checking the possible validity of the second largest peak in the autocorrelation function. This represents a 98% success rate of valid measurements for the given image conditions and particle concentration. In the locations where the autocorrelation PIV analysis failed to measure the velocity, the velocity vector was determined by least square interpolation of the valid velocity vectors. Figure 9 (a) is the two-dimensional in-plane velocity field and the out-of-plane vorticity (ω_z) field from the calculations, and Figure 9 (b) is the raw velocity field measured using autocorrelation PIV (with 2% interpolated velocity vectors) and the ω_z field calculated from the measured two-dimensional velocity field. The out-of-plane vorticity was calculated by

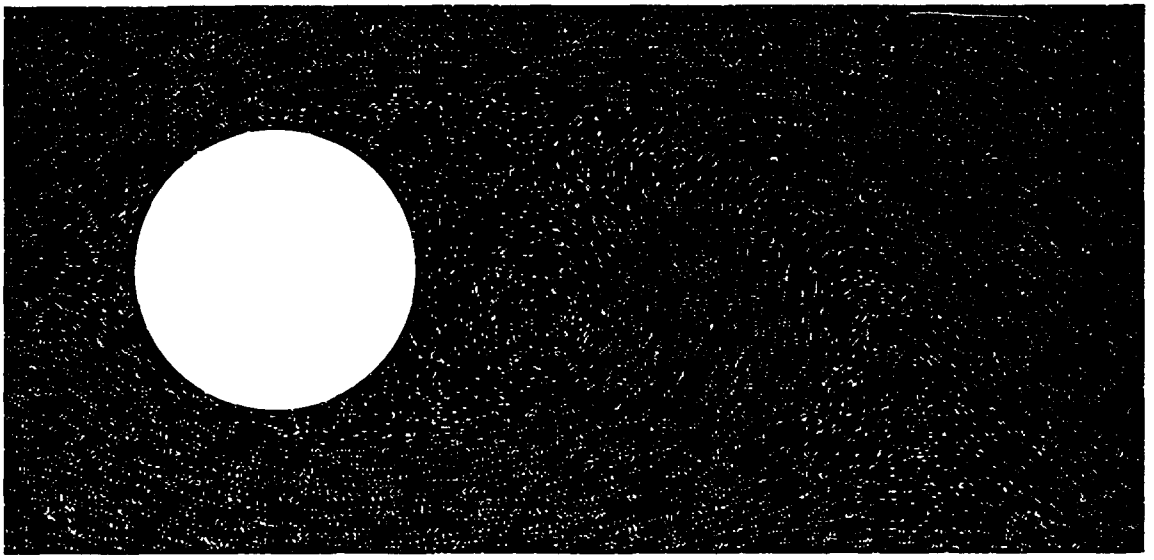

(a)

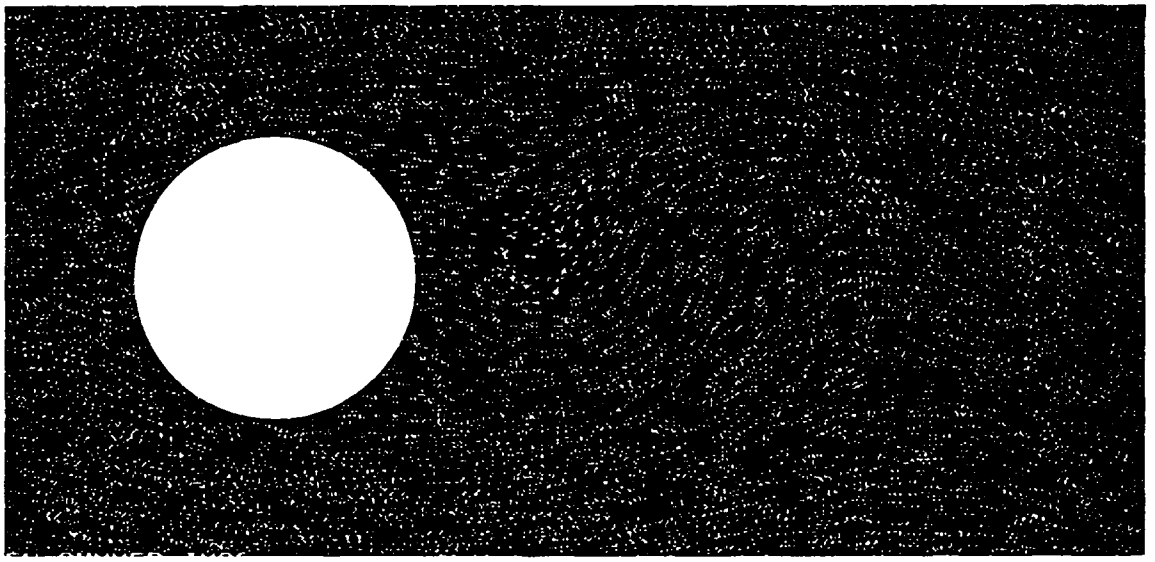

(b)

Figure 8. Computer generated double-exposed PIV image of flow around a cylinder at $Re = 200$ (a) no image shift, (b) with image shift.

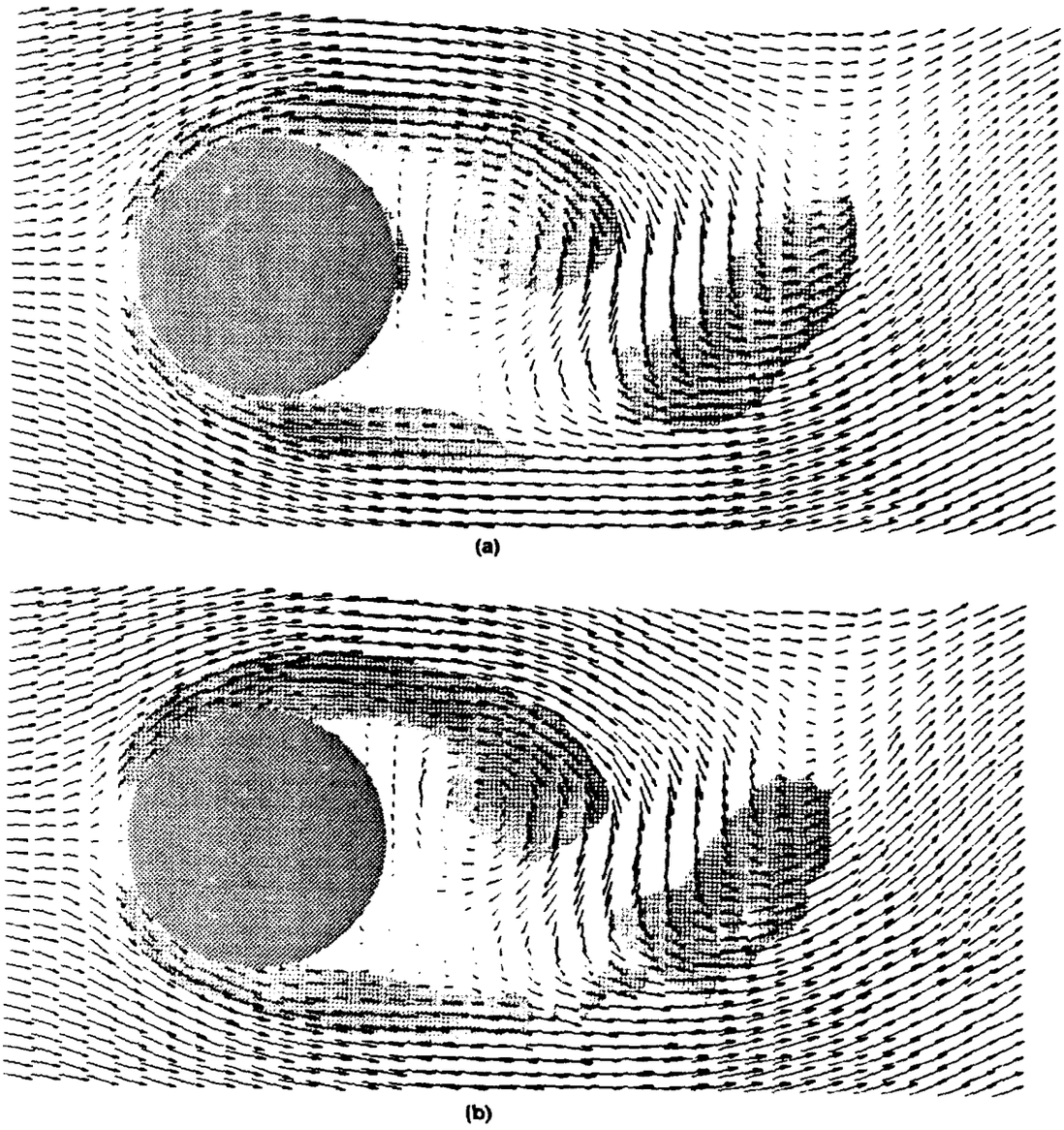

Figure 9. Comparison between the two-dimensional in-plane velocity field and out-of-plane vorticity, (a) *base* known fields, (b) *measured* field using autocorrelation PIV from image in Figure 8 (b).

least square fitting the velocity field to a polynomial of second order and differentiating the fitted velocity components to calculate ω_z using

$$\omega_z = \frac{1}{2}(\frac{\partial v}{\partial x} - \frac{\partial u}{\partial y}). \tag{16}$$

Comparing the *base* in-plane velocity field in Figure 9 (a) with the *measured* in-plane velocity field in Figure 9 (b) shows that qualitatively both velocity fields looks similar and exhibit the same structure. Quantitatively the velocity fields also compare favourably. A more sensitive measure is the vorticity field, which is derived from the derivatives of the velocity field, and derivatives tend to amplify errors. The vorticity field has the same structure in both the calculated version and the measured version. However, note that the thin high vorticity regions near the cylinder surface in the calculated data is more diffuse in the measured data of Figure 9 (b).

CONCLUDING REMARKS

The main features of autocorrelation PIV are discussed in this paper. Accurate PIV velocity field measurements rely on high quality images of the tracer particles in the flow, which are recorded on a high spatial resolution medium with each interrogation window containing many double-exposure particle images (preferably more than 10 image pairs). Guide lines have been pointed out to achieve high quality measurements. However the ultimate choice of parameters such as particle size, concentration, lighting, etc. depends on the particular experiment and the experimental conditions. As a general rule high accuracy-high resolution work should be performed using film rather than CCD arrays (video cameras) in order to achieve the spatial resolution necessary to resolve all important scales in the flow. This fact might change in the future with advances in electronic photo-detector technology and larger CCD array sizes.

It has been shown how it is possible to use computer generated double-exposed images of simple particle flow and complex flows to evaluate imaging parameters and their effect on the measurement accuracy of the autocorrelation PIV analysis method. Many factors concerning PIV such as the effect of out-of-plane motion, etc. have not been considered in this introductory type paper, but can be found in the literature and potential users of PIV should be aware of their effect if velocity bias is to be avoided.

Lastly, it must be remembered that PIV is not meant to replace more traditional fluid velocity measurement techniques (e.g. hot-wire, LDA, etc.) but to complement them when spatial velocity field information is necessary and desired.

ACKNOWLEDGMENTS

The author is grateful to the Fluid Mechanics Group at the CSIRO-DBCE for their support of some of this work and the use of their facilities. The author also would like to thank Dr M.S. Chong for the reading of this paper, his comments and helpful suggestions.

REFERENCES

Adrian, R. J. 1984 Scattering particle characteristics and their effect on pulsed laser measurements of fluid flow: speckle velocimetry vs. particle velocimetry. *Appl. Opt.* **23**, 1690–1691.

Adrian, R. J. & Yao, C.-S. 1985 Pulsed laser technique application to liquid and gaseous flows and the scattering power of seed materials. *Appl. Opt.* **24**, 44–52.

Adrian, R. J. 1986[a] Image shifting technique to resolve directional ambiguity in double-pulsed velocimetry. *Appl. Opt.* **25**, 3855–3858.

Adrian, R. J. 1986[b] Multi-point optical measurements of simultaneous vectors in unsteady flow - A review. *Int. J. Heat Fluid Flow* **7**, 127–145.

Adrian, R. J. 1991 Particle imaging techniques for experimental fluid mechanics. *Ann. Rev. Fluid Mech.* **23**, 261–304.

Agui, J. C. & Jimenez, J. 1987 On the performance of particle tracking. *J. Fluid Mech.* **185**, 447–468.

Arroyo, M. P. & Saviron, J. M. 1992 Rayleigh-Benard convection in a small box: spatial features and thermal dependence of the velocity field. *J. Fluid Mech.* **235**, 325–348.

Barker, D. B. & Fourney, M. E. 1977 Measuring fluid velocities with speckle patterns. *Opt. Lett.* **1**, 135–137.

Bracewell, R. N. 1986 *The Fourier Transform and its Applications.* McGraw-Hill.

Burch, J. M. & Tokarski, J. M. J. 1968 Production of multiple beam fringes from photographic scatters. *Optica Acta* **15**, 101–111.

Dong, R., Chu, S. & Katz, J. 1992[a] Quantitative visualisation of the flow within the volute of a centrifugal pump. Part A: Technique. *Trans. ASME* **114**, 390–395.

Dong, R., Chu, S. & Katz, J. 1992[b] Quantitative visualisation of the flow within the volute of a centrifugal pump. Part B: Results and analysis. *Trans. ASME* **114**, 396–403.

Dudderar, T. D., Meynart, R. & Simpkins, P. G. 1988 Full-field laser metrology for fluid velocity measurement. *Opt. Lasers Eng.* **9**, 163–199.

Goodman, J. W. 1988 *Introduction to Fourier Optics.* McGraw-Hill.

Grant, I., Owens, E. & Yan, Y. -Y 1992 Particle image velocimetry measurements of the separated flow behind a rearward facing step. *Exp. Fluids* **12**, 238–244.

Hesselink, L. 1988 Digital image processing in flow visualisation. *Ann. Rev. Fluid Mech.* **20**, 421–485.

Keane, R. D. & Adrian, R. J. 1990 Optimisation of particle image velocimetry. Part I: Double pulsed systems. *Meas. Sci. Technol.* **1**, 1202–1215.

Kompenhans, J. & Reithmuth, J. 1987 Two-dimensional flow field measurements in wind tunnels by means of particle velocimetry. *Proc Int Congr Appl Lasers and Electro-Optics, San Diego, USA.*

Lauterborn, W. & Vogel, A. 1984 Modern Optical Techniques in Fluid Mechanics. *Ann. Rev. Fluid Mech.* **16**, 223–244.

Liu, Z. -C., Landreth, C. C., Adrian, R. J. & Hanratty, T. J. 1991 High resolution measurement of turbulent structure in a channel with particle image velocimetry. *Exp. Fluids* **10**, 301–312.

Lourenco, L. M. & Krothapalli, A. 1987 The role of photographic parameters in laser speckle or particle image displacement velocimetry. *Exp. Fluids* **5**, 29–32.

Meynart, R. 1983 Instantaneous velocity field measurements in unsteady gas flow speckle velocimetry. *Appl. Opt.* **22**, 535–540.

Shepherd, R. F., LaFontaine, R. F., Welch, L. W., Soria, J. & Pearson, I. G. 1991 Measurement of instantaneous flows using particle image velocimetry. *Second World Conf. on Exp. Heat Transfer, Fluid Mechanics and Thermodynamics, Dubrovnik, Yugoslavia.*

Simpkins, P. G. & Dudderar, T. D. 1978 Laser speckle measurement in transient Benard convection. *J. Fluid Mech.* **89**, 665–671.

Shekarriz, A., Fu, T. C, Katz, J., Liu, H. L. & Huang, T. T. 1992 Study of junction and tip vortices using particle image velocimetry. *AIAA J.* **30**, 145–152.

Shekarriz, A., Fu, T. C, Katz, J. & Huang, T. T. 1992 Near-field behaviour of a tip vortex. *AIAA J.* **31**, 112–118.

Shih, C., Lourenco, L., Van Dommelen, L. & Krothapalli, A. 1992 Unsteady flow past an airfoil pitching at constant rate. *AIAA J.* **30**, 1153–1161.

Thompson, M. C. 1993 Private Communication .

Vogel, A. & Lauterborn, W. 1988 Time resolved particle image velocimetry used in the investigation of cavitation bubble dynamics. *Appl. Opt.* **27**, 1869–1876.

Wu, J., Soria, J., Hourigan, K., Welsh, M. C. & Welch, L. W. 1991 Flow-excited acoustic resonance in a duct: the feedback mechanism. *Fifth Int. Conf. on Flow Induced Vibrations, Brighton, U.K.*

Young, M. 1986 *Optics and Lasers.* Springer-Verlag, 3rd ed.

PRACTICAL CONSIDERATION IN THE USE AND DESIGN OF LASER VELOCIMETRY SYSTEMS IN TURBOMACHINERY APPLICATIONS

by

N.A. AHMED

Aerospace Engineering,
The University of New South Wales
P.O.Box 1, Kensington, NSW 2033

1. INTRODUCTION

Laser anemometry technique with its natural appeal as non-intrusive, non-calibrating and non-dependence on the thermo physical properties of flow is now considered as one of the most powerful flow measurement tools of modern times. The list of areas where it has been successfully used is long and impressive. It covers areas from wind tunnel flows to capillary flows, from atmospheric turbulence to ocean bottom flows, from chemically reacting flows including pre-mixed flames, from non-reacting duct flows to rotating flows within turbomachines and the list never seems to end.

In this paper, practical considerations in the application of laser anemometry to turbomachines and in particular, to the measurement of flows within impeller passages of a high speed centrifugal compressor is discussed.

2. FLOWS IN CENTRIFUGAL COMPRESSORS

Flows through turbomachines, and in particular, through centrifugal compressors are extremely complex. The centrifugal compressor is used in turbo machinery where high pressure ratios are required in a single stage such as in small gas turbine engines or turbochargers used in internal combustion engines. The centrifugal compressor accepts gas in an axial direction and expels it at higher temperature, pressure and velocity in a radial direction. In the time the flow remains in the centrifugal compressor, it is subjected to the effects of rotation, curvature and diffusion processes and becomes interactive, maldistributed and time dependent. Measurements of this flow are made more difficult by strong blade to blade and hub to hub velocity profiles with the flow restricted to narrow enclosed passages. Although, the non-intrusive, non-calibrating and high spatial resolution properties make laser anemometry a strong candidate for flow measurements of these flows, the practical problems of optical access, seeding or blade shadow renders it a particularly difficult task to accomplish.

To appreciate better the practical problems let us consider a particular experimental programme which requires data from the impeller passage of a high speed centrifugal compressor. The impeller is unshrouded, 100 mm in diameter and has a tip gap of 0.25 mm at inlet and 0.5 mm at outlet both measured under static conditions. The test impeller has 16 equally spaced vanes or blades half of which are splitter blades placed alternately between the 8 full blades. Measurements are to be taken when the impeller is rotating at 93,000 rev/min. This is in fact the description of the commercial impeller [Holsel 4LG (599)] of a standard

turbocharger unit [Holset HB3] used in an experimental programme at the high speed compressor test cell of Cranfield Institute of Technology, UK, Ahmed and Elder (1990).

3. PRACTICAL CONSIDERATIONS

3.1 CHOICE OF LASER ANEMOMETER SYSTEM

Although known by various names, there are essentially two separate methods namely the laser Doppler and the laser two focus (L2F) systems. Detailed descriptions of the two systems are readily available in literature Rudd (1968), Schodl (1974) and Ahmed et al (1991). The basic difference of the two systems is essentially in the way they create measurement volumes at the point of measurement. In fact, all laser systems depend on a few basic components, the laser light source, optics for beam splitting or focussing, detectors and signal processors. In general, most users will buy complete turnkey systems or build up any specialised systems from commercially available optical modules. Price is, therefore, an important consideration. The price of laser systems vary depending on the quality and function of each of the above components and whether the system has one-, two- or three-dimensional measurement capability. To give some idea, a 300 mW argon-ion laser may cost to-day A$16,000 whereas a 4W argon-ion laser by the same manufacturer may cost twice that amount. Similarly, a signal processor based on correlation technique may cost around A$35,000, whereas a signal processor based on fast fourier transform may cost twice that figure. The greatest cost, however, is associated in moving from a one- to two- or three-dimensional measurement capability, where polarisation, frequency shifting or multi-colour lasers have generally been used. These in turn require more than one light source, light transmitting or receiving module and signal processing unit, increasing the cost of the overall system dramatically. A three-dimensional laser system could cost over half a million Australian dollars. Even then, these three-dimensional systems suffer from a common drawback of poor spatial resolution, especially in the third dimension. To reduce cost and improve spatial resolution in all dimensions, the author of this Paper was involved in the design of a novel 3D laser-Doppler probe Ahmed et al (1990) which will be briefly described later in this paper.

For the experimental work in the centrifugal compressor mentioned above, the choice is dictated more than anything by the limited availability of optical access. This virtually rules out existing commercial 3D laser anemometer systems and 2D forward scattering systems . In the backscatter mode, the signal to noise consideration becomes quite important, Kiock (1984). The two-dimensional L2F system has a higher signal to noise ratio and requires less optical access area than laser Doppler System Schodl (1974). For measurement within rotating passages, some means of electronically strobing the scattered light signal, Powell (1980), is also required. The L2F system marketed by Polytec, Germany satisfies these requirements and was used for this study.

3.2 DESIGN OF OPTICAL ACCESS

The centrifugal compressor was never designed with laser anemometry application in mind. For the above turbocharger unit, the shroud encompassing the impeller has very limited space where optical access could be engineered. Great care has, therefore, to be exercised in the design of optical access windows. Fig. 1 shows the positions of the four measurement planes for which a single optical access recess was produced on the shroud casing. Four interchangeable inserts that directed the laser light along the four measurement planes were

then manufactured. These were essential but time consuming and costly operations. The choice of material used as the windows within these inserts was dictated mainly by temperature considerations which could approach 500°C at impeller rotation of 100,000 rev/min. Saphire windows can withstand up to 1000°C and were, therefore, used. Ideally the window should be aerodynamically designed, but this often leads to curved shapes which in turn produces aberration during optical focussing. It is possible, in theory to calculate the effect of curved windows on laser beam, but it is always preferable to limit its size so that flat windows could be used in practice without much compromise on aerodynamic shape. In order to avoid signal truncation at the maximum depth of measurement (about 20 mm shroud to hub inlet), the backscattered signal from the measurement volume was collected in a 12° inclined angle cone which necessitated a window diameter of 6 mm. Provision was also made so that the window could be cleaned from time to time or be replaced from the insert if it was necessary.

3.3 SEEDING

The backscatter mode, the level of light scattered back in comparison to what is projected into the flow give a low signal to noise ratio. The intensity of the scattered back signal may be increased by having higher laser power or larger seeding particles, both these solutions, however are not without problems. Increasing laser power increases background noise levels in enclosed passages and for high speed flows very fine seeding is required, typically less than one micron in diameter. Use of solid particles proved difficult as the solid particles tended to coalesce and coagulate very easily forming larger particles and contaminating optical access window very quickly. At one stage, the solid particles had completely blocked the end of the turbocharger exit pipe situated outside the test cell and departed with a big bang! Safety was immediately at the forefront of all thoughts and liquid seeding particles were thereafter used. Initially, various types of liquid ranging from propane diol to cooking oils were used to generate seedings by the atomisation of the liquid by an air-blast procedure with a separator system to collect larger particles. To maximise the chances of introducing seeding into the required measurement volume, seeding was introduced at the inlet of the bellmouth of the test rig through a tube which was positioned on a 3-axis automated traversing system and controlled remotely. Kerosine in the end proved to be the best seeding medium.

4. SELECTED RESULTS

Some selected results from the above experiment are given in Fig.2 which shows the expected potential flow at the splitter leading edge and the start of the wake region on the shroud surface at the next measurement plane. As the flow progresses through the impeller, wake grows in depth and moves towards the pressure side Moore and Johnson (1979). The contours are based on measurement grid of ten blade-to-blade and from ten to six hub-to-shroud measurements.

It may however, be recalled that the results were obtained using two-dimensional L2F which is insensitive to velocity components in the third dimension. As a result, much of the information regarding secondary flows within the impeller flows were not available.

5. DESIGN OF A NOVEL 3D LASER DOPPLER PROBE

To obtain 3D measurements, a cheaper option was attempted using a single laser source, a single detector and a single signal processor. The probe was based on laser Doppler System

using a digital correlator for signal processing. To obtain the 3D measuring capability, the fringe axis was arranged to be at an angle to the mechanical axis (Fig.3). Thus in a way, comparable to a slanted hot wire, three component measurements could be obtained by positioning the fringes at three different angles by rotating the probe. The flow vector could then be fully resolved from these measured velocity components Ahmed and Elder (1990). The availability of single mode high birefringent fibre enabled the completion of a small, compact probe head (Fig.4) that could be attached to the outside of the shroud with the optical fibres connecting the probe head to a remote laser source and detector. Some limited results (Fig.5) obtained by this probe suggest that the flow within the impeller passages is three dimensional and the velocity component in the third dimension could be as high as 15% of the total velocity. The probe still suffers from several drawbacks and further development is needed before it can be generally used on turbomachinery Ahmed et al (1991).

5. CONCLUSION

This paper outlines briefly some of the practical problems that have to be tackled to obtain velocity measurements in high speed flows of turbomachines. Full three-dimensional velocity information is still difficult to obtain in these situations. With advances in laser, optical fibre and other associated technologies, it is hoped that more reliable and efficient measurement techniques and systems will emerge.

REFERENCES

Ahmed, N.A. and Elder, R.L. (1990), "Flow Investigation in a Small High Speed Impeller Passage Using Laser Anemometry", ASME, Paper No. 90-GT-233.

Ahmed, N.A., Elder, R.L., Forster, C.P. and Jones, J.D.C. (1990). "Miniature Laser Anemometer for 3D Measurements", Meas. Sci. Technol.1, pp 272-276.

Ahmed, N.A., Forster, C.P. and Elder, R.L. (1991) . "Laser Anemometry in Turbomachines", Part G: J. of Aerospace Engineering, G 00190, pp.1 to 11.

Kiock, R. (1984). "Comparative Review of Laser-Doppler and Laser-Two-Focus Anemometry in view of Turbomachinery Applications". Technical Memorandum 34 of the von Karman Institute of Fluid Dynamics, Rhode Saint Genese, Belgium.

Moore, J. and Johnson, M.W. (1979). "The Development of Wake Flow in a Centrifugal Impeller". ASME Paper No. 79-GT-152.

Powell, J., Strazisar, A and Seaholz, R. (1980). "Efficient Laser Anemometry for Intra-Rotor Flow Mapping in Turbomachinery". Symposium for Intra Rotor Mapping in Turbomachinery, ASME Gas Turbine Conference, New Orleans.

Rudd, M.J. (1969). "A New Theoretical Model for the Laser Doppler Anemometer". J. Phys.E, Volume 2, pp. 723-726.

Schodl, R. (1974). "A Laser Dual Beam Method for Flow Measurement in Turbomachines". ASME, Paper No. 74-GT-157.

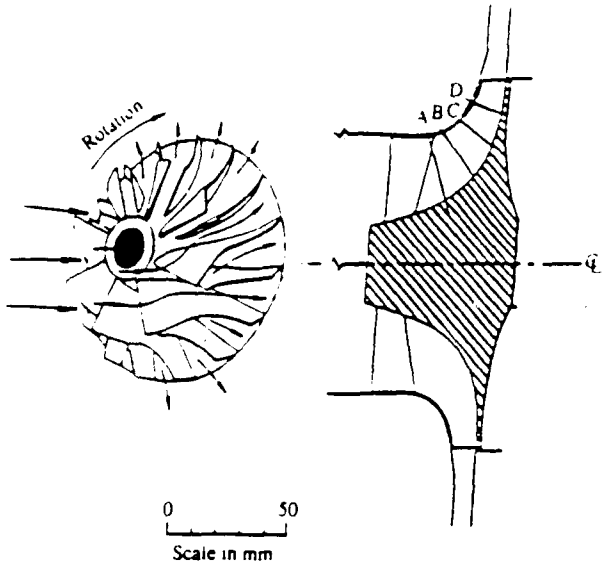

Fig.1 Location of measurement planes

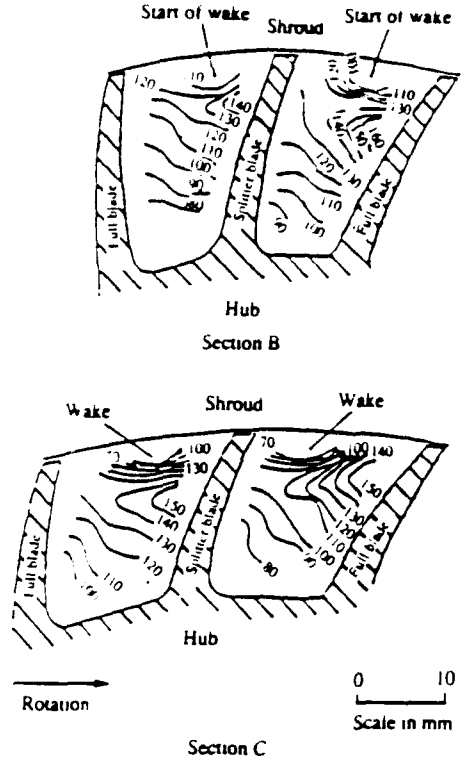

Fig.2 Some selected results. (*Passage velocity contours at impeller rotation of 93,000 rev/min and 0.47 m^3/s)*

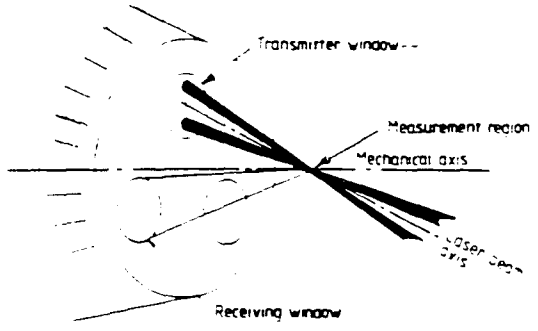

Fig.3 View at the front of the probe showing the measurement principle of the micro LDA

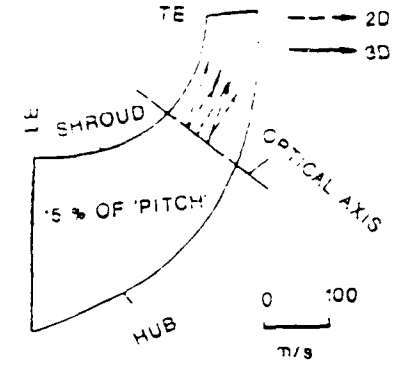

Fig.5 Vector representation of flow velocity projected on the meridional plane of the blade surface (*note: the term* 'PITCH' *above refers to full blade to full blade pitch measured from the pressure surface)*

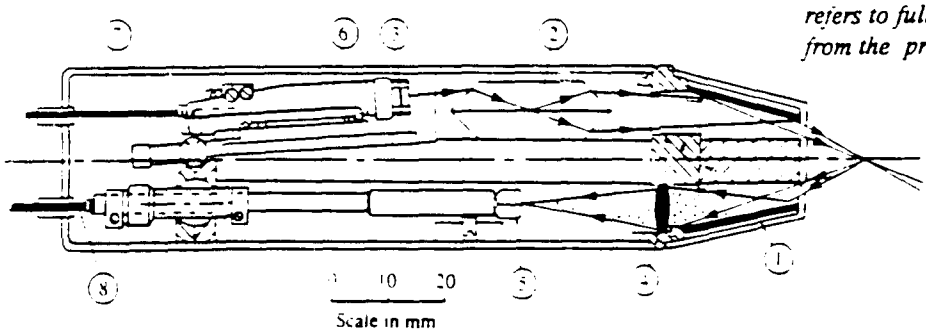

Fig.4 General arrangement of the micro LDA

PHASE DOPPLER MEASUREMENTS OF GAS-PARTICLE FLOW THROUGH A TUBE BANK

W. Yang[1], D. D. Atapattu[2] and Y. S. Morsi[1]

[1]*Modelling and Diagnostic Group*
Department of Mechanical and Manufacturing Engineering
Swinburne University of Technology
Hawthorn, Victoria 3122

[2]*G.K. Williams Cooperative Research Centre for Extractive Metallurgy*
Department of Chemical Engineering, The University of Melbourne
Parkville, Victoria 3052

ABSTRACT

Phase Doppler Anemometry (PDA) technique has been used to simultaneously measure the velocity and particle size distributions for flow through a tube bank arrangement. Some preliminary results are presented and discussed.

NOMENCLATURE

d - diameter of particle (mm)
U - axial velocity component (m/s)
V - transverse velocity component (m/s)
x,y,z - spatial coordinates, defined in Fig.1 (mm)

INTRODUCTION

The results presented here is a part of the general study on gas-particle flow through a tube bank arrangement. The main objective of the program is to examine the fluid flow and turbulence parameters including mixing of turbulence wakes which are formed by the array of tubes, using the hot wire and laser Doppler/phase Doppler techniques. The hot wire technique will be used to measure Reynolds stresses and turbulent heat fluxes where as the phase Doppler anemometer (PDA) will be used to measure the velocity and size of particles.

Data obtained are of interest to power generation industry and will enhance the current understanding on the erosion of economiser tubes. It is also anticipated that a numerical method will be developed and validated using the data. In this paper only some preliminary data, primarily to demonstrate the capability of Dantec PDA system, are given.

EXPERIMENTAL SETUP

THE WIND TUNNEL

A schematic diagram of the wind tunnel is shown in Figure 1. The wind tunnel has a working section of rectangular cross section (360 mm x 500 mm) with walls made of perspex of

thickness 20 mm. The contraction ratio of the wind tunnel is 9 : 1. The distance between the inlet and the test section is 3 meters and a flow straightener made up of a combination of cylindrical tubes is fitted at the entrance of the wind tunnel. Turbulence levels of about 2.2% were measured in the wind tunnel. A filter section was added downstream to facilitate removal of the particles from the air stream.

THE TUBE BANK

The tube bank model consists of four mild steel cylindrical tubes of 25.4 mm diameter equally spaced at 150 mm and housed in a perspex ducting of 360 mm x 500 mm. This model is easily installed in the wind tunnel (see Figure 1). To improve the signal to noise ratio (S/N), the tubes were painted black.

During the experiments a constant flow through the wind tunnel was maintained by measuring the maximum centreline air velocity 100 mm upstream of the first tube row using a combination of a Pitot tube and a micro manometer.

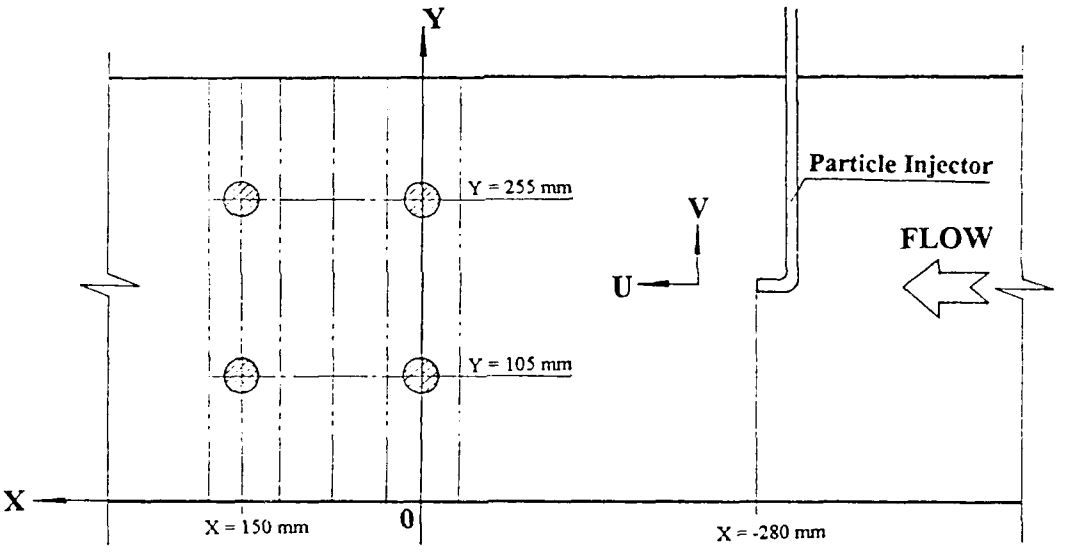

Figure 1 Schematic of the Tube Bank Model

PARTICLE INJECTION (SEEDING)

Smoke: For the measurement of air flow, glycol smoke was injected into the system using a smoke generator.

Glass particles: A particle injector unit, which has been fitted with a compressed air injector to control the flow rate, was used to inject spherical glass particles of medium diameter 66 μm. The particles are drawn from a fluidised pool of particles through a particle pick-up tube.

Particle injector was moved vertically each time a measurement was made so that a sufficient number of particles were present in the measurement volume.

MEASUREMENT PROCEDURE

The PDA technique is based on the fact that the phases from Doppler bursts between two or more photomultiplier bursts is proportional to the particle diameter (Durst and Zare 1975, Buchalo and Houser 1984 and Saffman et al 1984). In this investigation the Dantec PDA system was utilised to obtain velocity and particle size measurements. For sizing the particles an optimum scattering angle must be set (PDA user's manual 1992). This scattering angle depends on the mode of operation (i.e. reflection, refraction etc.) and the refractive indices of the particles and the medium. The system used is capable of measuring either two velocity components simultaneously or one velocity component and particle size. A schematic representation of the system is shown in Figure 2. This system incorporates an Ar-Ion laser together with a fibre optic system with a transmitting lens of focal length 400 mm. For each colour, a frequency shift of 40 MHz was introduced in one of the crossing beams to overcome the sign ambiguity of velocity measurements. A specially designed mechanism was used to traverse transmitting optics (fibre optic probe) as well as the receiving optics.

For the measurement of gas phase velocity, no particles were injected into the air stream and smoke was used to seed the flow and simultaneous measurements of velocity components **U** and **V** were obtained. However, to obtain information on velocity and size of particles, the PDA system was set to receive the signals at the optimum scattering angle. In this experiment, measurements were carried out in "refraction mode" and the scattering signals were collected at an angle of 145°. In obtaining the results, the software and the data acquisition system were configured with the following parameters:

- focal length of transmitting lens = 400 mm
- focal length of receiving lens = 600 mm
- beam separation (transmitting) = 38 mm
- measuring volume dimensions = 0.1943 mm x 0.1940 mm x 4.0908 mm
- range of particle diameter = 0 - 400 μm.

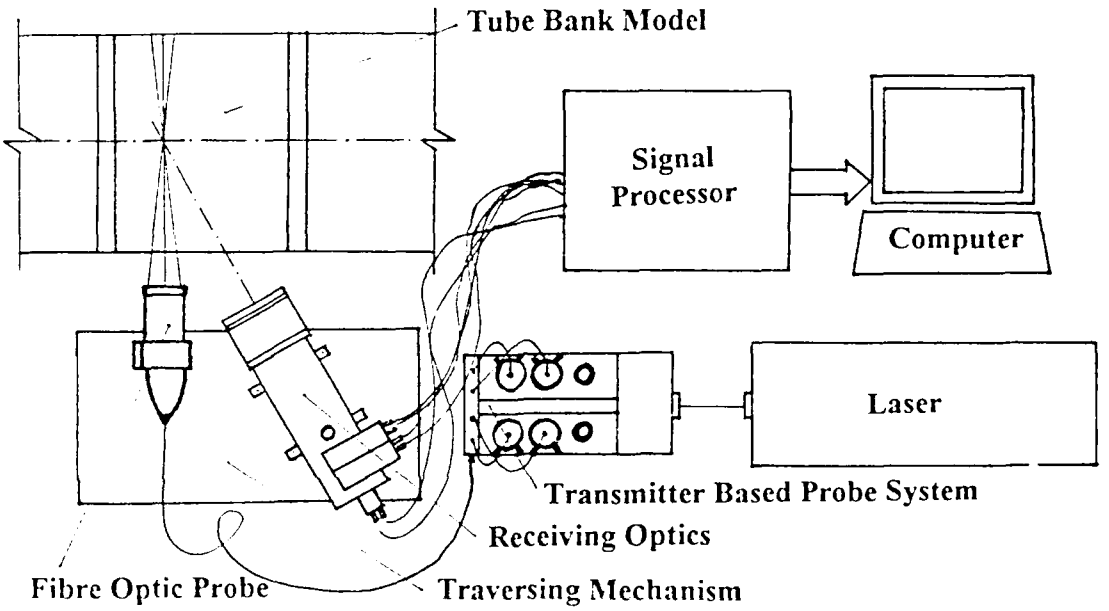

Figure 2 Schematic representation of the PDA setup

RESULTS AND DISCUSSION

Here we present only some preliminary results to demonstrate the capability of the PDA system used in this work. Data analysis was carried out using the software developed by Dantec, namely Sizeware. These results were obtained with particles injected at the same velocity as the main stream velocity of 8 m/s. A representative sample of the experimental results for the distribution of axial mean velocity of air and particles for X = -30 mm are shown in Figure 3. As expected, generally the particles are lagging behind the air and the particle velocity is higher than the velocity of air in the vicinity of the tubes. As the flow progressed through the tube bank, particles velocity tend to lag even further as evident from Figure 4 which shows the velocity distributions of air and particles at X = 150 mm. In the vicinity of the tubes, it has also been observed that the particles which strike the tubes loose some of their momentum and as a result an increased range of velocity magnitudes is recorded. This phenomena is shown in the histogram of velocity distribution of particles at X= -30 mm, Y= 100 mm, Z = 250 mm which is 30 mm upstream of the first tube row (see Figure 5).

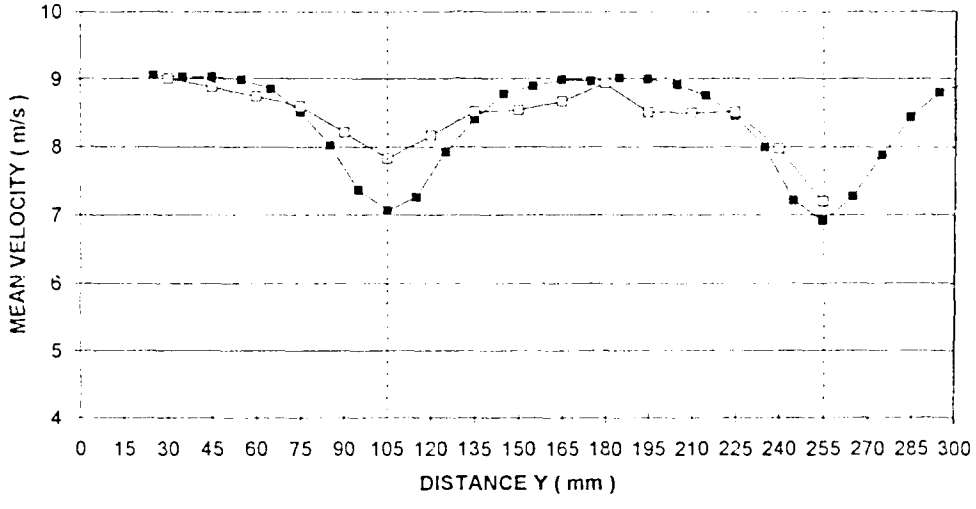

Figure 3 Axial velocity profiles for smoke (-■-) and glass particles (-□-); X = -30 mm

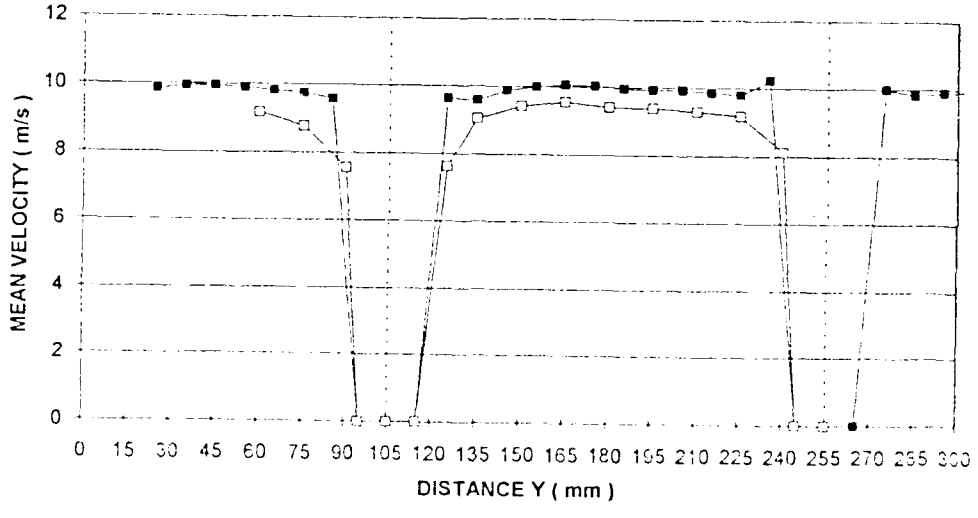

Figure 4 Axial velocity profiles for smoke (-■-) and glass particles (-□-); X = 150 mm

The medium diameter of glass particles as specified by the supplier is 66 μm. The histogram of the particle size distribution at a point located between the tubes, X = -30 mm, Y= 100 and Z = 250 mm is shown in Figure 6. It may be stated that the particle size distributions measured upstream agree well with the manufacturer's specifications. However, as shown in Figure 7, the particle size measurements downstream of the first tube row show an increase in the average particle size. This is in agreement with the work of Humprey (1990).

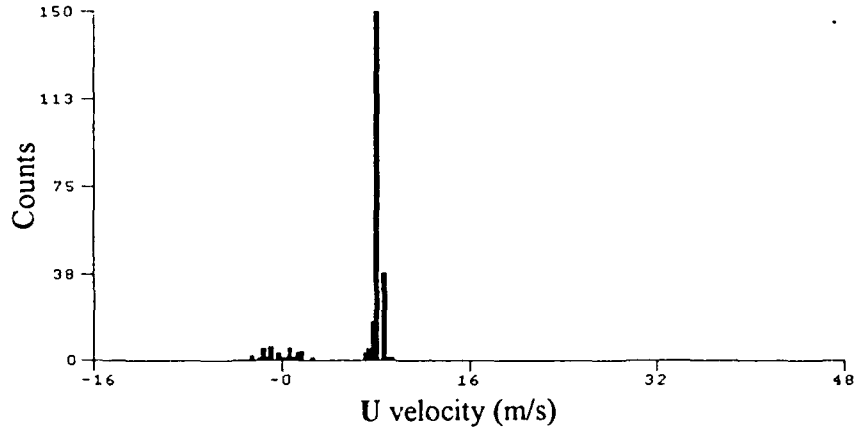

Figure 5 Histogram of velocity for particles (X= -30 mm, Y= 100 mm, Z= 250 mm)

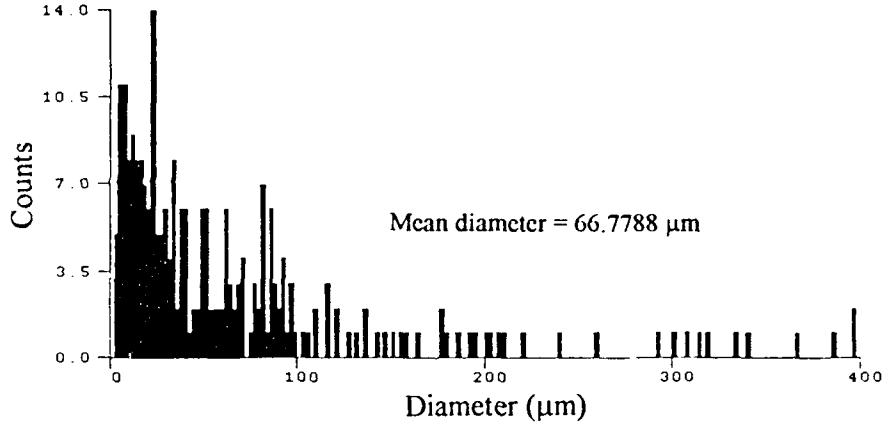

Figure 6 Histogram of particle size (X= -30 mm, Y= 100 mm, Z= 250 mm)

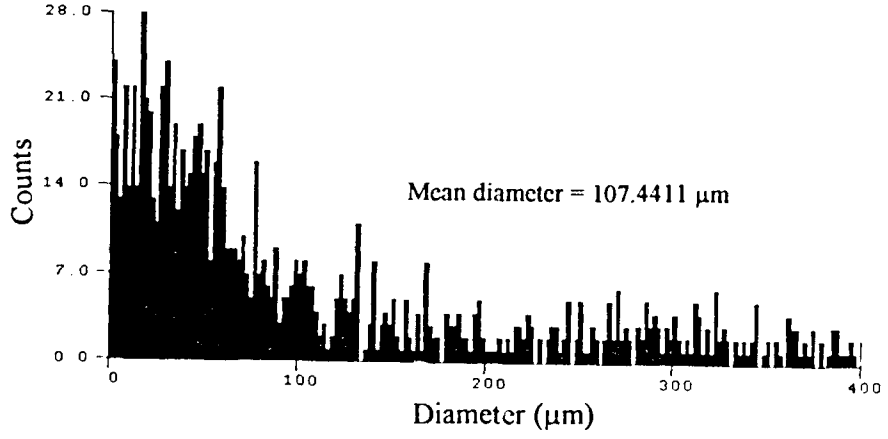

Figure 7 Histogram of particle size (X= 180 mm, Y= 165 mm, Z= 250 mm)

CONCLUSIONS

The PDA system can be used to provide useful information on velocity and particle size. Only spherical particles can be measured.

REFERENCES

Atapattu, D. D., Morsi, Y. S. and Gray, N. B. "Two-component velocity measurements in top submerged gas injection systems", *Proc. 13th Symp. on Turbulence*, University of Missouri-Rolla, USA, B13.1 - B13.14, 1992.

Buchalo, W. D. and Houser, M. J. "Phase Doppler Spray Analyser for simultaneous measurements of drop size and velocity distributions", *Optical Engineering*, **23**, 15, 183, 1984.

Durst, F. and Zare', M. "Laser-Doppler measurements in two-phase flows", *LDA-Symposium*, University of Denmark, 1975.

Humprey, J. A. C. "Fundamentals of fluid motion in erosion by solid particle impact", *Int. J. Heat and Fluid Flow*, **11**, 3, 170-196, 1990.

PDA User's Manual, Dantec measurement technology, Denmark, 1992.

Saffman, M., Bucchave, P and Tanger, H. "Simultaneous measurement of size concentration, and velocity of spherical particles by a laser Doppler method", *Second Int. Symp. on Application of Laser Anemometry to Fluid Mechanics*, Lisbon, July 1984.

Degenerate Four Wave Mixing for Shock Tunnel Studies of Supersonic Combustion

Peter Barker, Amberyn Thomas, Halina Rubinsztein-Dunlop.

The Department of Physics, The University of Queensland, Qld. 4072.

ABSTRACT

Resonant Degenerate Four Wave Mixing (DFWM) is a relatively new technique currently being considered for its applicability to combustion and flow field diagnostics.
In this work we study the influence of collisional processes on the DFWM signal. To this end, measurements were performed on gaseous molecular iodine I_2 contained in a glass cell where pressure, temperature and species concentration are easily and independently varied. Frequency doubled output from a seeded Nd:YAG laser and an excimer pumped dye laser were both used as excitation sources. We have studied the dependence of signal strength versus buffer gas pressure with pump intensity as a third parameter. It is evident from our results that for low intensities (1 MW/cm^2) there are two regimes of pressure dependence. In the low pressure regime the DFWM signal is very weak due to the strong washout of the grating within the duration of the laser pulse. The second regime occurs at higher pressures, where collisions significantly change the decay rates for the two level system. This leads to large changes in saturation intensity. At higher intensities of the order of (7 MW/cm^2) and pressures greater than 30 kPa, the two level model is not sufficient to describe the pressure dependence of the observed DFWM signal.

INTRODUCTION

New laser-based diagnostic techniques, developed primarily within the combustion community, offer considerable promise for measurements within supersonic and hypersonic flows. In the past, several methods have been proposed for nonintrusive measurements in gaseous flows. Some of the important physical properties such as concentration, temperature, velocity and density of stable and reactive species can be monitored using these methods. They provide high spatial and temporal resolution when light pulses of nano- or pico-second duration are employed. Among them, non-linear optical diagnostic methods have proved very valuable.

Recently a lot of interest has been directed towards the development and implementation of Resonant Degenerate Four Wave Mixing (DFWM) which represents a nonlinear optical process involving the third order susceptibility $\chi^3(\omega)$. DFWM has been successfully used for detection of low concentrations of both atomic and molecular species such as Na, OH, NH, NO, NO_2. It finds application in high resolution spectroscopy (because of its inherent Doppler free nature) and for measurements of ultra fast relaxation and diffusion phenomena. It has also been demonstrated as a useful method for temperature determination .

The DFWM signal is created by the scattering of light from a spatially modulated population grating. This grating is produced by interference from the three input light fields of the same frequency, ω. The most common geometry for DFWM is to use two strong counter propagating forward E_f and backward E_b beams that pass co-linearly through the medium. A weaker probe beam E_p enters the medium and crosses the strong pumps at a small angle θ to the stronger co-linear fields. A phase conjugate of the probe E_c is produced by the four wave mixing process and retraces exactly the path of the probe beam. This conjugate field can be collected and constitutes the DFWM signal.

Molecular iodine is one of the most spectroscopically studied diatomic molecules and hence a great amount of spectroscopic data is available. It has a large number of transitions in the visible region and most lasers emitting in the visible have access to one or more of its available transitions. I_2 sublimates from a solid to a fixed vapour pressure at a certain temperature, hence concentration is easily varied by a corresponding change in temperature. Iodine has been successfully used in the past as a seed molecule for flow diagnostics utilizing Laser Induced Fluorescence (LIF). It is therefore a useful and convenient species for studying DFWM processes.

The aim of this paper is threefold: Firstly we compare the spectral features of iodine simultaneously recorded with two methods: LIF and DFWM. Secondly, we investigate the dependence of the DFWM signal on buffer gas pressure and laser intensity. Finally, the comparison is made between the experimentally obtained results and theoretical predictions. The theoretical model used here is based upon the model first developed by "Abrams and Lind (1978)" with a modification to include the variation of the line shapes with pressure.

EXPERIMENTAL

A schematic diagram of the experimental set-up is depicted in figure 1. The laser light used in these experiments was generated by either an excimer pumped dye laser system or a narrow bandwidth Nd:YAG laser. The excimer pump laser operating on XeCl at 308 nm [Lambda Physik, LPX210] pumped a dye laser [Lambda Physik, FI 3002] producing light with a pulse duration of 17ns. The dye Coumarin 153 was used to cover the spectral region around 532.4 nm. The irradiance within the interaction region could be varied up to 4 MW/cm^2. The laser linewidth of 1 - 10 GHz was available depending on whether the laser was operating with or without an intracavity etalon. This spectral region was chosen so that the results could be compared with measurements performed using frequency doubled output from a Q-switched Nd:YAG (Continuum NY81-10) pulsed laser, where much higher laser intensities are available. When operated in the seeded mode a linewidth of 250 MHz is achieved. This laser is scannable in increments of 100 MHz under stepper motor control over approximately 80 GHz. Figure 1 shows the latter of the two laser systems. When performing the experiments utilizing the excimer pumped dye laser the experimental set-up remains the same with a different light source as the only modification.

The laser beam was collimated to approximately 2 mm in diameter. This beam was directed through a 70/30 beam splitter towards the interaction region. The division of the beams was such that 70% of the light was used as one of the pump beams and the reflected part used to form the weak probe beam. After the passage through the interaction region, the strong beam is retroreflected forming two counterpropagating beams. These pump beams are of the approximately the same intensity. The probe beam is directed at an angle of half a degree to the strong pump beams. The probe beam passes through a 50/50 beam splitter and the reflected portion is sent to a beam dump. The returning conjugate beam or signal is extracted by reflection from the 50/50 beamsplitter and directed approximately six meters away from the interaction region, through an iris and subsequently detected by a photodiode. The photodiode signal and the energy of the laser output are monitored by a boxcar integrator. The signal is averaged in a boxcar integrator (Stanford Research SR 165) over 10-30 laser pulses. The averaged signal is digitized and forwarded to the computer for display, storage and further data processing. Since the signal beam consists of a well-collimated coherent laser beam, the photodiode can be positioned far from the region of interaction, as well as far away from all of the incident beams (probe and pump beams) to minimize the influence of scattered light.

The iodine is introduced into the cell as solid crystals and sublimates into a gas with a pressure of approximately 10 Pa at room temperature. The vapour pressure is constant for a fixed temperature and hence the concentration of I_2 is also constant. Throughout the experiments the cell was kept at room temperature (293 K). High purity nitrogen 99% is used as a buffer gas and is introduced into the cell in order to study the effects of pressure on the resonant DFWM process. A glass (Pyrex) cell was used to contain the gases. The cell was 100 mm long and 50

mm in diameter. Three windows (40 mm in diameter) are used for optical access. Two windows are placed on either end of the cell for the DFWM experiments. The third window, perpendicular to the strong pump beams is used to monitor a fluorescence signal. The probe beam intersects the counterpropogating pump beams at the centre of the cell. Mirrors M1 and M2 are positioned as far away from the cell as possible on an optical table in order to minimise the angle between the probe and the pump beams. In this way a maximum overlap volume can be obtained for all input beams along the entire length of the cell.

Spectra of I_2 obtained from LIF and DFWM measurements were recorded in the region of 18786.5 cm^{-1} to 18788.7 cm^{-1} using the excimer pumped dye laser. The dye laser was used in this application since it is easily and quickly scanned over the region of interest. The study of the pressure dependence of the signal was performed on line 1109 of the iodine atlas using both laser systems. This particular spectral line was chosen as it has the greatest spectral isolation from other lines within the spectral region accessible within the tuneability of the Nd:YAG laser.

THEORY

The basic theory for resonant DFWM for a two level stationary absorber was developed by Abrams and Lind "Abrams and Lind (1978)". In this theory it is assumed that the medium consists of a ensemble of homogeneously broadened absorbers. The two energy levels are separated by an energy difference equal to or close to that provided by a monochromatic field. The reflectivity, R, of the medium can be envisaged as the ratio of the conjugate signal I_c to the input probe intensity I_p. The reflectivity is a function of the linear and nonlinear coupling coefficient, α and β, respectively, absorption coefficient, α_0, intensity of the pump field, I, and saturation intensity, I_s, which in turn is dependent upon transverse and longitudinal decay rates, γ_1 and γ_2, the frequency of the incident light field, ω, and the dipole moment of the studied transition, μ_{12}.

In this work we aim to include in the model the influence of the collisions on the DFWM process. The effect of molecular collisions on the longitudinal and transverse relaxation rates takes two forms. The first are collisions that lead to changes in the population of the two levels connected by the incident light field and also to other levels in the molecular system. The second type are phase changing collisions leading only to the changes in the transverse rate γ_2. We assume that state changing collisions are dominant and that γ_1 and γ_2 are equal over the relatively high pressure range of interest. Therefore, in order to include the effects of collisional de-excitation of the energy levels, we allow the longitudinal, γ_1, and transverse decay rates, γ_2, to vary with pressure according to the following expression:

$$\gamma_{1,2} = \gamma_{1_0,2_0} + \gamma_{1_p,2_p} \qquad (1)$$

Where the combined relaxation rates are given by the sum of the natural decay rate $\gamma_{10,20}$ and a pressure dependent rate $\gamma_{1p,2p}$. The pressure dependent decay rate is assumed to vary as:

$$\gamma_{1_p}, \gamma_{2_p} = const \cdot \frac{p}{(mT)^{1/2}} \qquad (2)$$

It can be seen from the above equation that for a fixed temperature the decay rates vary linearly with pressure. This leads to the expected quadratic dependence of the saturation intensity on pressure.

A modified reflectivity where the effects of quenching are taken into account is given by substituting the pressure dependent decay rates. The final reflectivity is given by:

$$R(p) = \left| \frac{\beta(p) \sin(\Gamma(p)L)}{\Gamma(p) \cos(\Gamma(p)L) + \alpha \sin(\Gamma(p)L)} \right|^2 \quad (3)$$

RESULTS AND DISCUSSIONS

The simultaneous DFWM and LIF measurements of I_2 spectra carried out with a laser bandwidth of 5-10 GHz at a total cell pressure of 6 kPa, show that DFWM is able to provide much higher resolution spectra then LIF, even when the relatively broad bandwidth laser is used. This is due to the inherent non-linear dependence on intensity in the production of the DFWM signal. A high resolution spectrum of the same region performed using the dye laser with intra-cavity etalon, resulting in a bandwidth of approximately 1GHz, enabled more detailed structure within the wavelength region studied.

Figure 2 shows the pressure dependence of the DFWM and LIF signals for relatively low laser energies (1.4 mJ/pulse) using the broadband dye laser. The dependence on pressure is very similar for both DFWM and LIF. At higher pressures, the DFWM and LIF both suffer from collisional effects in the same way. At low pressures the pressure dependence for each process differs markedly. The decrease of the DFWM signal at low pressures is believed to be due to grating washout (i.e. motion of the excited molecules during the duration of the laser pulse). It was found that significant saturation occurs for pressures below 7 kPa for this intensity and it is evidenced as a decrease in signal as the laser is tuned to resonance.

Figure 3 is a plot of signal versus pressure performed using the seeded Nd:YAG, which is tuned to line 1109 in I_2 with a laser output irradiance of 1.7 MW/cm^2. This also shows the expected dependence using the theory of Abrams and Lind. Excluding the effects of washout which is evidenced by a sharp decrease in signal below 20 kPa the theory fails to predict the strong almost constant signal with pressures above 30 kPa. This is believed to be due to the effect of overlapping lines at higher pressures due to pressure and power broadening. Although the model used includes these broadening effects, it only considers excitation between two levels (i.e. one transition). The effect of the neighbouring levels could be taken into account by summing the contribution from each line with a different detuning. We have also performed measurements of the dependence of the DFWM signal over the same pressure range as in figure 3, but for a laser irradiance of 7.1 MW/cm^2. As in figure 3 the dependence above 30 kPa differs from that expected. However, the degree to which the experimental results and model deviate at this higher intensity is much more pronounced. This may be expected if we again assume that the discrepancy between theory and experiment at pressures above 30 kPa is due to the interference from neighbouring lines. At low intensities where the transitions are not saturated, the strongest DFWM signals are found at line centre. With the onset of saturation, the strongest signals are now found at some detuning either side of the line centre. As the intensity of the laser is increased to values far in excess of saturation, the strongest signals are found far from line centre and hence the signal can be derived from the combined effect of many neighbouring transitions.

CONCLUSION

This work has shown that the two level model of DFWM is sufficient to qualitatively model the pressure dependence of the DFWM signal at moderate laser intensities. A rise in this signal with pressure as seen in this experiment is not expected within the framework of this theory even at the highest input intensities. At much higher intensities than used in this experiment a pressure independent signal is expected using the simple two level model. This process is unlikely to be seen in this part of the iodine spectrum due to the high density of transitions within this region. However, the fact that there is a very slight increase in signal over a large pressure range indicates that this may be useful when using iodine for quantitative measures of

concentration when the pressure range is large. In order to test the two level model at higher intensities without interference from adjacent transitions it would be more suitable to perform similar measurements on lighter molecules such NO or OH where the spacing between lines within the same bandhead are much greater. Pressure dependence measurements on these species would also be more useful since the above mentioned molecules are common flow and combustion products. As the pulse length (7 ns) of the laser is shorter than the natural lifetime of the transition (2.6 μs) the system at low pressures will not have reached a steady state. The same reasoning will also apply to washout effects, since during the pulse length of the laser significant movement of absorbers will occur. A more rigourous treatment including time dependence and washout effects is needed to properly include the motion of the absorbers and the short duration of the laser pulse.

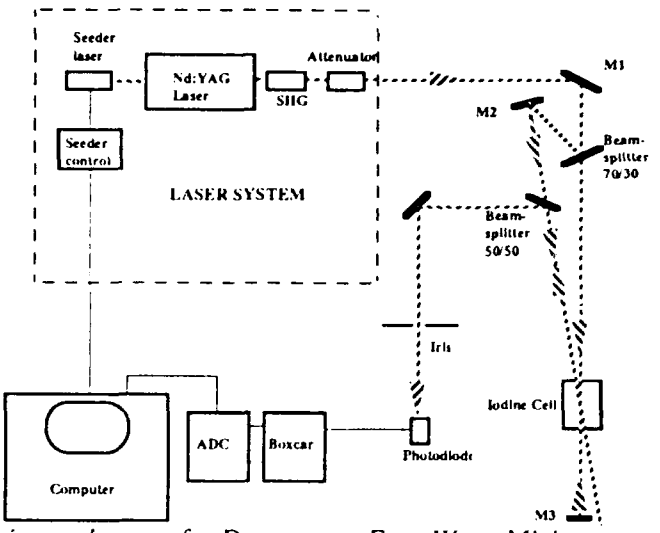

Figure 1: Experimental set-up for Degenerate Four Wave Mixing.

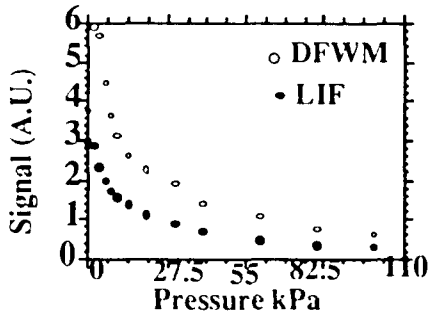

Figure 2: Degenerate Four Wave Mixing and Laser Induced Fluorescence signals as a function of pressure. The measurements are performed using the output from excimer pumped dye laser with energy 1.4 mJ/pulse.

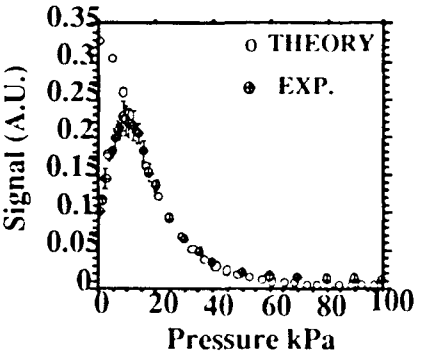

Figure 3: DFWM signal as a function of pressure (experiment and theory). Experimental data is obtained using seeded Nd:YAG output with energy 1.4 mJ/pulse.

References:

Abrams R.L. and Lind R.C. (1978) "Degenerate Four Wave Mixing in Absorbing Media", Optics Lett. 2, 94 - 96.

LASER INDUCED PHOTODISSOCIATION AND FLUORESCENCE (LIPF) OF SODIUM SPECIES PRESENT IN COAL COMBUSTION

Bruce Chadwick and George Domazetis
State Electricity Commission of Victoria, Herman Research Laboratory, 677 Springvale Rd, Mulgrave Victoria 3170
Greg Walker and Richard Morrison
Department of Chemistry, Monash University, Clayton Victoria 3168

INTRODUCTION

Sodium species are a major cause of fouling and slagging in Victorian coal-fired power plants. In addition, sodium species may cause problems in advanced clean-coal technologies such as combined-cycle integrated drying gasification, currently under development at the SECV's Herman Research Laboratory. Sodium residues may cause slagging and fouling, while any gas-phase species such as NaCl facilitate the fouling and corrosion of turbine blades. Methods for in-situ measurements of sodium species, under similar conditions to those found in power plants, would provide information on the distribution of sodium, and assist in the development of strategies for dealing with sodium related problems. Previous investigations on the fate of sodium in coal combustion have utilised a range of invasive sampling techniques including the use of quenching probes, flame atomic absorption spectroscopy and mass spectrometry. The value of such techniques is limited by their invasive nature and inability in distinguishing the concentration of the various molecular Na species present. The recently demonstrated technique of laser induced photodissociation and fluorescence [Oldenborg and Baughcum (1986)] shows promise in the determination of gas phase molecular Na species in combustion environments.

THEORY OF LASER INDUCED PHOTODISSOCIATION AND FLUORESCENCE

The LIPF technique provides a method for measuring the concentration of species which form dissociative electronic states. In contrast to the LIF technique, which generally requires a frequency tuneable laser, LIPF uses a fixed frequency ultraviolet laser (in our case a 193 nm ArF excimer laser) and is thus simpler in its application. In this technique light, at a suitably short ultraviolet wavelength, dissociates the species and leaves at least one of the fragments in an excited electronic state. Monitoring of the fluorescence from the fragment can be directly related to the concentration of the original species. Gaseous NaCl and other sodium species can absorb energy from radiation at 193 nm and subsequently fragment into electronically excited sodium atoms (Na*). After photodissociation the Na* may recombine with reactive species or, more probably, they may return to the ground state by collisions with other gaseous molecules - in both cases no fluorescence is emitted. Fluorescence results from the radiative decay of the Na* atom at characteristic wavelengths - including the well known sodium D lines (589.0 and 589.6 nm). The integrated intensity of the fluorescence from the excited fragments can be related to concentration of the parent species by the expression;

$$S(\lambda,T) = C\, N\, \sigma(\lambda,T)\, \phi(\lambda,T)\, [A / (A+Q(T))]\, I \ ,$$

where: S is the integrated fluorescence intensity, λ the photodissociation wavelength, T the temperature, C is a constant relating to the signal collection efficiency and the probe volume, N

is the number density of dissociated compound, σ the absorption cross section, ϕ the quantum yield of the fragment in the relevant electronic state, A is the emission rate, Q is the pressure and compositional dependant quenching rate of the excited fragment, and I is the laser fluence. The equation shows that the concentration of the parent gaseous compound can be quantitatively related to the intensity of the excited photo fragment fluorescence.

The energies and threshold wavelengths of the lowest Na 3^2P state production are reported as 145.9 kcal/mol (195.9 nm) for NaCl, and 130.0 kcal/mol (219.8 nm) for NaOH. It is possible therefore to photodissociate both NaCl and NaOH by using a wavelength of 193 nm. As has been noted by Oldenborg and Baughcum (1986) suitable choice of the photodissociation wavelength offers possibilities to discriminate between different sodium species. Using 193 nm photodissociation, we note that the measured fluorescence (at 589 nm) obtained from NaCl is a factor of 65 greater than that obtained for NaOH. The lower fluorescence intensity from NaOH is probably due to a reduced photodissociation efficiency, as well excess photodissociation energy leading to the production of highly excited Na* and OH*. Hence, partial speciation is obtained even when using 193 nm. We have observed fluorescence from OH as well as highly excited sodium after photodissociation at 193 nm. Observation of these emissions may lead to unambiguous determination of NaOH concentrations. In particular, we are currently evaluating Na fluorescence at 330 and 818 nm for chemical speciation in the coal combustion environment.

EXPERIMENTAL

The nature of the LIPF experiment is affected by experimental conditions such as gas mixture and pressure. Results taken in evacuated cells are therefore of only limited value. An atmospheric combustion system was constructed to more closely emulate gasification conditions. The apparatus consists of a tubular furnace into which an inconel reaction vessel was mounted (see Figure 1). An accurately measured quantity of coal can be placed within the vessel and subsequently heated. Platinum crucibles containing NaCl or NaOH may also be suspended in the middle of the reaction vessel for calibration purposes.

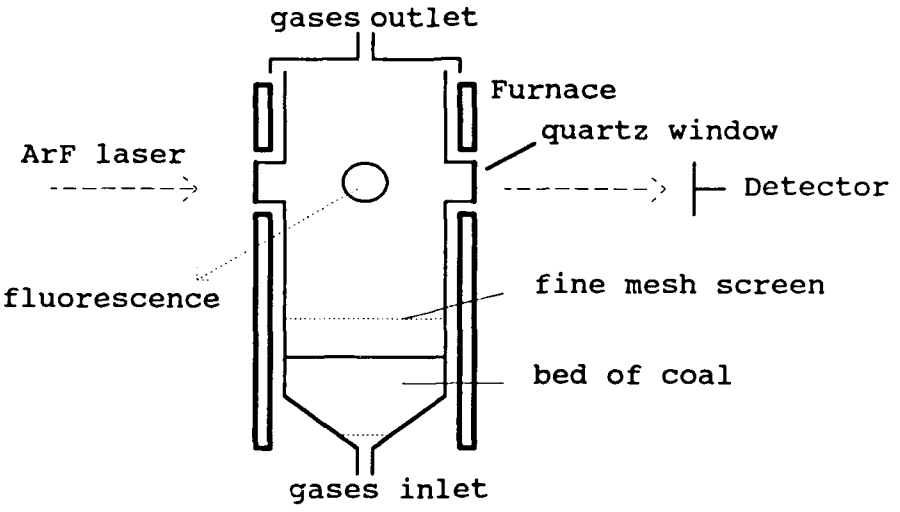

Figure 1: Apparatus for NaCl/NaOH Monitoring and Calibration

Flowing gases (usually nitrogen/oxygen) enter at the bottom of the reaction vessel while light from an ArF excimer laser transverses the furnace and exits onto a detector. The side-on fluorescence monitoring system consists of collection optics, monochromator, photomultiplier and boxcar averaging system.

Quantitative measurements of gaseous sodium species require calibration for each compound under similar conditions to the gasification experiment. Calibration is performed at atmospheric pressure by heating NaCl or NaOH in a platinum crucible within the furnace. The fluorescence signal intensity and the temperature of the cell are simultaneously recorded to form a signal intensity *vs* temperature plot. This plot is then converted to a calibration curve by using the equilibrium concentration of NaCl + Na_2Cl_2 vapour, calculated using the CSIRO Thermochemistry program, for the temperature range of the calibration experiment (note that the amount of dimer NaCl is generally negligible). A typical calibration curve for NaCl is shown below in Figure 2.

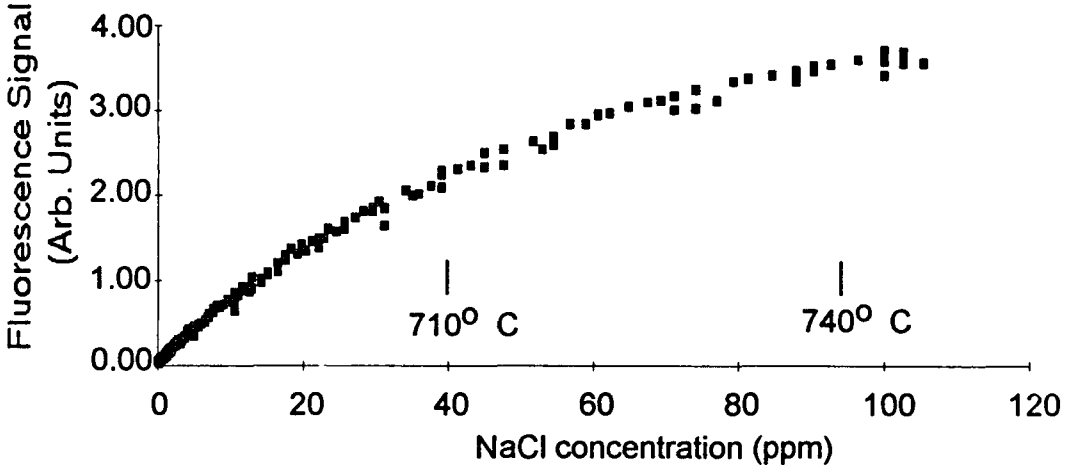

Figure 2: Calibration Curve for NaCl observed at 589 nm

The calibration experiment can be repeated using reducing atmospheres and in the presence of moisture and CO_2. Such calibration curves provide a direct method for measuring the concentration of NaCl and NaOH during gasification of coals in the laboratory tube furnace. The calibration curve for NaCl shows a linear response for low concentrations of NaCl which then plateaus at higher concentrations. This type of response is indicative of the radiation trapping phenomenon, which increases with higher NaCl (hence Na) densities. In the case of NaOH the calibration curve observed at 589 nm is similar to that obtained for NaCl, except it is much weaker. However, at 819 nm fluorescence is observed for NaOH where none is observed for NaCl owing to the different excess energies of the fragments after photodissociation. The corresponding calibration curve is shown in Figure 3.

As can be seen from Figure 3 the response is again highly non-linear. In this case the fluorescence intensity depends on the temperature of the sample, as well as concentration, since the 819 nm fluorescence results from a hot-band absorption. Hence, the vibrational energy distribution leads to an increased LIPF efficiency at higher temperatures (note higher temperatures correspond to higher concentrations in our calibration curve). Theoretical work is progressing to obtain an understanding of the NaOH photodissociation mechanism. Ultimately observation of the LIPF emission at both 589 nm and 819 nm should lead to complete speciation between NaCl and NaOH.

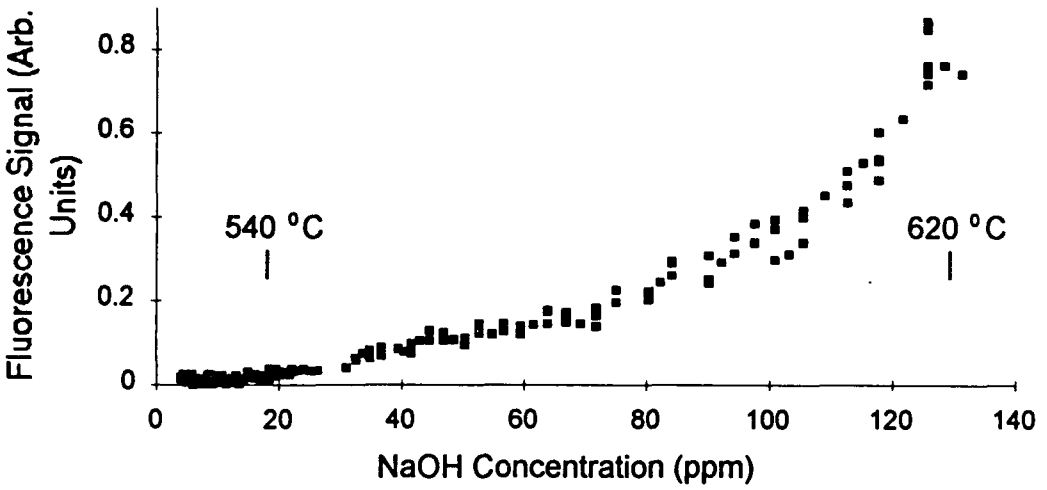

Figure 3: Calibration Curve for LIPF of NaOH observed 819 nm

The high sensitivity of the LIPF technique is illustrated in Figure 4, where the sodium D lines are recorded - by scanning the detection wavelength - for LIPF of just 15 ppb of NaCl in one atmosphere of nitrogen. Our ultimate sensitivity is less than 1 ppb of NaCl at atmospheric pressure.

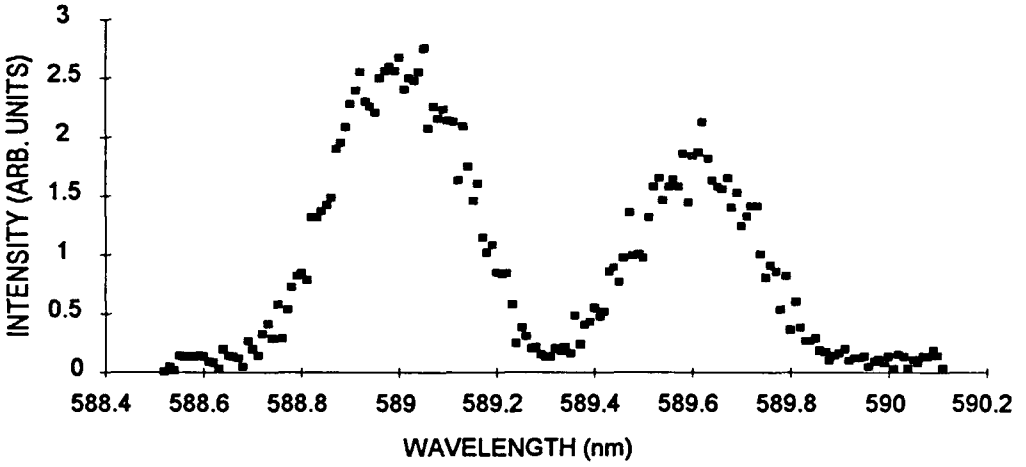

Figure 4: LIPF of 15 ppb of NaCl recorded in one atmosphere of nitrogen

MEASUREMENT OF GASEOUS SODIUM SPECIES FROM COAL

Experiments are carried out initially with a bed of coal placed within a platinum crucible which is located inside the lower part of the reactor and heated in an atmosphere of nitrogen or nitrogen/oxygen. These experiments pyrolyse the coal and allow measurements of the release of sodium species to 1000° C. The char is recovered and analysed for sodium and, in combination with the LIPF data, the distribution of sodium between its solid and gaseous phases may be ascertained. In Figure 5 below we see the sodium release from a 2g sample of Loy Yang 2301 coal as it is heated from 50 to 900 °C. In this experiment the LIPF signal at 589 nm is being monitored as the coal is heated. The signal intensity has been calibrated against the laser intensity and is given as a function of equivalent molecules/cm^{-3} of NaCl.

To convert the fluorescence signal intensity to NaCl concentration, a platinum crucible containing pure NaCl is lowered into the furnace, and the LIPF signal recorded. This provides a calibration point to which the signal can be referenced. As shown in Figure 2, the signal response is approximately linear for NaCl concentrations below 20 ppm (~2.10^{14} molecules/cm^{-3}). The fluorescence quenching is temperature dependent and this is accounted for by including its $T^{-1/2}$ dependence in the analysis. The total signal intensity shown in Figure 5, may be integrated to give the total mass of NaCl released, and in combination with ash analysis, a sodium mass balance can be obtained.

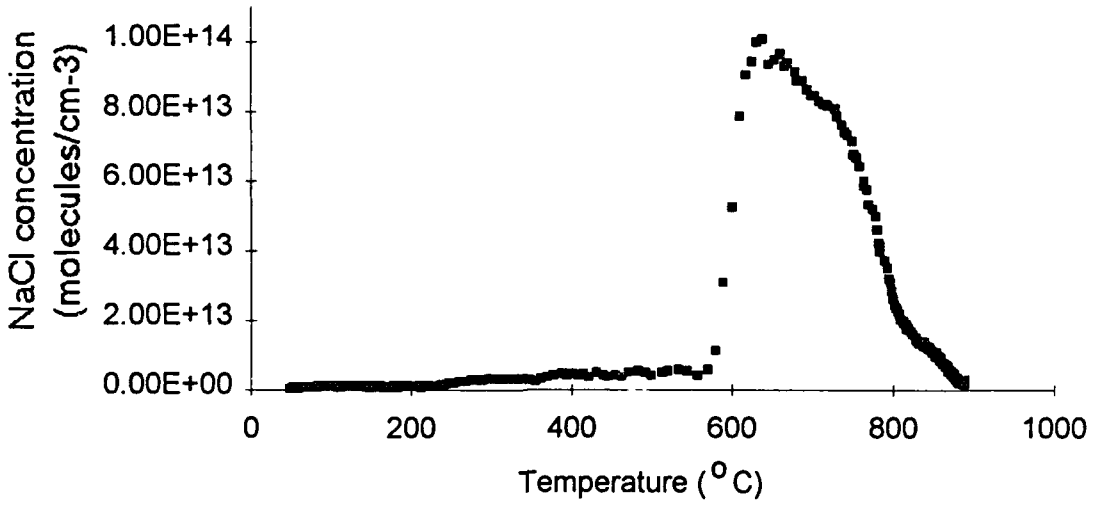

Figure 5: LIPF of Sodium recorded during heating of LY2301 coal in Nitrogen

CONCLUSIONS

LIPF has proven to be a sensitive means of monitoring the NaCl and NaOH vapour. In this work sensitivities lower than 1 ppb have been obtained for the measurement of NaCl under atmospheric pressure. Calibration is necessary under the conditions - of pressure, gas species etc. - which occur in the experiment, and in this work the vapour pressure of the pure salts is used for this purpose. NaOH and NaCl may be distinguished through selective observation of emission wavelengths produced after photodissociation. Further work is progressing in speciation between the different gas phase Na species present during coal combustion, and this effort is complementing chemical kinetics and thermodynamics modelling of the chemistry of sodium during the gasification of Victorian brown coal.

REFERENCES

R. C. Oldenborg and S. L. Baughcum, Anal. Chem. **58**, 1430 - 1436 (1986).
A. Turnbull and M. Wadsley, CSIRO-Thermochemistry System Version 5.1, CSIRO Division of Mineral Products, Australia, (1988).

ACKNOWLEDGEMENTS

The authors wish to thank the SECV for providing technical support for this research project and for providing permission to publish this material. ARC support for a fellowship held by one of us (BC) is also gratefully acknowledged.

3D HOLOGRAPHIC MEASUREMENTS INSIDE A SPARK IGNITION ENGINE

T.J.Chalko [1], **J.Liu** [2] ,
(1) Senior Lecturer (2) Postgraduate student,
University of Melbourne, Department of Mechanical and Manufacturing Engineering
Parkville, Victoria 3052 Australia

Abstract

Paper presents results of holographic recording and reconstruction of a combustion process inside a spark ignition engine. Recording was accomplished in a single cylinder engine with the optical access through a quartz piston crown. A double pulse exposure technique employing a Q-switched ruby laser was used. Interferogram of the combustion process provided the 3D recording of the changes in the refractive index field, encoded in the form of the 3D interference pattern (fringes). Authors developed an optimised grid method, enabling reconstruction of the 3D map of the refractive index field changes from recorded holographic interferogram, suitable for the restricted angle of view (~15 degrees). Using an approximate thermodynamic model, the 3D relative temperature map of the burned volume inside the combustion chamber was obtained for 3D grid of 2.25 mm with accuracy to few degrees K.

Introduction

Experimental observation of the combustion process as it occurs in the engine, specifically its flame propagation phase, is crucial not only from the point of view of investigation and understanding of the process itself, but also as the important step for validation of various hyphoteses and numerical models. Quantitative 3D measurements during the flame propagation process inside an engine cylinder pose significant challenge to researchers, due to the restricted optical access, combined with the rapidness of the process (1-2 ms). Various techniques have been reported to observe the combustion process : direct visualisation (photography), schlieren and shadowgraphy, 2D and 3D tomography and laser induced fluorescence [5]. Of these techniques , only the 3D tomography (Mantzaras 1988 [8]) provides any information about the burned volume shape. This technique, however, requires more than one window in the combustion chamber which makes it very difficult to app'y in the real engine. Holographic interferometry, on the other hand, not only can be used with a single optical window, which helps to preserve the combustion chamber geometry, but more significantly, it can provide true 3D measurements of the relative index of refraction and temperature field changes. Optimisation of the reconstruction method enables to achieve the spatial resolution of 2.25 mm for the optical setup with a view angle restricted to 15 degrees. This paper briefly describes following aspects of the holographic technique applied to study combustion in the engine: i) description of experimental rig ii) recording the hologram, iii) controlling the experiment, iv) reconstruction and analysis of recorded interferogram v) results: 3D distributions of relative index of refraction and relative temperature.

Holographic setup

The diagram of the optical system used for hologram recording is presented in Fig.1. Conventional off-axis arrangement is used, which doesn't impose excessive requirements for the photo-sensitive material and the system mechanical stability. Since the Q-switched ruby laser emits the light of limited coherence, the path lengths of the reference and object beams in the holographic system (Fig.1) were matched to within few mm to optimize the efficiency of the holographic recording. With the aid of the microprocessor based control system (described

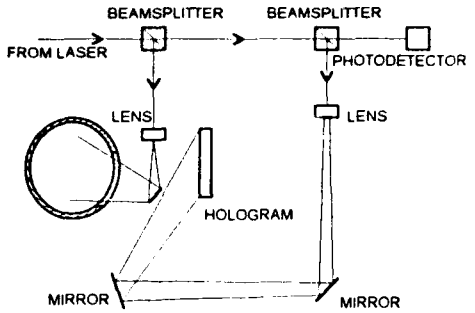

Fig.1. Holographic system

in the next section) the hologram was exposed twice, and two corresponding light wavefronts, representing the light scattered back from the engine head were recorded. The engine was developed by Watson et.al. [10]. Optical access to the combustion chamber of the engine was accomplished by using a special piston with the quartz window as shown in Fig.2., after the method of Bodwitch [1]. Engine parameters were : bore 0.089m, stroke 0.066m, compression ratio 10, fuel C_3H_8. More detailed description of the holographic system was published by Chalko et al [4].

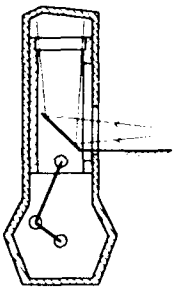
Fig.2. Optical access to combustion chamber

Experiment control

Recording of the combustion process in the selected phase of the flame propagation requires precise synchronisation of several processes occurring not only in the engine, but also in the pulse laser and the data acquisition system. The pulse laser requires activation of its flash lamps 1.2 ms before the light pulses occur. This is in conflict with the μs accuracy required for accurate measurement. In order to achieve temporal accuracy as well as repeatability of the holographic experiment, a special microprocessor control system was designed (Chalko and Kumar [2]). The system generates real-time corrected estimates for all triggered signals, and also records the occurrence of the laser pulses with accuracy to 1 μs. Additionally, positions of the engine crankshaft during the entire cycle are recorded with accuracy to 0.36 degree. The control system takes advantage of the parallel architecture of NOVIX NC4016 microprocessor and it is programmed in FORTH, its native machine language. Microprocessor and the interface board are installed inside the PC, and use the PC bus to utilise the keyboard, monitor and the hard disk. Real time response of the system has been measured to be between 3-8 μs. More detailed description of the control system is given in references [2] and [4].

Interferogram reconstruction

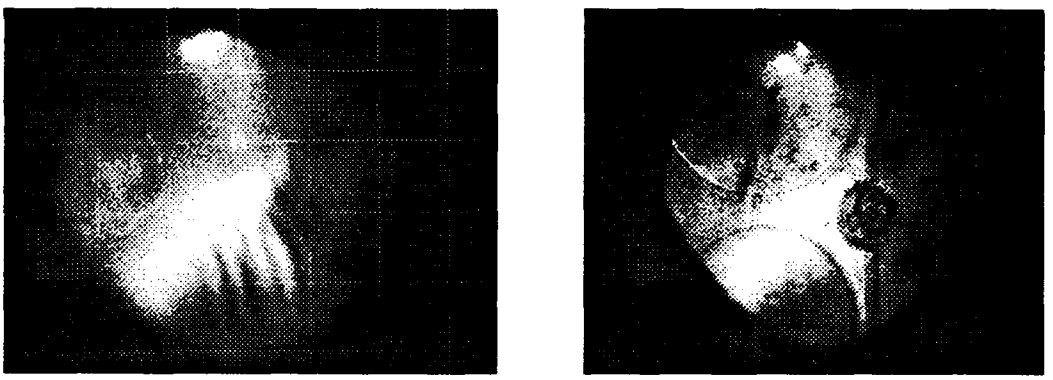

Fig 3. Image reconstructed from the hologram. Left: camera focused on the fringe pattern. Right: camera focused on the engine head and the spark plug.

Photographs of the virtual image reconstructed from the hologram are presented in Fig.3. Experiment conditions for this recording were as follows : average engine speed : 1200 RPM, separation of laser pulses 300 μs, timing of the first pulse 2 deg ATDC, ignition angle 20 deg

BTDC. Timing of the first exposure was selected to correspond to a very small flame kernel (less than 1 mm across). Observing the virtual image reconstructed from the recorded 2 exposure interferogram (Fig.3) it can be noticed, that the volume of the combustion chamber where the combustion occurred could be viewed only through a set of interference fringes. The fringes indicate the 3D changes in the index of refraction, which occurred during the time between exposures (300 μs). Since the fringe pattern is localised in a volume 80-120 mm away from the image of the engine head, it is quite difficult to present them using 2D photographs. Fig 3 demonstrates effects of different focusing of the camera.

3D refractive index reconstruction method

k-th dark fringe in the double exposure interferogram occurs, when the phase difference between rays of two recorded waves reconstructed from the hologram is [4]:

$$\phi_k = \varphi_2 - \varphi_1 = \pi(1+2k) \qquad ; \; k = 0,1,2... \tag{1}$$

where k is the fringe order. On the other hand, the phase difference between the two recorded waves could be described as a function of the path length difference Δ :

$$\phi = \frac{2\pi\Delta}{\lambda} \tag{2}$$

where λ is the wavelength of light. Since each wave was recorded at different phase of the combustion process, the rays forming them passed through different refractive index fields in the combustion chamber and their optical path lengths are different. Along the i-th ray the path length difference could be described as:

$$\Delta_i = 2\int_{s_i} [n_2(x,y,z) - n_1(x,y,z)]ds_i \tag{3}$$

where $n_2(x,y,z)$, $n_1(x,y,z)$ are refractive index fields corresponding to exposures 1 and 2 respectively and the integral is evaluated along the ray path s_i. It is assumed, that the illumination as well as the backscattered rays pass through the combustion zone along the same paths for both exposures. If the i-th ray passes through a dark fringe of the order k we can write :

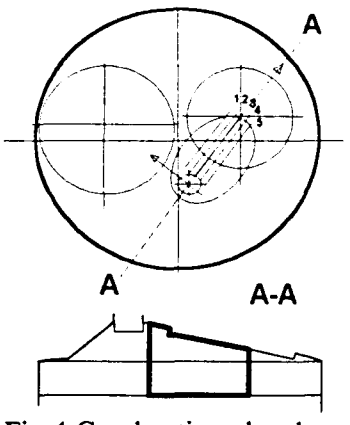

Fig.4 Combustion chamber. Shown are 5 planes for which refractive index reconstruction was made

$$\phi_k = \frac{2\pi\Delta_i}{\lambda} \tag{4}$$

Combining (1),(3) and (4) for every ray passing through a dark fringe of the order k we have:

$$\int_{s_i} n(x,y,z)ds_i = \frac{\lambda}{4}(1+2k) \qquad ; \quad k = 0,1,2,... \tag{5}$$

where $n = n_2 - n_1$ is the refractive index difference. Equation (5) is an integral equation from which values of the function *n(x,y,z)* can be found, when the right hand side is determined for sufficiently large number of rays. Similar relationship to (5) could be written for bright fringes. Authors used modified grid method, specially optimised for the particular geometry of the holographic setup. Modifications included selectable grid orientation angle, size, and the special shape grid elements on the chamber boundary. Optimisation was performed using the computer simulated experiment (index of refraction reconstruction for identical geometry [6]), which helped to establish the best grid orientation angle and size, shown in Fig.5 and Fig.6.

The fringe zone of the combustion chamber was divided into cartesian grid elements located in 5 planar cross-sections of the chamber (see Fig.4). Optimal grid size was 2.25 x 2.25 mm in each plane (Fig.5 and Fig.6). Reconstructed interferogram was observed from a matrix of directions (30 views). Approximately 3 times more fringe measurements were made that the number of unknown grid parameters, enabling the error minimisation using redundant data in the least mean square Singular Value Decomposition algorithm [6]. Results of the reconstructed relative index of refraction field in 5 planes are given in Fig.5. It should be pointed out, that presented values are relative, i.e they show changes in the index of refraction occurred during the time between exposures. By using computer simulation algorithm, it was estimated, that the average error of the relative index of refraction reconstruction was between 10-20%.

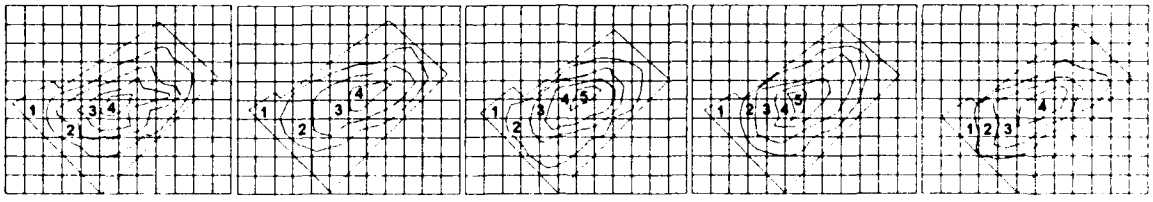

Fig.5 Reconstructed relative index of refraction in 5 planes shown in Fig.4. Shown grid 2.25x2.25 mm. Legend: **1**:0-0.25,**2**:0.25-0.5, **3**:0.5-0.75, **4**:0.75-1.0, **5**:1.0-1.25(*10^{-4})

3D temperature distribution

3D temperature distribution could be estimated from the refractive index distribution, if the composition of the gas as well as its pressure are known. Assuming homogeneous composition of the gas in the burnt volume in the combustion chamber, equations for the ideal gas could be used. For example, by combining the Gladstone-Dale equation with the state equation of the ideal gas, the following relationship could be obtained [6] :

$$\Delta T = \frac{kMP}{(n-1)R} \qquad (6)$$

where ΔT is the relative temperature difference, $k=0.226E\text{-}3\ [m^3/kg]$ is the Gladstone-Dale constant , $M=28.6$ is the (burnt) gas molecular weight, $P=7.19\ [MPa]$ is the pressure, n is the index of refraction and R is the universal gas constant. Temperature maps obtained from the index of refraction distribution presented in Fig.5 using relationship (6) are presented in Fig.6.

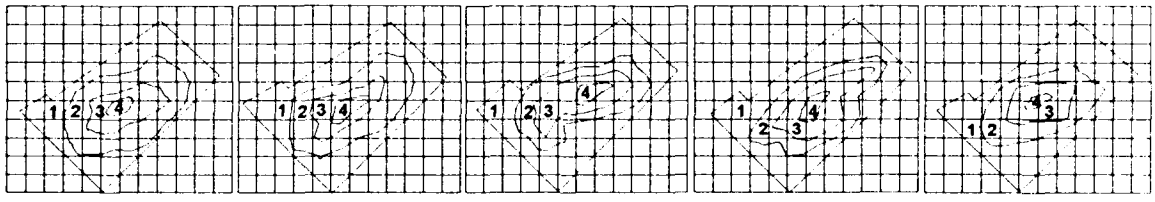

Fig.6 Reconstructed relative temperature distribution in 5 planes shown in Fig.4. Shown grid 2.25x2.25mm. Legend: **1**: 0-50,**2**: 50-75, **3**: 75-100, **4**: 100-125 (degrees K)

Conclusions

- Holographic interferometry enables 3D measurement of index of refraction and temperature distribution of an **undisturbed** combustion process in the engine, since no seeding or other modifications of the process are required.

- Optical access through a transparent piston enabled 3D holographic recording of the entire combustion chamber with limited view angle (15 degrees).
- Limited angle of view (15 degrees) was found to be the major limitation to accuracy of quantitative 3D measurements. Reconstruction of the refractive index field from the interferogram fringe pattern for such restricted view angle required optimisation of the grid method for the particular geometry using computer simulated experiment [6].
- Using the computer simulated experiment, it was estimated, that the accuracy of the relative refractive index and the relative temperature reconstruction was around 10-20%
- Measurements of the refractive index field and corresponding temperature distribution are relative, due to the nature of the double exposure holographic interferometry. Only relative changes in the index of refraction field and temperature occurring during the time between two exposures could be measured. Absolute values can only be obtained by another independent measurement performed simultaneously with the hologram recording.

Acknowledgments

Authors express their gratitude to Australian Research Council for funding which supported presented research.

References

1. Bodwitch, F.W., (1961) A New Tool for Combustion Research - A Quartz Piston Engine, *SAE Transactions* , **Vol 69** , pp 17-23
2. Chalko T.J , Kumar S. (1989) Real Time Control of Engine Combustion Experiment in FORTH, *Proceedings of JSME and HITACHI International Symposium on Advanced Computers for Dynamics and Design* , September 6-8 1989 , Tsuchiura , Japan p.13-17
3. Chalko T.J.,Kumar S. , Watson H.C. (1987) Application of Speckle Interferometry to velocity Measurements in the Combustion chamber of a High Speed High Swirl Spark Ignition Engine, *Proceedings NATO/ASI International Conference on Instrumentation for Combustion and flow in engines*, September 14-25, 1987, Vimeiro ,Portugal .
4. Chalko T.J., Kumar S., Kyaw Z., (1990) Holography of Combustion Process in a Spark Ignition Engine, *Proceedings of 5-th International Symposium on Application of Laser Techniques...*,9-12 July 1990 Lisbon, Portugal, pp.6
5. Kychakoff G., Paul P.H.,van Cruyningen, and Hanson R.K., Movies and 3-D Images of Flowfields Using Planar Laser-Induced Fluorescence, *Applied Optics*, **Vol 26** (13), 1987.
6. Liu J., (1992) *Holography of Combustion in a Spark Ignition Engine*, MSc thesis, University of Melbourne, Department of Mechanical and Manufacturing Engineering
7 Loye, A.O., Bracco, F.V., (1987) Two-Dimensional Visualisation of Premixed Charge Flame Structure in an I.C. Engine, *SAE* Paper No. 870454
8. Mantzaras J., Felton P.G., Bracco F.V., (1988) 3-D visualisation of premixed charge engine flames- Islands of reactants and products; fractal dimensions and homogeneity, *SAE* paper 881635
9. Sweeney D.W,Vest C.M ,(1973), Reconstruction of Three-dimensional Refractive Index Fields from Multi directional Interferometric Data, *Applied Optics* ,**Vol 12**, No 11 , p..2649-2664.
10. Watson H.C, Milkins E.E. (1978) and Roberts K., An Engine for study of performance optimisation of high speed and high output S.I. Engine, *Proceedings of I.Mech.E. Conference on small engine design*, pp 21-31

Laser Doppler Velocimeter Measurements in Compressible Flow

S.C. Favaloro

Aeronautical Research Laboratory
Defence Science & Technology Organisation
Melbourne

ABSTRACT

A two channel, two colour, backscatter LDV system, which has been optimised for high speed flow measurement, has been used to perform measurements of fundamental turbulence quantities in a cold flow experimental rig which simulates the flow environment in an idealised ramrocket combustor. The flowfield is characterised by a high stagnation pressure axisymmetric jet which is surrounded by a lower pressure airstream, both with and without some degree of swirl. Some results from this work are detailed in the paper, along with discussions on some of the particle dynamics problems associated with performing LDV measurements in highly compressible and turbulent flows.

INTRODUCTION

Recent developments in propulsion systems for tactical missiles have concentrated on variants of integral rocket/ramjets. The ramrocket (or ducted rocket) is one such variant wherein a high stagnation pressure, high temperature fuel rich efflux from a solid propellant gas generator expands into a combustion chamber (ramburner) and mixes with air ingested from the atmosphere through an intake system for further combustion. The mixing processes between these two streams, prior to combustion in the ramburner, have features which are unique to ramrockets and can effectively control the combustion performance of the system - some of the features include recirculating regions, overexpanded or underexpanded jets with accompanying shock and expansion waves, and free shear layers with high velocity gradients. To gain some insight into the parameters which impact on the mixing processes, measurements of fundamental turbulence quantities, using Laser Doppler velocimetry (LDV), and pressure distributions have been performed, and are continuing, in an axisymmetric, cold flow representation of a ramburner.

The advantages of applying LDV for fluid flow measurement have been well documented over the last twenty years. Since the LDV is non-intrusive, calibration free, and possesses high temporal and spatial resolution, its range of application has been diverse, covering low velocity to hypersonic flowfields, laminar to highly turbulent flow regimes, and combusting flows in gas turbines, furnaces, and internal combustion engines. However, some of the practical problems associated in applying LDV include high initial equipment cost, a requirement for aberration free optical access, and in most cases, the need to seed the flowfield with particles which will follow the flow with a reasonable level of accuracy. It is perhaps this latter requirement which becomes the most challenging when attempting to perform measurements in highly compressible and turbulent flowfields, such as those found in ramrocket combustors. A brief survey of some of the literature on particle tracking follows.

Other problems associated with LDV measurements in compressible turbulent flows include a number of biasing problems which arise directly from the fact that the instantaneous velocities are measured discretely, as opposed to the continuous signal from hot wire

anemometers. The errors that can arise from velocity, density, fringe, and clock biases have been extensively documented in the literature - discussion of these items in this paper will be limited to the methods adopted for their correction.

PARTICLE DYNAMICS

The ability of a particle to track the flow is most difficult in flow regimes with high frequency turbulent fluctuations, high accelerations and shock waves, all of which can be found in ramburner flowfields. Haghgooie et al (1986) performed a theoretical investigation of alumina particle relaxation in a nozzle, which accelerated the flow from rest to 60 m/s over a distance of 16 mm, and found that particles larger than 2 micron showed measurable velocity lag. Petrie (1984) used a single channel LDV system to compare the theoretical lag predictions of 1.0 and 1.5 micron particles after passing through an oblique shock wave with the lag of polydisperse particles which were generated by the atomisation of 50 cP silicone oil (using a TSI 6 jet atomiser). He proposed that the particle relaxation distance to a slip velocity of 1%, or less, of the normal gas velocity component was proportional to the particle diameter raised to the exponent of 1.732, for particles with a specific gravity of 1.0 and with diameters ranging from 0.5 to 10 micron over a stagnation pressure range of 300 to 600 kPa. His results showed that the TSI atomiser was generating particles of mean diameter of 0.8 to 1.0 micron. In a similar analysis to Petrie, Kuntz (1985) performed particle velocity measurements after an oblique shock to determine the mean particle size as seen by the LDV system. His results showed that the LDV was seeing particle sizes of 1.5 micron without frequency shifting and 2.0 micron with frequency shifting. Both Petrie and Kuntz used Basset's equation of motion for a particle in a viscous fluid, with an empirical drag coefficient determined from Walsh (1976), for their theoretical calculation of particle velocities.

The frequency response of particles in a turbulent flow is perhaps a more difficult concept than particle lag through a shock wave. Kuntz cites references that suggest that the main part of turbulent energy in a M2.25 shock wave-boundary layer interaction is in the 10 to 50 kHz region, while Petrie suggests that there are significant amounts of turbulence energy at frequencies of 100 kHz and higher in a M2.5 free shear layer. Johnson (1974), in his study of a M2.9 boundary layer, suggests that the frequency response of 0.3 and 0.5 micron particles are 120 and 60 khz respectively at the 3 db point, while Mazumder and Kirsch (1975) show that 0.5 micron particles follow acoustically excited oscillating flows with 95% fidelity at frequencies in excess of 51 kHz. Kuntz also cites references which suggest that the frequency response of 1 and 2 micron particles are around 40 and 10 kHz respectively. The above studies relate to frequency responses in an Eulerian (fixed) reference frame (ie, the instrumentation was fixed in space) whereas the particles are only subjected to turbulent frequencies in a Lagrangian (moving) reference frame. Johnson suggests that relating the particle frequencies to their counterpart in the Eulerian frame is difficult. However, he argues that if it is assumed that the turbulent fluctuations, relative to the moving particle, are approximately the same as would be observed in a reference frame moving at the local mean velocity, then the turbulent eddies, which are convected at the velocity u_c, are observed to have the velocity u_c-u, compared with the observed velocity u in the fixed frame. The ratio of the turbulent frequencies in the two cases is then scaled to the velocity ratio, $u_c/abs(u_c-u)$, which can be as high as 4 in compressible turbulent boundary layers. Applying this scaling factor, Kuntz suggests that the Eulerian frequency response of 1 and 2 micron particles are in the vicinity of 160 and 40 kHz respectively.

EXPERIMENTAL SETUP

A schematic of the configuration of the experimental rig, which is representative of an idealised axisymmetric ramrocket combustor is shown in Figure 1. The primary air, which represents the gas generator efflux, comes from storage vessels through a pebble bed heater at pressures up to 7 Mpa at 20-400°C and is regulated to the required test pressure by a pneumatic control valve. The air is then expanded in one of a series of conical supersonic or choked nozzles to form a high velocity jet in the test section. The secondary air, which represents the the air ingested through an intake system, is delivered to a settling chamber, adjacent to the test section, by a 2000 HP centrifugal compressor. The secondary flow is controlled to give a velocity of M0.15 at atmospheric pressure at room temperature in the test section. Optical access for LDV measurements is achieved through a flat strip of 3.2 mm thick float glass, mounted vertically in an assembly which can be translated axially along the length of the test section at 40 mm intervals. This arrangement allows full vertical traverses, for axial and radial velocity measurements, and roughly three quarter horizontal traverses (for axial and tangential velocity measurements) to be made with minimum disruption to the flowfield while maintaining the integrity of the incident laser beams.

LDV SYSTEM

The LDV in current use is essentially a TSI 9100-7 two channel, two colour system operating in backscatter with frequency shifting on both channels. The combination of 13 mm beam spacing, 2.75 beam expansion and a 750 mm focussing lens give ellipsoidal measuring volume dimensions of approximately 0.13 mm diameter and 4 mm length. The frequency/velocity conversions for both channels are usually around 8 m/s/MHz, but depend upon the final beam half angles which are measured once the crossing point is established. The whole system is mounted on an old milling machine base which allows the measurement volume to be located inside the test section with an accuracy of 0.05 mm. A 0.1 mm aperture in the field stop system reduces the measurement volume diameter seen by the photomultipliers, but the on-axis collection allows for velocity realisations to be made over the full length of the measurement volume. Both channels have Bragg cells in one beam, which provide a frequency shift of 40 MHz. Due to the expected velocity range under investigation, (-100 to 700 m/s) the beams in both channels are orientated at 45° (nominal) to the main flow direction. The combination of 40MHz frequency shifting against the mean flow direction (the downmixer circuits are bypassed) and 45° beam orientation effectively eliminates any fringe bias. The maximum expected Doppler frequencies are around 150 MHz, which are well inside the maximum photomutiplier frequency (200 MHz).

Two TSI 1990 counter processors, a TSI 1998 interface and a PDP-11 computer constitute the LDV data acquisition and processing system. The 1998 interface ensures that velocity measurements in both channels are coincident (within a preset time interval) and since the data transfer rate to the computer is via DMA, and always far exceeds the counter velocity realisation rates (typically 100 to 2000 Hz), in most sections of the flowfield the data is fully velocity biased. Corrections for velocity bias (and any density bias) are made by particle interarrival time weighting - the time between velocity realisations is transferred to the computer along with the velocity data. This is the preferred correction method for this study, since the possibility of low data rates and near zero velocity components in both channels inhibit the use of constant time interval sampling and velocity magnitude weighting respectively.

Although, it has been widely recognised that understanding the fluid dynamics of these devices is critical, only recently researchers, primarily due to recent developments of LDA (Laser Doppler Anemometery) were able to investigate the fluid flow phenomena of these devices. As a result a number of design concepts are now being examined by many researchers world wide. It is now well recognised by most workers in the field that the threshold level of Reynolds

SEEDING

The rig secondary flow was seeded with polydisperse sugar particles which were generated by the atomisation of a 5 per cent sugar and water solution in a TSI 6 jet atomiser. The seed was introduced to the flow in the settling chamber through a six point manifold, thereby providing a reasonably uniform particle distribution in the test section. Data published by TSI suggests that atomisation of a 5% salt/water solution will produce particles ranging from 0.5 to 3.0 micron, with a mean around 0.8 micron - slightly larger particles are expected with the equivalent sugar/water solution. A high pressure version of the TSI seeder was constructed to seed the primary flow. A 50 cP Dow Corning fluid was used as the seed base rather than a sugar/water solution - the possibility of water condensing out of the primary airstream and forming ice particles or condensation shocks after expansion through the nozzle was considered undesirable. Typical secondary/primary mass flow ratios were in the order of 5 to 20 - reasonably successful attempts were made to seed both flows with equal concentrations of particles by adjusting the number of operating atomisers and seeder supply pressures.

EXPERIMENTAL RESULTS

A selection of results from LDV measurements in the ramburner geometry (Figure 1) are shown in Figures 2 to 5. Other configurations (eg, supersonic nozzles, larger base recirculation regions, and different outer flow geometries) have been tested, but the results are not included in this paper. The secondary inlet flow was set at M0.15 (U2 = 52 m/s) while the primary pressure ratio was adjusted to provide M1.0 (ie, choked) flow at the nozzle exit. Axial mean velocity distributions (Fig 2) reveal flow reversals close to the nozzle exit plane, a centreline flow acceleration between 3 & 40 mm downstream of the nozzle exit, and a progressive broadening of the jet after 40 mm. Radial mean velocities (Fig. 3) are directed inwards in the central jet region up to an axial distance of 40 mm, after which they are directed outwards. These features indicate the presence of a vena contracta with minimum cross sectional area between 40 and 75 mm downstream of the nozzle exit. Axial turbulent velocities (Fig. 4) and Reynolds shear stress profiles (Fig. 5) reveal local maxima at the jet boundaries, and in the shear layer emanating from the edge of the centrebody, the maxima move radially outwards as the axial distance from the nozzle exit increases.

REFERENCES

Haghgooie, M., Kent, J.C., and Tabaczynski, R.J. (1986) " Verification of LDA and Seed Generator Performance ", Experiments in Fluids, Vol 4, pp 27-32.

Johnson, D.A. (1974) " Turbulence Measurements in a Mach 2.9 Boundary Layer Using Laser Velocimetry ", AIAA Journal, Vol. 12, No.5, pp 711 - 714

Kuntz, D.W. (1985) " An Experimental Investigation of the Shock Wave-Turbulent Boundary Layer Interaction ", PhD Thesis, University of Illinois.

Mazumder, M.K. and Kirsch, K.J. (1975) " Flow Tracing Fidelity of Scattering Aerosol in Laser Doppler Velocimetry ", Applied Optics, Vol. 14, No. 4, pp 884 - 901

Petrie, H.L. (1984) " A Study of Compressible Turbulent Free Shear Layers Using Laser Doppler Velocimetry ", PhD Thesis, University of Illinois.

Measurement Volume - The measurement volume is normally calculated by the focal length and beam spacing of the focussing lens and was around 2.10 mm. This limited the access to the boundary layer flow near the concave wall, caused a uncertainty in spatial location

Walsh, M.J. (1976) " Influence of Particle Drag Coefficient on Particle Motion in High-Speed Flow with Typical Laser Velocimeter Applications ". NASA-TN-D-8120

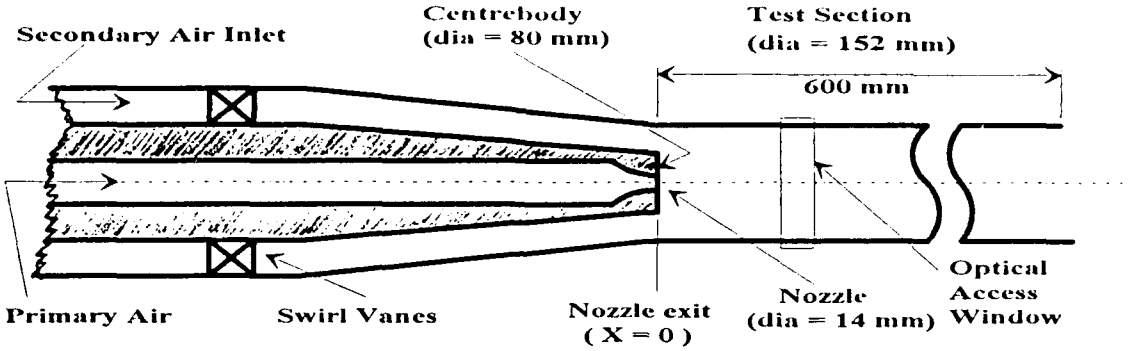

Figure 1 - Schematic of Experimental Rig

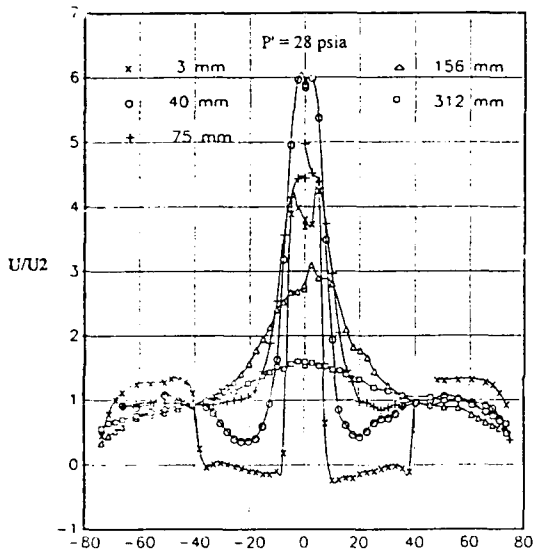

Figure 2 - Axial Mean Velocities

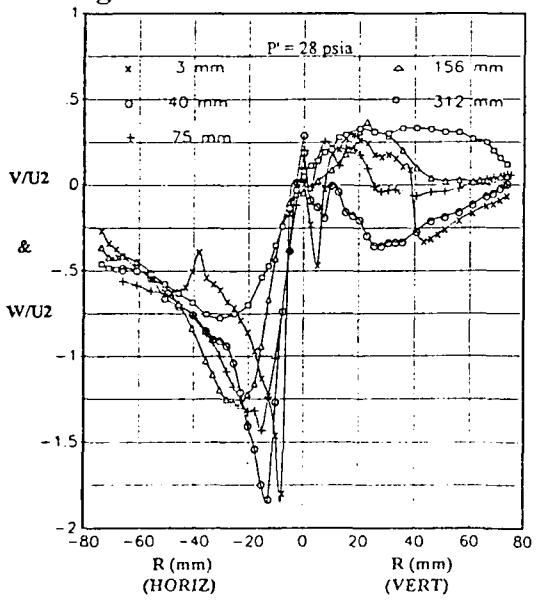

Figure 3 - Radial Mean Velocities

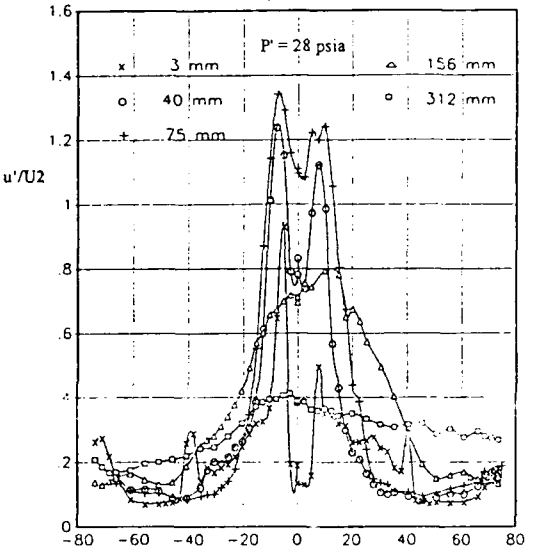

Figure 4 - Axial Turbulent Velocities

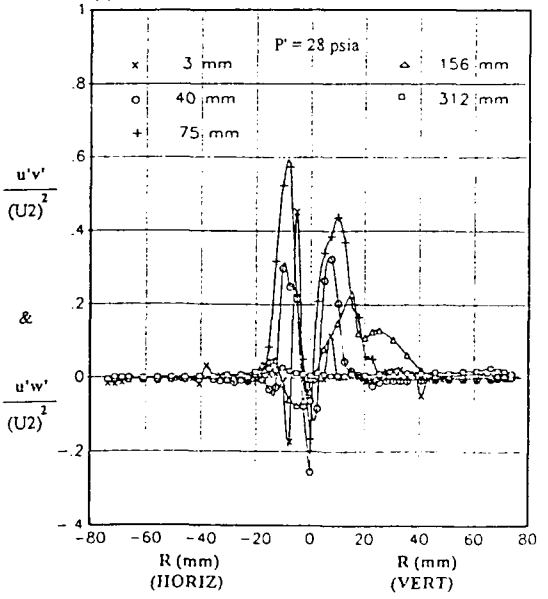

Figure 5 - Reynolds Shear Stresses

BURSTING IN A TORNADO VORTEX

BY

Peter N. Joubert and M.H. Wang

The University of Melbourne

A tornado vortex has been created in laboratory apparatus. The phenomenon of bursting was observed by fluorescein-natrium dye and a sheet of light from a laser beam.

The distributions of mean velocity across the tornado vortex flow have been measured using a TSI system 9100-7 Laser Doppler Anemometer which is a four-beam, two-colour and two channel system.

The criterion for vortex bursting proposed by Brown and Lopez was applied to the velocity measurements results.

INTRODUCTION

The term "vortex bursting" refers to an abrupt occurrence of widening of the vortex core together with a deceleration of the axial velocity at some axial location of a concentrated vortex with an axial flow.

The phenomenon of bursting in a tornado vortex has been documented for ages, as far back as 1780 (see Lugt 1989).

The systematic study of vortex bursting is often attributed to observations of Peckham and Atkinson (1957) in an experiment with a delta wing at high angles of attack. The phenomenon is of practical importance and scientific interest. The potential importance of vortex bursting is in the field of aeronautics, its occurrence in the wake of wings of a large aircraft is relevant to the safety of flight. The phenomenon of vortex bursting has been studied both experimentally and theoretically and many proposals have emerged in attempts to explain the phenomenon. So far, there is no general consensus on the physical mechanisms responsible for the occurrence of vortex bursting. Brown and Lopez (1990) have studied the vortex bursting phenomenon from a new perspective. Instead of concentrating on the stream function or the velocity and pressure field as has been common in the past, they emphasised physical mechanisms for vortex bursting phenomenon based on the production of a negative azimuthal component of vorticity. This leads to a criterion for vortex bursting which depends on the relationship between the angle of the vorticity vector and the velocity vector on stream surfaces upstream of bursting.

The present work examines vortex bursting in a tornado vortex created in laboratory apparatus. The tornado vortex was set up with bursting and non-bursting conditions respectively. In both cases the velocity distributions across the tornado vortex were measured using a two channel Laser Doppler Anemometer (LDA). The velocity distribution data obtained were used to examine the occurrence of vortex bursting based on the criterion proposed by Brown and Lopez (1990). The vortex flow was observed using flow visualisation techniques by a sheet of light from a laser beam.

EXPERIMENTAL APPARATUS

The experimental rig consisted of a suspended rotating right-circular cylinder of 630 mm diameter with a stationary floor underneath and a central suction tube above (see Fig. 1). Glass spheres (marbles) of 15 mm diameter were closely packed all over the stationary floor to simulate particles. The lower half of the cylinder was made of plexiglass and the upper half was of stainless steel mesh. Their combined height was 0.5 m. To avoid the lens effect caused by the circular surface of the cylinder when laser beams are transmitted, an external square section glass box filled with water surrounded the cylinder, thus forming a water tank.

Filtered water was used as the working fluid. The cylinder was rotated by a d.c. motor. Torque was transmitted via a rubber belt. The speed of rotation was measured with a stopwatch. Rotation of the cylinder led to the development of a tornado-like vortex in the centre where the fluid effused vertically. As it passed upwards in the vortex, the fluid was withdrawn (with the help of a pump) through the 20 mm diameter central suction tube coaxial with the vortex and connected to the suction side of the pump. The fluid was then returned to the tank through a 680 mm diameter sprinkler ring with one hundred and twenty, 3 mm diameter holes on its underside.

FLOW VISUALISATION

The vortex flow patterns were viewed and photographed using a laser-induced fluorescence technique for visualisation of the flow. The dye was injected into the vortex core through a hole in the centre of the stationary floor from underneath. The dye was gravity fed from a reservoir placed above the water tank. The surface level of the dye was kept approximately the same as that of the water in the tank. The dye used was fluorescein-natrium powder diluted with water to achieve neutral buoyancy.

The flow was illuminated by a Spectra Physics model 164 laser at a rated power of 0.8W. The laser beam passed through a 5mm diameter glass rod, from which it fanned into a thin straight and intense plane sheet of light. This sheet of light then passed through a concave lens, from which it spread to form a cone of light.

The observations were carried out when the vortex was at non-bursting condition and at the very start of bursting. To achieve this condition the suspended cylinder had to be rotated at a rate as low as eleven and half minutes a turn. Below that rate no bursting occurred.

VELOCITY MEASUREMENTS

A TSI System 9100-7 Laser Doppler Anemometer (LDA) employing a 5 watt Spectra Physics model 164 Arg-Ion laser source was used to measure the radial distributions of mean velocity components across the tornado-like vortex in the centre of the cylinder. The system 9100-7 LDA is a four-beam, two-colour and two channel system, incorporating two Bragg cells to permit determination of both the magnitude and direction of the velocity components being measured. The whole LDA was mounted on a table incorporating a fine traverse with three degrees of freedom. A TSI developed software FIND 6710 was used to process the analog output from the signal processor of the system so determining the mean velocity components being measured.

To measure the azimuthal velocity V, the bisector of the blue beam was oriented normal to, and passed through, the axis of the cylinder with both beams in the horizontal plane. Measurements of the axial velocity W were made with the bisector of the green beams

normal to the axis of the cylinder, but here the beams were co-planar with the axis. To measure the radial velocity U, the bisector of the blue beams was oriented normal to, and passed through the radius of the cylinder with both beams in the horizontal plane.

All three velocity components were measured under the assumption of axial symmetric flow. A signal processor 1990c counter model was used in the measurements. Owing to the lack of a second signal processor, simultaneous measurement of two components of velocity was not available. Each of three velocity components was measured individually.

To upgrade our existing LDV system there is a great need for a second signal processor and a multi channel interface which will make measurements of Reynolds stress available as well.

CRITERION FOR VORTEX BURSTING

Brown and Lopez (1990) proposed that a necessary condition, or criterion for vortex bursting to occur would be that the tangent of the helix angle for the velocity should be greater than that of the helix angle for the vorticity at some station upstream of bursting and this is,

$$\alpha_o = \frac{V_o}{W_o} > \beta_o = \frac{\eta_o}{\zeta_0},$$

where V_o, W_o and η_o, ζ_o are the values of the azimuthal and axial components of both the velocity i.e. V and W and vorticity, η and ζ, at some station upstream of bursting z_o.

RESULTS AND DISCUSSION

The vortex flow pattern observed remains non-bursting below a Reynolds number, Re, of about 800, where Re is based on the radius and tangential velocity at the edge of the rotating cylinder. The vortex twists up steadily with its core diameter remaining about constant (see Fig. 2). With the rotation rate of the cylinder gradually increased, at a Reynolds number of about 900, the vortex core underwent an abrupt bursting - widening of the vortex core (see Fig. 3). The radial distributions of all the velocities measured were plotted against the radial distance r from the centre of the rotating cylinder. The radius of the vortex core is defined by the location at which the azimuthal velocity V is a maximum. At Re = 900 the radial distributions of azimuthal velocity V, axial velocity W and radial velocity U measured are shown in Fig. 4, 5 and 6 respectively. The symbols represent the various measurements taken at different heights above the floor. It is clear from Fig. 4, that the vortex core suffers a sudden expansion as it moves away from the floor. It has all the appearance of a vortex burst . The variation of vortex core radii with the distance away from the floor was depicted in Fig. 4. From Fig. 4 at upstream station $z_o = 55\text{mm}$ from the floor, the radius of the vortex core r_o is 6 mm. At $r = r_o$ the azimuthal velocity V and the axial velocity W measured were $V_o = 66\,{}^{\text{mm}}/_{\text{s}}$ and $W_o = 28\,{}^{\text{mm}}/_{\text{s}}$ respectively. The tangent of the helix angle for the velocity at $r = r_o$ was $\alpha_o = \frac{V_o}{W_o} = 2.3$. The azimuthal and axial components of vorticity η and ζ have the forms

$$\eta = \frac{\partial U}{\partial z} - \frac{\partial W}{\partial r} \quad \text{and} \quad \zeta = \frac{\partial V}{\partial r} - \frac{1}{r}\frac{\partial U}{\partial \varnothing}$$

For reasons of axial symmetry the derivative with respect to $\varnothing$ may be dropped so that the ζ simply has the form $\zeta = \frac{\partial V}{\partial r}$. The variations of the radial velocities at the edge of the vortex core with the distance away from the floor, z, are shown in Fig. 7. At $r = r_o$ the value of the azimuthal and axial components of vorticity η_o and ζ_o were estimated based on the derivatives taken from the curves at $z = z_o, r = r_o$ in Fig. 7, Fig. 5 and Fig. 4 respectively. The tangent of the helix angle for the vorticity at $r = r_o$ obtained was $\beta_o = \frac{\eta_o}{\zeta} = 1.7$. Therefore, according to the criteria of Brown and Lopez $\alpha_o(2.3) > \beta_o(1.7)$, vortex bursting is predicted at Re=900.

At Re=800 the radial distributions of azimuthal velocity V, axial velocity W and radial velocity U measured are shown in Fig. 8, 9 and 10 respectively. There is no variation of vortex core radii with the distance away from the floor. Using the same procedure applied to the case of Re=800 the criterion for vortex bursting turned out to be $\alpha_o(1.54) < \beta_o(2.2)$ and the vortex should not burst which was observed.

For the lower Re case (non-bursting) the axial velocity decreases on the axis from 39 mm/s at z_o = 55 mm to 30 mm/s at z_o = 105 mm. However after bursting the axial velocity decreases from 67 mm/s at z_o = 55 mm to 33 mm/s at z_o = 105 mm. No reversal was found.

REFERENCES

Brown, G.L. and Lopez J.M. 1990. Axisymmetric vortex breakdown Part 2. Physical mechanisms. J. Fluid Mech. 221, 553 - 576.

Lugt, H.J. 1989. Vortex Breakdown in Atmospheric columnar vortices. Bul Am. Met. Soc. 70, No. 12, 1526 - 1537.

Peckham, D.H. and Atkinson, S. 1957. Preliminary results of low speed wind tunnel tests on a gothic wing of aspect ratio 1.0 Aero. Res. Counc. CP - 508.

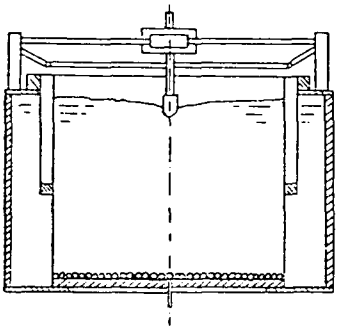

Figure 1. Rotating water tank

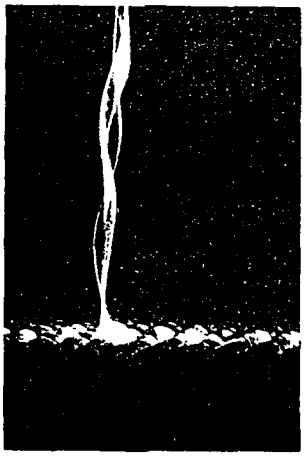

Figure 2. Non-bursting vortex

Figure 3. Bursting vortex

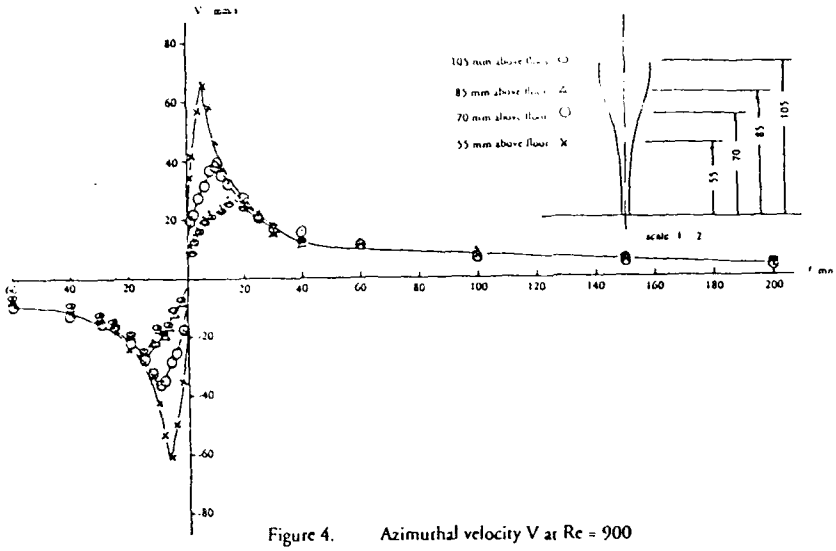

Figure 4. Azimuthal velocity V at Re = 900

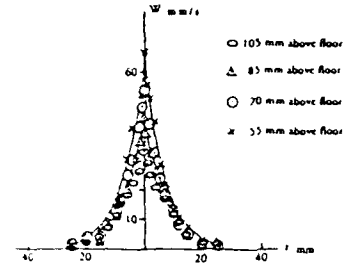

Figure 5. Axial velocity W at Re = 900

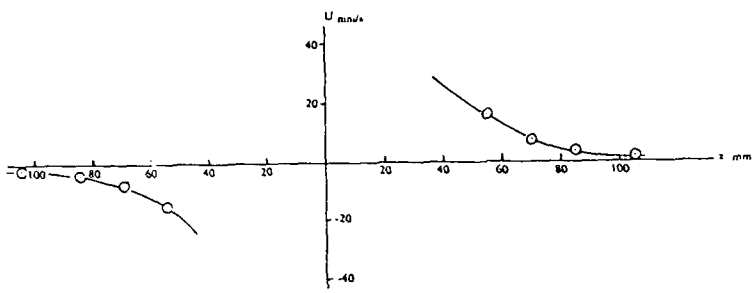

Figure 7. Radial velocioty U versus z at r = r_o, Re = 900

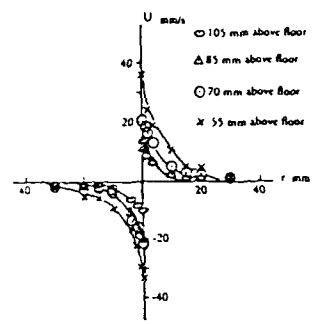

Figure 6. Radial velocity U at Re = 900

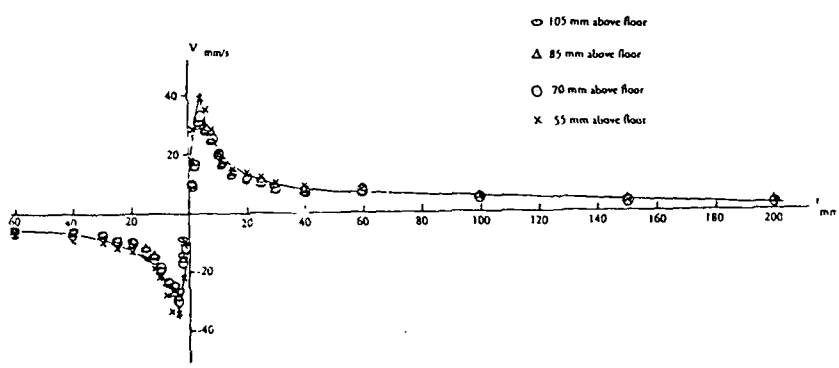

Figure 8. Azimuthal velocity V at Re = 800

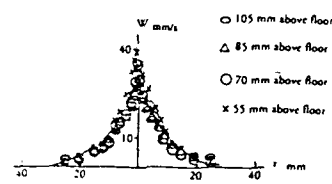

Figure 9. Axial velocity W at Re = 800

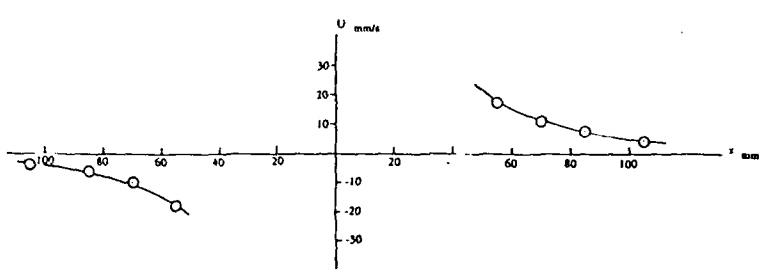

Figure 11. Radial velocity U versus z at r = r_o, Re = 800

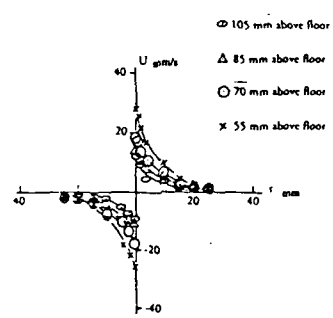

Figure 10. Radial velocity U at Re = 800

Quantitative Imaging of OH and Temperature Using a Single Laser Source and Single Intensified Camera

J.B. Kelman and A.R. Masri

Department of Mechanical Engineering
University of Sydney, NSW 2006, Australia

ABSTRACT

A method of obtaining quantitative images of OH number density using simultaneous images of Rayleigh scattering and OH LIF is presented. The technique uses a single Nd:YAG pumped dye laser and single intensified CCD camera. The Rayleigh scattering, the OH LIF and beam intensities are collected on the one camera.
Laminar flamelet calculations of similar fuels to the measured flames are used to estimate the effect of molecular quenching and ground state population variation. The images of temperature are used to correct the OH LIF signal.

1. INTRODUCTION.

Planar Laser-Induced Fluorescence (LIF) is one of the most widely used techniques to study reactive scalars and turbulence scales in turbulent diffusion flames. Imaging of fluorescence from the hydroxyl radical however, has been limited to qualitative results only, due to the marked effects of temperature on molecular quenching and ground state population. Approximate corrections for OH fluorescence can be generated as a function of temperature alone.
The aim of this paper is to present a procedure for joint quantitative imaging of temperature and the concentration of the hydroxyl radical, OH in turbulent diffusion flames. Temperature is obtained from Rayleigh scattering. Laser induced fluorescence is used to measure OH number density. Using laminar flame calculations over a series of stretch rates, calibration factors for OH are generated as functions of temperature to account for quenching and ground state population effects.

2. EXPERIMENTAL

2.1 BURNERS

A piloted diffusion flame of 31% Compressed Natural Gas (CNG)-69% hydrogen (by vol.) is used for the to demonstrate the method for this paper. This fuel mixture is designed to produce a Rayleigh cross section equal to that of air across the full mixture fraction range Dibble *et al* (1980).
Two other burners are used for calibration and verification. A 75 mm premixed flat-flame burner is used with a stoichiometric CH_4-air flame for calibration of the OH-LIF. A laminar diffusion flame burner, 15mm in diameter is also used to verify the technique by comparing measured and calculated values of OH.

2.2 OPTICAL

An Nd:YAG pumped dye laser (Spectra-Physics PDL3) operating at 562.2 nm and frequency doubled to 281.1 nm is used to excite the $R_1(6)$ (1,0) transition of the OH molecule Dieke *et al* (1962). Fluorescence from the OH (1,1) is collected broad band using a 10 nm bandwidth interference filter at 314 nm. The imaged area in the flame is 6 mm x 26 mm, with a resolution of 0.2 mm. Temporal resolution is ensured by the 8 nanosecond laser pulse and 500ns intensifier gating. A schematic of the optical layout is shown in Fig 1.

The beam profiles, Rayleigh image and the OH-LIF image are all collected on the same intensified camera. The Rayleigh scattering is collected with an 85mm camera lens, while the OH-LIF is collected with two paired f/6 fused silica lenses. The UV image is accepted

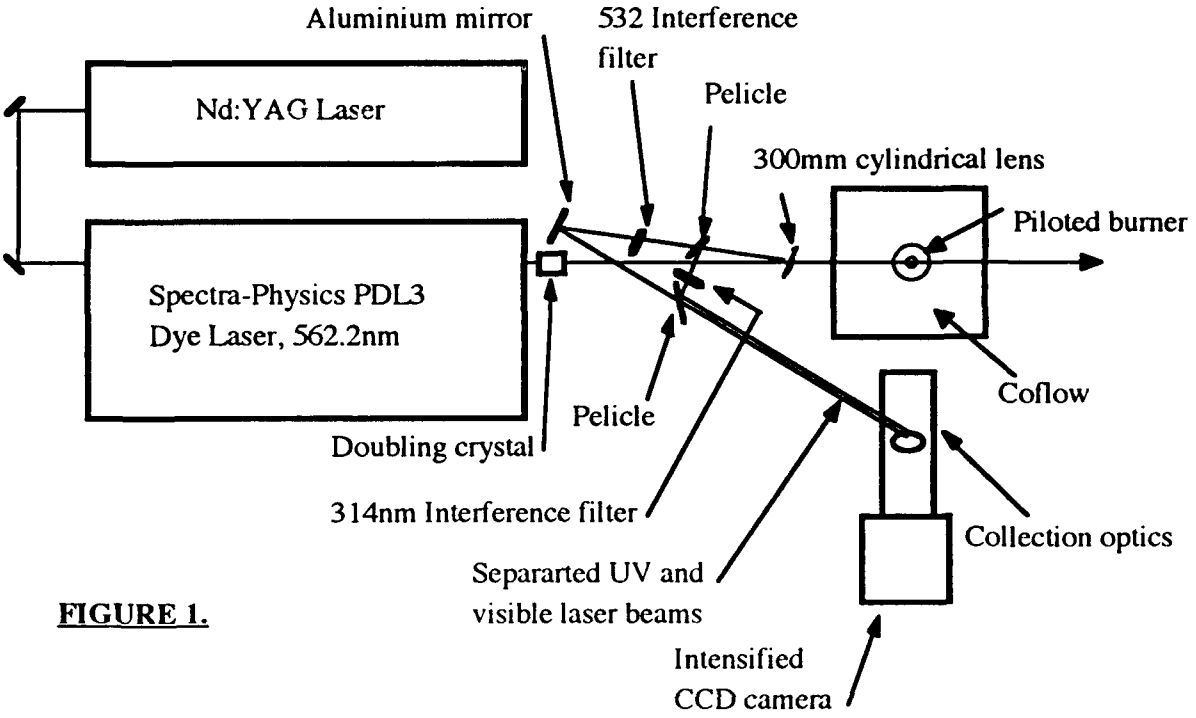

FIGURE 1.

through the interference filter, reflected through the UV dichroic mirror and the aluminium mirror. The beam profiles are directed through the back face of the UV dichroic. Fig 2.

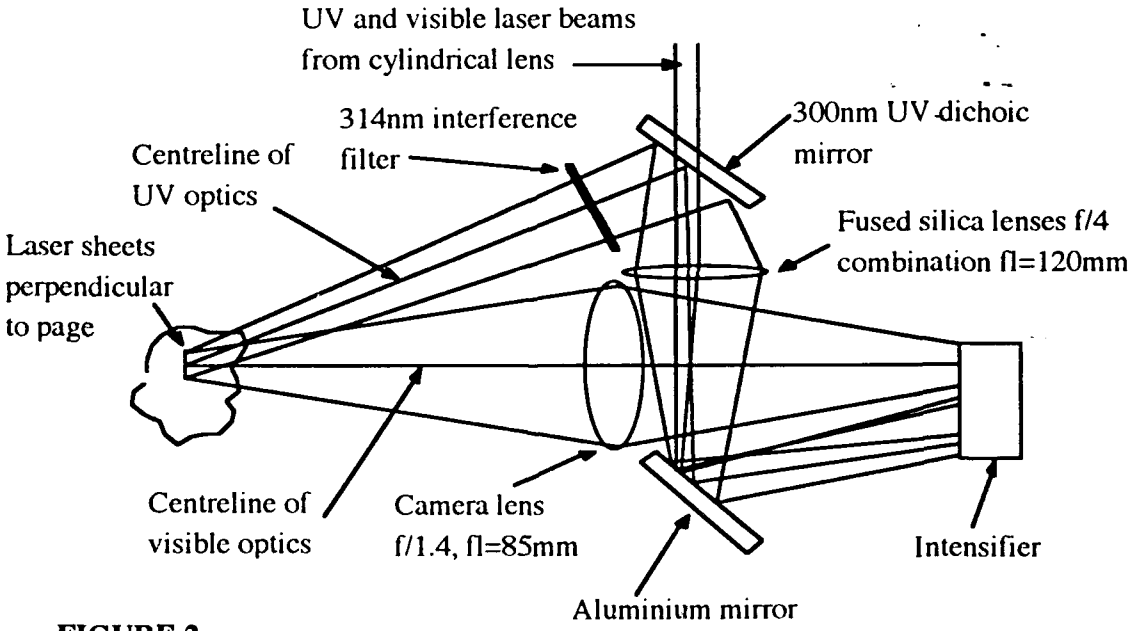

FIGURE 2.

3. CALIBRATION

The Rayleigh signal is calibrated against measurements made in pure air. A stoichiometric CNG-air flat flame is used to generate calibration factors for OH.

3.1 TEMPERATURE

Images of temperature are obtained from the instantaneous Rayleigh image and a calibration image of Rayleigh in air as follows:

$$T = T_a(R_a/R_f) \qquad (1)$$

where T is the measured temperature, T_a is the ambient air temperature, R_a and R_f are the Rayleigh scattered signals from air and the flame respectively.

3.2 OH-LIF

The number density of the hydroxyl radical, [OH] is given by:

$$[OH] = k.C_qC_g.(\text{fluorescence/laser energy}) \qquad (2)$$

where k is the constant to account for collection efficiency and optical throughput, C_q is the quenching correction and is the ratio of the quenching rate in the calculated flame relative to that in the reference flame and C_g is the ratio of the ground state population in the reference flame to that in the calculated flame. The constant k is determined from the calibration flame. Computations of laminar counterflow diffusion flames of similar fuels are used to calculate the combined factor C_qC_g. The combined factor C_qC_g is computed from the calculated structure of the laminar flame of the same fuel as under investigation. The temperature that would be measured in the computed laminar flame, assuming the flame has a Rayleigh cross section equal to that of air, is also calculated. This is called the adjusted temperature T_r:

$$T_r = T_f.(\sigma_f/\sigma_a) \qquad (3)$$

The factor C_qC_g is plotted in Fig. 3 versus T_r for a methane-hydrogen mix. A single curve is drawn representing a temperature dependent calibration C(T) which accounts for both C_q and C_g. This factor is used as follows:

$$[OH] = k.C(T)(\text{fluorescence/ laser energy}) \qquad (4)$$

3.3 VALIDATION

This technique is validated by performing measurements in laminar jet diffusion flames of CNG-air (1 to 3 by vol.) and pure hydrogen. These levels are compared to those of the laminar flamelet data. Both temperature and OH number density are in good agreement.

4. IMAGE PROCESSING AND RESULTS

4.1 TEMPERATURE

Images of temperature are obtained from the Rayleigh image as in Equation (1). The Rayleigh image in air may be obtained by two methods: (i) averaging several images of Rayleigh measured directly in air or, (ii) artificially creating a full image from pure air measured on the side of the flame image.

4.1.1 Error Estimates

Both methods of processing described above assume a constant Rayleigh cross section. Errors in the temperature measurements due to this assumption are estimated from the laminar flamelet computations. A signal to noise ratio of about 16 is achieved after processing. In t.. CNG-hydrogen there is a divergence of 13 percent from the true temperature just on the rich side of stoichiometric.

4.2 OH

The simultaneous Rayleigh image is critical to the quantitative measurement of OH. The curves of C_qC_g are plotted and the calibration factor C(T) generated for the investigated fuel. The factor C(T) is determined at each pixel using the measured temperature. The absolute number density of OH is given by Equation. 4.

4.2.1 Error Estimates

Errors introduced on the OH measurements due to the use of C(T) instead of C_qC_g are estimated from the laminar flame computations. The number density of OH, $[OH]_c$, that would be obtained from a laminar flame if C(T) was used instead of C_qC_g is given by:

$$[OH]_c = [OH]_{lf}.(C(T)/C_qC_g) \qquad (5)$$

where $[OH]_{lf}$ is the true number density of OH computed for the laminar flame. The error introduced on [OH] due to the usage of C(T) is given by the difference:

$$\Delta[OH] = [OH]_{lf}-[OH]_c = [OH]_{lf}.(1-(C(T)/C_qC_g)) \qquad (6)$$

Figure 4 shows plots of $\Delta[OH]/[OH]_{max}$ versus mixture fraction, where $[OH]_{max}$ is the maximum calculated OH number density. The CNG-hydrogen mix has an error of less than 14 percent. This error is additional to the shot noise. The CNG-hydrogen mixture has a maximum error on [OH] of around 25 percent after shot noise is included.

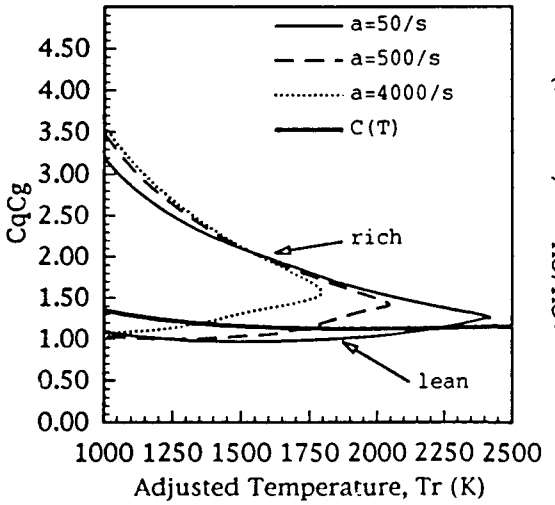

Figure 3. Flourescence quenching and population correction factor for OH versus adjusted temperature for a range of stretch rates in a laminar CNG-hydrogen flame.

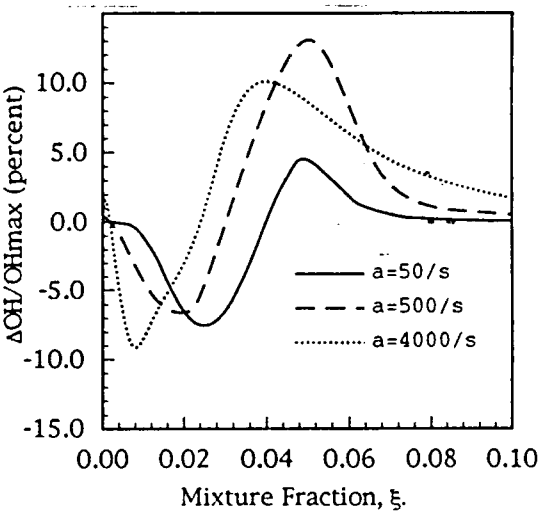

Figure 4. Estimated error on the [OH] due to the use of C(T) instead of CqCg for a range of stretch rates in a laminar CNG-hydrogen laminar flame.

4.3 IMAGES

A raw image demonstating the position of the Rayleigh, OH-LIF and beam intensities on the camera is presented in Figure 5. Simultaneous, quantitative images of temperature and OH number density are presented in Figure 6 for CNG-hydrogen flames

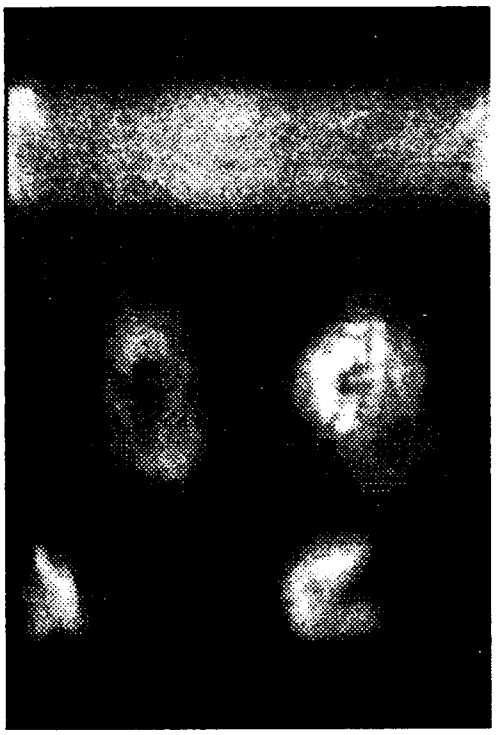

Figure 5. Raw Image showing Rayleigh scattering (top), beam intensities (centre, UV to left, visible to right) and OH LIF (bottom).

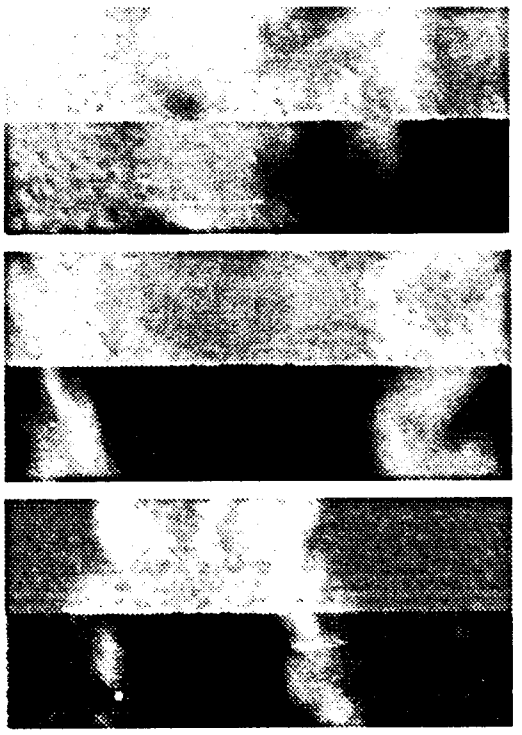

Figure 6. Processed images in a CNG hydrogen flame at XD=30, 15, 7 velocities (top to bottom).

5. SUMMARY

We have presented an experimental and calibration procedure to obtain joint quantitative images of OH number density and temperature in flames. The technique is validated by comparing measurements and computations in laminar diffusion flames. The experiment only requires a single laser source and one intensified CCD camera to collect the two images and the laser beam intensities. Calibration of the temperature is done using the surrounding air as the reference for the Rayleigh signal. Quantitative results are obtained for temperature based on the assumption of a constant Rayleigh cross section in the measurement domain. Correction of the OH LIF signal is done using laminar flame computations over a series of stretch rates to obtain a single, temperature dependant calibration factor for each mixture. The maximum errors associated with the temperature and OH number density are less than 15 and 25 percent respectively for CNG hydrogen.

REFERENCES

Dibble, R.W. and Hollenbach, R.E. (1980) "Laser Rayleigh Thermometry in Turbulent Flames," *Eighteenth Symposium (International) on Combustion*, The Combustion Institute, 1489-1499.

Dieke, G.H. and Crosswhite, H.M. (1962) "The Ultraviolet Bands Of OH: Fundamental Data," J. Quant. Spectrosc. Radiat. Transfer, **2**, 97-199.

Garland, N.L. and Crosley, D.R. (1986) "On The Collisional Quenching of Electronically Excited OH, NH and CH in Flames," *Twenty First Symposium (International) on Combustion*, The Combustion Institute, 1693-1702.

LASER DOPPLER MEASUREMENTS INSIDE AN ARTIFICIAL HEART VALVE

Christine M. Larson, Yos S. Morsi

Swinburne University of Technology
Modelling and Diagnostics Group
John Street, Hawthorn
Victoria

Presented at the Workshop on Laser Diagnostics in Fluid Mechanics and Combustion. 30 Sept. - 1 Oct. 1993.

Summary

A simple steady flow experiment was conducted to examine the fluid flow phenomena through a prototype jelly fish valve. A two component LDA system was used to determine the velocity and turbulence parameters of the inlet flow as well as the flow downstream of the valve. The velocity profiles and turbulence shear stress parameters are presented and it was found that the valve produces a low value of shear stress.

Nomenclature

U	mean velocity along x axis
V	mean velocity along the y axis
u,v	local instantaneous velocity components
uv	mean of the multiplication of u and v
u',v'	fluctuations about the local u and v components of velocity
σ_u	standard deviation of the u component
x	transverse direction along streamwise flow
y	vertical direction normal to the xz-plane
z	transverse direction normal to x
τ_R	Reynolds Shear Stress
T	coincident time window
K	number of samples in a record

Introduction

One of the key areas in artificial heart research is the design and construction of suitable valves. Mechanical valves have been traditionally used in conjunction with artificial hearts. However, they have exhibited the problems of ring thrombus due to uneven interface between the valve and the pump device, leakage due to inertial properties , and mechanical failure due to water hammer effect.

Although, it has been widely recognised that understanding the fluid dynamics of these devices is critical, only recently researchers, primarily due to recent developments of LDA (Laser Doppler Anemometery) were able to investigate the fluid flow phenomena of these devices. As a result a number of design concepts are now being examined by many researchers world wide. It is now well recognised by most workers in the field that the threshold level of Reynolds stress for hemolyis in a free jet is 400 N/ m^2 and was reported by Sallam and Hwang in 1984.

In ensuring the performance of mechanical valves, Yoganathan et al. (1979) measured velocity profiles for the Bjork Shiley aortic prosthetic valve. Later in 1981, the same group measured in a caged-ball valve and reported maximum aortic wall shear stress of 160 N/m^2 downstream from the valve ring. Tillman et al. (1984), using flush mounted shear stress probes, examined three different types of mechanical valves and found a peak value of 120-140 N/m^2 at the large orifice of a Bjork Shiley valve, 12-15 N/m^2 at the large orifice of a Lillehei-Kaster valve and 85 N/m^2 at the valve ring of Starr-Edwards valve. Einav et al (1988a) evaluated a polymeric tri-leaflet valve for the shear stress distribution along the cusps and in 1990 Einav evaluated the fluid flow inside the valve structure and reported maximum shear stress values of 170 N/m^2.

In this study a new type of valve known as a jellyfish valve which was developed by Professor Imachi at the University of Tokyo is being examined by the Swinburne Modelling and Diagnostics Group. It is believed that this valve has low cost and is unique in design because it incorporates a thin polymer membrane supported by a rigid frame providing both a responsive and strong structure, furthermore, the diaphragm has a much lower moment of inertia than the traditional mechanical valve resulting in relatively lower regurgitation flow.

Experimental Setup

The results presented in this paper are part of a study investigating the steady and pulsatile flow through a series of artificial heart valves and VAD devices. Here only the jelly fish valve under steady flow conditions was examined. A flow rate of 16 l/min. was used to approximately simulate the average blood flow rate at peak systolic pressure of the human cardiac cycle. This condition is normally used to quantify the maximum flow parameters. A diagram of the flow setup is shown in figure 1.

In most valve studies only one downstream location is examined, here we investigated one upstream location and six downstream locations providing a more complete picture of the structure and subsequent development of the flow.

The LDA system used in this investigation is shown in figure 2. As shown, the system consisted of a two colour four beam optical arrangement utilising the green (514.5 nm) and blue (488 nm) lines of a 5 watt Spectra Physics 2020 Argon-Ion Laser. A two-component fibre-optic probe was incorporated into the system for easy access to the flow, with two Bragg cells to measure flow reversals. The fibre optic probe lens had a beam separation of 15 mm and a focal length of 105 mm, provided two overlapping, orthogonal ellipsoid shaped measurement volumes with approximate diameters of 142.6 microns and lengths of 2.10 mm. TSI 1980B counter signal processors along with a MI990 interface and FIND software were used for data collection and analysis.

LDA Considerations

In setting up the diagnostic technique used, a number of issues were addressed.

Frequency Shift -Two components of frequency shift were considered necessary in evaluating this flow because flow reversals were expected in both directions. Frequency shift also provided the benefits of dynamic range equalisation, fringe bias reduction and boundary detection. This made it easier to detect simultaneous u and v components, ensured that more measurements were made regardless of trajectory angle and provided a reliable boundary detection method using the real-time histogram output.

Measurement Volume - The measurement volume is normally calculated by the focal length and beam spacing of the focussing lens and was around 2.10 mm. This limited the access to the boundary layer flow near the concave wall, caused a uncertainty in spatial location equal to its length, and may have caused a broadening of the data histogram leading to a false turbulence component due to possible velocity gradients along the measurement volume.

The concave shape of the test tube (diameter 20 mm) acts as a lens to the incident laser beams. To overcome this curvature effect, a special designed glass box (n = 1.4) was fitted around the glass tube and filled with water (n = 1.33). This reduced the index of refraction difference between the curved surface and the incident beams and improved access to the boundary with subsequent improvement to the SNR (signal to noise ratio).

Seeding - Seeding is always an important consideration in using the LDA technique. Often in water flow experiments the natural seed particles in water may suffice. However, it was found necessary to introduce special seed particles to the flow. For this experiment metallic coated sphere were used because of their high reflectance portion of the their index of refraction. This is an important parameter because reflectance is the major component of backscatter light collection. The drawback, however, is that they are not neutrally buoyant which meant that we had to ensure particle settling did not happen to any significant extent.

Data Analysis

Due to the random, discrete nature of LDA measurements, true time based statistics are not provided by commercially available signal processors and software programs. In contrast to HWA, (where data is evenly sampled over a set period of time) the LDA data arrival is random and the set record length is based on a preset number of samples. This means a ensemble average of particle velocities is calculated to determine the mean velocity at a certain point. To overcome this problem the flow in all LDA experiments is considered stationary, where the ensemble average, corrected for velocity bias, is considered to be equal to the time average.

Using the above concept the commercial data analysis flow package FIND defines the mean, RMS, turbulence intensity and Reynolds shear stress as follows.

$$U = \sum_{i=1}^{K} u / K \qquad (1)$$

$$\sigma u = \left[\sum_{i=I}^{K} u^2 / K - U_2 \right]^{1/2} \qquad (2)$$

$$\text{Turbulence \%} = \sigma u * 100 / U \qquad (3)$$

$$\tau_R = \overline{uv} - U*V \qquad (4)$$

Results and Discussion

A diagram of the test section and the notation used in this study is shown in figure 3. Using the above described system two velocity components (u and v) were measured in the x and y directions. Measurements were made in cross sectional slices 10 mm upstream and 5, 10, 12, 15, 20, 30, and 40 mm downstream of the valve. We were able to make anywhere from 15-18 measurements in 1 mm increments across the diameter of the glass tube.

A plot of the inlet streamwise, mean velocity and turbulence intensity at 10 mm upstream of the valve is shown in figure 4. Mean velocity plots of the corresponding cross sectional flow

downstream of the the valve are shown in figure 5. The plots reveal flow reversals strongly at 5 mm downstream which gradually decay along the tube and are totally dissipated at 40 mm. The contour plot in figure 6 indicates a region of re-circulation flow around the hub of the valve and suggests jetting in the vicinity of the walls.

Reynolds shear stress values were calculated using equation 4 at the z axis coordinates of 7-10 mm and the x axis coordinates of 10, 12, 15, 20, and 30 mm respectively downstream of the valve as shown in figure 7. For each point 3072 random measurements of the instantaneous u an v velocity components were made. Since the u component was in the dominant flow direction the majority of the 3072 measurements were for the u component. The corresponding time between data for each measurement was recorded as well. A coincident time widow T was selected based on the average particle transit time . This coincident time T was used as the criteria to match pairs of u and v measurements and yielded between 50-150 measurements per spatial point. The results of the calculated Reynolds shear stress are given in Table 1.

Conclusion

The LDA technique has been used to determine the fluid flow and turbulence parameters inside an artificial heart valve. It was found that magnitude of shear stresses were on the order of 5-30 N/m^2 which is considered to be too low compared with published data. However, in order to base this conclusion on firm footing further study is called for.

Acknowledgement

We thank Professor Umezu of Waseda University and Professor Imachi of The University of Tokyo for providing guidance and support during the initial stages of the project.

References

Einav, S., Stolero, D., Avidor, J.M., Elad, D. and Talbot, L., "In Vitro LDA Measurements of the Velocity Field in the Core of Tri-Leaflet Prosthetic Valves", Laser Anem.-Proc. 3rd Int. Conf., L.A., CA USA 1990, pp.523-532.

Einav, S., Stolero, D., Avidor, J.M., Elad, D. and Talbot, L., "LDA Evlauation of Wall Shear Stress Distribution Alongthe Cusp of a Tri-Leaflet Prosthetic Heart Valve", Proc. 4th Int. Symp. on Appl. of Laser Anem. to Fluid Mech., Lisbon Portugal, 1988a, pp. 7.21.1-3.

Sallam, A.M. and Hwang, N.H.C., " Human Red Blood Cell Hemolysis in Turbulent Shear Flow: Contribution of Reynolds Shear Stress", Biorheology, 21 , 1984, p. 783.

Yoganathan, A.P., Reamer, H.M., Harrison, E.C., Shulman, I.A., and Parnassus, W., "The Starr-Edwards Aortic Ball Valve: Flow Characteristics, Thrombus Formation and Tissue Overgrowth," Artificial Organs, Vol. 5, 1981, pp. 6-17.

Yoganathan A.P., Corcpran, W.H., Harrsion, E.C., and Car, J.R., "In Vitro Velocity Measurements in the Near Vicinity of the Bjork-Shiley Aortic Prosthesis Using LDA," Med. & Biol. Eng. & Comp., Vol. 17, 1979, pp.453-459.

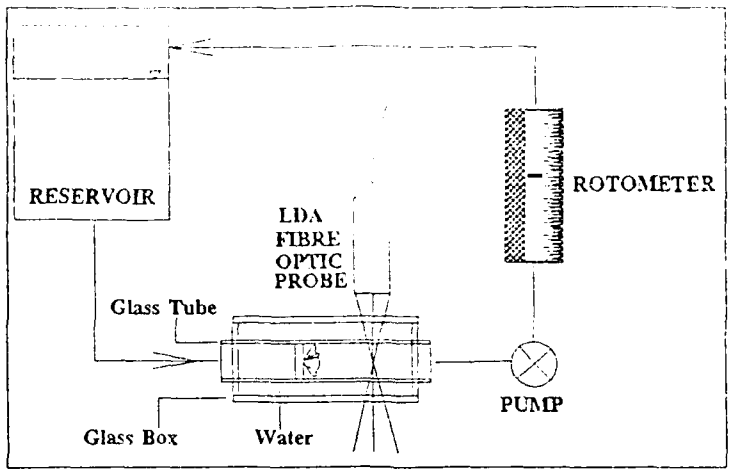

Figure 1

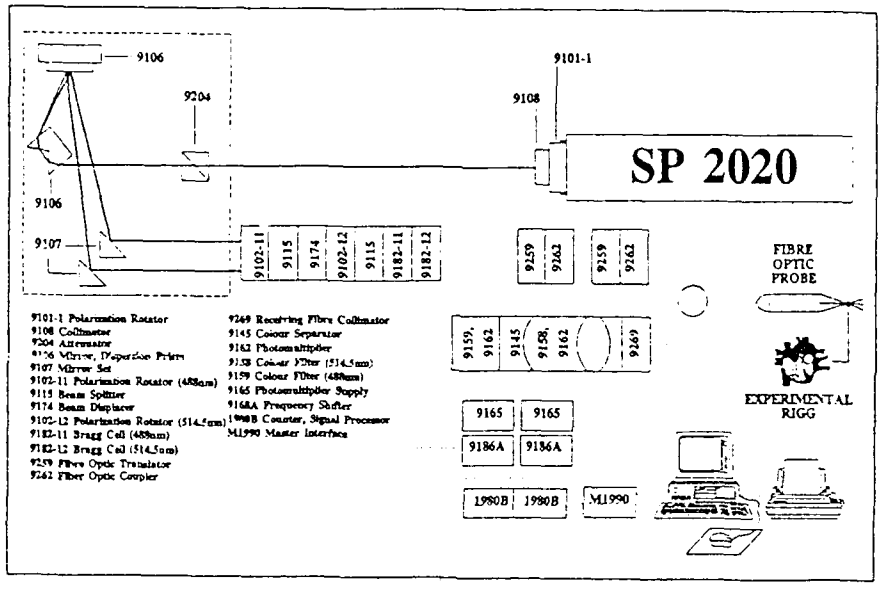

Figure 2

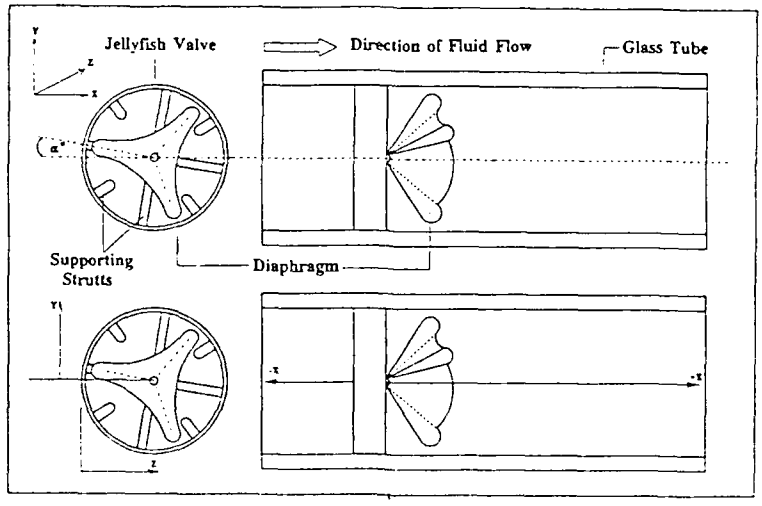

Figure 3

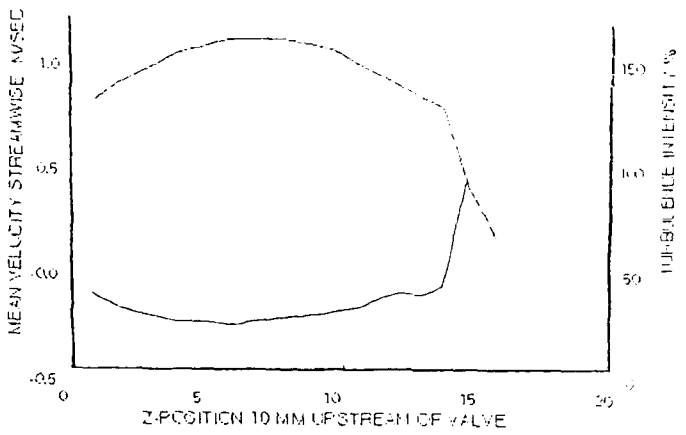

Figure 4

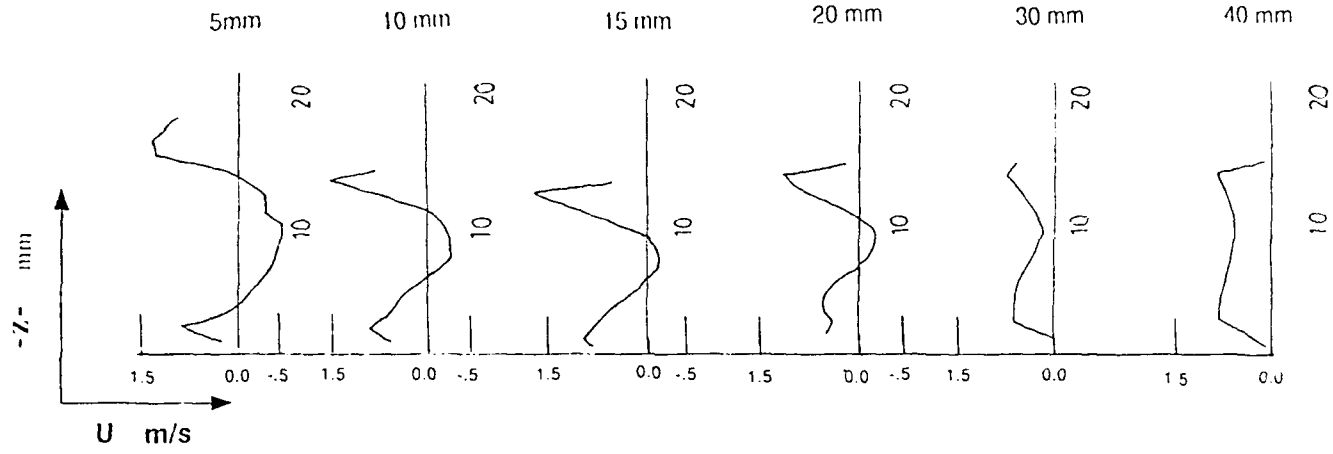

Streamwise Mean Velocity Profiles

Figure 5

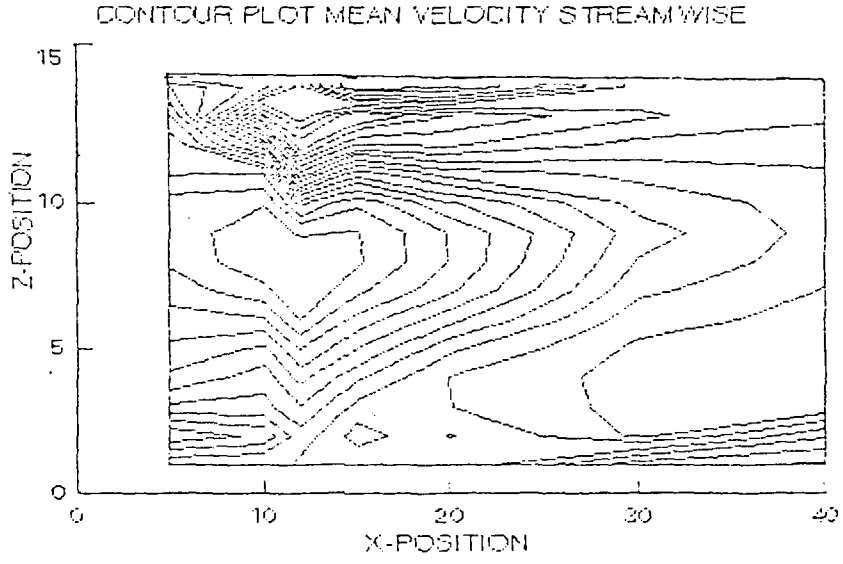

Figure 6

Reynolds Shear Stress Calculations

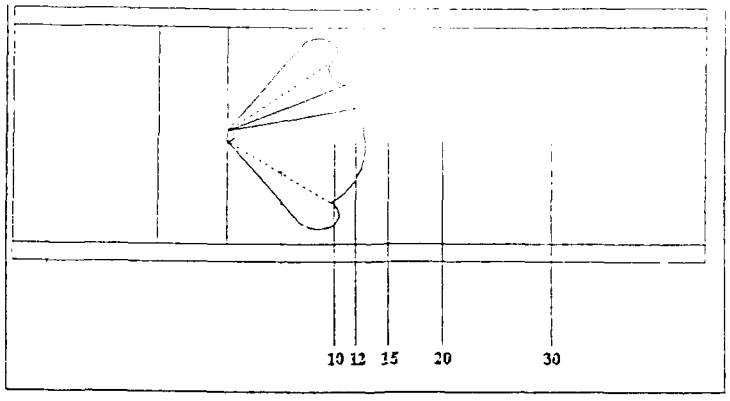

Figure 7

Reynolds Shear Stress Values

Position (mm)			$U'U'$ (m^2/sec^2)	$\rho\, U'U'$ (N/m^2)
X	Y	Z		
10	0	9	.009677	9.677
10	0	10	.00542	5.42
10	0	11	.024782	28.4782
10	0	12	.00297	2.97
12	0	9	.02832	28.32
12	0	10	.025122	25.122
12	0	11	.023665	23.665
12	0	12		
15	0	9	.012835	12.835
15	0	10	.020662	20.662
15	0	11	.02525	25.25
15	0	12		
20	0	9	.01838	18.38
20	0	10	.0118	11.80
20	0	11	.01675	16.75
20	0	12	.00151	1.51
30	0	9	.009	9.00
30	0	10	.00372	3.72
30	0	11	.012229	12.29
30	0	12	.01096	10.96

Table 1

Detection of Nitrogen Dioxide Using LIF and DFWM: Effect of Buffer Gas

Berenice Mann and Flyn White

CSIRO, Div of Building, Construction and Engineering, PO Box 56, Highett, Vic 3190.

ABSTRACT

The techniques of Degenerate Four-Wave Mixing and Laser-Induced Fluorescence have been applied to the molecule NO_2 in a static cell. The behaviour of both types of signal have been compared using a fixed quantity of NO_2 and varying the amount of nitrogen buffer gas.

INTRODUCTION

The general aim of this work has been to use laser spectroscopic techniques to detect minor species concentrations and temperatures in combustion environments. In particular there is interest in detection of pollutants such as NO_x and we have concentrated on NO_2, which has previously been difficult to detect *in situ*.

Previous techniques for detecting NO_2 have generally involved physical probes, which are both intrusive and inaccurate, giving widely varying results (Reuther *et al* 1988). Laser techniques such as Laser Induced Fluorescence (LIF) also have problems associated with detection of NO_2 since there is severe quenching even at moderate pressures (atmospheric pressure) causing loss of LIF signal. Some imaging work has been done at low pressures, seeding NO_2 (700ppm) into a combustion torch ignition chamber to trace the progress of flame propagation, (Cattolica, 1987).

In previous work the technique of Degenerate Four-Wave Mixing (DFWM) has been applied to detection of NO_2, (Mann *et al,* 1992). This technique overcomes some of the problems of quenching experienced with LIF, and, like LIF can be extended to a two-dimensional imaging format. In addition it has the advantage of producing a signal in the form of a coherent beam and therefore enables remote detection. Previous results have indicated that this will be a useful technique for combustion diagnostics in general, and NO_2 in particular.

In this paper we extend the previous work to compare the effect of buffer gas on both DFWM and LIF signals in NO_2 in a static cell.

DFWM TECHNIQUE

DFWM is a third order non-linear technique, used primarily as a source of phase conjugation, (see Fisher 1983). A typical beam geometry is shown in Fig 1. It is also an excellent spectroscopic technique, producing high resolution sub-Döppler spectra. The three input beams and the output phase conjugate signal are all at the same wavelength, hence the term "degenerate". The probe beam may be at any convenient angle since phase-matching is automatic, hence the technique is suitable where optical access is limited. There is no need for a 90° window as is required in LIF.

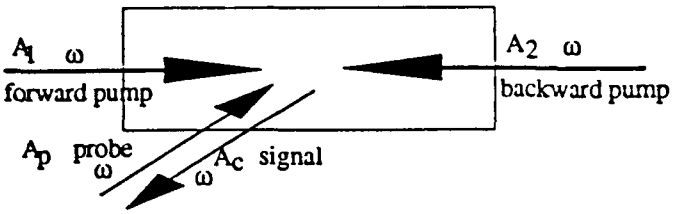

Fig 1. Typical beam geometry for DFWM

LIF TECHNIQUE

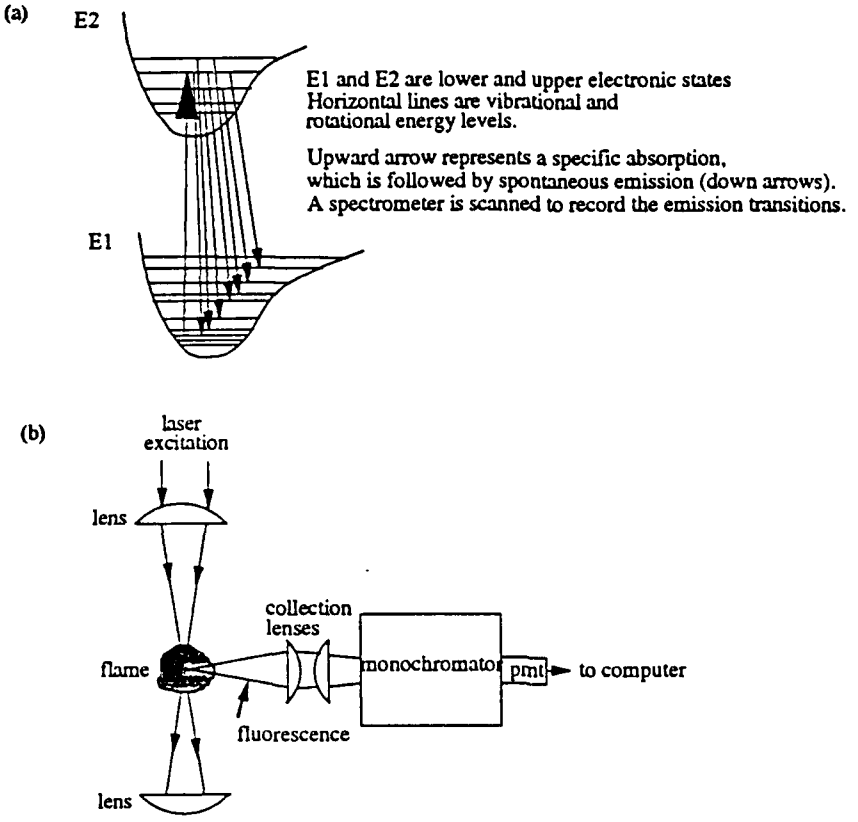

Fig 2. a) LIF Spectroscopy, b) Schematic of LIF Experiment

The LIF technique involves the resonant laser excitation of a molecular transition followed by fluorescent decay (Figure 2a). Figure 2b shows a typical experimental set-up, in which the detection is at 90° to the laser excitation. Inherent problems with this technique are the occurrence of Rayleigh or Mie scattering at the resonant wavelength and the quantification of results, which requires a detailed knowledge of quenching rates and other spectroscopic terms. The problem of scatter can be eliminated by detecting off-resonance, but quantification requires a number of approximations and assumptions to be made. LIF has become a more common diagnostic in recent years due to simplicity of experimental set-up, detectibility of minor species and it's more recent extension to a two-dimensional imaging format.

EXPERIMENTS

A DFWM experiment was set up using the format shown below. A fused silica cell was used with a window at each end and one on the side to allow LIF detection. This cell was connected to a vacuum pump, pressure gauges and gas inlet manifold. The laser used was a Questek excimer using XeCl. This was used to pump a dye laser using Coumarin 460 dye in methanol giving a tunable range of 450-480 nm. The DFWM signal was redirected with a beam-splitter and detected using an amplified photodiode situated a few metres from the experiment. Additional DFWM detection was performed using a gated (5ns) dual micro-channel image-intensified CID camera (ITT F4573/11123) for comparison of signal strength and detectibility with the LIF signals. The LIF experiments were performed by blocking the DFWM probe beam and detecting the signal at 90° to the beam using the same CID camera and 2 collection lenses.

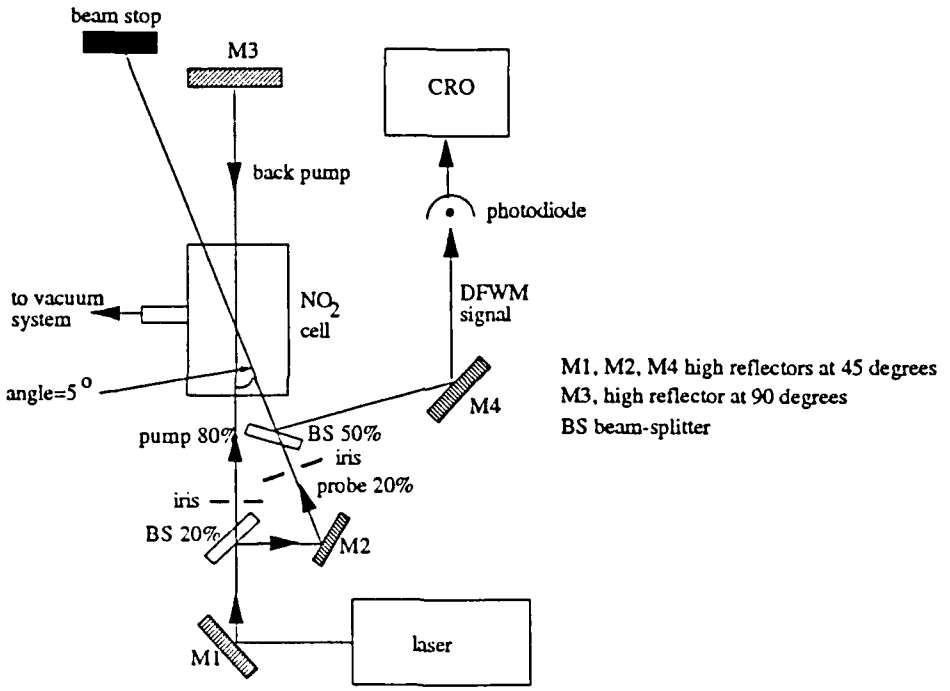

Fig 3. Schematic of DFWM Experiment

Essentially the experiments were to investigate the effect of buffer gas (air and nitrogen) on the signal intensity of both DFWM and LIF in NO_2. Previous experiments with NO_2 had shown that the DFWM signal in NO_2 increased considerably with the addition of buffer gas up to atmospheric pressure. This contrasts with the decrease in LIF signal usually associated with the addition of buffer gas or measurements at atmospheric pressure. The increase in DFWM signal is a combination of pressure broadening, which enables more spectral lines to be incorporated into the laser linewidth, and the formation of thermal gratings which may well be the dominant process in this case.

For both techniques the cell was initially filled with pure NO_2, to a pressure of 7.6 Torr. Then the buffer gas was added in gradual steps and a measurement or image was recorded for each

pressure. The buffer gas used was nitrogen. Previous DFWM buffer gas dependences have been carried out with nitrogen and air for comparison (Mann, 1991). Further LIF experiments were then performed using air as buffer gas to see if the presence of oxygen made any difference to the behaviour of NO_2 fluorescence.

RESULTS AND DISCUSSION

A graph of DFWM signal versus total gas pressure is shown in figure 4a. A similar graph for LIF is shown in figure 4b. The LIF results are the result of averaging of the pixel intensities on the CID camera in a defined region around the line. Two LIF images are also shown (Fig 5a and b), one of pure NO_2 and one of NO_2 in nitrogen with a total pressure of 760 Torr (standard atmospheric pressure). The LIF signal is considerably weaker (by a factor of 15), and the signal to noise ratio is seriously degraded at higher pressures of buffer gas. Using air as buffer the LIF signal could not be distinguished after a pressure of 250 Torr was added. The LIF results contrast with those of DFWM which can clearly be seen to increase with increasing buffer gas pressure. Images of the DFWM signal using the camera as detector are shown (Fig 5c and d) for pure NO_2 and for NO_2 in nitrogen at atmospheric pressure. The signal to noise ratio is greater than 2000:1 for DFWM in NO_2 in nitrogen at 760 Torr, giving an indication of its usefulness for detection of this molecule in atmospheric pressure conditions. Previous work has shown that it can also be detected in imaging format seeded into a flame (Mann *et al* 1992).

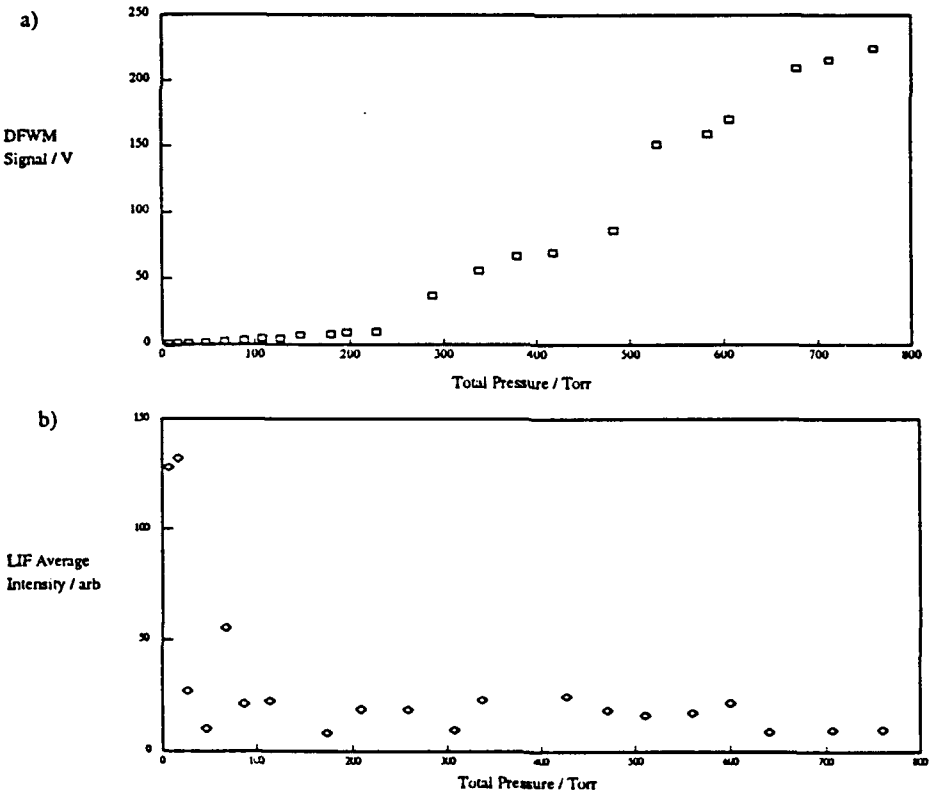

Fig 4. a) Dependence of DFWM Signal in Nitrogen dioxide on Buffer Gas
b) Dependence of LIF Signal in Nitrogen dioxide on Buffer Gas
in each case the same quantity of Nitrogen dioxide was used and
the pressure of buffer gas (nitrogen) was varied.

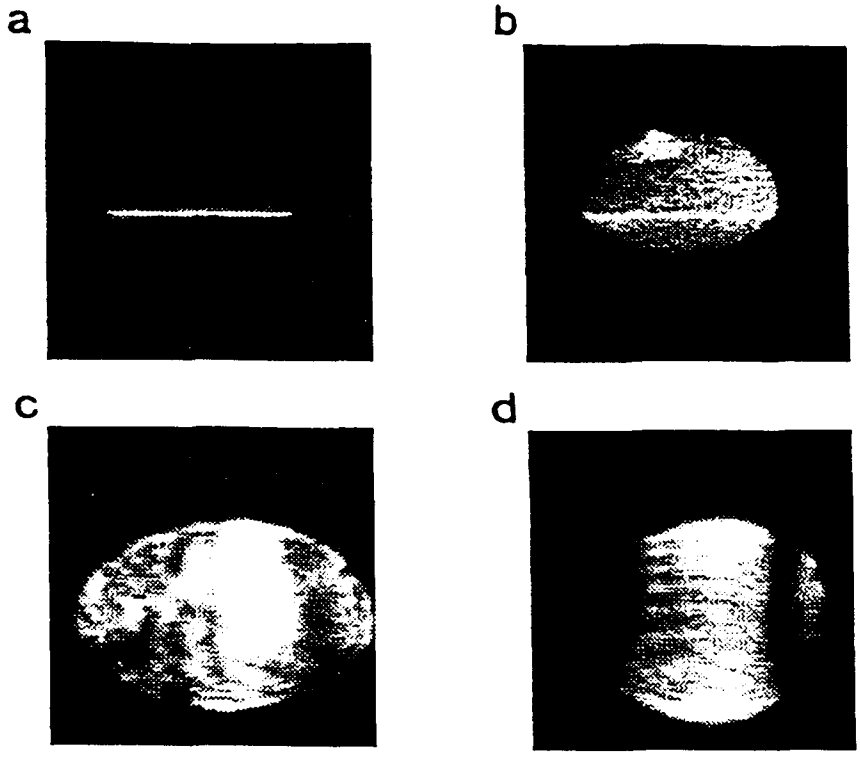

Fig 5. a) Line LIF 7.6 Torr NO_2. Camera gain 4.2. b) Line LIF in 1% NO_2 in nitrogen at 760 Torr. Gain 6.4. c) DFWM in 7.6 Torr NO_2. Gain 4.0,. d) DFWM in 1% NO_2 in nitrogen at 760 Torr Gain 1.4.

CONCLUSIONS

The usefulness of LIF for certain molecules is limited by factors such as quenching, or lack of a fluorescing transition. In this case other techniques have to be adopted, and DFWM is currently being investigated by several groups as a useful alternative for minor species detection. In the particular case of NO_2 it has been demonstrated that LIF is not going to be suitable for detection of minor concentrations in atmospheric pressure situations, particularly in air, due to collisional quenching. However DFWM appears to be a viable alternative, with increased sensitivity at atmospheric pressure.

REFERENCES

Cattolica R.J. (1987) "Visualization of Flame Propagation by Laser-Fluorescence Imaging of Nitrogen Dioxide." *Combust Sci and Tech* **54**, 61-68.

Fisher R.A. (1983) "*Optical Phase Conjugation*" Academic Press.

Mann B.A, SV. O'Leary, A.G. Astill and D.A. Greenhalgh (1992). "Degenerate Four Wave Mixing in Nitrogen Dioxide: Application to Combustion Diagnostics." *Appl. Phys. B.* **54**, 271-277.

Mann B.A. (1991) PhD Thesis "*Novel Coherent Laser Spectroscopic Techniques for Minor Species Combustion Diagnostics.*" Reading University, UK.

Reuther J.J, I.H. Billick and A.J. Gaynor. (1988) "The Measurement of NO_2 from Gas Flames." *Combust and Flame* **71**, 331-335.

Laser Doppler Velocimetry Noise Reduction.

Robert Mierisch
Swinburne University of Technology.

INTRODUCTION.

Laser doppler velocimetry has become a simple quick and effective tool for diagnostic fluid mechanics. Application of the method requires an understanding of the limitations and the common practical problems associated with the method. Many of the methods of extending the operating limits, common problems and their practical solutions are hidden in the detail of the literature. Some of the methods are known to researchers but have never appeared in the literature.

This paper presents a structured approach to the recognition of noise in LDA systems. It details means by which the effects of noise can be reduced. It is intended to be used by newcomers to the field to reduce the confusion which can result from information overload. It is hoped that others will publish further guidelines in general terms to help users to avoid reinventing the wheel. Even quite simple methods can be far from obvious to the newcomer.

EQUIPMENT.

Experience and experimentation has been gained using dual beam backscatter (the most common arrangement) with 5 watt and 2 watt "Spectra-Physics" Argon-ion lasers and a 10 mW Helium Neon laser. Only photomultipliers and counter type processors (TSI 1980B with MI990 multiplexer) have been used. Simultaneous two component frequency shifted systems with and without fibre optic probes have also been used. A 100 MHz three channel analogue oscilloscope, a TSI water atomiser and a laser power meter have been essential for the satisfactory optimisation of signal noise ratio (SNR).

BACKGROUND.

Dual beam laser doppler velocimetry is based on the phase interaction of light from two sources scattered by a particle(s). The light must be coherent and polarised in the plane normal to the plane containing the two beams.

The doppler frequency results from the change in the phase difference of the light reaching the particle from the two sources. The phase difference changes as the particle moves across the region where the beams cross. The beam intersection region is known as the measurement volume. The phase interaction of the light is such that light and dark fringes are apparent in the measurement volume. The light to dark contrast of the apparent fringes influences the signal noise ratio.

The coherence of the light beam which is split to provide the two sources has a large effect on the SNR. Coherence can be defined as the degree of phase matching of the light from a source. The coherence of a source can vary with the position within a beam, the distance from the source and with time. Coherence of Helium-Neon lasers

is much better than the coherence of Argon-ion lasers (Drain (1980)). The use of Fabry-Perot interferometers known as etalons (TSI Flow Data (1989)) can dramatically improve the monochromaticity and hence the coherence of laser light sources. Figure 1 below (from TSI Flow Data 1989) shows the effect of an etalon. Unfortunately their use in two component LDA systems improves the signal noise ratio of only one of the signals and will adversely affect the other. Etalons are available which can be optimised for both the 488 nanometer and 514.5 nanometer beams but the two cannot be simultaneously optimised (Spectra-Physics private communication, 1993).

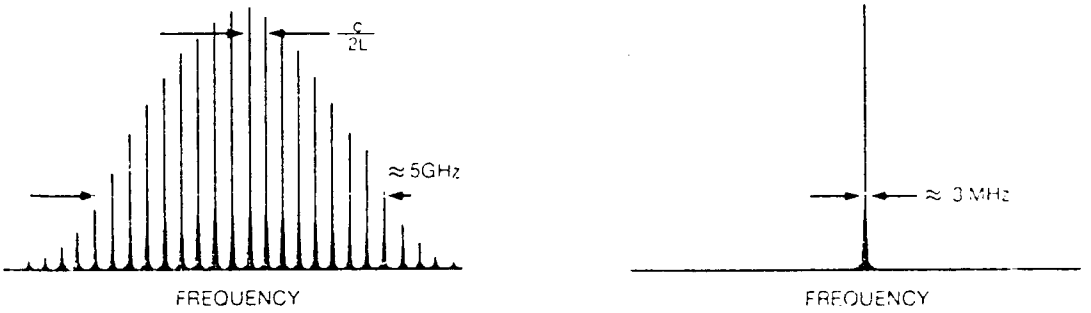

Without an Etalon. With an Etalon

Figure 1 The Effect of an Etalon on Monochromaticity.

Counter type processors are unable to correctly determine velocity with acceptable accuracy when two or more particles of comparable size are illuminated by the two sources. The two sinuisoidal signals will be mixed and will produce various invalid velocity measures.

LDA system use optics to ensure that only light from the measurement volume enters the photodetectors. An image of the measurement volume location is produced. An aperture or the end of an optic fibre is located to accept only light from the direction of the measurement volume. Only the light emanating from the measurement volume will be in focus at the plane. Light approaching from the same direction but not emanating from the same point will be attenuated.

Most processors use high and low filters to reduce the noise intensity. Setting filters to values which are less than a multiple of three different from the expected doppler frequency can condition noise to approximate valid data. The prediction of Signal Noise Ratio which can ideally be achieved is treated well by Adrian and Early (1976). Ideally achievable SNR should always be calculated to determine the possibility of success. Signal Noise Ratios of less than 10 dB make measurement with counter type processors very difficult indeed.

RECOGNITION OF NOISE.

Noise can produce oscilloscope traces and software outputs which are very similar to valid data traces. Finding signals with doppler frequency in the appropriate range is no guarantee of valid data. Whenever data is present some noise will be present. Noise levels can change during a traverse with no apparent change in conditions. Whenever data collection rate changes or amplification level is changed noise contamination must be suspected.

Before any data is recorded the validity of the data should always be tested. The validity of data is most effectively tested by changing the velocity component magnitude. Repeatable change in the velocity measurement in line with known change in velocity is a complete proof of valid data. No change or mismatch of the change direction or magnitude indicates that noise must be present and the data is invalid. Alternately the frequency shifting frequency or downmixing frequency can be altered to simulate changes in the velocity component. Care must be taken to assure that high and low frequency filters are not set at values which "block" any of the doppler frequencies or the downmixed frequencies.

SOURCES OF NOISE.

All air, particularly the air in cities, contains significant numbers of dust particles of mean size 0.6 micrometre and a significant proportion up to 2 micrometre. Such particles are usually present in large enough concentration (100 to 300 parts per billion) to give more than one particle in the LDA measuring volume at a time. More than one particle in the measurement volume creates apparent noise. The use of dust for LDA measurement is possible but is not often used with counter type processor.

A common source of noise is the presence of more than one particle in the measurement volume at one time. The number of particles in the measuring volume at one time can be estimated by considering the cube of the ratio of measurement volume diameter (approximately 300 micrometre) to the particle size and comparing the volume ratio with the concentration of the particles in the flow. The formula below permits calculation of the approximate number of particles in the measurement volume at one time.

$$N \approx C_{v/v} \left(\frac{d_p}{D_{e^{-2}}}\right)^3$$

Where N is the number of particles in the measurement volume.

$C_{v/v}$ is the concentration of particles in the fluid volume per unit volume.

d_p is the diameter of the seeding particles.

$D_{e^{-2}}$ is the nominal laser beam diameter.

Generally larger particles give higher SNR. Particles need to be 2.5 times the size of most of the dust particles to give signals 6.25 times greater; assuming equal reflectivity. Signal 6.31 times greater will give a maximum of 8 dB SNR. The seeding particle size for air should therefore be at least 5 micrometre. Particles of this size in

air are a very dangerous health hazard (Environment Protection Authority private communication 1992) as they are small enough to be breathed into the lungs. The published Threshold Limit Value for 5 micrometre particles of Aluminium Oxide is 10 mg/m^3. Only sterile water or pure and sterile sea salt are proven safe for breathing without discomfort. Salt in air can be a hazard for asthmatics.

The use of much larger particles can be inappropriate. Particle acceleration distances of larger particles can be so long that the velocity of the gas phase cannot be measured accurately. Also large particles can produce effects similar to having more than one particle in the measuring volume. Glass spheres of up to 200 micrometre have been used without difficulty.

PRACTICAL EXAMPLES OF NOISE CONTROL.

Light scattered by objects not in the measurement volume which are much larger, more reflective or more numerous than the seeding particles can produce noise. Although the optics attenuate the intensity of light from outside the measurement volume it is not eliminated. The intensity of backscatter light can be predicted for spherical particles of known size but practical variations can be dramatic. Backscatter light is sometimes one millionth the intensity of forward scattered light. It is common to find that unwanted light is much more intense than the signal light. Such light may be scattered by the back wall or the window or result from the diffusion of a reflected laser beam which reaches the output lens.

Much of the noise in practical models comes from the windows through which the system fuctions. The use of coated optical windows for models and, for liquids, the matching of the refractive indices of the liquid and windows is desirable. Optical coating reduces unwanted reflection and diffusion by a nominal factor of 20. Even weakly reflected laser beams should be blocked to prevent them reaching the lens collecting the light for the photomultiplier. In backscatter mode the collection lens is usually the output lens. A matt black bar about 1.5 to 2 mm wide can be mounted in front of the lens to block all specular reflection from the windows of models which are normal to the beams. The bar can be bent at 45 degrees near each end to avoid blocking the output beams and the ends mounted on the lens mounting.

Reducing the concentration of particles larger than one tenth the size of the seeding particles will improve SNR. HEPA (High Efficiency Particulate Air) filter catridges are widely available and they will trap 99.97 percent of particles of 0.6 micrometre diameter. The pressure drop through these filters can be considerable and the cost can be prohibitive. In closed circuit systems such filters are a very practical proposition.

A similar approach with water model is possible by fitting open filtration systems using 1 micron filter bags and then using at least 5 micrometre seeding particles. The open system filters do not require a pressure vessel. The filtered water is simply returned to a covered holding tank. Circulating the water until satisfactorily clean is recommended and the filter should be removed or bypassed when seeding particles are added.

CONCLUSIONS.

Experience has shown that improvements in Signal to Noise Ratio of 10 to 15 dB are often achieved by simple measures. Often the measures are not required for experimental situations which are not demanding. Demonstration of the function of a system with relatively large seeding particles, clean fluid and coated windows can give a misleading impression of the facility of use of LDA systems. The apparent facility can be achieved if the measures outlined here are applied.

REFERENCES.

Adrian, R.J. and Earley, W.L. "Evaluation of LDV Performance Using Mie Scattering Theory." Symposium on Laser Anemometry, University of Minnesota, October 1975.
Drain L.E. ,1980 "The Laser Doppler Technique."
Menon, R.K. "Selection of Seed Particles for LDV Measurements." Proceedings of the International Conference on Fluid Dynamic Measurement and its Application, Beijing, October 1989.
TSI Flow Data 1989.

Simultaneous OH-LIF and Rayleigh Measurement of Premixed Flames

O'Young, F. and Bilger, R. W.

Department of Mechanical Engineering
The University of Sydney
August 1993

Simultaneous Rayleigh and Laser Induced Fluorescence technique is used to obtain multiscalar measurements in turbulent premixed flames. The diagnostic system employed gives good spatial and temporal resolution and 2-D images of density and relative OH concentration are obtained.

INTRODUCTION

Recent developments in laser diagnostic methods, in particular in two- and three-dimensional imaging techniques, have allowed new insight into the course of turbulent combustion processes as well as the possibility of testing model calculations. Laser imaging techniques such Rayleigh scattering and Laser Induced Fluorescence (LIF) (see Cattolica and Vosen 1987) able us to investigate scalars in flames non-intrusively with greater spatial resolution than conventional probes. Simultaneous measurement techniques like joint Rayleigh and Raman (see Masri *et al* 1988) bring time-resolved, multiscalar measurements which yield important information on the effects of turbulence-chemistry interactions on species formation. In this experiment simultaneous Rayleigh and LIF is used to probe turbulent premixed flames and the resulting two-dimensional images are presented here.

EXPERIMENTAL

EXCITATION

Figure 1a shows the layout of major equipment used for this laser diagnostics experiment. The fundamental wavelength of a pulsed Nd-YAG laser (Spectra-Physics DCR-11) is frequency-doubled with a KDP crystal to produce 532 nm in wavelength. A beamsplitter splits this laser into two beams of 100 mJ and 80 mJ in energy. The 80 mJ beam is then directed to pump a tunable dye laser (Spectra-Physics PDL-3). The Rhodamine 590 dye solution used produces a peak energy output at 560 nm. After doubling its frequency with another KDP crystal the wavelength is tuned to 281.18 nm which corresponds to the $R_1 7$ branch (see Dieke and Crosswhite 1962) of OH ($X^2\Pi$-$A^2\Sigma^+$, 1,0 transition). This UV beam is then recombined collinearly with the 100 mJ Nd:YAG beam to pass through a set of beam expanding fused silica lenses. The final beam width is about 18 mm and a minimum thickness of about 0.4 mm with a pulse width of 7 ns.

DETECTION

Figure 1b displays the optical setup of the scattering detectors employed. Two systems, one for Rayleigh scattering and the other for laser induced fluorescence (LIF), sit at either side of the laser beam with their optical axis perpendicular to the beam and collinear to each other. The Rayleigh scattering detection system consists of a 576 × 384 pixel, 12-bit CCD camera (Photometrics STAR I) coupled to an image intensifier (Varo S-20) via two f1.2 lenses. The field lens for this system is a F.L. 85 mm f1.4 optic which provides a final spatial resolution of 65 μm. The LIF detection system has a similar construction except that the image intensifier is

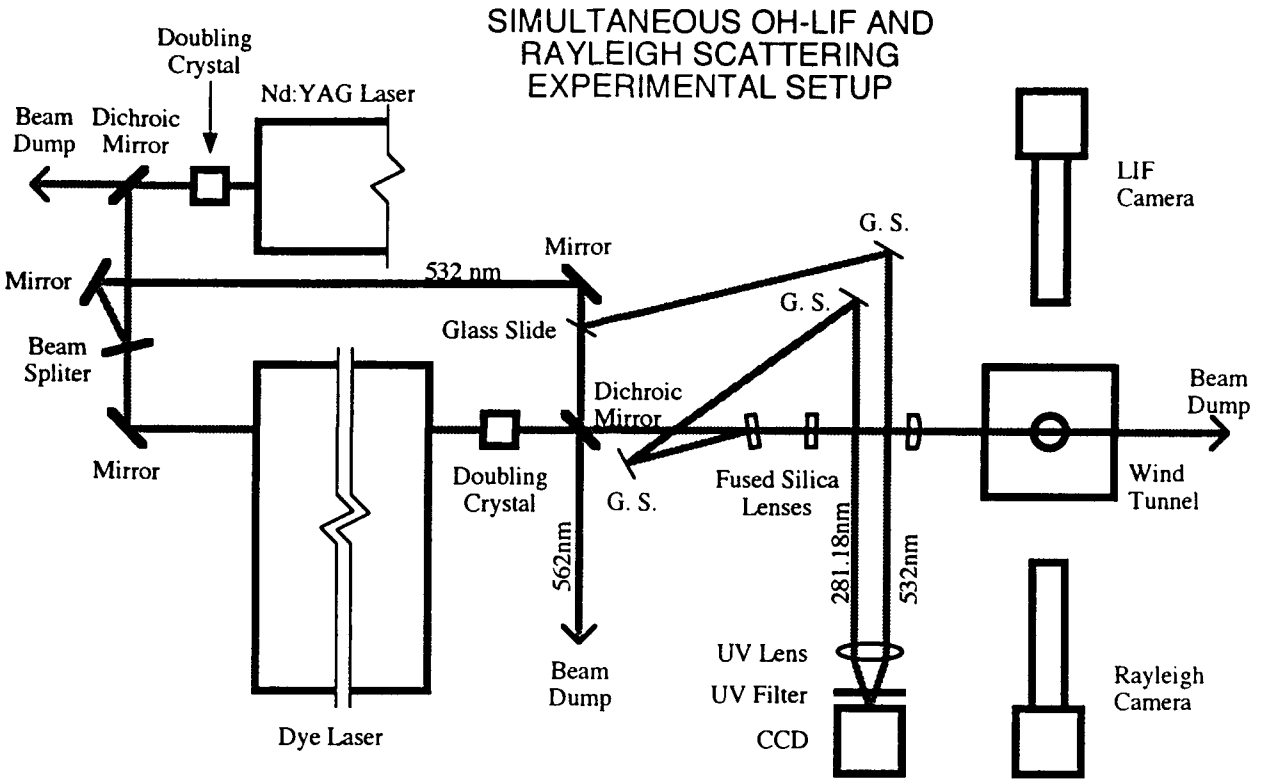

(a)

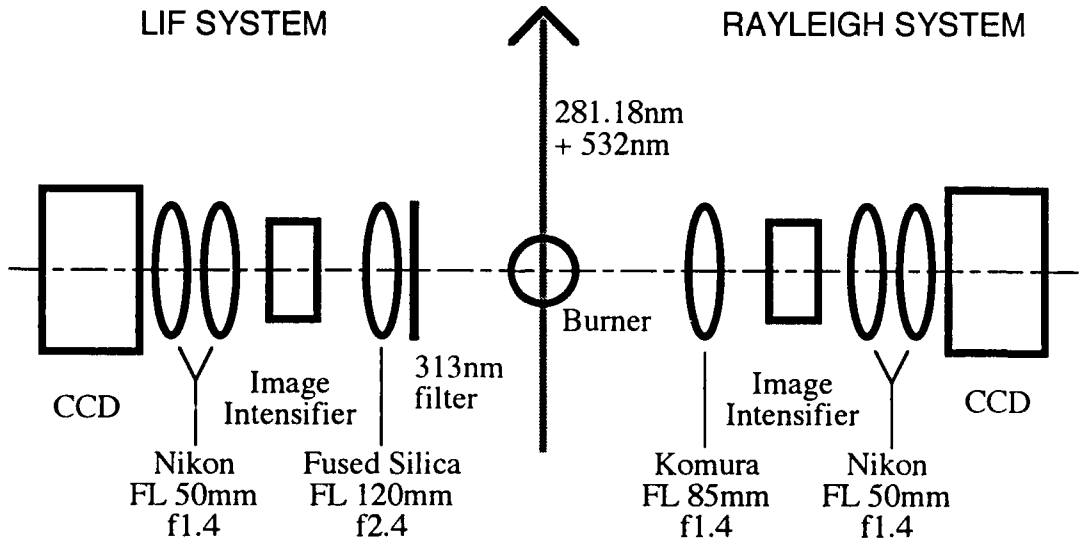

(b)

Figure 1. (a) Schematic of the experimental setup for simultaneous Rayleigh and LIF detection. (b) Optical arrangement of the detection systems.

also sensitive in the UV range and the field lens is UV-transparent with 120 mm focal length. A 313 nm interference filter is used to select the fluorescence signal from OH. Both image intensifiers are used here as shutters with a gate time of 600 ns, short enough to eliminate most of flame's luminescence. A third CCD camera is also employed to monitor the intensity of the laser beams by splitting off weak portions from the main beams.

RESULTS

IMAGE PROCESSING

Four qualitative image corrections are considered for the raw 2-D image collected:

(i) Background noise
(ii) Non-uniform optical response
(iii) Shot-to-shot laser power fluctuation
(iv) Non-uniform laser spectral distribution

Figure 2 shows a Rayleigh image of a premixed flame before and after image corrections have been performed. The brighter sections of the image are areas of unburnt fuel and air mixture and the darker parts are areas of burnt product gas.

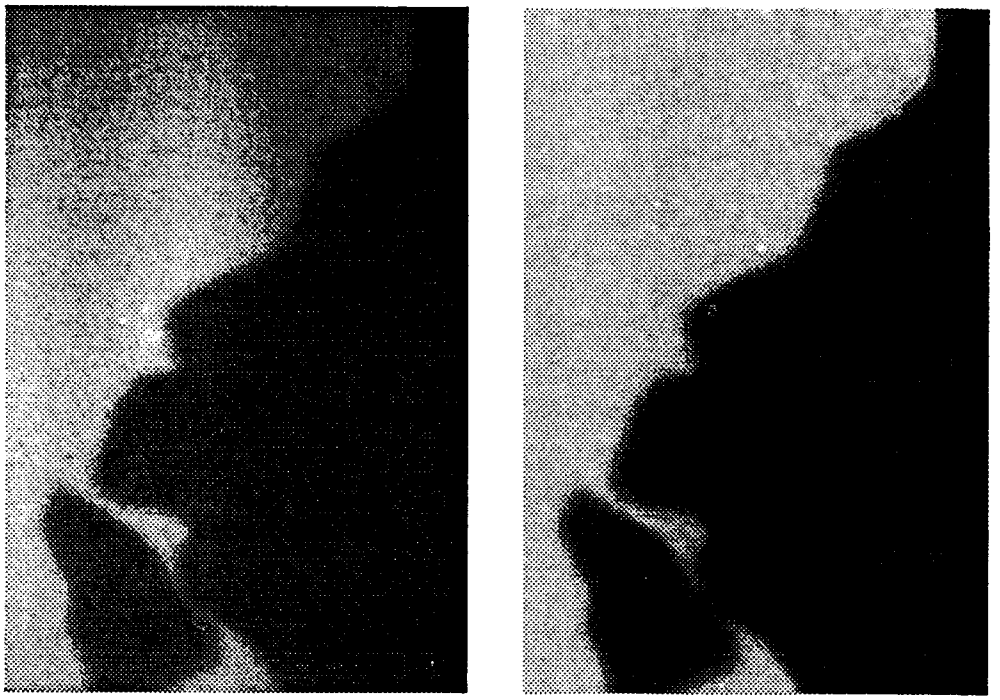

(a) (b)

Figure 2. (a) An uncorrected Rayleigh image. (b) Same image but corrected.

An uncorrected signal S can be expressed as

$$S = P \times R \times (L \times I + B) - E$$

where P is the relative laser power, R is the optical response, L is the laser's spectral distribution, I is the corrected signal, B is the background noise without the electronic bias, and E is the electronic bias.

IMAGE EXAMPLES

Figure 3 displays some examples of simultaneous Rayleigh scattering and OH-LIF images of

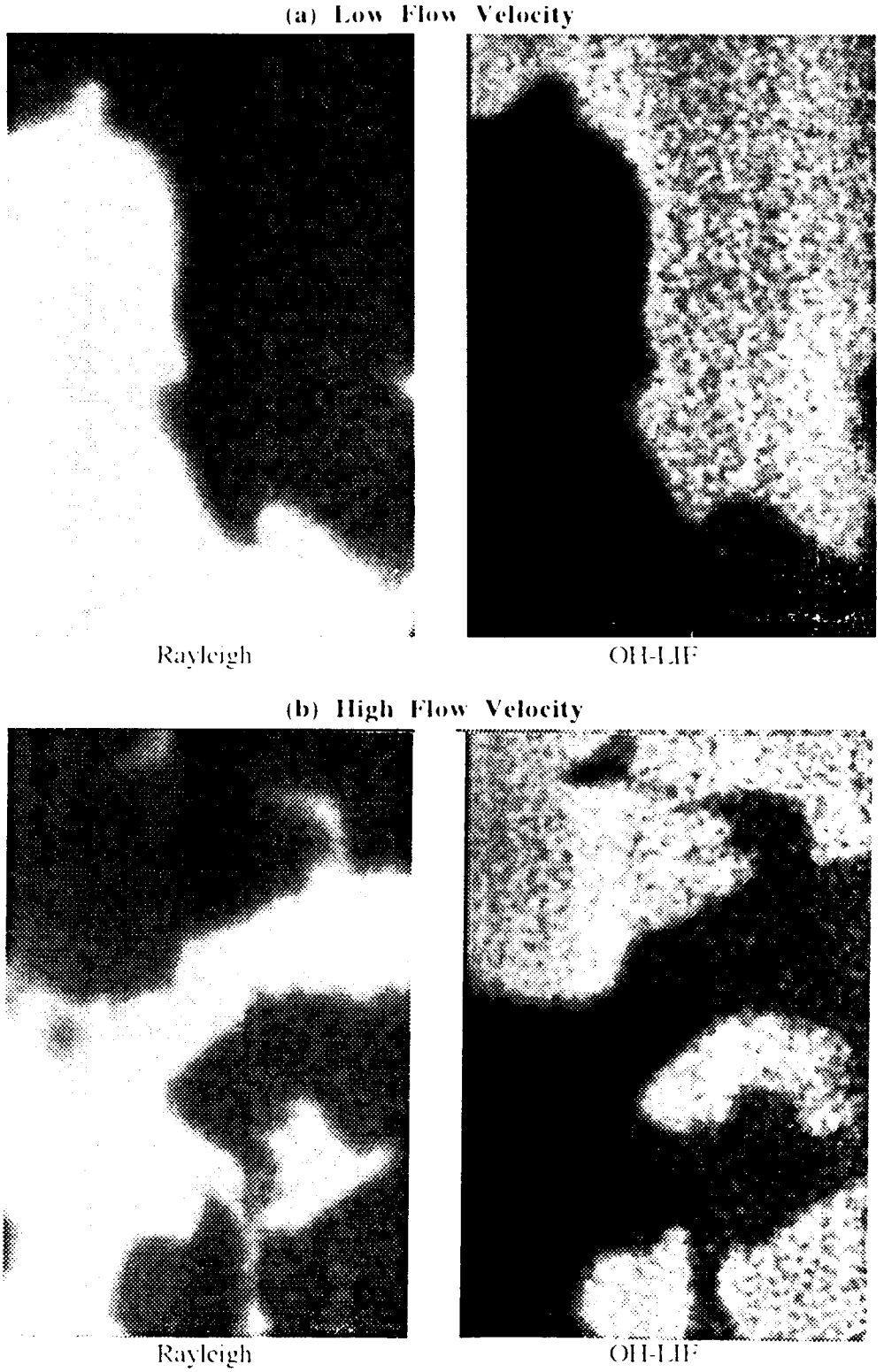

Figure 3. (a) Simultaneous Rayleigh and OH-LIF of a premixed flame with a lower turbulence intensity compared to the flame in (b).

premixed flames at different turbulence intensities. The image pair of Figure 3(a) was taken with a lower flow velocity than that of Figure 3(b). Most of the turbulence is generated by a grid designed to provide Kolmogorov scales smaller than the reaction zone thickness. The spatial resolution of the camera is not fine enough to resolve scales smaller than Taylor length scale (about same order of magnitude) but is sufficient to resolve the thermal flame front thickness in Rayleigh images. Typically the signal-to-noise ratio for the unburnt Rayleigh is about 30 and approximately 15 for the burnt gas. Because the energy output from the dye laser is not as high as desired the signal-to-noise ratio for the LIF images is around 10. The temporal resolution is given by the pulse duration of 7 ns, which is three orders of magnitude smaller than the scale of flame propagation if a resolution of 65 μm is desired.

SUMMARY

Using simultaneous Rayleigh and OH-LIF imaging, planar images of density and OH concentration in flames are obtained with good spatial and temporal resolution. With proper image correction process quantitative scalar (not presented here) such as temperature and relative OH concentration are calculated. Increased laser power for OH excitation is desired to improve the signal-to-noise ratio of the LIF images. Simultaneous imaging with independent lasers will be used in future experiments.

REFERENCES

Cattolica, R. and Vosen, S. (1987) "Combustion-Torch Ignition: Fluorescence Imaging Of OH Concentration", *Combust. Flame*, **68**, 267.
Dieke, G. H. and Crosswhite, H. M. (1962) "The ultraviolet bands of OH: Fundamental Data", *J.Q.S.R.T*, **32**, 97.
Masri, A. R., Bilger, R. W. and Dibble, R. W. (1988) "Turbulent Nonpremixed Flames of Methane Near Extinction: Probability Density Functions.", *Combust. Flame*, **73**, 261.

Proposed Four Wave Mixing Experiments In Hypersonic Flows

P.C. Palma, A.F.P. Houwing and R.J. Sandeman

Aerospace and Laser-based Diagnostic Research Laboratory
Department of Physics and Theoretical Physics, Faculty Of Science
Australian National University, Canberra, ACT, 0200

ABSTRACT

Proposed measurements on hypervelocity reacting and non reacting flows using Degenerate Four Wave Mixing (DFWM) spectroscopy are discussed. The advantages of DFWM over other techniques used for the study of hypersonic flows, such as laser induced fluorescence (LIF) and coherent anti-Stokes Raman spectroscopy (CARS), are also discussed. A technique for producing high intensity UV radiation by Raman shifting of the output of a tunable excimer laser is compared to more conventional methods of generating UV laser radiation.

INTRODUCTION

Hypervelocity flows produced by shock tunnels provide a very demanding proving ground for the use of optical diagnostic techniques due to the high pressures and temperatures that are typical of these flows. The attraction of laser based optical diagnostics lies with the non-intrusive, species specific nature of the techniques and the high spatial and temporal resolutions which are attainable. Coherent anti-Stokes Raman spectroscopy (CARS) is a proven tool for temperature measurements in hostile environments (see Pulford *et al* 1993, Eckbreth and Anderson 1985, Lucht 1987, Bruckner and Hinderlang 1983). The coherent nature of the signal beam allows high collection efficiencies and stray light rejection. However, CARS measurements require very high power densities to get appreciable signal strength and can generally only be performed as a point wise measurement. Laser induced fluorescence (LIF) is also a widely tested technique and can be used for two dimensional mapping of temperature, concentrations and velocities (see Palmer *et al* 1992, Lee *et al* 1992, Hanson *et al* 1990). The main disadvantage with LIF is primarily due to rotational and vibrational redistribution of excited state molecules as well as collisional quenching, saturation and depletion effects. To account for these problems, sophisticated rate models are necessary. Predissociation of the excited state can be used to remove the problem of collisional quenching when the predissociation rate is much greater than the collisional quenching rate. However, this technique results in significantly reduced fluorescence (see Andresen *et al* 1988, Sutton *et al* 1993).

Resonant degenerate four-wave mixing (DFWM) has enjoyed a renewed popularity in recent years (see Dreier and Rakestraw 1990, Ewart *et al* 1989, Farrow and Rakestraw 1992). It has the highly desirable properties of both the CARS and LIF techniques, namely, a coherent signal beam, high sensitivity for detecting trace species, and high signal strengths which allow flow field imaging. DFWM also has the unique advantage that the signal beam is the phase conjugate of the probe beam. This property allows superior imaging of flow fields through the distorting media that would be expected in shock tunnel produced flows. Finally, as with CARS, quenching effects are minimised due to the very short interaction time (pulse duration ~ 10ns).

DESCRIPTION OF DFWM

In DFWM, three laser beams at the same frequency overlap in a nonlinear medium and produce a fourth (signal) beam at the same frequency. When the frequency of the radiation corresponds to a transition in the nonlinear medium, resonant enhancement of the signal is observed. Figure 1 shows the conventional experimental geometry. Two pump

beams with wave vectors k_f (forward) and k_b (backward) counterpropagate through the medium. The probe beam (k_p) crosses the two pump beams at an angle θ. Since $k_f = -k_b$, the phase matching condition is satisfied for all θ and therefore $k_s = -k_p$ (ie. the signal propagates anti-parallel to the probe beam). This removes the complicated alignment problems associated with CARS experiments.

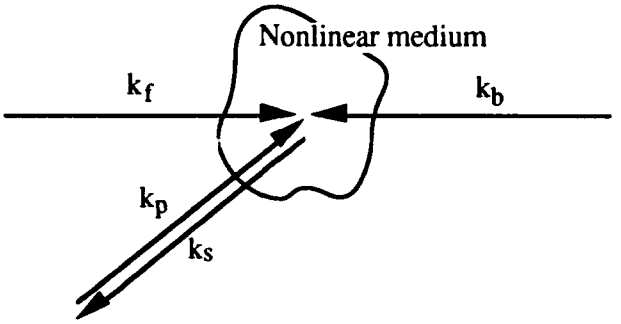

Figure 1. Conventional arrangement of beams for degenerate four-wave mixing. The four wave vectors represent the forward (f) and backward (b) pump beams, the probe beam (p) and the phase conjugate signal beam (s).

The theory of Abrams & Lind (1978) describes a two level absorbing system where the intensities of the forward beam (I_f) and backward beam (I_b) are assumed to be equal ($I = I_f = I_b$) and also much larger than the probe beam intensity ($I >> I_p$). Assuming undepleted pumps and a slowly varying I_s in the medium, they found that the signal beam is the phase conjugate of the probe beam and, under certain conditions, can show amplification (ie. $I_s > I_p$). Farrow *et al* (1992) have demonstrated the dependence of the signal intensity on pump intensity and transition dipole moment. They found that the spectrally integrated signal intensities in the limits of low- and high-intensity pumps are

$$I_s^{int} \propto \mu_{12}^8 \, T_1^2 \, T_2^3 \, I^3 \qquad (I << I_{sat})$$

$$I_s^{int} \propto \mu_{12}^3 \, T_1^{-\frac{1}{2}} \, T_2^{\frac{1}{2}} \, I^{\frac{1}{2}} \qquad (I >> I_{sat})$$

where μ_{12} is the transition dipole moment, T_1 is the longitudinal relaxation time, T_2 is the transverse relaxation time and I_{sat} is the frequency dependent saturation intensity. These relations show that the dependence of the dipole moment is third order in the saturated case while eighth order in the low-intensity limit. Similarly it is seen the dependence on T_1, T_2 and I is significantly less in the high-intensity limit. The benefits of using saturating intensities include: improved signal to noise ratio; higher sensitivity; higher signal strength; and improved pulse to pulse reproducibility due to the lesser dependence on the laser intensity. It has been demonstrated experimentally that the integrated signal intensity is well described by $I_{sat} \propto \mu^4 \, n^2$ where n is the unperturbed ground level population (see Dreier and Rakestraw 1990, Rakestraw *et al* 1990). This power dependence on the dipole moment agrees well with the qualitative theory described by Farrow *et al* (1992).

GENERATION OF UV RADIATION

UV radiation is often required to electronically excite the atoms or molecules of combustion or flow species for diagnostic purposes. The most common method of UV production is undoubtedly frequency doubling of tunable dye laser radiation. The tunable dye laser offers unsurpassed flexibility with wavelength selection and when pumped by a powerful laser (eg. excimer or Nd:YAG) can achieve very high beam energies (up to approximately 50 to 100mJ per pulse). When used in conjunction with the appropriate doubling crystal it is not uncommon to generate several millijoules of UV radiation per pulse

(see McMillin *et al* 1992). A method often employed when a Nd:YAG laser is the pump laser involves frequency mixing the 287nm frequency doubled dye output with the 1064nm first harmonic of the Nd:YAG laser. This leads to approximately 4mJ per pulse of 226nm radiation which can be used for exciting nitric oxide or atomic oxygen (see Farrow *et al* 1992, Goldsmith *et al* 1990).

The alternative to tunable dye lasers is tunable excimer lasers. Bandwidths less than 0.003nm and beam energies of several hundred millijoules per pulse are typical. Various wavelengths are available depending an the gas type employed (ArF:193nm, KrF:248nm, XeCl:308nm, XeF:351nm) but the major drawback is that the tuning range is typically only 1nm. Despite this, tunable excimers have been used extensively because some molecules of importance in combustion and flow diagnostics (eg O_2, NO, OH) can be probed at these wavelengths (see Miles *et al* 1987, Andresen *et al* 1988 and 1990, Wodtke *et al* 1988, Ketterle *et al* 1992, Yang *et al* 1991, Versluis *et al* 1992).

Stimulated Raman Scattering (SRS) has been used extensively to produce tunable coherent radiation in the UV and vacuum UV. In particular, its use in fluorescence experiments (see Alden *et al* 1982, Bischel *et al* 1982, Lucht *et al* 1983, Goldsmith 1987) and laser spectroscopy (see Lewis et al 1988, Gibson 1990) is well documented. Recently it was shown by Kim *et al* (1991) and Dreier *et al* (1992) that SRS could be used to extend the range of tunable excimers for use in LIF of combustion and flow species. Conversion efficiencies of 10 to 30% for lower order stokes and up to 5% for anti-stokes are possible and in general the SRS light is more intense than what can be achieved by frequency doubled dye lasers. Table 1 shows a few of the species and transitions that can be reached using a tunable KrF excimer laser and which appear to be very promising for laser diagnostic research (for a more extensive list see Dreier *et al* 1992).

Raman Medium	Stokes / Anti-Stokes Order	Tuning Range (nm)	Species	Transition
H_2	1 AS	224.8 - 225.7	NO	$A^2\Sigma^+$-$X^2\Pi$ (0–0)
H_2	2 S	312.4 - 314.0	OH	$A^2\Sigma^+$-$X^2\Pi$ (0–0/1–1)
D_2	2 S	291.2 - 292.6	OH	$A^2\Sigma^+$-$X^2\Pi$ (1–0/2–1)

Table 1. Favourable transitions for laser diagnostics which are accessible by Raman shifting the output of a KrF tunable eximer laser

Although DFWM has been performed successfully with relatively low laser energies (approximately 1 mJ) the benefits of these higher beam energies have been listed in the previous section. Increased beam energy also allows the possibility of performing two dimensional measurements (see Ewart *et al* 1989, Ewart and Kaczmarek 1991) and it must be remembered saturation intensities will be higher at higher pressures.

APPLICATION TO HYPERSONIC FLOWS

Pulsed high enthalpy flows present many unique problems such as the need for instantaneous single shot measurements. Multiplex DFWM involves exciting multiple transitions with the one laser pulse and this allows temperatures to be calculated from the relative line strengths (see Ewart and Snowdon 1990, Yip *et al* 1992). Single shot two dimensional imaging has already been demonstrated by Mann *et al* (1992) and Rakestraw *et al* (1990). Double phase conjugate four-wave mixing (DPCFWM) has been used to measure OH number densities and rotational temperatures in high pressure flames (up to 9 bar, see Feikema *et al* 1992, Winter and Radi 1991). This technique eliminates fluctuations in the interaction volume due to the misalignment of the pump beams by phase conjugating the backward pump to the forward pump beam. Stimulated Brillouin Scattering (SBS) in liquid hexane was used as a phase conjugate mirror (PCM) to produce the phase conjugated

backward pump. The decrease in intensity due to the 20% reflection at the PCM is compensated for by the improved overlap of the pump beams. PCM's with greater reflectivity are also possible (see Eichler *et al* 1986). For the high pressures and distorting optical paths encountered in shock tunnel studies of hypersonic flows this technique could be highly advantageous.

CONCLUSIONS

It has been shown that DFWM and its derivative techniques (Multiplex DFWM, DPCFWM) offer significant advantages over other laser-based diagnostic techniques, such as CARS and LIF, for the use in hypersonic flows. The extreme conditions encountered in these flows mean a substantial amount of theoretical and experimental work is still required in order for DFWM to become a reliable diagnostic tool. In particular, problems associated with molecular motion, level degeneracies, pulsed excitation, overlapping transitions, collisional processes, rotational transfer, quenching and polarisation effects still need to be quantified. Experiments in stabilised flames in our laboratory are continuing in preparation for the use of DFWM as a diagnostic tool for hypersonic flows produced by high enthalpy shock tunnels.

REFERENCES

Abrams RL and Lind RC (1978) "Degenerate four-wave mixing in absorbing media", *Opt Lett*, **2**, 94-96:*Opt Lett*, **3**, 205-207.

Alden, M, Edner H, Grafström P, Svanberg S (1982) "Two photon excitation of atomic oxygen in a flame", *Opt Commun*, **42**, 244-246.

Andresen P, Bath A, Gröger W, Lülf HW, Meijer G, ter Meulen JJ (1988) "Laser-induced fluorescence with tunable excimer lasers as a possible method for instantaneous temperature field measurements at high pressures: checks with an atmospheric flame" *Appl Opt*, **27**, 365-378.

Andresen P, Meijer G, Schlüter H, Voges H, Koch A, Hentschel W, Opperman W, Rothe E (1990) "Fluorescence imaging inside an internal combustion engine using tunable excimer lasers", *Appl Opt*, **29**, 2392-2404.

Bischel WK, Perry BE, Crosley DR (1982) "Detection of fluorescence from O and N atoms induced by two photon absorption", *Appl Opt*, **21**, 1419-1429.

Bruckner S and Hinderlang FJ (1983) "*Proceedings of the 14th International Symposium on Shocktubes and Shock Waves*," University Of Sydney, 615-620.

Dreier T and Rakestraw DJ (1990) "Degenerate four-wave mixing diagnostics on OH and NH radicals in flames", *Appl Phys B*, **50**, 479-485.

Dreier T, Dreizler A, Wolfrum J (1992) "The application of a Raman-shifted tunable KrF excimer laser for laser-induced fluorescence combustion diagnostics", *Appl Phys B*, **55**, 381-387.

Eckbreth AC and Anderson TJ (1985) "Dual broadband CARS for simultaneous multiple species measurements", *Appl Opt*, **24**, 2325.

Eichler HJ, Pohl D, Gunter P (1986) "*Laser-induced dynamic gratings*", Springer series in Optical Sciences, Vol 50, Springer, New York.

Ewart P, Snowdon P, Magnusson I (1989) "Two dimensional phase-conjugate imaging of atomic distributions in flames by degenerate four-wave mixing", *Opt Lett*, **14**, 563-565.

Ewart P and Snowdon P (1990) "Multiplex degenerate four-wave mixing in a flame", *Opt Lett*, **15**, 1403-1405.

Ewart P and Kaczmarek M (1991) "Two-dimensional mapping of temperature in a flame by degenerate four-wave mixing in OH", *Appl Opt*, **30**, 3996-3999.

Farrow RL, Rakestraw DJ, Dreier T (1992) "Investigation of the dependence of degenerate four-wave mixing line intensities on transition dipole moment", *J Opt Soc Am B*, **9** 1770-1777.

Farrow RL and Rakestraw DJ (1992) "Detection of trace molecular species using degenerate four wave mixing", *Science*, **257**, 1894-1900.

Feikema DA, Domingues E, Cottereau MJ (1992) "OH rotational temperature and number density measurements in high pressure laminar flames using double phase-conjugate four-wave mixing", *Appl Phys B*, **55**, 424-429.

Gibson ST, Lewis BR, Baldwin KGH, Carver JH (1991) "Rotational features in the fluorescence excitation spectrum of $O(^1D_2)$ from vacuum ultraviolet laser photodissociation of O_2", *J Chem Phys*, **94**, 1060-1068.

Goldsmith JEM (1987) "Photochemical effects in two-photon-excited fluorescence detection of atomic oxygen in flames", *Appl Opt*, **26**, 3566-3572.

Goldsmith JEM, Alden M, Westblom U (1990) "Photochemical effects in multiple species fluorescence imaging in hydrogen-nitrous oxide flames", *Appl Opt*, **29**, 4852-4859.

Hanson RK, Seitzman JM, Paul PH (1990) "Planar laser fluorescence imaging of combustion gases", *Appl Phys B*, **50**, 441-454.

Ketterle W, Schäfer M, Arnold A, Wolfrum J (1992) "2D single-shot imaging of OH radicals using tunable excimer lasers", *Appl Phys B*, **54**, 109-112.

Kim GS, Hitchcock LM, Rothe EW, Reck GP (1991) "Identification and imaging of hot O_2 (v"=2,3 and 4) in hydrogen flames using 193nm- and 210nm-range light", *Appl Phys B*, **53**, 180-186.

Lee MP, McMillin BK, Palmer JL, Hanson RK (1992) "Planar fluorescence imaging of a transverse jet in a supersonic crossflow", *J Prop Power*, **8**, 729-735.

Lewis BR, Gibson ST, Baldwin KGH, Carver JH (1989) "Vacuum-ultraviolet absorption linewidth measurement using high-order Raman-shifted radiation", *J Opt Soc Am B*, **6**, 1200-1208.

Lucht RP, Salmon JT, King GB, Sweeney DW, Laurendeau NM (1983) "Two-photon-excited fluorescence measurement of hydrogen atoms in flames", *Opt Lett*, **8**, 365-367.

Lucht RP (1987) "Three laser CARS measurements of two species", *Opt Lett*, **12**, 78-80

Mann BA, O'Leary SV, Astill AG, Greenhalgh DA (1992) "Degenerate four-wave mixing in nitrogen dioxide: application to combustion diagnostics", *Appl Phys B*, **54**, 271-277.

McMillin BK, Palmer JL, Antonio AL, Hanson RK (1992) "Instantaneous, two-line temperature imaging of a H_2/NO jet in supersonic crossflow", AIAA-92-3347.

Miles R, Cohen C, Connors J, Howard P, Huang S, Markovitz E, Russell G (1987) "Velocity measurements by vibrational tagging and fluorescent probing of oxygen", *Opt Lett*, **12**, 861-863.

Palmer JL, McMillin BK, Hanson RK (1992) "Planar laser-induced fluorescence imaging of velocity and temperature in shock tunnel free jet flow", AIAA-92-0762.

Paul PH, Lee MP, Hanson RK (1989) "Molecular velocity imaging of supersonic flows using pulsed planar laser-induced fluorescence of NO", *Opt Lett*, **14**, 417-419.

Pulford DRN, Newman DS, Houwing AFP, Sandeman RJ (1993) "Coherent anti-Stokes Raman scattering in the T3 shock tunnel", *Shock Waves*, **3**.

Rakestraw DJ, Farrow RL, Dreier T (1990) "Two-dimensional imaging of OH in flames by degenerate four-wave mixing", *Opt Lett*, **15**, 709-711.

Sutton DS, Houwing AFP, Palma PC, Sandeman RJ (1993)"Vibrational temperature measurements in a shock layer using laser-induced predissociation fluorescence", *Shock Waves*, **3**.

Versluis M, Boogaarts m, Klein-Douwel R, Thus B, de Jongh W, Braam A, ter Meulen JJ, Meerts WL, Meijer G (1992) "Laser-induced fluorescence imaging in a 100kW natural gas flame", *Appl Phys B*, **55**, 164-170.

Wilke V, Schmidt W (1978) "Tunable UV-radiation by stimulated Raman scattering in hydrogen" *Appl Phys*, **16**, 151-154.

Winter M and Radi PP (1992) "Nearly degenerate four-wave mixing using phase-conjugate pump beams", *Opt Lett*, **17**, 320-322.

Wodtke AM, Huwel L, Schlüter H, Voges H, Meijer G, Andresen P (1988) "Predissociation of O_2 in the B state", *J Chem Phys*, **89**, 1929-1935.

Yang X and Wodtke AM (1991) "Direct observation of orbit rotation predissociation in the O_2 Schumann-Runge system", *J Chem Phys*, **94**, 2469-2474.

Yip B, Danehy PM, Hanson RK (1992) "Degenerate four-wave mixing temperature measurements in a flame", *Opt Lett*, **17**, 751-753.

Timing Problems in Laser Based Combustion Diagnostics

I.G. Pearson*

CSIRO Division of Building, Construction & Engineering
PO Box 56, Highett VIC 3190, Australia

**Telephone +61 3 252 6132* **Fax +61 3 252 6240*
**Email (Internet) Ian.Pearson@dbce.csiro.au*

ABSTRACT

Laser based combustion diagnostics such as Laser Induced Fluorescence (LIF) and Degenerate Four Wave Mixing (DFWM) require wavelength tunable, pulsed lasers. Excimer laser pumped dye lasers generally fulfil the requirement.

When using these techniques to temporally resolve transient phenomena, timing difficulties of both the pump lasers and the detection equipment become obvious. Pulsed laser beam durations of 10 nanoseconds are commonplace and the diagnostic techniques in question require temporal resolution of this order. Conventional laboratory electronic equipment is not up to the task. Discussion of the problems concerned is made and some techniques to overcome some of these difficulties are presented.

LASER INDUCED FLUORESCENCE

Fluorescence is the spontaneous emission of radiation from an upper energy level which has been excited in any of a variety of ways, eg., collisions with photons, electrons or molecules (chemically or thermally). Lasers are by far the most convenient manner in which to provide spatially and spectrally selective excitation. Laser-induced fluorescence (LIF) is best viewed as, an absorption, followed after some finite period of time, by spontaneous emission from the excited manifold. If the fluorescence is at the same wavelength as the excitation, ie., from the same levels involved in the absorption, it is termed resonance fluorescence. For diagnostic purposes it is convenient to view shifted fluorescence to avoid interferences from spuriously scattered laser light or Mie scattering. Unfortunately, this is not always possible and thus temporal resolution is required to recover the signal. Absorption processes, being resonant, have much larger cross sections than do Raman effects in which the molecule is perturbed far from resonance. Consequently, fluorescence is many orders of magnitude stronger than Raman scattering which provides LIF with higher detection sensitivities and allows probing

of flame radicals with species concentrations below 0.1%, the level at which Raman based approaches fail due to incapability of detection.

DEGENERATE FOUR WAVE MIXING

Degenerate four wave mixing (DFWM) is a new, sensitive method of imaging (both point wise and two dimensionally) atomic and molecular species in hostile environments. DFWM is a third order nonlinear optical process in which three beams of frequency ω interact in a nonlinear medium to produce a fourth beam which, by conservation of energy, also has frequency ω. Resonant enhancement of the nonlinearity involved in the process enables it to be used as a spectroscopic tool. Further development by Ewart and O'Leary (1986) demonstrated that a two dimensional map of an atomic species could be obtained. The generation of the DFWM signal may be considered as a simultaneous formation and read-out of a volume hologram, or grating, created in the nonlinear medium by interference between the probe and either the forward-going or backward-going pump beam. Each pump beam contributes a signal by Bragg type scattering off the grating formed by the probe and the other pump beam. The generated signal wave appears as a reflection of the incoming probe and propagates in exactly the reverse direction. Any phase distortions imposed on the incoming probe are thus reversed as the signal beam traverses the same aberrating medium but in the opposite direction.

Again, because of the resonant processes involved, temporal resolution of the signal beam is required.

DETECTORS

Modern laboratory laser systems for combustion diagnostics customarily employ pulsed lasers (see Eckbreth 1988). They may be solid state (YAG:Nd) or excimer based. Pulse durations as short as 10 nanoseconds are not uncommon. To allow synchronism of experiment with laser pulse requires detectors that can temporally resolve the laser pulse.

Although semiconductor light sensing devices may be fabricated from a single element semiconducting material, most are based upon one or more combinations of *p-n* junctions. In the photoconductive mode (the most commonly used for rapid response), the junction is reverse biased and photons induce a flow of charge carriers which are measured via the voltage drop in the load resistor. Photon absorption in the *n* or *p* regions is undesirable relative to the depletion region for two reasons. First, recombination of electron-hole pairs may occur before the minority carrier arrives at the depletion region field, thus lowering the quantum efficiency. Second, because the carriers produced must diffuse to the field region, the speed of the photodiode response is lowered. Consequently, most "fast" semiconductor photodiodes employ a *p-i-n* structure where a pure (or intrinsic) semiconductor is sandwiched between the *p* and *n* materials. Most of the potential drop occurs across the intrinsic region. The size of the intrinsic region is made large enough so that most of the light absorption occurs there, but not so large as to slow the response considerably. PIN photodiodes can be

manufactured with near 100% quantum efficiencies and response speeds of the order of half a nanosecond.

To visualize and measure these single-shot waveforms from PIN diodes requires an oscilloscope of sufficient bandwidth and digitisation rate to enable viewing of pulse rise times of the order of half a nanosecond. This means a minimum bandwidth of 500 MHz and a minimum digitisation rate of 2 gigasamples/second. This is a very specialised oscilloscope.

Gated, intensified, micro-channel plate (MCP), charge coupled device (CCD) or charge injection device (CID) cameras are frequently used to gather two dimensional light data. To enable viewing and capture of data from a resonant LIF experiment requires temporal positioning of the gate window just after the laser pulse. This requires knowledge of when the laser pulse arrives (relative to the trigger), the time width of the laser pulse and the fluorescence lifetime of the species or radical in question. This data can sometimes be variable and needs to be determined for each arrangement. Modern ,"bucket brigade" (CCD) delays with delay times of the order of 5 nanosecond are available to allow time staging of the camera gate opening. Cabling schemes and propagation delays in devices and cables also need attention when working at short time intervals of this nature.

The synchronisation of the probing with laser pulses and the experimental phenomena also needs addressing. As we have already seen, short time intervals are involved and need to be taken care of. Modern excimer lasers have trigger delays of some one microsecond with trigger jitter of $\pm$ 2 nanoseconds. If multiple laser experiments are required, the timing problems become more manifest.

Another important phenomenon that is sometimes overlooked is the fact that light does take finite time to travel. The speed of light in air is approximately 3×10^8 metre/second - this corresponds to 300 mm / nanosecond. A pulse of laser light emitted from a laser at the far end of your laboratory, say 10 meters away, will take some 33 nanoseconds to reach you.

I have raised the spectre of only some of the experimental difficulties of timing involved with this sort of diagnostic work. The topics discussed so far all have solutions, problems of the future may be a different thing altogether.

REFERENCES

Eckbreth, A.C (1988) *Laser Diagnostics for Combustion Temperature and Species*, Abacus Press, Kent UK.

Ewart, P. and O'Leary, S.V. (1986) Opt. Lett. **11**, 279.

Coherent Anti-Stokes Raman Scattering in a Free Piston Shock Tunnel

D.R.N. PULFORD, D.S. NEWMAN, A.F.P. HOUWING & R.J. SANDEMAN

Australian National University
Faculty of Science
Department of Physics and Theoretical Physics
Canberra A.C.T. 0200 Australia

ABSTRACT: Single pulse broadband coherent anti-Stokes Raman scattering experiments taken in a shock tunnel flow and employing a folded box phase-matching geometry are presented. Ro-vibrational spectra of molecular nitrogen, inside a Super-sonic Combustion Ramjet (SCRAMJET) model for a range of flow enthalpies, are examined. Difficulties peculiar to the application of the optical technique to a high enthalpy pulse flow facility are discussed and measurements of flow temperatures are presented.

1. INTRODUCTION

Coherent Anti-Stokes Raman Scattering (CARS) (eg Eckbreth 1988) is a proven diagnostic technique for probing processes occurring in hostile environments. A coherent process in which the final signal emerges as a coherent beam resulting it gives high detection efficiency and rejects spurious interference. This is particularly important in our application where high intensity isotropic background radiation is caused by the presence of metallic impurities. Previous applications of CARS to measure temperatures behind shock waves were performed in the stagnation region behind the reflected shock wave in a shock tube using collinear CARS (Knapp et al 1981 and Bruckner et al 1983). Spatial resolution was limited to the dimensions of the confocal parameters of the laser beams. Densities in this earlier work were higher and test times longer than those being considered here. The motivation for applying single shot CARS to a high enthalpy pulsed flow is based in future experimental work designed to measure the fuel-air mixing and combustion rates in a supersonic combustion engine (SCRAMJET) (Stalker et al 1988) at enthalpies much higher than those corresponding to the conditions of previous supersonic combustion CARS experiments (Andreson 1992). These were performed in a flow facility having a run time between 60 and 90 s. CARS has also been used to study hypersonic flows in arc-driven wind tunnels where measurements were performed over several hours (Grisch et al 1993). By comparison, the steady flow period of our pulsed facility is of the order of 500 μs. Hence, whereas averaging techniques could be used in the longer running facility, single shot measurements must be made in the pulsed facility.

2. THEORETICAL CONSIDERATIONS

The theoretical description of CARS is well established. Incident laser beams at frequencies ω_1 and ω_2 (the pump and Stokes beams respectively) interact through the third order non-linear susceptibility $\chi^{(3)}(\omega_3)$ of the medium to generate a polarization field which acts as a source for anti-Stokes radiation at frequency $\omega_3 = 2\omega_1 - \omega_2$. The intensity, $I_3(\omega_3)$, of the CARS beam can be expressed as

$$I_3(\omega_3) = \left\{\frac{4\pi\omega_3}{c^2 n_3}\right\}^2 I_1^2(\omega_1) I_2(\omega_2) \left| 3\chi^{(3)}(\omega_3) \right|^2 f(\mathbf{k_1},\mathbf{k_2},\mathbf{k_3}) \qquad ...(1)$$

where c is the velocity of light; n_3 is the refractive index at ω_3; and f is a function of the wave vectors $\mathbf{k}_1$, $\mathbf{k}_2$ and $\mathbf{k}_3$ of the pump, Stokes and anti-Stoles beams respectively. For maximum signal, these vectors must satisfy the phase matching condition: $\mathbf{k}_3 + \mathbf{k}_2 - 2\mathbf{k}_1 = 0$.
The nonlinear susceptibility can be written in terms of a resonant and nonresonant parts. The nonresonant part χ^{nr} is the contribution from electrons and remote resonances. The resonant term is associated with a homogeneously broadened Raman transitions. The total non-linear susceptibility may then be expressed as

$$\chi^{(3)} = \sum_j \frac{4\pi c^4}{h\omega_2^4} N\Delta_j g_j \left(\frac{\partial\sigma}{\partial\Omega}\right)_j \frac{\omega_j}{\omega_j^2 - (\omega_1 - \omega_2)^2 - i\Gamma_j(\omega_1 - \omega_2)} + \chi^{nr} \qquad ...(2)$$

where h is Plank's constant; N the total species number density; Δ_j the population difference between the levels involved in the transition; g_j the line strength factor; $(\partial\sigma/\partial\Omega)_j$ the Raman cross section, Γ_j the Raman linewidth; and ω_j the transition frequency.

From equation (1), the experimental measurement of I_3 for an isolated Raman transition allows the determination of $\chi^{(3)}$. Provided the nonresonant component is known the measurement of the susceptibility allows the determination of $N\Delta_j$ from equations (1) and (2). Assuming a Boltzmann distribution based on the rotational (T_r) and vibrational (T_v) temperature for Δ_j it is possible to determine T_r and T_v using data fitting techniques. For broadband CARS, ω_2 has a range of values; the Stokes laser intensity I_2 has a nonuniform intensity over this range; and the CARS signal I_3 is dispersed using a spectrometer. In this case, $I_3(\omega_3)$ as measured by a detector attached to the spectrometer, is a convolution of the pump laser profile, the Stokes laser profile, the Raman line profile and the instrument function of the spectrometer-detector system. Provided these convolutions are appropriately accounted for, the values of T_r and T_v can be found using the data fitting techniques.

3. THE EXPERIMENTAL ARRANGEMENT

The laser beams crossed at a point (folded box car) restricting the dimensions of the interaction volume and resulting in very high spatial resolution. The flow was the pulsed supersonic flow produced in a SCRAMJET model at the exit of a nozzle of a free piston shock tunnel (Stalker 1972). The flow produced by this nozzle corresponds to the upstream conditions of the intake of the SCRAMJET engine studied in previous work (Stalker et al 1984 and Stalker et al 1988). The objectives of the experiment was to measure the temperature and nitrogen species density of the supersonic stream in the intake just before combustion. However, only the temperature measurements are reported here. The flow conditions in the shock tube and the nozzle were calculated using an algorithm (Vardavas 1984), which took into account chemical rate processes, but assumed $T_v = T_r = T$ throughout.

The CARS system employed a doubled Nd:YAG laser giving approximately 1J per pulse at 1064nm with a typical pulse width of 8.5ns. Frequency doubling produced a beam of 180mJ at 532nm which was further divided into two pump beams. The remaining 1064nm was doubled to pump a broadband dye laser which produced a 42mJ beam at 607nm. The Stokes and pump beams were then combined for folded box phase matching with a 500mm focal length lens. At this lens the pump beams were separated by 25mm giving a spatial interaction region approximately 4mm in length and 250μm in radius. A 10% reflecting beam splitter before the main focusing lens generated two interaction regions, one in the test section of the shock tunnel, the other in a calibration cell containing air at atmospheric pressure. Care was taken to ensure that both interaction regions had the same confocal parameters so that the reference signal from the cell could be used to normalise the laser beam characteristics for the particular shot. The CARS signals generated were passed into a spectrometer imaged onto a gated dual microchannel plate image intensifier, fibre optically coupled to a charge injection device (CID) camera. The overall gain was about 10^6 and the final camera resolution of 0.01nm/pixel. The chip was cooled by a Peltier device to 258K to reduce thermal noise.

An IBM compatible PC synchronised the triggering of the laser and camera system with the establishment of steady flow in the test section. Before the shock tunnel was fired, the laser was operated at 10Hz repetition rate for approximately 20 minutes while slowly increasing the output to full power to ensure that the laser and harmonic generating crystals would achieve thermal equilibrium. On firing the shock tunnel the recoil of the compression tube activated a motion transducer whose signal was used to halt the repetitive firing mode of the laser and initialise it for a single shot. The shock wave moving down the shock tube triggered a pressure transducer in the nozzle reservoir region which activated counter-based delay circuits to trigger the laser flashlamps, Q-switch and camera to capture an image when equilibrium flow conditions were established. The camera was gated simultaneously with the Q-switch to provide a 90ns detection window around the laser pulse.

4. RESULTS

A series of CARS spectra were recorded for flow enthalpies H = 4.3, 8.7, and 12.1 MJ/kg. A significant amount of processing of the raw data was required to account for: the profile of the Stokes laser; fluctuations in laser intensities; background noise and convolution of the CARS signal with the instrument function. The experimental data were divided by a Gaussian fit to the dye laser spectrum to take into account the finite bandwidth of the dye laser, while Fourier transform analysis was used to remove the high frequency structure caused by the dye laser. A spectrum obtained from the calibration cell is presented in figure 1(a) The high frequency noise superimposed on the spectra is due to intensity fluctuations in the spectrum of the dye laser and shot noise from the CID camera. The processed spectra for the three conditions are presented in figure 1(b-d). The peaks in the spectra represent the unresolved Q branch rotational lines in the (v',v") vibrational transitions in the ground electronic state $X^1\Sigma_g$ of molecular nitrogen.

To determine the rotational and vibrational temperatures, corresponding to the different CARS spectra, theoretical CARS spectra were generated from the isolated line model (Hall 1979) assuming that rotational and vibrational equilibrium was established. The use of the isolated line model is reasonable because the pressure in the test section was of the order of 100kPa during the experiment. An instrument function - determined from measurements of the of the 632.82nm HeNe line at a variety of positions and intensities across the CID chip - was used to account for the spectrometer dispersion, distortion introduced by the image intensifier and the pixel size on the CID chip, and the pump laser linewidth (0.02nm). The processed data was compared, using a least squares fitting procedure, to theoretical spectra calculated over the temperature range 250 - 3100K in 25K intervals. The temperatures obtained from the mean of three shots at each of the three enthalpy conditions in the shock tunnel are presented in Table 1 along with the calculated values (section 3.1) of flow temperatures in the free stream of the shock tunnel test section. The instrument functions for the two higher enthalpy conditions was de-convolved from room temperature CARS spectra. This was required because of a large back ground noise level in the HeNe spectra used caused unacceptably large errors in the calculation of the theoretical spectra.

Table 1. Calculated and free stream temperatures and temperatures inside the SCRAMJET inlet measured using CARS at various stagnation enthalpies

H (MJ/kg)	T [theory]	T [CARS]	p (kPa)
4.3±0.1	1160	1110 ± 390	99
8.7±0.3	2370	2930 ± 300	124
12.1±0.4	3040	3516 ± 400	114

The temperatures at low enthalpy show good agreement. Those at higher enthalpies though do not agree well. This may be due to a shock system compressing the air through a series of shocks and expansions as it enters the SCRAMJET intake. Justification for the validity of the experimental method and data analysis can be gained from the calibration cell spectra which

yielded a average room temperature of (315± 63)K. The errors quoted in this table represent the single shot error and statistical error from combination of the individual measurements.

5. DISCUSSION AND CONCLUSIONS

Saturation effects (Gierulski et al 1987) tend to cause an overestimation of the flow temperature by stimulated Raman pumping into higher vibrational levels, and is an important consideration at high laser powers. These effects have been considered in detail using the model of Herschel et a al (Herschel et al 1982). In the cases here the induced population changes in the difference between consecutive vibrational levels are less than 2.5% over 2500K. This means that saturation effects do not explain the high temperature of the two higher enthalpy results compared to the free stream calculations. The spectra in figure 1 show a great deal of noise which is believed to have been produced by mode noise in the Stokes laser and shot noise due to the very low intensity of the CARS signals. The mode noise in the dye laser produces fluctuations from shot to shot in the spectral profile of the stokes laser. The CID camera however has introduced the largest source of errors. The instrument function of the camera has been found to be a function of both the signal intensity and the signals position on the surface of the detector. This has made analysis of the signals difficult and is responsible for the errors of up to 35%. A new CCD chip camera has been constructed in house and promises lower noise and improved linearity.

6. ACKNOWLEDGMENTS

Our thanks go to Mr Paul Walsh for his competent operation of the shock tunnel and ancillary equipment, and to Mr Graeme Pike and Mr Paul Tant for their excellent craftsmanship in the construction of the scramjet model. We are grateful to Dr Richard Morgan for his design of the SCRAMJET model. This work has been financially supported by the Australian Research Council and NASA contract number NAGW 1467.

7. REFERENCES

1. Anderson, T.J. and Ecbreth, A.C., (1992), "Simultaneous Coherent Anti-Stokes Raman Spectroscopy Measurements in Hydrogen-Fuelled Supersonic Combustor", J. Propulsion, Vol. 8, No. 1, pp 7-15.
2. Bruckner, S. and F. J. Hinderlang, (1983), Proceedings of the 14th 615.
3. Eckbreth, A.C., (1988), "Laser Diagnostics for Combustion Temperature and Species", Abacus Press (now Gordon and Breach), Kent, England, UK, pp 3-24.
4. Gierulski, A., Noda, M.,Yamomoto, T., Marowsky, G. and Slenczka, (1987), "Pump-induced population changes in broadband coherent anti-Stokes Raman scattering", Optics Letters, Vol.12, No 8., pp608-610.
5. Grisch, F., Bouchardy, P. and Pealat, M., (1993) "CARS Studies in Hypersonic Flows", AIAA 24th Fluid Dynamics Conference July 6-9, 1993, Orlando, FL, # 93-3047
6. Hall, R. J., (1979), "CARS Spectra of Combustion Gases", Combustion and Flame, Vol.35, pp47-60.
7. Herchel, W. and Schreiber, P., (1982), "Saturation and Secondary Stoke effects in Coherent Anti-Stokes Raman Spectroscopy", Applied Optics Vol. 21, No. 5, 1 March 1982, pp 941-948.
8. Knapp, K. and Hinderlang, F. J. , (1981), Proceedings of the 13th International Symposium on Shocktubes and Shock Waves, Niagara Falls, 132.
9. Stalker, R. J.,(1972), The Aeronautical Journal of the Royal Aeronautical Society, 373.
10. Stalker, R. J., Morgan, R. G. and Netterfield, M. P., (1988), "Wave Processes in Scramjet Thrust Generation" Combustion and Flame, 77, 63.
11. Vardavas,I.M., (1984), "Modelling reactive gas flows within shock tunnels", Aust. J. Phys., Vol.37, p157.

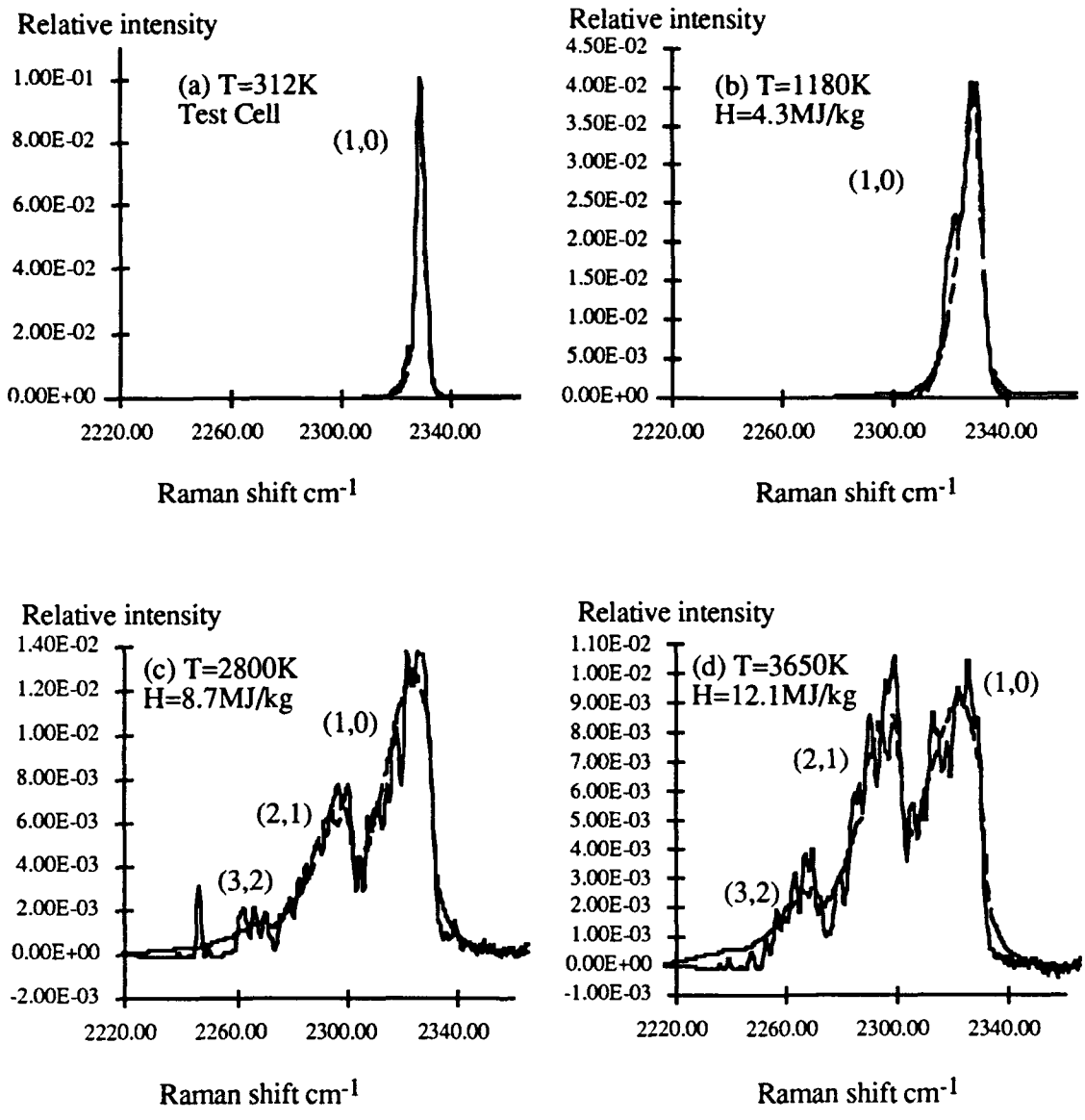

Figure 1 (a), (b), (c) and (d)

Laser-Based Methods for Hypervelocity Flow and Combustion Diagnostics.

Halina Rubinsztein-Dunlop, Peter Barker, Amberyn Thomas, Margaret Wegener, ***The Department of Physics, The University of Queensland, Qld. 4072 and*** **R.J. Stalker,** ***Department of Mechanical Engineering, The University of Queensland, Qld. 4072.***

World-wide interest in supersonic combustion and flow is being stimulated by current developments of new generation aerospace vehicles. These vehicles are expected to employ a supersonic combustion ramjet (SCRAMJET) engine as the means of propulsion for part of their launch trajectories. These will lead to making launch vehicles more efficient. Space vehicles in flight travel at hypersonic velocities. Both supersonic combustion and hypersonic flows cna be produced in shock tunnels.

Australian Researchers have played an important role in hypersonic aerodynamics since the 1960's, when free piston shock tunnels were pioneered and developed into test facilities with unique capabilities "Stalker (1972)". Recently further research has led to the development of the super-orbital expansion tube "Morgan & Stalker (1992)". This super-orbital facility has been using air and CO_2 test gases, the latter corresponding to the major atmospheric constituent of Mars. Operation is also proposed using methane, constituent of the atmosphere of Titan.

The super-orbital expansion tube operates by compounding together a series of shock tubes in such a way that very high velocity is produced for a short time in a small sample of test gas. In doing so, the quality and duration of the flow of test gas is determined by a number of complex, interacting phenomena which are not yet fully understood.These include rate chemical kinetics, laminar, transitional and turbulent viscous effects interface stability, diaphragm rupturing modes, gas ionisation and radiation, unsteady flow processes, and the transmission and amplification of disturbances. The effects of these processes can be estimated analytically and numerically, and the good agreement found between these estimates and experimentally measured parameters gives confidence that the pilot super-orbital tunnel is producing usable test flows at approximately the conditions calculated. However, precise determination of critical flow parameters is not possible without further extensive research. Many of the parameters of interest can be studied by laser-based methods.

With the availability of high power tuneable laser sources, optical spectroscopy has gained widespread application as a diagnostic tool to detect and visualize stable and reactive species in a gas phase system. Laser-based methods are non-intrusive and provide high spatial and temporal resolution when light pulses of nano- and picosecond duration are employed and probe volumes are reduced by overlapping or focusing the beams. These characteristics are of interest for example for flow diagnostics applications.

The primary parameters which the laser based optical techniques can be used to measure directly and remotely are the rotational temperature and concentration levels of selected species, as well as providing three-dimensional flow visualization of major flow features. These parameters are fundamental to understanding the flows produced, and for doing meaningful experiments therein. Temperature is coupled to density, velocity and Mach number, which are important for determining the appropriate dimensionless scaling parameters. Hypervelocity flows involve reactions, and chemical storage of energy. To understand these effects chemical composition must be known.

Linear spectroscopic techniques such as Laser Induced Fluorescence (LIF), Planar Laser Induced Fluorescence (PLIF), absorption, Rayleigh and spontaneous Raman scattering have found widespread application in mapping concentration profiles in flames. Spontaneous Raman and Rayleigh scattering are mainly used for measuring temperatures, major species (N_2, O_2, H_2O, CO_2, fuel) concentrations and density due to their lower sensitivity. Laser induced fluorescence and absorption techniques can be employed for detection of reactive species (OH,

CH, CN, NH_2, NH, NCO, C_2H, CS, S_2, etc), their temperature and general flow behaviour "Shwarzwald et.al. (1988)", "Miller et.al. (1989)", Hanson et.al. (1990)", Andersen et.al. (1989)", Mc.Millan et.al. (1989)", "Lee et.al. (1986)".

Nonlinear optical diagnostics have also proved very valuable. Among them, Coherent Anti-Stokes Raman Spectroscopy (CARS) offers the capability to measure temperature and major concentrations even in hostile environments "Eckbreth & Anderson (1985)".

Recently a lot of interest has been directed to the development and use of the Degenerate Four Wave Mixing technique (DFWM) "Dreier & Rakestraw (1990)", "Ewart et.al. (1989)". This nonlinear optical method presents a very attractive alternative to the other above mentioned methods, as it can be utilized for two-dimensional mapping of a wide range of species while avoiding problems stemming from background emission and scattering. It also ensures ease of optical access to the interaction region. The advantage of this method compared with other nonlinear methods such as CARS, for example, is that it utilizes only one laser wavelength. It has been demonstrated that this technique works for both atomic and molecular species yielding very high sensitivity so that unlike CARS it can be used for detection of minor species.

Holographic Interferometry (HI) is yet another laser-based method which provides means of visualization of the total flow field. It can render results concerning shock shape and boundary layer development as well as give quantitative data about flow density.

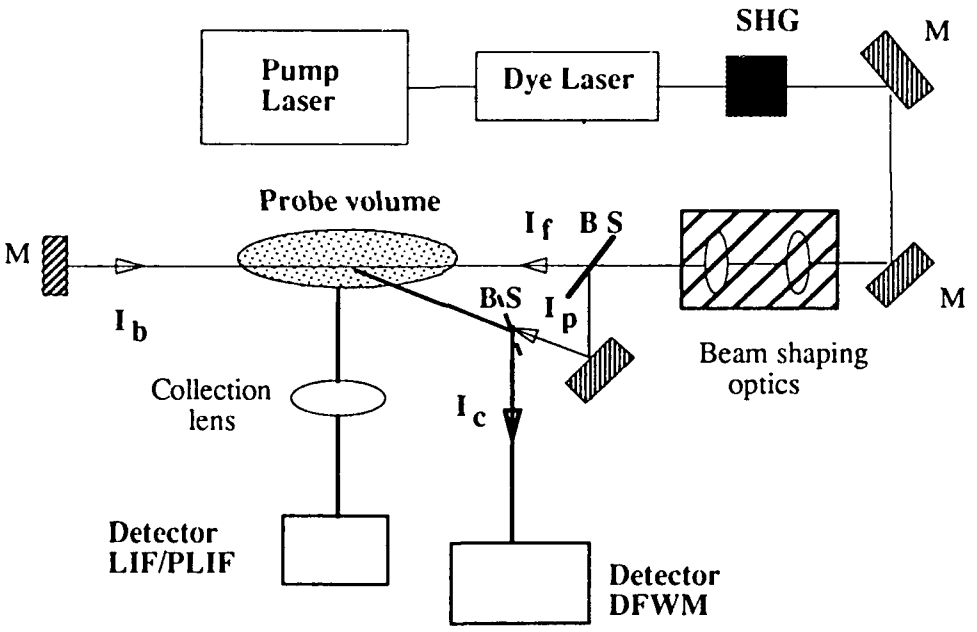

Figure 1: Experimental set-up for LIF/PLIF and DFWM. Beam shaping optics is changed depending on the experiment.

In this paper we describe the development of a versatile laser-based experimental system which is going to be used in conjunction with the super-orbital facility to provide an information about the parameters important for the characterization of the flow. The techniques which are going to be used are PLIF, DFWM and HI. The schematic diagram of the experimental set-up is shown in figure 1 for PLIF and DFWM while figure 2 depicts our set-up for Holographic Interferometry.

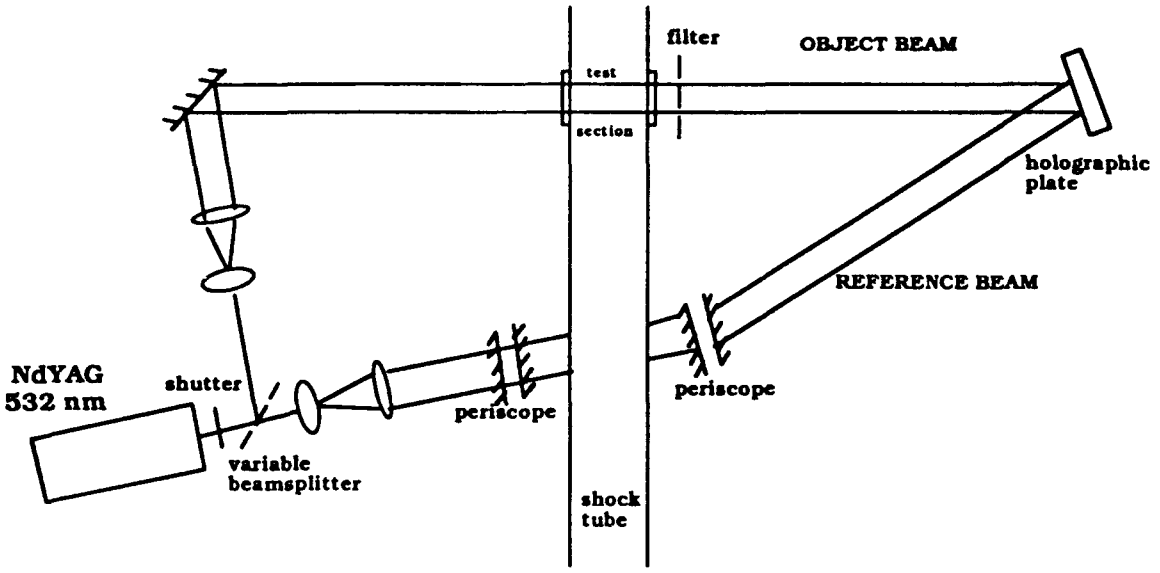

Figure 2: Experimental set-up for holographic interferometry

In the LIF and PLIF technique, resonantly tuned laser light excites molecules to specific excited states from which they rapidly return to low lying states by spontaneous emission at wavelengths characteristic for the species under study. The use of resonantly tuned laser light makes the LIF technique very sensitive as well as selective. LIF gives point measurements while PLIF gives planar information which is achieved by directing a thin sheet of laser light through the desired plane of observation. Figure 1 shows a typical configuration for PLIF measurements. Light from a versatile laser system, consisting of a pump laser pumping a dye laser equipped with a second harmonic generation unit, is directed through beam shaping optics into the probe volume (a test section with optical access). The laser is tuned to a desired transition for the species of interest. The subsequent fluorescence light is monitored perpendicularly to the direction of the incident light. The detection system consists of an image intensified Charge Coupled Device (CCD) camera and a computer for signal processing.

Laser induced fluorescence has successfully been used in many applications to give two-dimensional maps of species distribution and temperature. Qualitative species imaging has proved an effective tool for locating flames, regions of burned and unburned gases, recirculation zones and shock waves. Instantaneous images (with single laser shot) have been obtained. Both one- and two-photon PLIF have been reported to detect species such as OH, NO, O_2, CO, CH, etc. Images with simultaneous measurements at up to 10^6 flowfield points are feasible with current solid state cameras. When LIF/PLIF is performed in the high pressure regime, as found in shock tunnel flows, the method is disadvantaged by quenching occurring through the collisional de-excitation. The quenching phenomena, however, can be addressed through calibration procedures on known concentrations of specific molecules, and then relating them to PLIF measurements in the region of interest. If only relative mole fraction is of interest, for example in the studies of mixing, the fluorescence intensity data can be used directly, after the correction for background signal and nonuniform sheet illumination. The other possibility in rendering PLIF quantitative for species is to select excitation wavelengths which lead to predissociated upper states, for which the rate of predissociation dominates the collisional quenching. In such a situation collisional quenching rate becomes a constant independent of mixture composition and temperature leading to a constant fluorescence yield (fluorescence intensities are then directly proportional to species mole fraction) "Hanson et.al. (1990)", "Palmer et.al. (1992)".

The usefulness of PLIF for temperature measurements has also been demonstrated. One of the methods which can be utilized for this type of measurement is relying primarily on the

temperature dependence of the population fraction in the absorbed state. As long as the mole fraction remains relatively fixed the PLIF signal becomes a known function of the temperature "Hanson et.al. (1990)".

Degenerate Four Wave Mixing is an optical phase conjugation technique that incorporates nonlinear optical effects to precisely reverse both the direction of propagation and the overall phase factor for each plane wave component in an arbitrary beam of light. The process can be regarded as a unique kind of "mirror" with very unusual image transformation properties. In DFWM three input beams of the same frequency (one laser wavelength) overlap in a nonlinear medium under phase matching conditions (see figure 1). In the phase conjugation geometry, two of the beams - so called pump beams - counterpropagate. The third beam - a probe beam - having the same frequency intersects the two pump beams under small crossing angle. Through Bragg scattering of gratings produced by the interacting pump and probe beams a signal beam is generated with the same wavelength. The phase-conjugate signal beam propagates in the opposite direction to the probe beam path. This signal is dependent on the intensities of all three input waves. The spectroscopic response of the medium (through which the waves are propagating) to the applied electric fields is contained in the complex third order susceptibility. When the frequency of the laser matches that of an atomic or molecular electronic transition there will be a resonance enhancement of the DFWM signal.

In an unsaturated and optically thin medium the resonance DFWM signal is proportional to N^2, where N is the local concentration of the species in the interaction region, which is responsible for the nonlinearity of the medium. Consequently, a laser tuned to an atomic or molecular resonance will give DFWM signal in the form of a reflected beam whose intensity profile is determined, inter alia, by the value of N^2. Successful implementation of DFWM for mapping of concentrations has been demonstrated for several species "Dreier & Rakestraw (1990b)". It also has been shown that DFWM can be used for temperature measurements "Dreier & Rakestraw (1990a)". In the saturation regime the squared dependence of the DFWM intensities over the local concentrations is still valid. If *Boltzman* distribution can be assumed within the rotational manifold then Boltzmann plot can be used to derive the rotational temperatures.

The practical experimental arrangement shown in figure 1 emphasises that with only minor modifications to previously described set-up for PLIF planar DFWM can be utilized simultaneously. A beam splitter is placed after beam shaping optics to divide the incident light beam into two strong counterpropagating pump beams and a weak probe beam, which then enter the interaction region. The conjugate signal beam is extracted by placing another beam splitter in the path of the probe beam. The signal is detected by a CCD camera. The simultaneous PLIF and DFWM measurements will then render complementary information about the studied species.

The most important feature of the use of DFWM for imaging is that the entire image information can be extracted in one single collimated beam. There is no need for large collection angles for image reconstructions as in most other techniques - for example in PLIF technique. The high sensitivity together with the directionality of the DFWM signal beam is the basis for the measurements in inaccessible situations.

Interferometry is based on th principle that distortions acquired by a light wave on passing through an object field can be encoded and made visible by interference with a reference wave. In the case of a gas object field, the interference fringes represent changes in the gas density (integrated over the path of the light). Holographic interferometry produces a three dimensional image overlaid with interference fringes caused by changes in the object and hence provides an opportunity for obtaining infprmation in three dimensions about the density distribution in an object field.

Double exposure holographic interferograms are used in our laboratory to record one instant of flow compared with another, as can be seen in figure 2. The 532 nm output from a frequency doubled NdYAG injection seeded pulsed laser is used for illumination. Each exposure (one

pulse) lasts less than 10 ns, ensuring that the flow field will appear frozen during the exposure time, even for high flow velocities. The reference beam is diverted around the shock tube. The object beam passes through the test section perpendicularly to the flow and through an interference filter to combat self luminescence of the shock wave. A variable beam splitter is used to adjust the intensities of the reference and object beams to optimise fringe quality. This adjustment is very important as there is considerable absorption of light in the tube. Interferograms are recorded on reusable thermoplastic plates. The images are conviniently reconstructed using a single mode HeNe laser. The reconstructed images, as seen from a number of different viewpoints, are recorded digitally with a CCD camera. Each undergoes Fourier transform-based image processing to isolate the desired phase information. Some knowledge of the physical set-up enables conversion from phase to density. Finally in a process of a tomographic reconstruction, the series of two-dimensional maps obtained from each interferogram will be combined into a three-dimensional map of the density at all points within the test section "Trolinger et.al. (1992)".

Preliminary experiments have been performed using a set-up as described above but with a flame substituted for the test section of a shock tube. A flame represents a source of gas flow and of broadband radiation. Our results indicate strongly the feasibility of the method.

References:

Andersen P., Bath A., Gröger W., Lüft H.W., Meijer G. and Meulen J.J. , (1989) Appl. Optics, **27**, 365.

Dreier T. and Rakestraw D.J., (1990a), Optics Lett. **15**, 72 .

Dreier T. and Rakestraw D.J., (1990b), Appl. Phys. B50, 479.

Eckbreth A.C., Anderson T.J. , (1985), Appl. Optics, **24**, 2731 .

Ewart , Snowdon P. and MagnussonI., (1989), Optics Lett. **14**, 563.

Hanson R. ,Seitzman R., and Paul P.H., (1990), Appl. Phys. **B 50**, 441.

Lee M.P., Paul P.H. and Hanson R.K., (1986), Optics Lett. **11**, 7.

Miller J.A. et.al. Ibid. **20**, 673 (1989). Miller J.A. et.al. Ibid. **21**, 965 (1986). Atakan B. and Wolfrum J. , (1991) Chem. Phys. Lett. **178**, 157.

Mc.Millan B.K., Lee M.P. , Paul P.H., and Hanson R.K., (1989), AIAA-89-2566, 25th Joint Propulsion Conference, Monterey, CA.

Morgan R.G., Stalker R.J. , (1992) Proc. XVIII Int. Symp. on Shock Waves, Sendai, '91, (Springer Verlag) 1031.

Palmer J.M., McMillan B.K. and Hanson R.K., (1992), AIAA 92-0762, 30th Aerospace Science Meeting, Reno, Jan.

Schwarzwald R. , Monkhouse P. , and Wolfrum J., (1988), Symposium (International) on Combustion, The Combustion Institute **22**, 1413

Stalker R.J., (1972) Aero.J. of Royal Aero. Soc., June, 374.

Trolinger J.D., et.al., (1992), NATO Advanced Research Workshop - New trends in instrumentation for hypersonic research, France, April.

Velocity Measurement Using Particle Image Velocimetry

I. C. Shepherd and R. F. La Fontaine

CSIRO Division of Building, Construction and Engineering,
P.O. Box 56, Highett, Victoria 3190, Australia.
Tel: +61 3 252 6160; FAX: +61 3 252 6252

ABSTRACT

The theory and application of Particle Image Velocimetry is presented. A digital system that was developed at the CSIRO Division of Building, Construction and Engineering is described. Examples of measurements and a guide to possible future uses of PIV is presented.

INTRODUCTION

Particle Image Velocimetry (PIV) is a relatively new technique of flow measurement which is based on flow visualisation. A transparent fluid is seeded with light scattering particles which are assumed to follow the fluid motion. For two-dimensional measurements, the flow is illuminated by a plane sheet of light, and the motion of the particles in the plane recorded by imaging the illuminated plane on a recording medium, as in flow visualisation. In PIV, velocity information is encoded onto the image by rapidly modulating the light in a predetermined fashion. Typically two flash illuminations, displaced a known amount in time, are superimposed on a single image frame so that each illuminated particle produces two dots on the film. In this way, the displacement of each particle, over a known amount of time, is recorded. Thus, a complete field of movement is recorded on a single image. In the Particle Tracking technique, individual particles are identified as "before and after" pairs, prior to determining the displacement of each. However, where data is required at many points simultaneously on the plane, many marker particles are needed and tracking becomes imposibly complex. PIV uses a different approach.

The image is stored digitally or on film, and interrogated one small area at a time by Fourier transforming the local distribution of image brightness. For digital images, this is can be done on a computer. For images stored on film, this is accomplished by passing a fine laser beam through the point of interest on the film negative and collecting the transmitted light in a lens. If the lens is positioned one focal length from the film negative, the Fourier transform will appear at the back focal plane of the lens. The spacing and orientation of the fringes produced in the Fourier transform, are related to the average displacement of the particle images in the target area. The target area must be small enough to assume that the velocity is essentially constant.

Reviews of PIV techniques and theory are given by Adrians (1983), Shepherd et al (1991) and Shepherd and La Fontaine (1992). The method has been used at CSIRO to map velocity distributions around various bodies, and in fan and pump housings. The unique feature of this method is that it utilises a continuously variable illumination function to record the image. The illumination function is designed to eliminate much of the computation to resolve velocities. This paper describes the system and gives examples of its application.

THEORY

Shepherd et al (1991) showed that the fringe pattern revealed by the Fourier transform, is the product of a broad pattern, which is related to the size and distribution of individual particle images, and an envelope function, which is related to the Fourier transform of the illumination history. A one dimensional form of the relationship is illustrated diagrammatically in Fig. 1. Since all the relevant information resides in the envelope function, the objective of analysis is to determine the scale and orientation of the envelope which best fits the observed pattern. For double-pulse illumination, the envelope has the form of Young's fringes and the fitting process amounts to a further two-dimensional Fourier transform of the intensity of the fringe pattern. However, much can be gained by invoking more general illumination functions, designed to produce envelopes which are better defined and thus reduce processing time.

For example, Lourenco and Krothapalli (1987), Cenedese and Palialunga (1990) and Sharp et al (1989) have used more than two pulses to sharpen the fringes in the Fourier transform plane. Illumination of the form

$$I = (1 + cos(\omega t))\, W(t) \qquad (1)$$

where I = illumination intensity,
ω = radian frequency $2\pi f$.
f = frequency,
W = the time window function and
t = time.

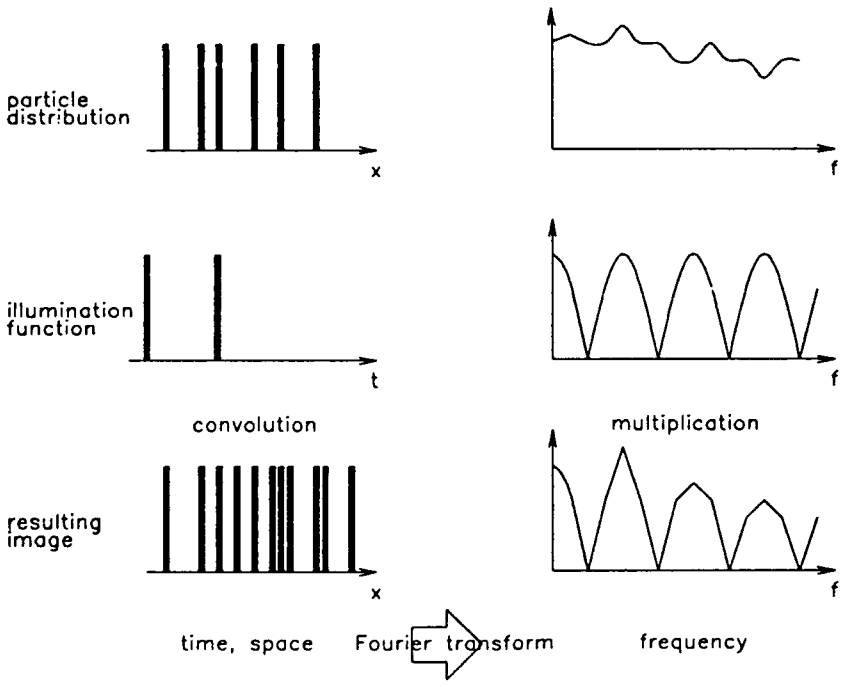

Fig. 1 Diagram showing the role (in one dimension) of the Fourier transform in analysing a double flash exposure.

was suggested by Shepherd et al (1991). The window function $W(t)$ could be a smoothing window of cos^2 form or a ramp to indicate directional sign. The envelope which results from a

function of this type has three narrow ridges, one passing through the origin and one to each side (and parallel to) the central ridge. A one-dimensional illustration of the fringe formation is shown in Fig. 2. The processing required to estimate the band spacing and orientation is greatly reduced since a further Fourier transform is unnecessary.

The flow vector is often not determined completely. The sign of the flow direction is clearly ambiguous if a symmetric illumination function is used. With an asymmetric illumination function, the sign of flow direction is evident on the flow image but less clear in the Fourier transform plane where it is reflected in the phase gradient. If the optical method of Fourier transform is used, the phase information is not retained in the intensity pattern of the fringes, so the sign of direction is lost. An important advantage of direct digital image analysis is that the phase information is preserved in the complex Fourier transform. Thus the sign ambiguity can be resolved provided a non-symmetric illumination function is used. Furthermore, if the image is stored digitally, the direction sign can also be determined from the image itself. Experience has shown this to be more reliable than operating in the Fourier transform plane.

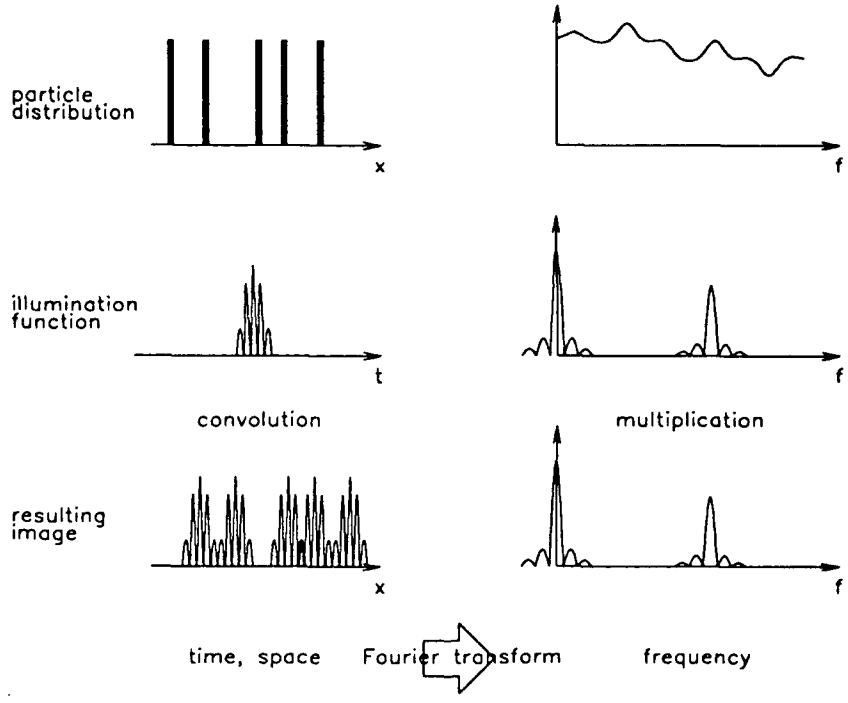

Fig. 2 Diagram of the fringe pattern generated by a tone burst illumination

A DIGITAL PIV SYSTEM

While the optical Fourier transform with a lens is elegant and effectively instantaneous, it does have liabilities. One is the loss of important information related to the sign of the direction, as described above. Another is that the mechanical process of traversing a laser beam across a grid of points on the film is ultimately the limiting factor in the speed of data processing. The speed is limited to a few points per second. With a PC equipped with an array processor, the time to perform a digital Fourier transform is negligible so that the digital system is faster in terms of processing speed.

A digital system has been developed at CSIRO for general use in flow research. Digital images of the flow marker are captured with a Kodak Megaplus camera(1280 x 1024 pixels). Fourier transforms (FFT) of small areas of the image are then performed directly by an array processor installed in a PC. The system, named FLOMAP, incorporates three suites of routines. One suite controls and synchronises the illumination and image capture, one processes the image into velocity data and the other provides post-processing operations like merging, interpolating, ensemble averaging and editing. Menu driven choices are available in all the routines.

The image shown in Fig. 3, of the flow leaving the trailing edge of a thick plate, was made in a water tunnel with hydrogen bubbles of 50 to 100 μm diameter as markers. Illumination was provided by a 5 W Ar-ion laser through an Acousto-Optic Modulator (AOM), which allowed the shape of the illumination function to be controlled, to a glass rod where it was expanded into a sheet of light. The AOM and camera shutter were controlled by the PC.

At each interrogation point, the intensity of a small area surrounding the point is Fourier transformed in two-dimensions to obtain a fringe pattern. With the illumination function described above, the typical pattern consists of three fine, parallel bands as shown at the top left-hand corner of Fig. 4, which is the FLOMAP screen displayed while reducing images to velocity vectors. The orientation of the bands is determined by integrating the intensity along a straight line at various angles through the centre, while searching for a maximum. The fringe spacing is determined by integrating along straight lines at the fringe orientation, but at increasing distances from the central fringe, while searching for the maximum. The array processor allows about 30 points to be processed per second.

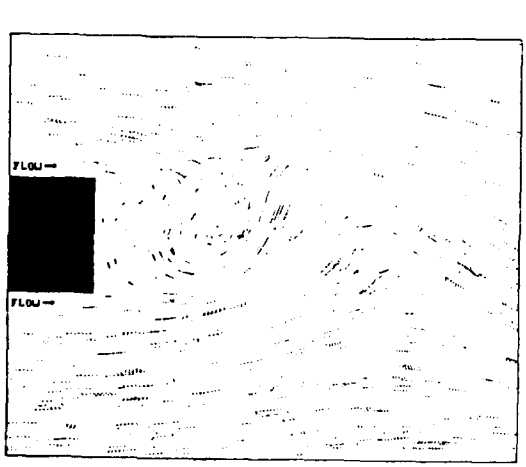

Fig. 3 Streak pattern behind a plate

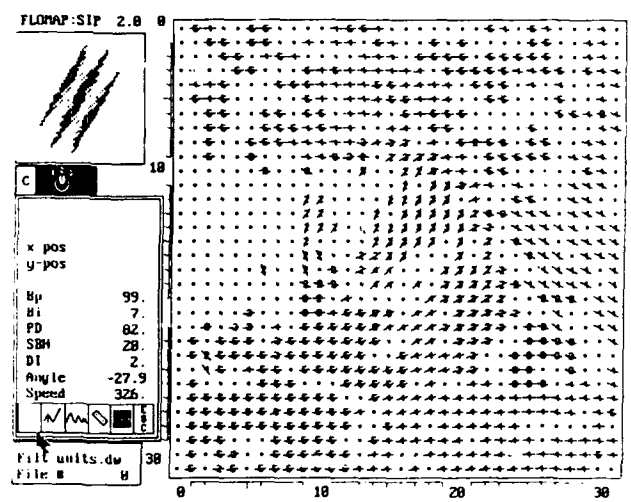

Fig. 4 Screen for automatic analysis of frame

Figure 5 displays the velocity field as a collection of vector arrows after the post-processing software had interpolated the missing data points. There are still a few remaining blanks in the flow field close to the trailing edge and in the cores of vortices. The velocity at those areas was outside the dynamic range of the system.

CONCLUSIONS

An improved method of producing PIV fringe patterns for velocity measurements in fluids was described. The FFT bands were sharper and brighter than the Young's fringes obtained using the normal technique, and a Fourier transform (or equivalent averaging process) of the fringe pattern was not required.

A system based on a high resolution digital camera was described. The processing rate was about 30 points per second and the directional ambiguity was resolved automatically.

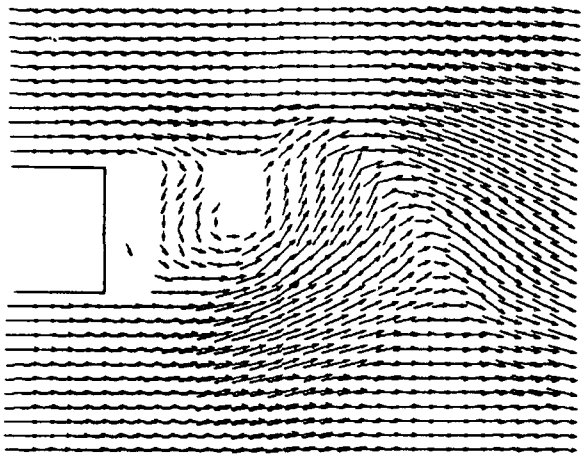

Fig. 5 Processed velocity vectors

ACKNOWLEDGMENT

The authors wish to express appreciation to Mr J. Wu of the CSIRO Division of Building, Construction and Engineering for providing some of the data presented.

REFERENCES

ADRAIN, R J AND YAO, C S (1983) Development of pulsed laser velocimetry for measurement of turbulent flow. Proc. 8th Symposium on Turbulence, University of Missouri-Rolla, USA, 170-186.

CENEDESE, A AND PAGLIALUNGA, A (1990) Digital direct analysis of a multi-exposed photograph in PIV. Experiments in Fluids, 8(5), 273-280.

LOURENCO, L AND KROTHAPALLI, A (1987) Role of photographic parameters in laser speckle or particle image displacement velocimetry. Experiments in Fluids, 5(1), 29-32.

SHARPE, J P, GREATED, C A, GRAY, C AND CAMPBELL, D M (1989) Measurement of acoustic streaming using particle image velocimetry. Acustica, 68(2), 168-172.

SHEPHERD, I C ; LAFONTAINE, R F WELCH, L W ; SORIA, J AND PEARSON, I G (1991) Measurement of Instantaneous Flows Using Particle Image Velocimetry. Second World Conference on Experimental Heat Transfer, Fluid Mechanics and Thermodynamics, Dubrovnik, Yugoslavia, June 23-28.

SHEPHERD, I C ; LAFONTAINE, R F (1992) Mapping instantaneous velocity fields using Particle Image Velocimetry. Eleventh Australasian Fluid Mechanics Conference, Hobart, 14 - 18 DEc. 1992.

LIGHT SCATTERING MEASUREMENTS IN A CO-FLOWING JET

Andrew Snowden & Simon Henbest
Defence Science & Technology Organisation, Aeronautical Research Laboratory
Melbourne

ABSTRACT

Simultaneous measurements of two scalar quantities, biacetyl vapour concentration and micron-sized particle concentration, issuing from a round nozzle into a lower velocity uniform co-axial flow are presented. The biacetyl concentration was measured using laser induced fluorescence (LIF) and the particle concentration using Mie light scattering (MLS). Details of the experimental methods are given and some of the problems encountered in carrying out the work are detailed.

NOMENCLATURE

D	nozzle diameter
FWHM	Full Wave Half Maximum
LWP	Long wave pass
r	Distance from nozzle axis
z	Axial distance from nozzle exit
γ	Fluctuating concentration
Γ	Mean concentration
τ	Transmission
λ	Wavelength (nm)

Subscripts

B	Biacetyl vapour
P	Particles
C	Centreline
O	Nozzle exit centreline value

Overbar temporal average

1. INTRODUCTION

Many engineering problems involve the dispersion of small particles using turbulent mixing processes. Here, a simple two-phase flow experiment in a moderate Reynolds number fully turbulent co-flowing jet has been carried out. One of the aims of this experiment was to determine the adequacy of using micron-sized particles as scalar markers of the jet fluid. Kennedy (1989) has carried out similar experiments for a round jet dispersing into quiescent air. In the measurements of Kennedy, the correlation coefficient between the fluctuating particle concentration and the fluctuating jet fluid concentration was significantly less than unity. Kennedy was unable to determine whether this diminution of the correlation coefficient was owing to a lack of flow fidelity of the particle field or was owing to the contributions from the uncorrelated marker shot noise on the particle concentration signal and the uncorrelated electronic shot noise on the jet fluid concentration signal.

2. EXPERIMENTAL APPARATUS & METHODS

2.1 WIND TUNNEL

Figure 1 details the flow under investigation: a 10 $m\text{-}s^{-1}$ flow from a 10 mm round jet issuing into a uniform co-axial flow of 5 $m\text{-}s^{-1}$. For more detailed information on the wind tunnel see Henbest & Yacoub (1992).

2.2 SEEDING OF ROUND JET

The round air jet was seeded with micron-sized particles and/or biacetyl vapour. Air was seeded with micron-sized dibutyl-phthalate oil particles using a TSI 9306 particle generator. The mean aerodynamic diameter of particles so generated is quoted by Agarawal & Johnson (1981) as 0.8 μm, with a geometric standard deviation of 1.9 (see their Fig 3). The particle generator output concentration is of order 10^{13} particles-m^{-3}. A separate supply of air was seeded with biacetyl vapour as shown in Figure 2. Air enters the bottom of a pressurised canister, bubbles through a sump of biacetyl, passes over fibreglass cloth saturated with biacetyl and passes out through the top of the canister. It was necessary to provide a slow, counter-flow of biacetyl over the fibreglass cloth using a small pump. The two seeded streams are combined prior to entering the central nozzle assembly in the wind tunnel (see Henbest & Yacoub).

2.2 LIGHT SCATTERING SYSTEM

A Lumonics TE-860 Excimer laser was used to generate 10ns pulses at 308 nm and pump a Lumonics Hyperdye-300 pulsed dye laser using Stilbene 420 in methanol to produce pulses at 416 nm. The 416 nm output pulses were passed through a fibre optic link to the light scattering apparatus shown in Figure 3. The output from the fibre optic coupler was passed through a beam expander/collimator and focussed using a 500 mm biconvex lens. The waist of the focussed beam was nominally 0.5 mm in diameter. All photo-multiplier tubes (PMT) used were EMI 9814B. PMT2 was used to detect the particle Mie light scattering (MLS) signal. The f1.4-50 mm camera lens (L2) and 0.08 mm slit (S2) gave a detected beam length of 0.64 mm at the waist. PMT3 was used to detect either particle MLS or laser induced fluorescence (LIF) from the biacetyl vapour. The lens system (L3) was comprised of a 175 mm dia, f = 450 mm and a 175 dia, f = 250 mm plano-convex lens, which when coupled with a 0.2 mm slit (S3) gave a detected beam length of 0.36 mm at the waist. The outer 50% of L3 was masked to reduce the transverse spherical aberration at the focus. Optical interference filters (F3) were used to pass the wavelength shifted LIF and to reject the elastic MLS. To detect MLS with PMT3, it was necessary to use neutral density filters to reduce the MLS intensity below the saturation level of the PMT3 anode.

The shot energy of each pulse was detected using PMT0 and used to normalise the PMT2 and PMT3 outputs. The data acquisition system is described in Kennedy (1989). In the present work, the trigger for the 70 nano-second gating of the PMT signals, prior to the analogue to digital conversion, was taken from another PMT (not shown) which detected the output from the Excimer laser.

2.3 FILTER SELECTION

Figure 4 (from Kennedy 1989) shows the absorption-emission spectrum of biacetyl. The peak in the absorption spectrum is centred about 400 nm (Epstein 1977) and the wavelength shifted emissions are made up of a long-lived phosphorescence and short-lived fluorescence. The phosphorescence is strongly quenched by oxygen and the fluorescence emission dominates (Groh 1953). Kennedy has confirmed the linearity of the fluorescent emission with incident intensity.

Figure 5 details the spectral transmission characteristics of various filters. The 500nm and 550nm LWP filters had inadequate rejection of the MLS and were unsuitable. The 10 nm FWHM bandwidth filters centred about 486nm and 514nm had excellent rejection of MLS at

416nm; however, the transmitted LIF was low and a high PMT3 gain was necessary, leading to an unacceptable electronic shot noise (ESN) of order 30% rms relative to the mean. The 40nm FWHM filter centred about 500nm gave adequate MLS rejection and enabled PMT3 to be operated at moderate gain. The ESN was of order 14%. To further improve the rejection of MLS, the particle concentration was reduced significantly. The approximate volume fraction of particle seeded air was 25% and the remainder was made up of biacetyl vapour seeded air or clean air.

3. EXPERIMENTAL RESULTS

Three sets of measurements were taken

(i) PARTICLE (LOW GAIN) - PARTICLE (LOW GAIN). The optical system was set up to measure the particle concentration using PMT2 and PMT3 (no filter on PMT3). The gains of the PMTs were relatively low and the combined ESN and marker shot noise (MSN) on PMT2 was 2% and on PMT3 was 4%. For this case the seeding was 25% particle seeded air and 75% clean air.

(ii) PARTICLE (LOW GAIN) - BIACETYL (HIGH GAIN). Here the gain on PMT3 was high and the combined ESN and MSN was of order 14%. For this case the seeding was 25% particle-seeded air and 75% biacetyl vapour seeded air.

(iii) PARTICLE (LOW GAIN) - PARTICLE (HIGH GAIN). The optical set up was identical in all respects to case (ii), except the 500nm-40nm FWHM interference filter F3 was replaced with a neutral density filter of optical density 4 ($\tau = 10^{-4}$) to reduce the MLS intensity to that of LIF signal from PMT3 in case (ii). The seeding was as in case (i).

Figure 6a shows the centreline concentrations normalised by the centreline nozzle exit concentration for each of the six measurements detailed above. The agreement between all measurements is good. Figure 6b shows cross-stream concentration profiles measured 16 diameters downstream from the nozzle exit. The concentrations have been normalised by the centreline values. Again, the agreement is reasonable. Figure 6c shows cross stream profiles of the correlation coefficient for two fluctuating concentrations measured 16 diameters downstream from the nozzle exit, eg: for the PARTICLE-BIACETYL measurements the coefficient is $\overline{\gamma_B \gamma_P}\ (\overline{\gamma_B^2}\ \overline{\gamma_P^2})^{-0.5}$. For the PARTICLE(LOW GAIN) - PARTICLE(LOW GAIN) measurements the correlation coefficient is high. The correlation in the PARTICLE-BIACETYL measurements is diminished. The question is, has the correlation coefficient diminished due to lack of correlation between the particle fields and the biacetyl vapour fields in the jet or has the influence of the uncorrelated ESN and MSN led to a diminution of the coefficient ? The results of the PARTICLE(LOW GAIN) - PARTICLE(HIGH-GAIN) measurements show a similar diminution of the correlation coefficient when PMT3 gain is high. The conclusion is that ESN and MSN have led to a diminution of the correlation coefficient and that there is no measurable difference between the particle and concentration fields, at least for the measurements presented here.

4. DISCUSSION AND CONCLUSION

Within the accuracy of the measurements presented, it has been shown that both biacetyl vapour and micron-sized oil particles are adequate markers of the jet fluid. No systematic measurable difference occurs between the biacetyl vapour field and the particle field, for the flow case studied. The agreement between the measured centreline and cross-stream profiles show that even high PMT gains do not affect mean values. However, the significant decrease in correlation coefficient with increasing PMT gain clearly demonstrates the need to keep

PMT gains to a level where uncorrelated ESN no longer makes measurable contributions to the fluctuating values.

REFERENCES

AGARWAL, J.K. & JOHNSON, E.M. (1981) "Generating Aerosol for Laser Velocimeter seeding." TSI Quarterly, **VII** Issue 3.

HENBEST, S. & YACOUB, E. (1992) "An Experimental Investigation of an Axisymmetric Co-Flowing Jet" *Trans Multi-Disciplinary Engineering*, **GE16** No 2, 101-108.

KENNEDY, I.M.K. (1989) "Pulsed laser measurements of particle and vapour concentrations in a turbulent jet." *Exp. Fluids*, **7**, 49-55.

GROH. H.J. JR. (1953) "The fluorescence of biacetyl vapour." *J. Chem. Phys.*, **21**, 674-677.

EPSTEIN, A.H. (1977) "Quantitative density visualization in a transonic compressor rotor". *Trans ASME J. Eng Power*, **99**, 460-475.

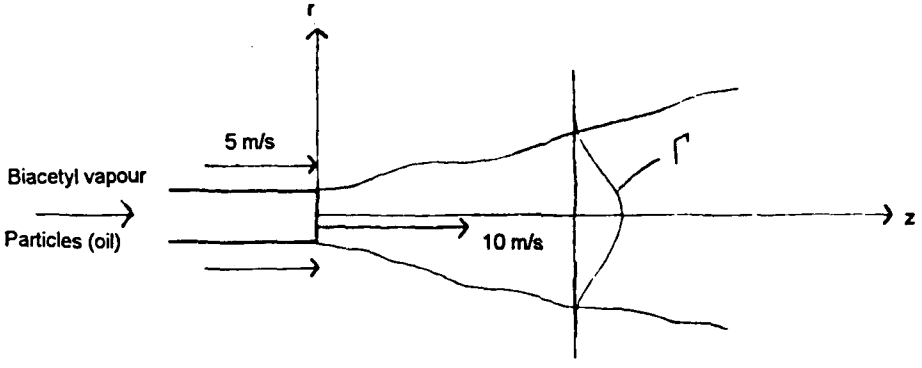

Figure 1. Flow details.

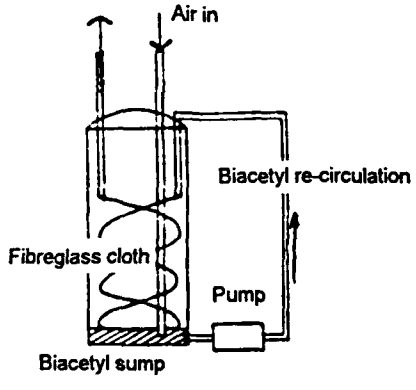

Figure2. Biacetyl vapour supply.

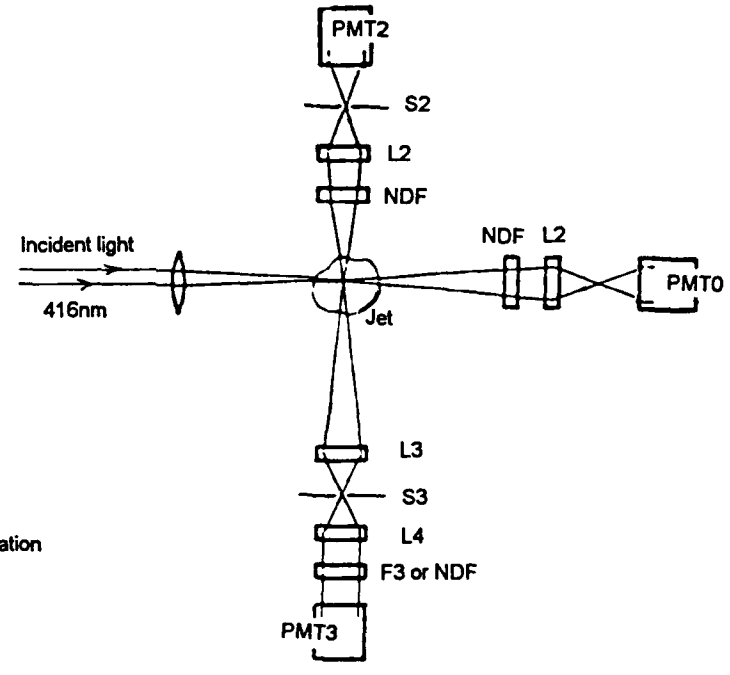

Figure 3. Light scattering apparatus.

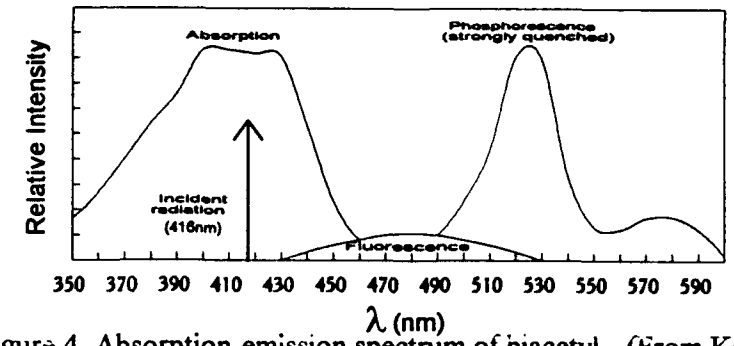

Figure 4. Absorption-emission spectrum of biacetyl (From Kennedy 1989)

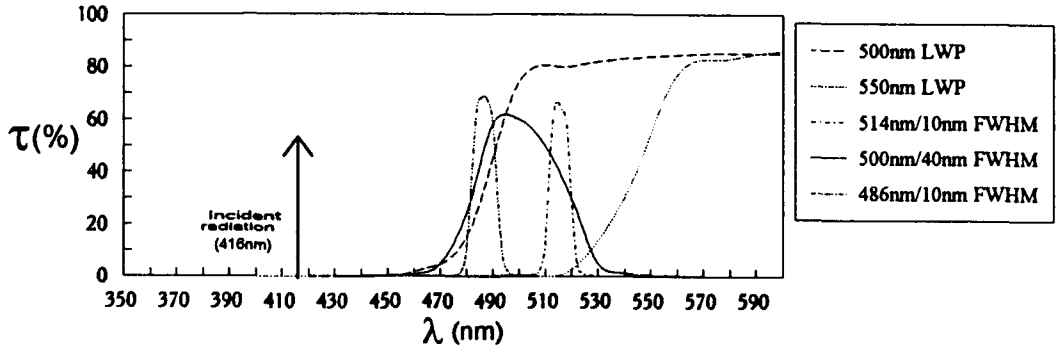

Figure 5. Filter Characteristics

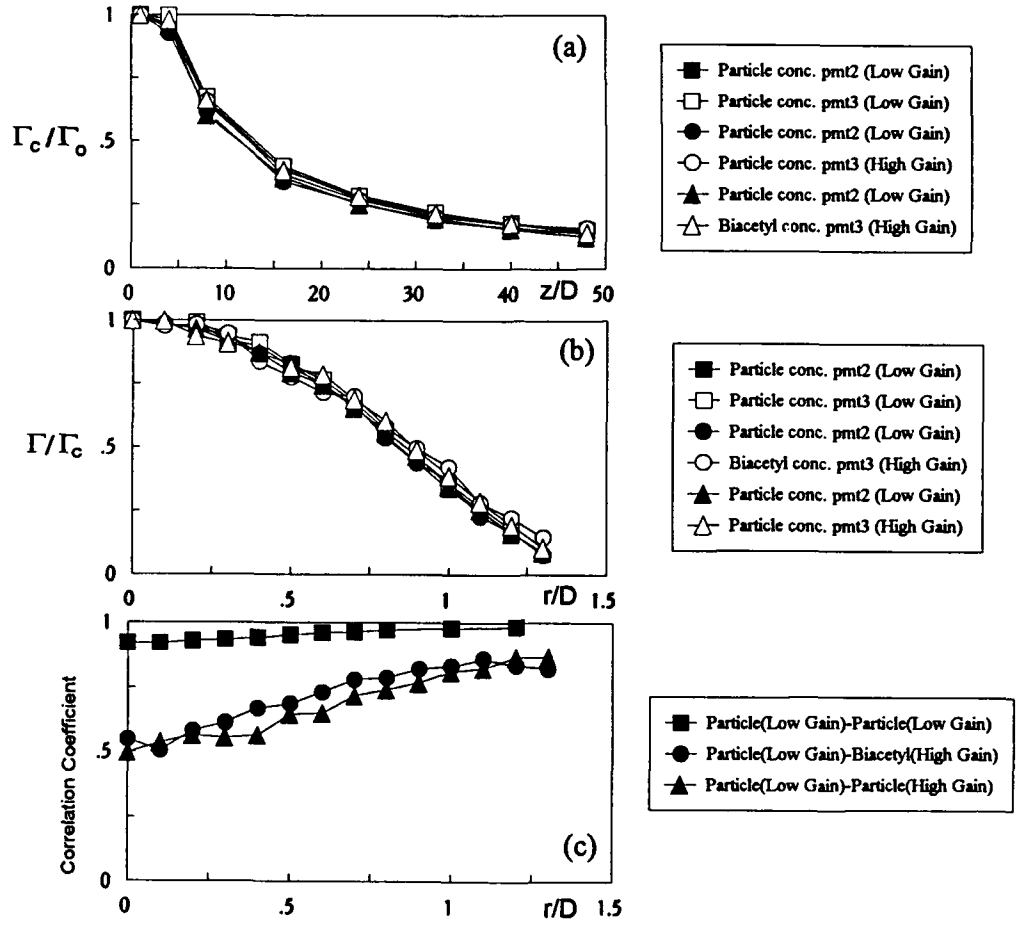

Figure 6. (a) Centreline concentrations , (b) Cross-stream concentrations at z/D=16 , (c) Cross-stream correlation coefficients at z/D=16.

Laser Induced Predissociation Fluorescence, its application to Vibrational Temperature Measurements in a Shock Layer

D.J. Sutton*, A.F.P. Houwing, R.R. Boyce & R.J. Sandeman

Department of Physics and Theoretical Physics,
Faculty of Science, The Australian National University,
Canberra, A.C.T. 0200 Australia

**Current address : Defence Science Technology Organisation,*
P.O. Box 1500, Salisbury, S.A. 5108 Australia

SUMMARY

The application of laser induced predissociation fluorescence (LIPF) to the measurement of vibrational temperatures in a shock layer flow around a cylinder in a pulsed supersonic free stream is described. Single shot spatially and spectrally resolved LIPF measurements of the vibrational temperature of O_2 are presented and a comparison with computational fluid dynamic predictions is made.

INTRODUCTION

The measurement of temperature in the shock layer on a blunt body is a useful way to test theoretical models that describe nonequilibrium reacting flows. The use of laser induced fluorescence (LIF) to make these measurements is often complicated by the problem collisional quenching (Seitzman & Hanson 1992). Collisional quenching is especially important in the application of LIF to pulsed high enthalpy flows because of the high collision rates in such environments. The development of LIPF (Kelly & Hudson 1985), where the effect of quenching is avoided by exciting the molecule to a fast predissociating state, from which the fluorescence is emitted only during the predissociation lifetime laregly overcomes this problem. Provided the predissociation lifetime is sufficiently short, the probability of deexcitation collisions is extremely small, and hence there will be insignificant quenching even at high pressures. Compared to standard LIF, however, LIPF signals are very weak and hence the presence of strong emission lines from flow impurities (Palma et al 1993), has the potential to make LIPF studies difficult in shock tunnel flows.

THEORETICAL CONSIDERATIONS

The qualitative features of the LIPF scheme are illustrated in figure 1, which shows a number of rovibrational levels defined by rotational and vibrational quantum numbers N and v respectively. The laser is tuned to the wavenumber $w_{i''i'}$ of a transition which promotes a molecule from a rovibrational level |i''> in a lower electronic state to a rovibrational level |i'> in an upper electronic state. This upper level subsequently decays by the emission of a photon of wavenumber $\omega_{i'i'''}$ to another rovibrational level |i'''> in the lower electronic state. By pumping two levels simultaneously with the same laser, it is possible to induce two fluorescence schemes. The vibrational temperature Tv may be determined by measuring the ratio ϕ_1/ϕ_2 of fluorescence from the two different schemes and is given by (Sutton et al 1993)

$$T_v = \frac{(G_{2\cdot\cdot} - G_{1\cdot\cdot})hc}{k\ell n\left(\dfrac{g_{2\cdot\cdot}\phi_1\tau_{P2}E_2 q_{2\cdots 2}\cdot q_{2\cdots 2}\cdot S_{2\cdot\cdot 2}\cdot S_{2\cdots 2\cdot}}{g_{1\cdot\cdot}\phi_2\tau_{P1}E_1 q_{1\cdots 1}\cdot q_{1\cdots 1}\cdot S_{1\cdots 1}\cdot S_{1\cdots 1\cdot}}\right)} \qquad (1)$$

where $G_{i''}$ are the vibrational energy terms; $g_{i''}$ are the degeneracy of the rotational energy levels; ϕ_i are the fluorescent yields; τ_{Pi} are the predissociation lifetimes; E_i are the laser energies

coincident with the absorption lines; $q_{i''i'}$ and $q_{i''i'}$ are the Franck-Condon factors; $S_{i''i'}$ and $S_{i''i'}$ are the Hönl-London; h is Planck's constant; c is the speed of light and k is Boltzmann's constant; the subscripts i = 1 or 2 indicate the fluorescence scheme; while the single double and triple primes refer to the levels illustrated in figure 1.

EXPERIMENTAL ARRANGEMENT

The optical arrangement is illustrated in figure 2. A pulsed ArF excimer laser operating in tunable mode was used to produce a narrowband pulse (0.02 nm FWHM), directed vertically downwards into the shock layer flow around a 25.4 mm diameter cylinder. The laser beam was rectangular in cross section and unfocussed. The region pumped by the laser in front of the cylinder was a vertical rectangular prism, with a width of 20 mm along the axis of the cylinder and a thickness of 5 mm measured perpendicular to this axis. The cylinder was mounted with its axis perpendicular to the incident flow direction. The LIPF signals were imaged into a diffraction grating spectrometer (dispersion 0.7 nm/mm). The imaging system allowed spatial resolution along the length of the entrance slit, and had a magnification of 0.2. With this arrangement, it was possible to determine the variation of LIPF signals, and hence vibrational temperatures, along a vertical line in the flow. The signals dispersed by the spectrometer were imaged onto a two dimensional detector, with an overall gain of approximately 10^6. The laser wavelength was tuned using the following method. An additional mirror was placed in the laser beam path to direct it into the flame from a H_2/O_2 burner. The fluorescence signals from the flame were then imaged onto to entrance slit of another spectrometer, set to transmit the (10,8)R(17), (10,8)P(19), (16,9)R(19) and (16,9)P(21) lines of the $B^3\Sigma u^- \rightarrow X^3\Sigma g^-$ system of O_2 at 232.0 nm. The fluorescence signal transmitted by the spectrometer was detected by a photomultiplier and output to a boxcar integrator. The tuning mirror of the excimer laser was scanned at a constant rate so that the laser scanned through its entire tuning range. The excitation spectrum thus produced was compared with the excitation spectra from earlier work (Kim et al 1991) to identify the pumping transitions. The tuning mirror was then repositioned by the stepper motor to reproduce the peak on the excitation spectrum corresponding to the desired pumping transitions.

The experiments were performed on the Australian National University's T2 free piston shock tunnel (Stalker 1967) which produced the supersonic air flow over the model illustrated in figure 2. The flow conditions were calcuated using the algorithm described by Vardavas (1984). For the flow through the nozzle, a chemical reaction rate model was used, with allowances made for vibrational freezing, using the algorithm described by Rein (1989). The test conditions calculated in this manner are summarised in table 1. In order to synchronise the firing of the laser and the gating of the 2D detector to coincide with the short steady flow period produced by the shock tunnel, it was necessary for a PC controlled sequence to be employed. Two pressure transducers situated at different positions along the shock tube were used to determine the transit time (and hence the speed) of the primary shock wave. The output of the second of these transducer was used to initiate the PC controlled sequence, which sent pulses to trigger the laser and gate the camera. The signals from the transducers were displayed on an oscilloscope to facilitate the measurement of shock speeds and pressures. A synchronisation pulse from the laser was displayed on a second oscilloscope together with the signal from the nozzel reservoir transducer. This enabled the determination of the time delay between shock reflection at the nozzle entrance and the firing of the laser. The choice of this delay is based upon an understanding of the nozzle starting processes (Smith 1966) and is chosen so that flow conditions over the cylindrical model are reasonably steady at the time the laser and detector are triggered.

RESULTS

The LIPF signals recorded by the 2D detector were transferred to a workstation for image processing, which involved the removal of background signals generated by the thermal noise of the camera and the extraction of several dispersed emission spectra from different positions above the stagnation streamline to determine the intensity of the LIPF lines, background radiation and shot noise. The LIPF lines were identified by comparison with LIPF lines

produced in a flame. In this way, the LIPF lines were determined to be the (16,12)R(19); (16,12)P(21); (10,11)R(17) and (10,11)P(19) emission lines. The dispersed fluorescence spectra contain a significant amount of background radiation, which was determined to be laser-induced, though did not appear to be significantly dependent on the laser wavelength, as it was still present when the laser was detuned from the absorption frequency. The variation of the intensity of one of the LIPF lines with distance through the shock layer is displayed in figure 3. It is apparent that there is a significant reduction in the intensity of the LIPF signals with penetration through the flow. All the LIPF lines and the laser induced background display similar behaviour, suggesting that the cause is a reduction in the intensity of the laser with distance into the shock layer. A significant level of shot noise was also present in the data. The relative level of this noise was reduced by spatially averaging the data, at the expense of spatial resolution. Such spatially averaged spectra are presented in figures 4a and 4b, together with fitted curves to the background and the LIPF lines. The curve fits to the lines are Gaussian shapes, each of identical width, superimposed on the background plateau. The fitted width is consistent with that of the instrument function of the spectrograph and detector system. The integrated line intensity was calculated as the area between the fitted Gaussian profile and the fit to the background. The ratio of the photon counts ϕ_1/ϕ_2 required for use in equation (1) is determined by dividing the integrated line intensity from one of the (16,12) lines by the integrated line intensity from one of the (10,11) lines. The positions and sizes of the two regions (a) and (b), corresponding to the spectra displayed in figures 4a and 4b, are indicated by the rectangles displayed in figure 5. The errors in the measured values of ϕ_1/ϕ_2 are estimated by determining the discrepancy between the fitted curves and the data points and the estimating the uncertainty in the background level. Because of the different number of samples used in the averaging of the data from the two regions, the errors in the measured values of ϕ_1/ϕ_2 for region (b) are much less than those for region (a). By determining the convolution of the laser profile with the excitation transitions it is found that E_1/E_2 (the ratio of laser energies used to pump the two LIPF systems) is equal to 2.5 ± 0.2.

The vibrational temperatures determined from the data given in figures 4a and 4b are presented in table 2. The predissociation linewidths, Hönl London factors and Franck Condon factors used were obtained from Lewis et al (1986), Tatum & Watson (1971) and Harris et al (1969), respectively. The percentage errors associated with the spectroscopic data are much less than those associated with the values of ϕ_1/ϕ_2 and E_1/E_2. It can be seen from the values in this table that, for region (a), there is a significant discrepancy between the value of T_v determined from the P lines and that determined from the R lines. This is a result of the difficulty of deconvoluting the LIPF signals from the laser induced background. This background contains a significant amount of spectral structure. However, an examination of different spectra at different positions in the flow shows that this structure does not contain a strong spatial correlation. Hence by spatially averaging the data over a larger region, such as region (b) in figure 5, the background is smoothed and can be easily subtracted from the data. When this is done, the discrepancy between the values of T_v determined from the different lines is removed.

The nozzle flow calculation indicates that the rotational and vibrational temperatures in the freestream are significantly different (T_r = 325 K, T_v = 1040 K). Behind the bow shock, the collision rate is much higher than in the freestream and equilibrium between rotation and vibration is quickly established. The shape of the shock wave and the temperature distribution inside were determined by a CFD Code (Mundt 1992) which accounted for nonequilibrium chemistry. This code yielded theoretical values for the spatially averaged temperatures, which are in good agreement with the experimentally measured values.

CONCLUSION

The current work has demonstrated the application of LIPF to the measurement of vibrational temperatures in the shock layer. While the presence of a laser induced background has led to noise problems, it has been possible to reduce this noise through spatially averaging the data. There appears to be significant absorption of the laser in the shock layer, resulting in a reduction in the LIPF signals.

ACKNOWLEDGEMENTS

We express our thanks to Mr Paul Walsh for his assistance with the design of the experiment and his constructive technical advice. We are grateful to Mr David Cooper and Dr Stan Newman for their work in the design and construction of the timing electronics. We are indebted to Dr Aidan Byrne for his assistance in the data reduction and to Dr Christian Mundt for his assistance with the CFD calculations. This work has been financially supported by the Australian Research Council and NASA contract number NAGW 1467.

REFERENCES

Harris, R., Blackledge, M., and Generosa, J. (1969) Rydberg-Klein-Rees (RKR) Franck-Condon factors for the O_2 Schumann-Runge system including high vibrational quantum numbers., J. Molec. Spectrosc., **30**, 506

Hanson, H.K., Seitzman, J.M. & Paul, P.H. (1990) Planar laser-fluorescence imaging of combustion gases., Applied Physics B, **50**, 441

Hiller, B. & Hanson, R.K. (1988) Simultaneous planar measurements of velocity and pressure fields in gas flows using laser-induced fluorescence., Applied Optics, **27**, 33

Kelly, P.B. and Hudson, R.S. (1985) Chem. Phys. Lett., **114**, 45.

Kim, G.-S., Hitchcock, L.M., Rothe, E.W., and Reck, G.P. (1991) Identification and imaging of hot O_2 ($v'' = 2$, 3, or 4) in hydrogen flames using 193nm- and 210nm-range light., Applied Physics B, **53**, 180

Lewis, B.R., Berzins, L., Carver, J.H. and Gibson, S.T. (1986) Rotational variation of predissociation linewidth in the Schumann-Runge Bands of $^{16}O_2$., J. Quant. Spectrosc. Radiat. Transfer, **36**, 187

Mundt, Ch.(1992) Calculation of hypersonic, viscous non-equilibrium flows around reenrty bodies using a coupled boundary layer/Euler method., AIAA paper 92 - 2856

Palma, P.C., Houwing, A.F.P., and Sandeman, R.J. (1993) Absolute intensity measurements of impurity emissions in a shock tunnel and their consequences for laser induced fluorescence experiments., Shock Wave Journal, **3**,

Rein, M. (1989) Surf : A program for calculating inviscid supersonic reacting flows in nozzles., GLACIT FM 89-1

Seitzman, J.M. and Hanson, R.K. (1992) Quantitative fluorescence imaging: A comparison of linear, predissociative and saturated pumping techniques., AIAA paper 92 - 0879.

Smith, C.E. (1966) The starting process in a hypersonic nozzle., J. Fluid Mech., **24**, 625

Stalker, R.J. (1967) A study of the free piston shock tunnel., A.I.A.A. J., **5**, 2160

Sutton, D.J., Houwing, A.F.P., Palma, P.C. & Sandeman, R.J. (1993) Vibrational temperature measurements in a shock layer using laer induced predissociation fluorescence. to be published Shock Wave Journal.

Tatum, J.B. and Watson, J.K.G. (1971) Rotational line strengths in $^3\Sigma^{\pm}$ - $^3\Sigma^{\pm}$ transitions with intermediate coupling., Can. J. Phys., **49**, 2693

Vardavas, I.M. (1984) Modelling reactive gas flows within shock tunnels., Aust. J. Phys., **37**, 157

Table 1. Theoretically Calculated Shock Tunnel Conditions

Speed of primary shock =	1.86 km/s			
Nozzle reservoir pressure =	3.1×10^7 Pa	Nozzle reservoir temperature =		3480 K
Free stream pressure =	3.0×10^3 Pa	Free stream temperatures	T_r =	325 K
Free stream Mach number =	7.8		T_v =	1040 K

Table 2. Experimentally Measured Vibrational Temperatures

region	ϕ_1/ϕ_2 (P lines)	T_v (P lines)	ϕ_1/ϕ_2 (R lines)	T_v (R lines)	T_v (CFD)
(a)	0.29 ± 0.05	2682 ± 500 K	0.35± 0.05	3473 ± 500 K	3250 K
(b)	0.31± 0.02	2890 ± 300 K	0.31± 0.02	2960 ± 300 K	3100K

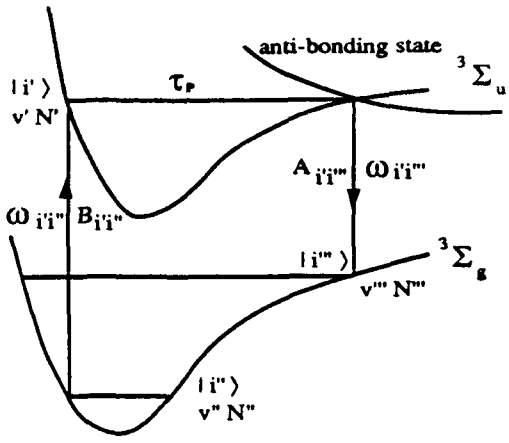

Fig 1 : Schematic of LIPF scheme.

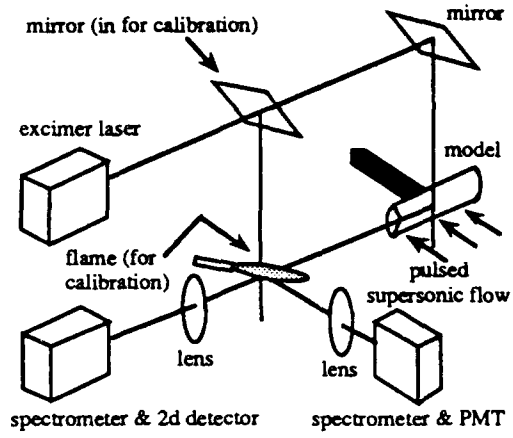

Fig 2 : Experimental arrangement.

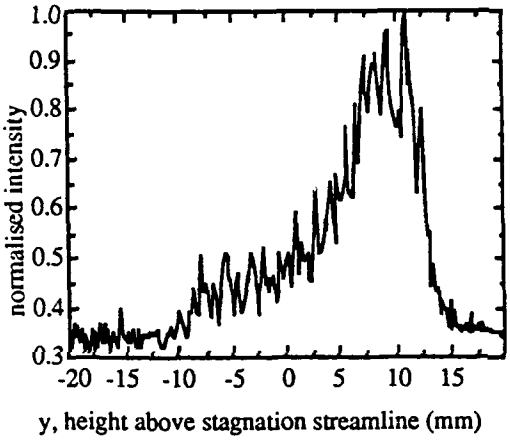

Fig 3 : Variation of LIPF with position.

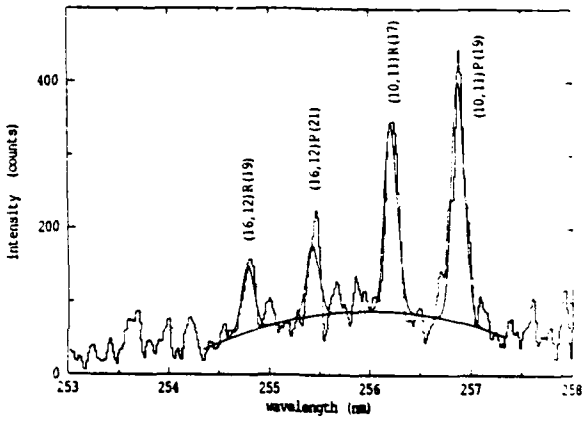

Fig 4a: Emission spectrum for region (a).

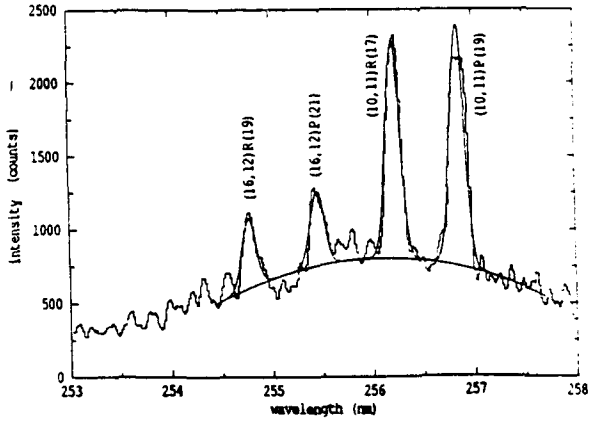

Fig 4b : Emission spectrum for region (b).

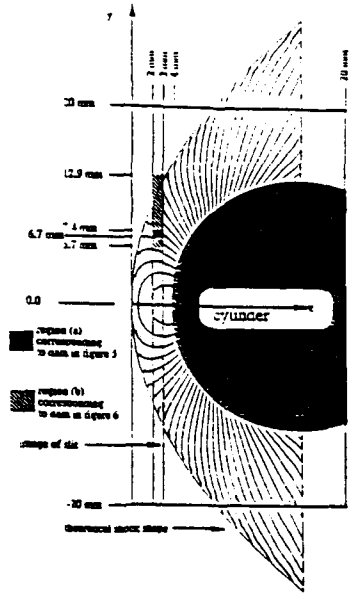

Fig 5 : Model, shock & regions interrogated.

The Development of Planar Laser Induced Fluorescence for Studies of NO in Hypersonic Flow.

Amberyn Thomas, Peter Barker, Halina Rubinsztein-Dunlop
The Department of Physics,
The University of Queensland,
Queensland, 4072.

Ray J. Stalker
The Department of Mechanical Engineering,
The University of Queensland,
Queensland, 4072.

ABSTRACT

The detailed study of hypersonic combustion processes is of great importance for the correct operation of SCRAMJETS. As nitric oxide plays an important role in the thermochemical behaviour of high temperature air, it is of particular interest to hypervelocity aerodynamicists. We report here on the development of planar laser induced fluorescence (PLIF) for studies of nitric oxide concentration and distribution in a shock tunnel environment. Preliminary PLIF and LIF experiments have been performed using an ArF excimer laser for the detection of nitric oxide in different environments. These include experiments undertaken with NO in a cell, where we were able to obtain two dimensional pictures of NO for concentrations down to 50ppm. Images and spectral fluorescence of NO in a flow situation were also recorded.

INTRODUCTION

Of recent years, the development of non-intrusive laser-based diagnostics has been a priority area for those interested in supplementing the information available from traditional flow-field measuring techniques. Of particular interest to the hypersonic community, is the use of laser-based methods as a form of flow visualisation that has the capability of providing spatially-resolved species-specific information, such as concentration, temperature and velocity (see Hanson *et al* 1990). One such technique that has to date been used for qualitative and limited quantitative imaging purposes is the two-dimensional extension of laser induced fluorescence, referred to in the literature as Planar Laser Induced Fluorescence, or PLIF (see McMillin *et al* 1991).

In PLIF, a laser beam resonant with a particular atomic or molecular species present in the flow is formed into a sheet of light that traverses the field under study. Typically, the laser has a pulsed output, such that the duration of a single pulse is sufficiently short to freeze the flow. The selected species absorbs the incoming radiation and subsequently fluoresces. A fraction of the fluorescence from the illuminated region is then imaged onto the photocathode of an intensified CCD array, maintaining spatial information. The signal received at each pixel will then be a function of the fluorescence yield from the corresponding flow-field point, which in turn represents the concentration of the particular species at that point.

Our work is concerned with the development of this technique for the study of nitric oxide in the hypersonic flow of a high enthalpy shock tunnel, known within the shock tunnel community as T4 (see Stalker 1988). Nitric oxide is a naturally occurring species in the flow and it has previously been measured using mass spectrometric techniques. (see Crane and Stalker 1977). The results obtained using this technique disagree with theoretical model predictions. As nitric oxide plays an important role in the chemical kinetics of high temperature air, it is hoped that it will prove possible to extract quantitative information from

the two-dimensional PLIF images obtained. This information will then either validate the results of the previous experimental work, or confirm the model predictions.

Ideally, we are aiming towards obtaining a two-dimensional concentration map of nitric oxide. Although PLIF has been used in a shock tunnel environment, quantitative data concerning concentration profiles has been difficult to extract (see Van Cruyningen *et al* 1990). The difficulty lies in the fact that the fluorescence yield is dependent on the quenching rate, a quantity that is highly sensitive to temperature and pressure, and the estimation of which demands a detailed knowledge of the collision cross-sections of all collision partners of the excited species. This is information that is generally not known when investigating hostile environments such as the flow produced in a shock tube.

In this paper we present PLIF results of NO obtained in both a room temperature quartz cell and a 'nozzle' flow, and we discuss a model that has been developed to predict excitation and fluorescence spectra of NO.

THEORETICAL MODEL

A simple two-level scheme fails to describe the processes involved in the excitation and subsequent fluorescence of a molecular system. A molecule is more correctly represented as a multi-level system, consisting of electronic states, each of which also has ro-vibrational levels. In an attempt to predict nitric oxide fluorescence spectra, a rate equation analysis was applied to a system where each rotational level within a given vibrational and electronic level was considered separately. Molecular constants specific to NO and the particular electronic transition of interest were obtained via a thorough literature search and included in the model. From this work, we are able to synthesise absorption and fluorescence spectra, as well as the relative populations of the excited states. The model takes into account such parameters as pressure, temperature, laser linewidth and quenching rates, and we are therefore able to model how the spectra are effected by these.

We have been unable to verify the valididity of the model for narrowband excitation in the D-X trasitions around 193nm, owing to limitations in our experimental equipment. However, the verification of the model was achieved by comparison of model predictions with an excitation scan performed on the A-X(0,0) transition of NO. This experiment was carried out at a different geographical location using the frequency doubled output of an excimer-pumped dye-laser system to excite NO in a counter-flow atmospheric pressure methane-oxygen diffusion flame. The excitation was around 226nm, and broadband fluorescence was detected at 237nm. The two spectra are shown in figure 1, and are seen to be qualitatively in agreement. If it were possible for us to experimentally obtain fluorescence spectra in the environment of interest, then it is conceivable that temperature and quenching rate predictions could be made by comparison with the theoretically generated results.

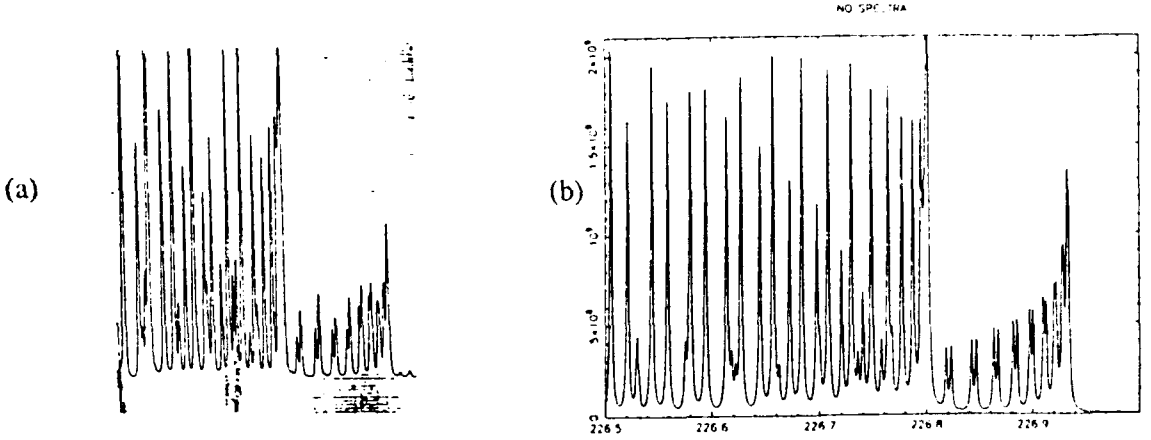

Figure 1 - (a) experimental and (b) theoretical excitation scan of the A-X(0,0) transition of NO.

EXPERIMENT AND RESULTS

The complete experimental arrangement is shown in figure 2, where 2(a) depicts the set up for LIF measurements in a flow field, and 2(b) the setup for PLIF.

The excitation source is a homebuilt ArF excimer laser. The wavelength of the radiation, 193nm, coincides with transitions in NO, the species under study. Shot-to-shot reproducibility in the laser output is rather poor, and the beam profile is not ideal due to the quality of the discharge. Output energies are in the range 5 - 30 mJ/pulse, and the temporal decay of the laser output is such that there is little or no lasing after 20 minutes. The duration of the laser pulse is 17ns, and the repetition rate is 1Hz. The FWHM of the laser has been measured to be approximately 0.6nm, and an unavoidable consequence of this is that we do not have state selective excitation. Indeed, species specificity cannot be guaranteed as transitions in molecular oxygen are also accessed by the laser, which significantly complicates the interpretation of broadband fluorescence data when both oxygen and nitric oxide are present in the environment being probed (see Dionnet *et al* 1992).

In order to perform PLIF, the laser beam has to be carefully shaped to the desired geometry. All beam shaping optics are uv graded quartz. Both cylinderical and spherical lenses are used to form a laser sheet from the rectangular beam profile of the laser for the planar experiments. Spherical lenses are used for imaging purposes.

The detection system for PLIF consists of a lens-coupled intensified CCD array. The CCD camera is computer controlled, and is complete with frame grabbing software which enables instantaneous viewing of experimental results. In order to eliminate the influence of scattered laser light, a BG24 Schott glass filter is used at the intensified camera aperture.

For laser-induced fluorescence measurements, a solar blind photomultiplier tube and monochromator were employed for detection purposes. Initially, a Jobin Yvon 1/4m path monochromator with dispersion of 8nm/mm in the plane of the slits was used. For higher resolution spectral detection, a Jobin Yvon monochromator with a 1m path length and a dispersion of 1nm/mm is used, with the intensified CCD array mounted with the photocathode of the image intensifier in the exit plane of the monochromator. In a single shot, with this latter setup, it is possible to obtain a spectrum spanning a spectral window of approximately 30nm.

Figure 2

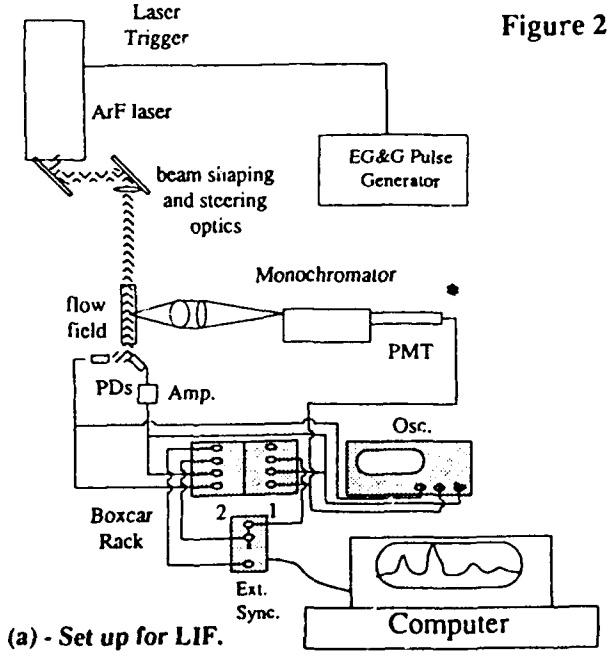

(a) - Set up for LIF.

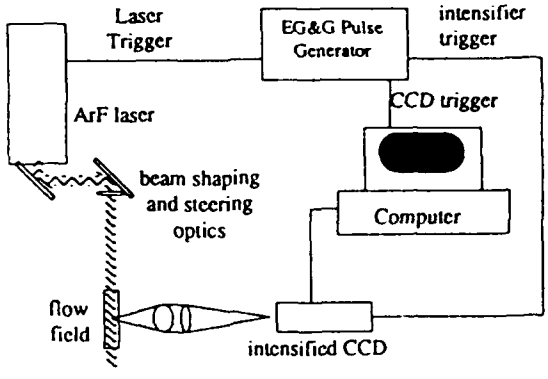

(b) - Set up for PLIF.

* The intensified CCD camera can also be used at the exit of the monochromator for LIF detection.

MEASUREMENTS IN A CELL

Initial fluorescence measurements of NO were performed in an air/acetylene flame. The possibility of seeding the flame was considered, but owing to the more complicated reaction chemistry responsible for the production of NO above 2000K this idea was abandoned, and it was obvious that a controlled environment was required.(see Malmsten *et al* 1993). To this end, a cell was constructed with quartz access windows, and compressed, 99% pure NO was used for controlled cell experiments. Ultra-high purity nitrogen was used as a buffer gas for the cell, and measurements were performed with the cell at atmospheric pressure for varying partial pressures of NO. LIF spectra and PLIF images were obtained for NO concentrations down to about 50ppm in atmospheric nitrogen. A PLIF image from the cell is shown in figure 3.

NOZZLE FLOW MEASUREMENTS

PLIF is a non-intrusive method that is useful as a flow visualisation technique. To illustrate this diagnostic feature, a small nozzle with a diameter of 1.5mm was constructed. A mixture of approximately 1% NO in a nitrogen flow was forced through this to create a nitric oxide containing flow field for imaging purposes. A PLIF image of the resulting flow field captured by the intensified CCD is shown in figure 4. The outline of the nozzle resulting from scattered laser light is visible in the lower part of 4(a), whilst (b) is the same flow-field with a BG24 filter eliminating scattered laser light. There was no possibility for calibration or seed control, however, one can deduce from the pictures obtained that the method is valuable for building immediate flow-field understanding of a qualitative nature.

Figure 3 (left) - PLIF image of 500ppm NO in atmospheric nitrogen in a room temperature cell.

Figure 4 (below) - PLIF images of NO in a nozzle flow. 4(a) (left) - without BG24 filter, 4(b) (right) - with filter to eliminate scattered laser light.

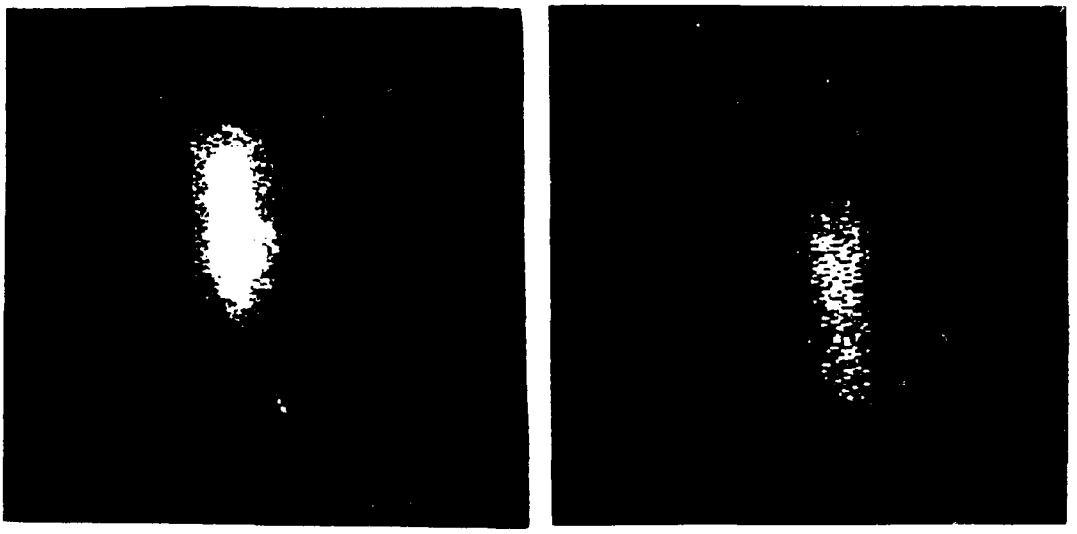

4(a) **4(b)**

CONCLUSION

Laser induced fluorescence and the planar extension thereof, have proven to be qualitatively successful flow-field diagnostics. Nitric oxide has been detected for concentrations down to 50ppm in atmospheric nitrogen at room temperature. Given that the expected concentration within the small shock tube currently operational is about 1%, PLIF results thus far show that the method should be succesful as a flow field diagnostic in this environment, despite equipment limitations. However, the question of how quenching effects the fluorescence yield in such an environment is yet to be answered. The difficulty will then be to extract quantitative information, a problem that is not only complex because of the nature of the flow, but additionally challenging given the broadband excitation and the method of detection.

REFERENCES

Crane, K. C. A., and Stalker, R. J., (1977) "Mass-spectrometric analysis of hypersonic flows", *J. Phys. D:Appl. Phys.*, **10**, 679-695.

Dionnet, F., Mouard, J., and Puechberty, D., (1992) "Broad band excimer laser induced fluorescence applied to hypersonic and supersonic air flows." *NATO Advanced Research Workshop, New Trends in Instrumentation for Hypersonic research, April 27 - May 1, ONERA Le Fauga-Mauzac, France.*

Hanson, R. K., Chang, A. Y., Seitzman, J. M., Lee, M. P., Paul, P. H., and Battles, B. E., (1990) "Laser-induced fluorescence diagnostics for supersonic flows", *28th Aerospace Sciences Meeting, Reno, Nevada.*

Malmsten, Y., Thomas, A., Barker, P., Axner, O., Rubinsztein-Dunlop, H., and Olsson, J., (1993) "Nitric Oxide and OH measurements for concentration and temperature determinations in a counter-flow atmospheric pressure methane-oxygen diffusion flame by laser-induced fluorescence", preprint for *Conference on reduction of combustion pollutants , Portugal.*

McMillin, B. K., Lee, M. P., Palmer, J. L., and Hanson, R. K., (1991) "Two-dimensional imaging of shock tube flows using planar laser-induced fluorescence", *18th International Symposium on Shock Waves, July 21 - 26, Sendai, Japan.*

Stalker, R. J., (1988) "Hypervelocity Areodynamics in Australia", *Journal of the British Interplanetary Society*, **41**, 611-618.

Van Cruyningen, I., Lozano, A., and Hanson, R. K., (1990) "Quantitative imaging of concentration by planar laser-induced fluorescence", *Experiments in Fluids*, **10**, 41-49.